Exploring magnetic and electronic properties in -Al2O3/SrTiO3

Christensen, Dennis Valbjørn

Publication date:
2018

Document Version
Publisher's PDF, also known as Version of record

Ph.D. Thesis
Doctor of Philosophy

DTU Energy
Department of Energy Conversion and Storage

Exploring magnetic and electronic properties in γ-Al_2O_3/$SrTiO_3$

Dennis Valbjørn Christensen

Roskilde 2018

Section for Electrofunctional Materials
Department of Energy Conversion and Storage
Technical University of Denmark

DTU Risø Campus
Frederiksborgvej 399
4000 Roskilde, Denmark
Building 779

Prof. Dr. Nini Pryds
Phone: +45 4677 5752
E-mail: nipr@dtu.dk

ISBN 978-87-92986-63-4

Summary

The increasing impact of electronic devices on our daily lives has caused the strong market pull that has empowered the tremendous development in realizing faster, smaller and more energy efficient devices. Two routes are used to satisfy this market pull: (i) Improving existing devices or (ii) designing devices with new functionalities. The functionalities that can be achieved in devices are determined by the constituent materials. Appealing functionalities may thus be realized by using materials beyond the semiconducting materials that currently constitute the backbone of state-of-the-art electronic devices. An example is the 3D-Xpoint memory technology introduced in Intel/Micron's next generation of memory devices, which are using new memristive functionalities in chalcogenides rather than the traditional semiconducting floating gate transistors used in solid state drives (SSD).

In 2004, a new material platform was discovered, which in the following decade remarkably turned out to exhibit a plethora of functionalities. The material platform was formed by depositing a thin film of $LaAlO_3$ (LAO) epitaxially on $SrTiO_3$ (STO). Despite both oxides were considered non-magnetic and insulating, conductivity and magnetism emerged at the interface. Numerous other functionalities were also discovered including gate-tunable superconductivity, non-volatile resistive switching, and a giant Seebeck coefficient.

In 2013, LAO was replaced with γ-Al_2O_3 (GAO) resulting in an improved epitaxial growth and electron mobility. Open questions remained, however, regarding the origin of the electron gas confined at the interface and whether GAO/STO would exhibit appealing functionalities similar or perhaps superior to LAO/STO. In this thesis, I first describe the non-isomorphic epitaxial growth of the spinel GAO on perovskite STO and how it leads a useful symmetry breaking at the interface. Second, I present how oxygen vacancies lead to the emergence of an electron gas at the GAO/STO interface. The electron gas is highly tunable by deposition control, postannealing in oxygen, electrostatic gating and light exposure. At room temperature the electron mobility is limited to 12 cm^2/Vs by phonon scattering. At 2 K the mobility exceeds 100,000 cm^2/Vs, which I propose is due to an electron-donor separation. The electron gas exhibits a colossal positive magnetoresistance of 80,000% at 2 K and 15 T with a great potential for realizing extraordinary magnetoresistance. In addition, a strain-tunable magnetic state is observed in GAO/STO. The thesis ends with my view on how the understanding and number of functionalities can be improved further.

Resumé

Elektronisk udstyr bliver en større og større del af vores dagligdag, hvilket har intensiveret udviklingen i at lave hurtigere, mindre og mere strømbesparende komponenter. Der kan skelnes mellem to udviklingsprocesser: (i) Optimering af eksisterende udstyr og (ii) design af udstyr med nye funktionaliteter. De funktionaliteter, der kan opnås i elektriske komponenter, bestemmes af de materialer, de er bygget af. Attraktive funktionaliteter kan således realiseres ved at anvende andre materialer end de halvledere, som udgør rygraden i moderne elektronik. Et konkret eksempel er hukommelsesteknologien 3D-Xpoint, der introduceres i Intel/Microns nye generation af hukommelsesenheder. Her bruges nye memristive funktionaliteter i chalcogenider frem for de traditionelle halvledende floating-gate transistorer, der i dag anvendes i SSD-hukommelse.

I 2004 blev en ny materialeplatform opfundet, som i det følgende årti udmærkede sig ved at udvise en overflod af funktionaliteter. Materialeplatformen blev dannet ved at deponere en tynd film af $LaAlO_3$ (LAO) epitaksialt på $SrTiO_3$ (STO). Til trods for at begge oxider bliver betragtet som ikke-magnetiske og isolerende, opstod der ledningsevne og magnetisme på grænsefladen. Talrige andre funktionaliteter blev også opdaget, herunder gate-tuning af superledning, resistansændringer og en kæmpe Seebeck-koefficient.

I 2013 blev LAO erstattet af γ-Al_2O_3 (GAO), hvilket resulterede i en forbedret epitaxial deponering og elektronmobilitet. Spørgsmål omkring oprindelsen af ledningsevnen i GAO/STO forblev dog uafklarede, og det var ligeledes uvist, om GAO/STO ville udvise attraktive funktionaliteter svarende til eller bedre end LAO/STO. I denne afhandling beskriver jeg først den epitaksielle deponering af spinel GAO på perovskit STO, og hvordan det fører til et brugbart symmetribrud ved grænsefladen. Herefter viser jeg, hvordan ilt-vakancer skaber elektrongassen på grænsefladen af GAO/STO. Elektrongassen kan tunes drastisk vha. en ændring i deponeringsbetingelserne, bagning i oxygenrigt miljø, elektrostatisk gating og lyseksponering. Ved stuetemperatur begrænses elektronmobiliteten til 12 cm^2/Vs af kollisioner med fononer, mens den ved 2 K kan overstige 100.000 cm^2/Vs formodentligt pga. en elektron/donor-separation. Elektrongassen udviser en kolossal positiv modstandsændring på 80.000% under påtrykkelse af et magnetfelt på 15 T ved 2 K med et stort potentiale til at kunne videreudvikles til en ekstraordinær magnetoresistans. GAO/STO udviser desuden også magnetisme, som kan tunes mekanisk. Afhandlingen afsluttes med en beskrivelse af, hvordan forståelsen og antallet af funktionaliteter kan forbedres yderligere.

Preface

This PhD thesis is submitted in the partial fulfillment of the requirements for acquiring the PhD degree at the Technical University of Denmark. The content of the thesis is based primarily on research collaborations between Department of Energy Conversion and Storage at the Technical University of Denmark, Center for Quantum Devices at the University of Copenhagen, Physics Department at Bar-Ilan University, Department of Physics and Astronomy at University of Würzburg and Department of Physics at University of Fribourg.
During the course of this PhD project, I have worked with different technologies and materials as reflected by the publication list provided in Appendix A, but the thesis only includes the part concerning the γ-$Al_2O_3/SrTiO_3$ heterostructure. In order to present a coherent story, my own contributions are described on equal terms with the research conducted by other groups. My contributions can be discriminated by the reference format: Roman letters (e.g. [XI]) refer to articles published as part of this PhD, whereas Arabic numbering (e.g. [11]) is used for articles from other groups.

Principal supervisor:
Prof. Nini Pryds, Technical University of Denmark

Co-supervisors:
Dr. Yunzhong Chen, Technical University of Denmark
Dr. Anders Smith, Technical University of Denmark

Assessment committee:
Prof. Chang Beom Eom, University of Wisconsin-Madison
Dr. Fabio Miletto Granozio, CNR-SPIN Institute Naples
Prof. Jesper Nygård (chairman), University of Copenhagen

Roskilde, July 21st, 2017

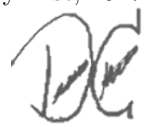

Dennis Valbjørn Christensen

Acknowledgements

I will like to acknowledge the help, support and collaboration from family, friends, coworkers and supervisors:

First, I would like to thank the head of my department Søren Linderoth and section leader Nini Pryds for making this PhD project possible. I am particularly grateful that I was provide the freedom to define my own research, which motivated my creativity, ignited my curiosity and enabled me to work on a broad range of research topics beyond exploring the γ-Al_2O_3/$SrTiO_3$ heterostructure. Despite the free working conditions, support could always be found from my supervisors Nini Pryds, Yunzhong Chen and Anders Smith if needed. Mutual support was also provided within our group at Risø, in particular between my fellow students Felix Trier, Merlin von Soosten, Yulin Gan, Yu Zhang and Wei Niu, and by our closest collaborators at Center for Quantum Devices at University of Copenhagen, most noticably Thomas Sand Jespersen and Guen Prawiroatmodjo. A special thanks goes to Felix for the thesis template and to our technical administrative personnel including our skilled technician Jørgen Geyti, secretary Anita Voss and project controller Christina Mølkjer.

The receipt of the EliteForsk travel grant from the Danish ministry of higher education and science, and the short term scientific mission support provided by the European COST program TO-BE headed by Fabio Miletto Granozio have been highly appreciate. The funding allowed me to establish fruitful international collaborations and enabled my external research stays abroad. In this regard, I would like to thank Beena Kalisky, Yiftach Frenkel and all the other fun people in the groups of Beena Kalisky and Amos Sharoni at Bar-Ilan University, Israel, for receiving me open-heartedly during my stay there. The good collaborations on photoemission are also highly appreciated, in particularly the collaboration with Philipp Schütz, Philipp Scheiderer, Michael Sing and Raelph Claessen from Würzburg University in Germany and Zhiming Wang and Milan Radovic from Paul Scherrer Institute in Switzerland. I acknowledge especially Felix Gunkel and Regina Dittmann for the high-temperature equilibrium conductance measurements that provided an interesting view on the origin of the conductivity in $SrTiO_3$-based heterostructures. The infrared optical measurements on γ-Al_2O_3/$SrTiO_3$ were also very interesting, and my appreciation goes to Christian Bernhard and Yazdi Meghdad for this collaboration. In addition, I have highly appreciated the scientific discussions with Lior Klein, Felix Gunkel, Jeremy

Levy and Fabio Miletto Granozio.

I would also like to share my appreciation of the inspiring collaborations that has not (yet) led to collaborative publications on the topics of (i) magnetism and electron pairing with Jeremy Levy, Lu Chen and Jianan Arthur Li from University of Pittsburgh in USA, (ii) surface phonon polaritons at the γ-Al_2O_3/$SrTiO_3$ surface with Nicolas Stenger, Asger Mortensen and Sanshui Xiao from the Technical University of Denmark, (iii) spin-injection in γ-Al_2O_3/$SrTiO_3$ with Sander Kamerbeek and Tamalika Banerjee from the University of Groningen in Holland, (iv) pulsed laser plume diagnostics of the Al_2O_3 plasma plume with Salvatore Amoruso and Xuan Wang from the University of Naples in Italy, (v) inkjet-patterning of the γ-Al_2O_3/$SrTiO_3$ interface conductivity with Christophe Gadea from the Technical University of Denmark, (vi) transport measurements of strained γ-Al_2O_3/$SrTiO_3$ with Iliya Radulov and Oliver Gutfleisch from the Technische Universität Darmstadt in Germany and (vii) pyroelectricity of $SrTiO_3$ surfaces with David Ehre and Igor Lubomirsky from the Weizmann Institute in Israel.

Lastly, I would like to thank my family and friends for support. The long nights in the lab surely were crowned by worried flat mates alerting the Israeli police due to my mysterious disappearance. Likewise, my intense period of thesis writing certainly would not have been the same without the Jazz-festival invitations, receipt of vacation photos etc. that reminded me of what awaits after the completion of the thesis. Amager Beach Park deserves my last appreciation as its wooden pontoon served as an excellent office during the thesis writing.

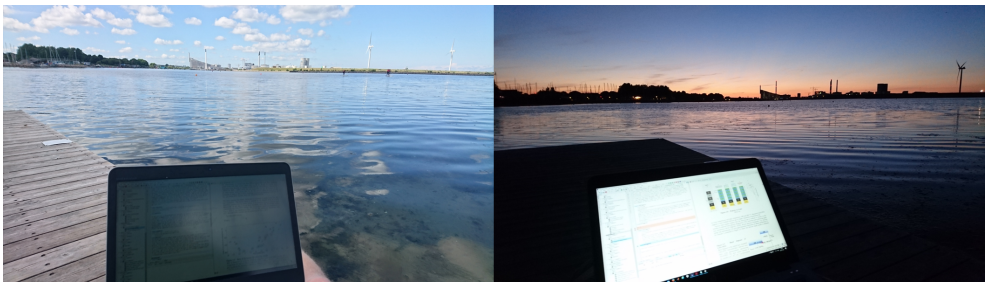

List of acronyms & symbols

Symbol	Quantity	Value
$e > 0$	elementary charge	$1.602 \times 10^{-19}\,\mathrm{C}$
m_0	free electron mass	$9.109 \times 10^{-31}\,\mathrm{kg}$
$h = 2\pi\hbar$	Planck constant	$6.626 \times 10^{-34}\,\mathrm{J\,s}$
k_B	Boltzmann constant	$1.381 \times 10^{-23}\,\mathrm{J/K}$
μ_B	Bohr magneton	$9.274 \times 10^{-24}\,\mathrm{J/T}$
ε_0	vacuum permittivity	$8.854 \times 10^{-12}\,\mathrm{F/m}$

Physical constants

Acronym	Definition
2-DEG	two-dimensional electron gas
a-AO	amorphous alumina
a-LAO	amorphous $LaAlO_3$
AFM	atomic force microscope
ALD	atommic layer deposition
ARPES	angle-resolved photoemission spectroscopy
c-AFM	conducting-atomic force microscope
DFT	density functional theory
EELS	electron energy loss spectroscopy
FET	field effect transistor
GAO	γ-Al_2O_3
HTEC	high temperature equilibrium conductance
LAO	crystalline-$LaAlO_3$
LSM	$La_{7/8}Sr_{1/8}MnO_3$
MBE	molecular beam epitaxy
MR	magnetoresistance
PLD	pulsed laser deposition
RHEED	reflection high-energy electron diffraction
SQUID	superconducting quantum interference device
STO	$SrTiO_3$
XPS	x-ray photoelectron spectroscopy

Acronyms with definitions

Symbol	Quantity	Unit
α	electron-phonon coupling strength	-
a_{STO}	lattice constant of $SrTiO_3$	Å
a_{GAO}	lattice constant of γ-Al_2O_3	Å
x, y, z	spacial directions	-
d_{xy}, d_{xz}, d_{yz}	3D orbitals	-
$p\mathrm{O}_2$	oxygen partial pressure	mbar
T	temperature	K
B	magnetic field	T
E	electric field	kV/cm
E_a	activation energy barrier	eV
E_g	bandgap between valence and conduction band	eV
E_F	Fermi energy	meV
ω_c	angular frequency of the electron cyclotron motion	s^{-1}
ω_{LO}	angular frequency of the longitudinal optical phonon	s^{-1}
I	current	nA
V	voltage	V
V_g	voltage applied on gate	V
$R = 1/G$	resistance, equaling the inverse conductance	Ω
$R_s = 1/G_s$	sheet resistance, equaling the inverse sheet conductance	Ω/sq
R_{high}, R_{low}	resistance of high and low-resistive state	Ω
R_{xy}	Hall resistance	Ω
τ	magnetotorque	Nm
τ_s	scattering time	ps
μ	electron mobility	$\mathrm{cm}^2/(\mathrm{V\,s})$
n_s	sheet carrier density	cm^{-2}
$m^\star$	electron effective mass	$\mathrm{m_e}$
m_p	polaron effective mass	$\mathrm{m_e}$
$m_b^\star$	band effective mass	$\mathrm{m_e}$
ε	dielectric constant	ε_0

Physical and miscellaneous variables with adopted units

Contents

CHAPTER 1

Motivation

As the impact of electronic devices continues to increase, the demands for fast, small and energy-efficient electronics strengthen. The immense market pull has caused an incredible progress in the development of electronics. A prominent example is the number of transistors pr. electronic chip, which has followed Moore's law for more than half a century with the number of transistors on a chip doubling roughly every 24 months. In comparison, if the same progress was seen elsewhere, after less than 50 years a regular car would drive faster than the speed of light and a single liter fuel would suffice to drive a distance comparable to making a round trip to the sun. Two strategies can be used to satisfy the intense market pull: (i) Existing devices and technologies can be improved and (ii) novel devices can be designed by implementing new technologies. The two strategies can be conveniently illustrated using the next generation of transistors and memory devices:

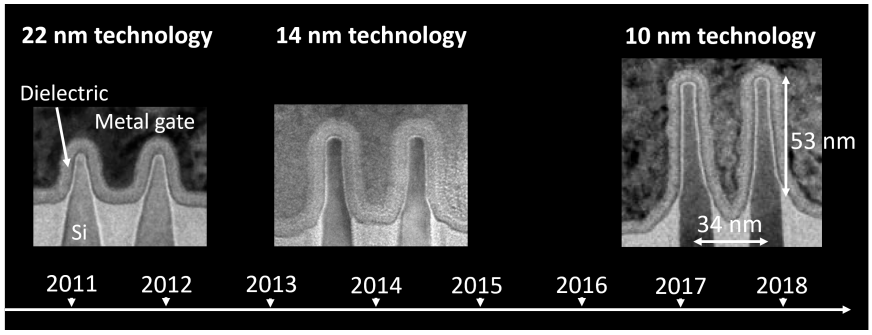

Figure 1.1 – Transistor down-scaling by Intel
Timeline of the three recent tri-gate field effect transistor generations fabricated by Intel using 22 nm, 14 nm and 10 nm technology. The figure is created based on Ref. [1].

1.1 Optimizing existing devices: the 10 nm technology transistors

The dominant transistor on the market is the field effect transistor (FET). Intel alone produces more field effect transistors pr. second than there are people on the planet [1]. In the typical metal-oxide-semiconductor FET (MOSFET), the conductivity of the semiconductor (typically silicon) is changed by applying an electric field through an oxide dielectric using a metal gate. The FET can be implemented using different geometries and materials with e.g. the mobility of the semiconductor being an important material parameter when designing fast transistors. In 2011 Intel introduced the tri-gate FET where metal covered fin-shaped silicon leads to accumulation of electrons on three sides (see Figure 1.1). Since then, further improvements have been incremental while still fulfilling Moore's law [1].

1.2 Designing novel devices: the 3D-Xpoint memory technology

Contrary to the incremental optimization of the FET, Micron and Intel has in a partnership developed a new memory device using the so-called 3D-Xpoint memory technology. The memory device is fast, inexpensive and non-volatile. The latter ensures that data remain stored after the power is turned off. The active part in 3D-Xpoint is shaped in columns and connected to contacts on either side by metal in a cross-bar (X-point) configuration (see Figure 1.2). The configuration is stackable in 3D. The active part consists of a memory cell and a selector, both made out of chalcogenides. A specific memory cell can be addressed by application of voltages on the two metal contacts sandwiching the memory cell (see inset of Figure 1.2). A current flow heats up the memory cell and causes a structural phase change. By controlling how fast the current is switched off, the cooling can either induce a crystalline or a glass state with a large difference in the resistance. The set resistance state is stable over time, and can thus be used to store data (0 or 1) in a non-volatile fashion. The state can be read off non-perturbatively by sensing if the resistance between the contacts is high or low using a small current. If the resistance is high, whereas the three neighboring memory cells are in a low-resistive state, the probing current could flow through these memory cells instead of the intended memory cell. This current bypassing would cause an error reading if a selector was not used to prevent this. The selector can e.g. work by having a suitable threshold voltage V_{thres}, which allows current to pass a single selector as needed for the intentional reading, but not the three selectors required for the erroneous current bypassing ($V_{thres} < V_{read} < 3V_{thres}$).

The 3D-Xpoint memory is considered a new, disruptive technology, although the underlying phase change memory was discovered and patented more than 50 years

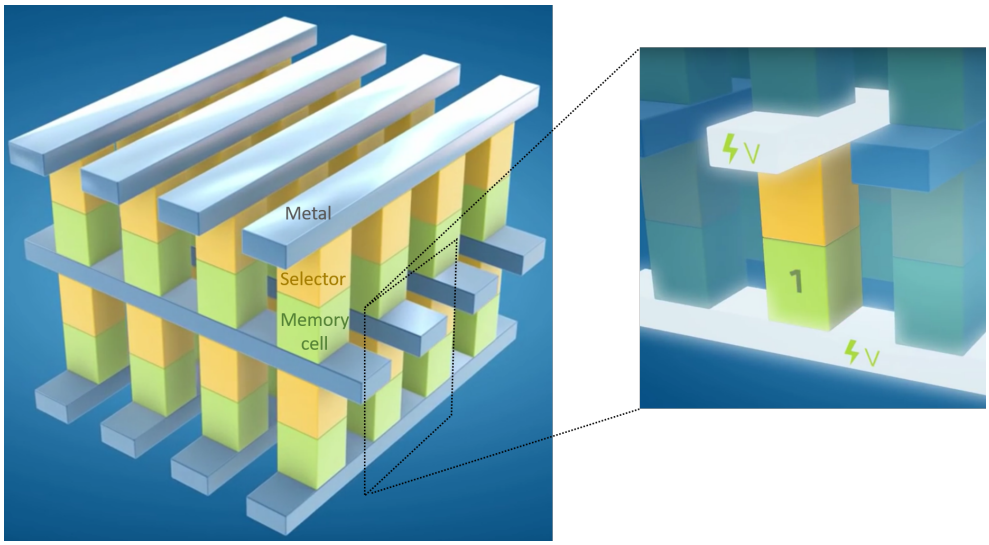

Figure 1.2 – 3D-Xpoint memory
Architecture of the 3D-Xpoint introduced by Intel where a 3D matrix of memory cells and selectors is contacted by metal electrodes in a cross-bar geometry. The inset shows how a single memory cell can be addressed uniquely for reading or setting purposes by applying a potential on the two bordering electrodes. The figure is created based on Refs. [2, 3].

ago [4]. It serves as a prime example of how the search for new functionalities in material research can pave the way for future mass-produced devices.

1.3 Functionalities and oxides

Oxide materials exhibit a particularly broad spectrum of functionalities and remarkable properties, including similar memristive properties as used in 3D-Xpoint. The spectrum of electronic properties spans from insulators with bandgaps exceeding 8 eV [5] or dielectric constants of $300\varepsilon_0$ [6] to metallic conductors with electron mobilities in excess of 1,000,000 cm^2/Vs [7] and high-temperature superconductors with critical temperatures larger than 130 K [8]. Coupling charge and lattice degrees of freedom further results in ferroelectricity [9] and polaron formation [10]. Adding spin degrees of freedom gives strong ferromagnetism [11], spin polarization [12], colossal magnetoresistance [13] and multiferroic materials [14]. By virtue of the broad spectrum of functionalities, oxides have found applications in e.g. transistors, displays, memory devices, and superconducting magnets. A roadmap of electronic oxide materials and interfaces created thereof has recently been published [15].

Combining several functionalities may lead to new application prospects. Two prominent examples are data storage using memristive devices combining ionic motion and electron conductivity, and displays utilizing transparent conductors/transistors combining a large bandgap and (gate-tunable) conductivity. A particularly wide range of exciting properties is observed in the oxide $SrTiO_3$ (STO) as discussed in the subsequent chapter.

CHAPTER 2

$SrTiO_3$-based electronics

2.1 $SrTiO_3$

"*If $SrTiO_3$ had magnetic properties, a complete study of this material would require a thorough knowledge of all of solid state physics*". This sentence was coined by M. L. Cohen in 1969 [16] and describes the opportunities and challenges of using $SrTiO_3$ (STO) with its multifunctional nature spanning most of solid state physics. After 1969 magnetic properties have furthermore been observed in STO [17, 18]. STO remains one of the most popular oxides for electronic purposes. The popularity stems mainly from two aspects:

The first aspect relates to the compatibility between STO and other oxides. STO is a cubic perovskite at room temperature with a lattice parameter of 3.905 Å [19]. The cubic unit cell is composed of strontium, titanium and three face centered oxygen anions as depicted in Figure 2.1. In addition, the (001) surface of STO can be prepared to be atomically flat and terminated solely by TiO_2. The crystal structure and surface termination make STO compatible with epitaxial growth of numerous other oxides.

The second reason for the extensive use of STO originates from its multifunctional nature. STO features a high dielectric constant increasing from 300 at room temperature to more than 20,000 below 10 K [20]. The large increase occurs as STO is on the verge of becoming ferroelectric by displacing titanium ions relative to the oxygen ions. Quantum oscillations, however, prevents the ferroelectric transition and STO instead becomes a quantum paraelectric below $\sim$40 K with a large dielectric constant [21]. Modifying the lattice through application of strain can result in stabilization of the ferroelectric phase even at room temperature [22]. Together with the room temperature observation of ferromagnetism [17, 18], strained STO is likely to be a room temperature multiferroic material, albeit the coexistence of room-temperature ferroelectricity and ferromagnetism has not yet been demonstrated. Cooling down STO below 105 K causes a cubic-to-tetragonal phase transition with formation of three types of domains where the cubic unit cell is expanded along either the [001], [010] or

[100] crystallographic direction. The domain walls are ferroelastic in addition to likely being ferroelectric [23] and ferromagnetic (see Chapter 9). At low temperatures, the high dielectric constant causes a high electron mobility exceeding 20,000 cm^2/Vs [24] with a possibility to increase the mobility up to 120,000 cm^2/Vs by straining STO with a three-point bending device [25]. Below $\sim$300 mK, STO is superconducting at low carrier densities [26, 27].

Breaking the lattice symmetry of STO by interfacing it with a solid material may lead to emergent properties beyond those found in the parent materials. Importantly, a confined electron gas can be formed at the interface, which enables the gate-tunability that has lead to the large success of modern semiconductor technologies.

2.2 Growth of $SrTiO_3$ heterostructures

STO-based heterostructures can be created in various ways. Figure 2.1 summarizes the typically experimental steps:

1. As-received polished STO surfaces contain a mixed termination of SrO and TiO_2. Chemical treatment is used to obtain surfaces with only TiO_2-termination and a subsequent thermal annealing is then used to relieve surface tension introduced by polishing STO. The chemical treatment is a specific removal of SrO which can be done in various ways including etching by acids such as HF or HCl/HNO_3 or immersing STO in hot water [28–30].
2. Thin films are deposited on the TiO_2-terminated STO surface. Pulsed laser deposition is often used, however, numerous other deposition techniques have been employed including molecular beam epitaxy [31], atomic layer deposition [32, 33] and metal evaporation [34]. Reflection high energy electron diffraction (RHEED) is often used to probe the thickness and crystallinity of the deposited thin film [35]. The resulting interface properties are found to be highly dependent on the deposition conditions and type of material deposited [35–37].
3. The final step is preparation for the subsequent measurements. If electronic properties are investigated, the buried interface is typically contacted in a van der Pauw or Hall bar geometry using deposited metal contacts or wedge bonding penetrating the heterostructure.

2.3 $LaAlO_3/SrTiO_3$

The pioneering $LaAlO_3$ (LAO)/STO heterostructure was discovered in 2004 by Ohtomo and Hwang [35]. Here, conducting interfaces between the two insulators were obtained when LAO was grown epitaxially on STO. LAO is a rhombohedrally distorted perovskite, which can be approximated as cubic with a lattice parameter of 3.789 Å [35]. The resulting lattice mismatch is $\sim 3\%$ with STO exerting tensile stress on LAO.

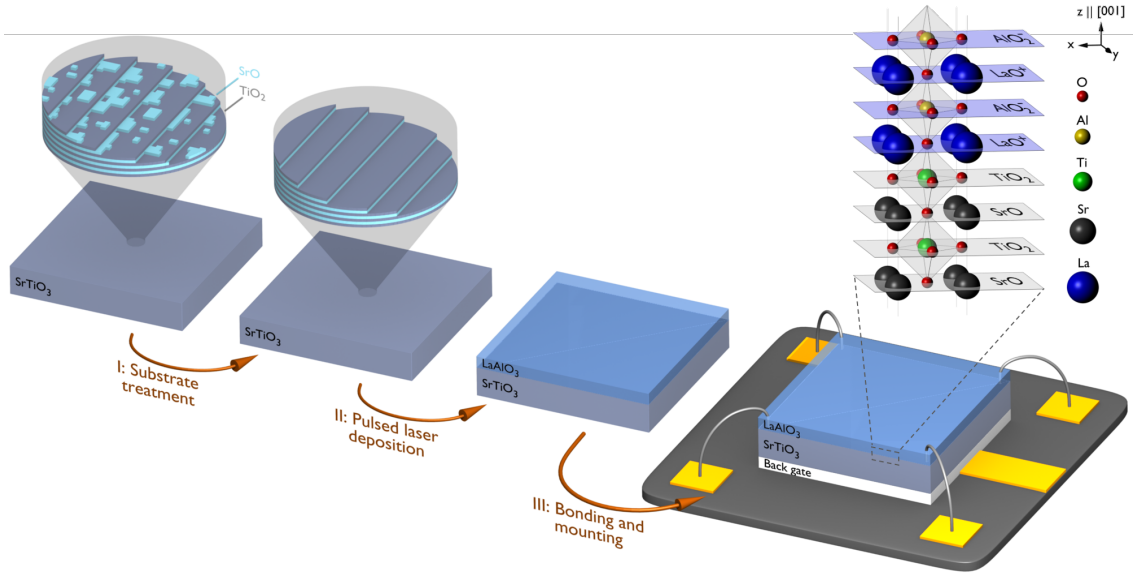

Figure 2.1 – Experimental overview
The creation of multifunctional STO-based heterostructures are typically done in the following steps: (I) Chemical TiO_2-termination of STO, (II) deposition of a thin film (here $LaAlO_3$), oftentimes using pulsed laser deposition and (III) preparation for further characterization, e.g. by mounting a backgate on the heterostructure and contacting the interface electronically using ultrasonic wedge bonding. The insets show the mixed SrO- and TiO_2-termination surface, a TiO_2-termination surface and the crystal structure across the LAO/STO interface.

LAO furthermore undergoes a stress-dependent transition to cubic at 810 K [38]. The LAO/STO interface proved to be highly multifunctional soon after its discovery.

2.3.1 Multifunctionality

The conducting interface was found to crucially dependent on the LAO thickness (see Figure 2.2a): Depositing 3 unit cells of LAO or less resulted in an insulating interface, whereas LAO thicknesses of 4 unit cells and above created conductivity. At a LAO thickness of 3 unit cells, conductivity could be induced macroscopically using a backgate or on the nanoscale using a biased tip of a conducting atomic force microscope (see Figure 2.2b-d). Both methods change the (local) resistance by orders of magnitude in a non-volatile fashion. Along with the observation of magnetism and superconductivity in LAO/STO [36, 39], this initiated a large interest in the heterostructure and a plethora of remarkable properties were soon discovered. Table 2.2 provides a non-exhaustive list of the functionalities observed in LAO/STO. Many

of the properties are inherited directly from STO, but the electron confinement often allows the properties to be gate-tunable in LAO/STO. Reviews of the STO-based interface conductivity are found in Refs. [40, 41].

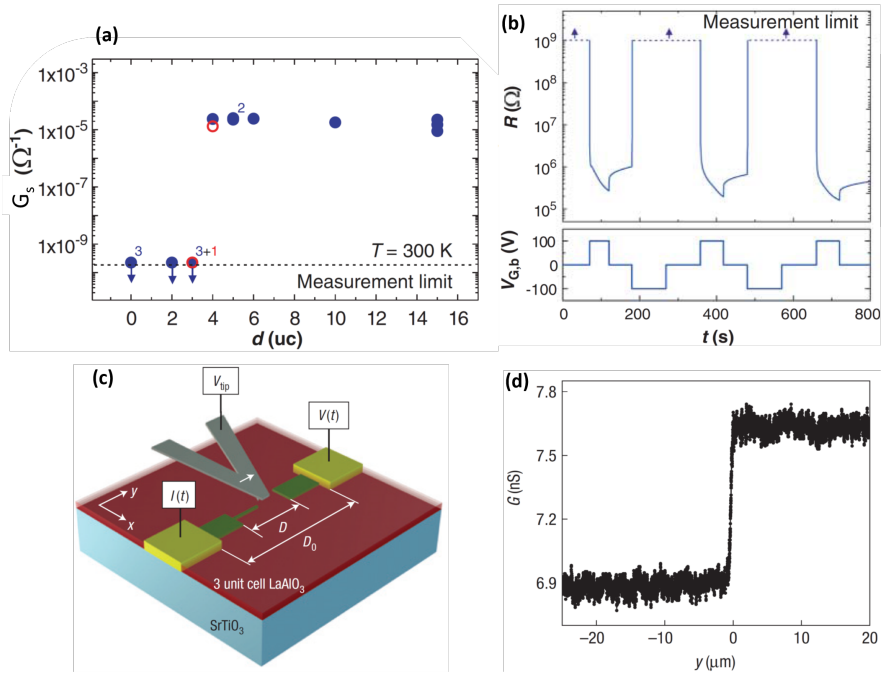

Figure 2.2 – Critical thickness and gate-tunability
(a) The sheet conductance (G_s) as a function of the LAO thickness (d) in unit cells. Data shown in blue and red are pulsed laser depositions of LAO at 770 °C and 815 °C, respectively. The numbers next to the data markers indicate the number of samples with indistinguishable sheet conductance. (b) Changes in the interface resistance (R) upon applying back-gate voltages ($-100\ \text{V} \leq V_{G,b} \leq 100\ \text{V}$) to a LAO/STO sample with a LAO thickness of 3 u.c. (c) Setup for inducing nanoscale conductivity at the LAO(3 u.c.)/STO interface using a positively biased conducting atomic force microscopy tip. (d) Conductance between two contacts when the tip is scanned along y from one contact to the other. An increase in the conductance (G) is found when the two contacts connect electrically via the induced conducting line. The figures are adopted from [42, 43].

Functionality	**Key finding**	**Refs.**
Electrical conductivity	Emergence of an electron gas at the interface between two oxide insulators.	[35]
Electron mobility	High electron mobility exceeding 6,000 cm^2/Vs in 2D-confined electron gases and 20,000 cm^2/Vs in 3D-conducting or 1D-confined electron gases	[44] [45] [46]
Resistance switching	Non-volatile resistance change with $(R_{high} - R_{low})/R_{low} > 10^5$ induced with a back-gate potential	[42]
Conducting nanowires	Non-volatile resistance change induced on the nanoscale using a biased conducting-AFM tip	[43] [47]
Magnetism	Magnetic order observed at low temperatures. A magnetic phase is found to be gate-tunable and persist up to room temperature.	[36] [48] [49]
Superconductivity	Superconductivity with $T_c \approx 200\,\mathrm{mK}$. The superconductivity is gate-tunable and exists in samples also showing magnetism.	[39] [50] [48]
Electron pairing	Electron pairing exists without superconductivity	[51]
Polaron formation	Formation of a polaronic metal state by coupling of electrons and lattice distortions	[52]
Spin/orbit coupling	Gate-tunable Rashba spin/orbit coupling	[53]
Magnetoresistance	Large positive and negative magnetoresistance observed by applying transverse or parallel magnetic fields	[36] [54]
Photoconductivity	Giant persistent photoconductivity at room temperature with $(R_{high} - R_{low})/R_{low} > 10^5$	[55]
Photogeneration	Generation and detection of terahertz radiation from a 10 nm junction	[56]
Piezoelectricity	Giant piezoelectric effect with $\mathrm{d}z/\mathrm{d}V \approx 1$ nm/V observed using a scanning-single electron transistor	[57]
Thermoelectricity	Gate-tunable Seebeck effect with $S \sim 10^5\,\mu\mathrm{V/K}$	[58]

Table 2.1 – Functionalities found in the $LaAlO_3/SrTiO_3$ heterostructure.

2.3.2 Origin of the conductivity

Despite extensive research the origin of several of the remarkable properties is still not clear, including the emergence of interface conductivity. Several different mechanisms have been proposed. Below I shortly review the most used explanations where the conductivity arises from either oxygen vacancies, the polarity in LAO or a combination of these:

Oxygen vacancies

The large electronegativity of oxygen causes it to attract electrons from neighboring atoms leaving it with an oxidation state of O^{2-}. When an oxygen vacancy is formed by removing neutral oxygen from STO, the electrons are donated to the lattice (see Figure 2.3). Here, the electrons can localized around the neighboring titanium ions or contribute to the conductivity by delocalizing over the titanium 3d conduction band (see Articles [XII, XX] in Appendix B). The ability to create conductivity from oxygen vacancies is observed by changing STO from an insulator to a metallic conductor when annealing STO in vacuum at elevated temperatures (Article [XII]). In the case of LAO/STO, the LAO deposition is typically performed in a low oxygen partial pressure with STO heated to above 500 °C, which may cause oxygen vacancies to form in STO either due to the heat-treatment in vacuum alone or the deposition of LAO [37, 59].

Polar discontinuity

As depicted in Figure 2.4a, the (001) planes of STO are charge neutral whereas the planes in LAO are charged with an alternating charge density of ± 1 elementary charge pr. surface unit cell. If the charges are left uncompensated, an electric field will form between the layers resulting in a monotonically increasing electrostatic potential. This potential adds to the energy of the electrons in LAO, and electron donation to STO occurs when the occupied electronic states obtain a higher energy than the STO conduction band (Figure 2.4b). The electrons may originate from the valence band or

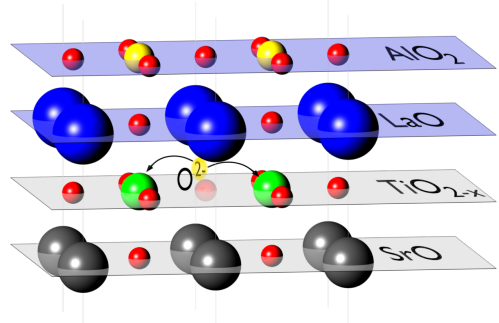

Figure 2.3 – Conductivity by oxygen vacancy
Schematic illustration of how forming a neutral oxygen vacancy donates two electrons to the lattice. The electrons can either be localized or delocalized.

in-gap defect/surface states of LAO. The electron transfer to STO is only expected when the LAO thickness exceeds a critical value consistent with the experimental observations.

Polarity-induced defect formation

The mechanisms based on oxygen vacancies and LAO polarity were reconciled by the polarity-induced defect mechanism [61]. Here, the polarity of LAO causes the spontaneous formation of oxygen vacancies at the LAO surface above a critical LAO thickness of ~ 4 u.c. An electron transfer to STO occurs as the oxygen defect level is higher than the conduction band of STO, which in turn counteracts the potential build-up in LAO. To date, this mechanism is likely to be the explanation for the conductivity in LAO/STO that is most agreed upon.

2.4 Other $SrTiO_3$-based material systems

In the wake of the remarkable findings found in the LAO/STO heterostructure, various other related oxide material systems were formed. Besides expanding the long list of functionalities, studying heterostructures beyond LAO/STO proved to be useful for determining the origin of the conductivity in the various material systems, including LAO/STO itself. An example of this is given in Chapter 5.1.1. By considering oxides systems beyond LAO/STO, it was found that conductivity could be formed in STO surfaces by e.g. cleaving STO in vacuum [62]. In addition, both LAO and STO were substituted with other materials: Substitution of STO led to conducting

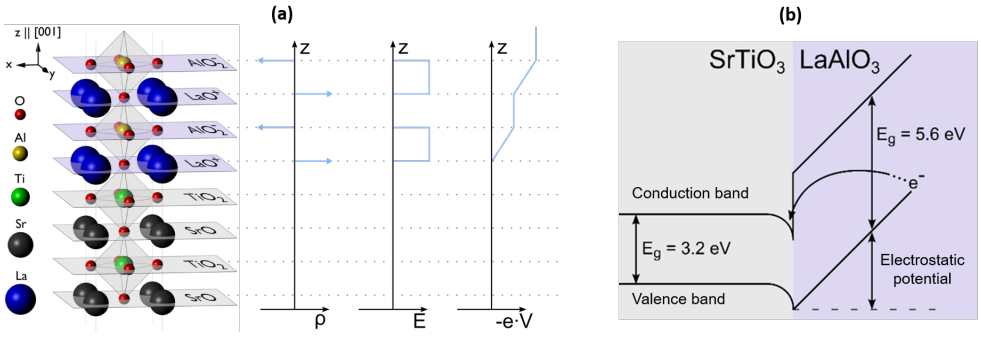

Figure 2.4 – Conductivity by LAO polarity
(a-b) Schematic illustration of how the polarity in LAO may cause an electrostatic potential build-up resulting in an electron transfer from LAO to STO above a critical LAO thickness. The electron transfer may occur from the LAO valence band or from in-gap states. The figure is inspired by Ref. [60].

interfaces in e.g. LAO/$BaTiO_3$ [63], TiO_2/LAO [64] and LAO/TiO_2 [XXII]. Substituting LAO has resulted in conducting interfaces when STO is capped with e.g. Al_2O_3 [34, 65], STO [37], $CaZrO_3$ [IV], Mn-doped LAO [XXVII] and $CaHfO_3$ [66]. The γ-Al_2O_3/STO heterostructure has attracted particular attention primarily due to its high mobility, and this heterostructure will be the subject of the remainder of the thesis.

CHAPTER 3

The γ-Al_2O_3/$SrTiO_3$ heterostructure

An interesting STO-based heterostructure is formed when crystalline γ-Al_2O_3 (GAO) is deposited on the TiO_2-terminated (001) surface of STO. In 2013, where the current PhD project was initiated, a few reports were published on this heterostructure with three main findings [32, 34, 65]: First, it was observed that a pseudoepitaxial growth of crystalline GAO was possible on STO despite different crystal structures [65]. Second, the growth of amorphous or crystalline Al_2O_3 induced an electron gas at the interface [32, 34, 65]. Third, high electron mobilities and carrier densities could be obtained in the GAO/STO heterostructure. The itinerant electrons were suggested to originate from oxygen vacancies in STO, but the origin remained an open question as the influence of a possible polarity in GAO was undetermined. Moreover, it remained undemonstrated whether GAO/STO could be the host of the interesting interface phenomena found in LAO/STO, and potentially show properties superior to these.

In the recent years, significant progress has been made, and in the following I describe what is currently known about the GAO/STO heterostructure. First, I present the different crystal structures of GAO and STO, and discuss how GAO can be grown pseudo-epitaxially on STO leading to a large symmetry breaking at the interface. Second, I introduce the electronic properties of the GAO/STO heterostructure and discuss the origin and transport of the itinerant electrons. Having laid the foundation for understanding the electronic properties, I describe how the knowledge can be used to tune the electron density at the interface in various ways. I then show three appealing properties observed in GAO/STO, namely the high electron mobility, colossal magnetoresistance and emergent magnetism. Lastly, I will suggest interesting future directions to be studied. The outline is presented in Figure 3.1 where each topic includes the relevant articles published as part of this thesis. A full publication list is found in Appendix A, and a selection of the most relevant articles is found in Appendix B.

In order to make a coherent story with a clear common thread, the thesis describes the research conducted by other groups on equal terms with the studies performed as part of this PhD project. To distinguish my own contributions to the field, articles

published, submitted or prepared as part of my PhD project are referenced using Roman letters (e.g. [XXIII]), whereas articles published by other groups without my contribution are referenced using Arabic numbers (e.g. [34]). A list of my contributions to each scientific article published during the PhD project is found in Appendix A.

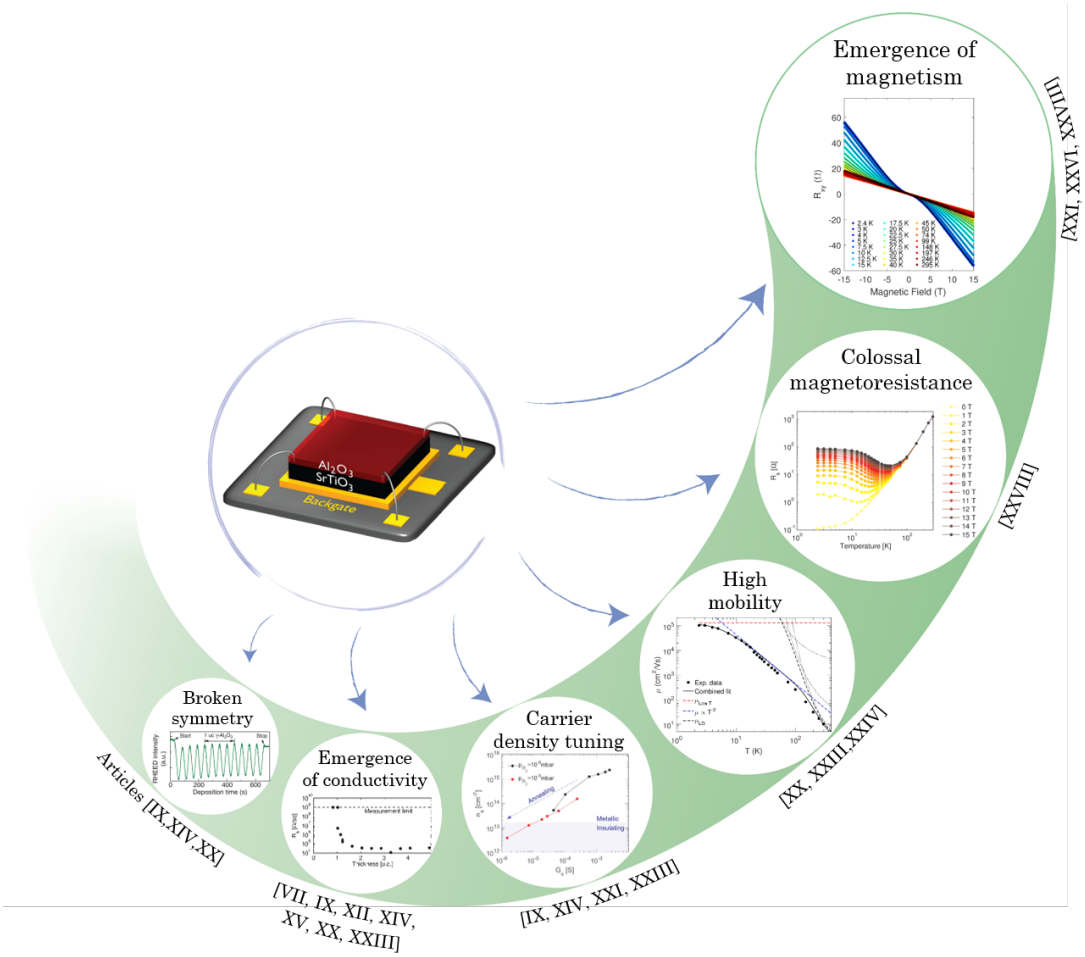

Figure 3.1 – Versatile properties of GAO/STO
An overview of the various phenomena observed when GAO is deposited on STO. A chapter is devoted to discuss each phenomena. The figure includes relevant articles published as part of this PhD.

CHAPTER 4

Crystal structure & non-isomorphic growth

As discussed in Chapter 2, perovskite LAO can be grown epitaxially on perovskite STO with a lattice mismatch of 3% with STO exerting tensile stress on LAO. The growth of GAO thin films on STO, however, represents a non-isomorphic epitaxial growth combining two major oxide families, the spinels (AB_2O_4) and perovskites (ABO_3). The cubic spinel unit cell is composed of 32 oxygen anions, 16 B site cations placed in an octahedral environment and 8 tetrahedrally coordinated A site cations (see Figure 4.1). In the case of γ-Al_2O_3 both A and B site cations are occupied by Al^{3+}, and $2\,{}^{2}/_{3}$ aluminum vacancies pr. unit cell are required to obtain charge neutrality ($Al_{21\,{}^{1}/_{3}}O_{32}$). Two factors make the different crystal structures compatible and enable the non-isomorphic epitaxial growth: First, the oxygen sub-lattice in GAO has a closed-packed arrangement, which matches excellently with the oxygen sub-lattice in STO (see Figure 4.1). Second, the lattice constant of GAO, $a_{\mathrm{GAO}} = 7.911$ Å [67], is approximately a factor 2 larger than STO ($a_{\mathrm{STO}} = 3.905$ Å) and gives an effective lattice mismatch of $(a_{\mathrm{STO}} - {}^{1}/_{2}a_{\mathrm{GAO}})/a_{\mathrm{STO}} = -1.3\%$. Contrary to LAO/STO with a lattice mismatch of +3%, the GAO thin film is under compressive strain and is better lattice matched.

A manifestation of the spinel/perovskite compatibility is the epitaxial layer-by-layer growth of GAO on STO using pulsed laser deposition (PLD). This was realized by Chen et al [65] based on oscillations with reflection high-energy electron diffraction (RHEED) (see Figure 4.2). Prior to the deposition, atomic force microscopy images show that the STO substrate is atomically flat [XXI] and a high reflectance to a grazing incident electron beam is observed. As the layer-by-layer growth of GAO starts, the surface smoothness and hence the surface reflectance initially decreases. When approaching full coverage of GAO the smoothness and reflectance increase and eventually a maximum is reached at full coverage. The oscillation corresponds to the growth of a charge neutral unit, which for GAO is two atomic layers ($\,{}^{1}/_{4}$ u.c. ≈ 2

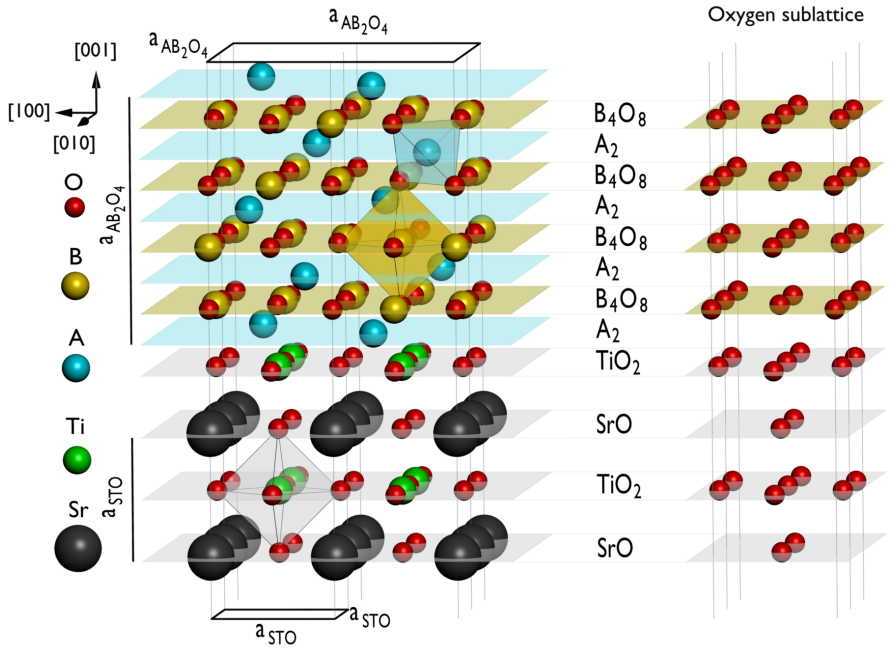

Figure 4.1 – Schematic of the spinel/perovskite heterostructure
Atomic structure of the spinel/perovskite heterointerface formed by depositing a lattice-compatible AB_2O_4 spinel on STO. In the case of γ-Al_2O_3, both tetrahedral A and octahedral B site atoms are occupied by Al^{3+} with intrinsic aluminum vacancies on 11.1% of the sites. a_{STO} and $a_{\mathrm{AB_2O_3}}$ denote the lattice constant of the STO and spinel unit cell, respectively. The compatible oxygen sublattices of the spinel and cubic perovskite crystal structure are shown on the right.

nm) with aluminum placed in tetragonal and octahedral symmetry in each layer (see Figure 4.1). RHEED monitoring therefore allows for a thin film growth with sub-unit cell thickness control. Remarkably, layer-by-layer growth of thin GAO films is possible with PLD even when STO is kept at room temperature [68] where growth of other thin films usually results in an amorphous phase [37]. Clear RHEED oscillations can, however, be impeded by the superposition of the oscillating RHEED signal with a non-oscillating signal stemming from inelastically scattered electrons as investigated by Schütz et al [69]. In this case, slight tilting or rotation of the sample relative to the electron beam can be used to separate the oscillating part of the RHEED signal from the non-oscillating contribution.

The conducting GAO/STO heterostructure was originally discovered using pulsed

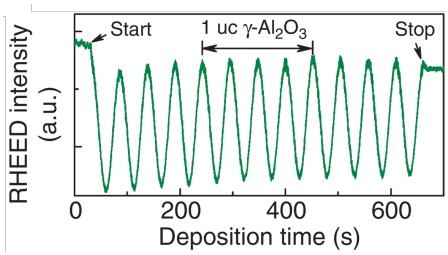

Figure 4.2 – Monitoring layer-by-layer growth of GAO
Reflection high-energy electron diffraction (RHEED) oscillations during the pulsed laser deposition of 3 u.c. GAO on STO at 600 °C. Each oscillation corresponds to the growth of $^1/_4$ u.c. of GAO. The figure is taken from Ref. [65].

laser deposition [65], but both all-crystalline GAO/STO and amorphous alumina (a-AO) on STO has been realized with other physical and chemical deposition techniques. Crystalline GAO/STO was recently realized by molecular beam epitaxy (MBE) [70] and atomic layer deposition (ALD) [71]. During the MBE growth, metallic aluminum was evaporated on STO and both the STO substrate and the molecular oxygen in the deposition chamber acted as oxygen sources for the oxidation of aluminum into GAO [70]. In the ALD process trimethylaluminum (TMA, $Al(CH_3)_3$) and H_2O were used as chemical precursors for the GAO growth with aluminum bonding chemically to the film under the release of carbon-containing gases [72]. Lowering the deposition temperature generally favors the growth of a-AO on STO as insufficient thermal energy is available for the crystallization as realized by ALD [32, 71, 72], electron beam evaporation at room temperature [34] and PLD under certain deposition conditions [73, 74]. Generally, the GAO or a-AO films are deposited on TiO_2-terminated STO as described in Section 2.2, but it was shown with electron beam evaporation that conducting interfaces could also be obtained with polished STO with mixed SrO and TiO_2-termination. The various deposition techniques used to make a-AO or GAO films each has their advantages. PLD features a high energy of the alumina plasma species exceeding 10 eV as they reach the STO surface [75], which allows for crystalline growth at room temperature [68] and kinetic enhancement of surface reactions [75]. On the contrary, MBE and electron beam evaporation are low-energy deposition techniques that produce less defects in the substrate as the species arrive on the substrate surface with energies on the order of $k_B \cdot 1000\ \mathrm{K} \sim 0.1$ eV. Lastly, in ALD the materials do not suffer from bombardment effects and it is a low-cost deposition technique suitable for mass production of thin films [72].

The GAO/STO heterostructures grown by ALD, MBE and PLD can all exhibit good crystallinity. Examples are given in Figure 4.3 where PLD and ALD grown GAO/STO heterostructures are images along the [100] and [110] directions using transmission electron microscopy. The GAO/STO heterostructure has further been thoroughly characterized structurally by x-ray diffraction [65, 68, 70, 71], electron holography [76], electron energy loss spectroscopy [65, 76], high- and low-energy electron diffraction [65, 68–71] and atomic force microscopy [65, 68]. The structural studies confirm the compatibility between spinel GAO and perovskite STO where the

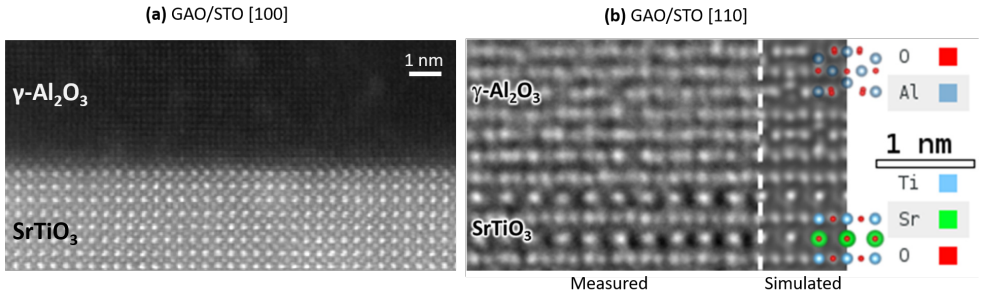

Figure 4.3 – Transmission electron microscopy image of GAO/STO
Aberration-corrected transmission electron microscopy image of the atomic structure of GAO/STO (a) grown by pulsed laser deposition and imaged along the [100] direction [65] and (b) grown by atomic layer deposition and imaged along the [110] direction [76]. In (b) both an experimental image and simulated image are shown for comparison. The figures are taken from Ref. [65, 76].

layer-by-layer growth results in GAO thin films with atomically flat surfaces. PLD grown GAO/STO further shows diffusion of aluminum $\sim$1 nm into STO and diffusion of titanium more than 5 nm into GAO [65].

The change in the atomic structure when crossing any interface causes a breaking of the symmetry, which is often central for the understanding and utilization of heterostructure properties. For perovskite/perovskite heterostructures this leads to electron donation [35, 60] and electron confinement close to the interface [77, 78] as well as splitting of band degeneracy [79] and spin/orbit coupling [53]. The symmetry breaking at the spinel/perovskite GAO/STO interface is fundamentally different from the perovskite/perovskite interface owing to the changing crystal structure across the interface and it thus offers new possibilities. Although I will present a few examples of this later, using the symmetry breaking to obtain functionalities beyond those observed in LAO/STO is, to date, a largely unexplored opportunity.

CHAPTER 5

Conductivity between insulators

Although STO and GAO are both insulators, conductivity can be induced at the GAO/STO interface by the deposition of GAO. Under typical pulsed laser deposition conditions (see, e.g., [IX]), the interface remains insulating when the GAO thickness is 1 u.c. or less. However, the resistance decreases by more than 4 orders of magnitude and turns metallic conducting upon deposition of an additional ½ u.c. GAO (see Figure 5.1a). The sharp transition from an insulator to a n-type metal is observed for different deposition techniques and is caused by a large increase of delocalized electrons (see Figure 5.1b). As it will be discussed in Chapter 6, the GAO/STO heterostructure can be prepared in various states ranging from highly insulating to metallic conducting, as observed in Figure 5.2 where annealing in oxygen is used to control the conducting state. The metallic state is generally characterized by little or no carrier freeze-out and an increasing electron mobility upon lowering the temperature. In order to understand the emergent interface conductivity arising when combining the two insulators, it is paramount to understand (i) the origin of the delocalized carriers and (ii) how they move through the crystal:

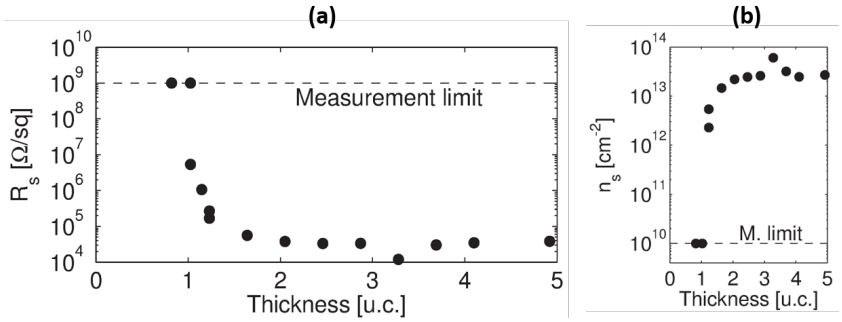

Figure 5.1 – Thickness dependent transport properties
(a) Sheet resistance (R_s) and (b) carrier density (n_s) of PLD-grown GAO/STO heterostructures with varying GAO thicknesses. The figure is from Article [IX].

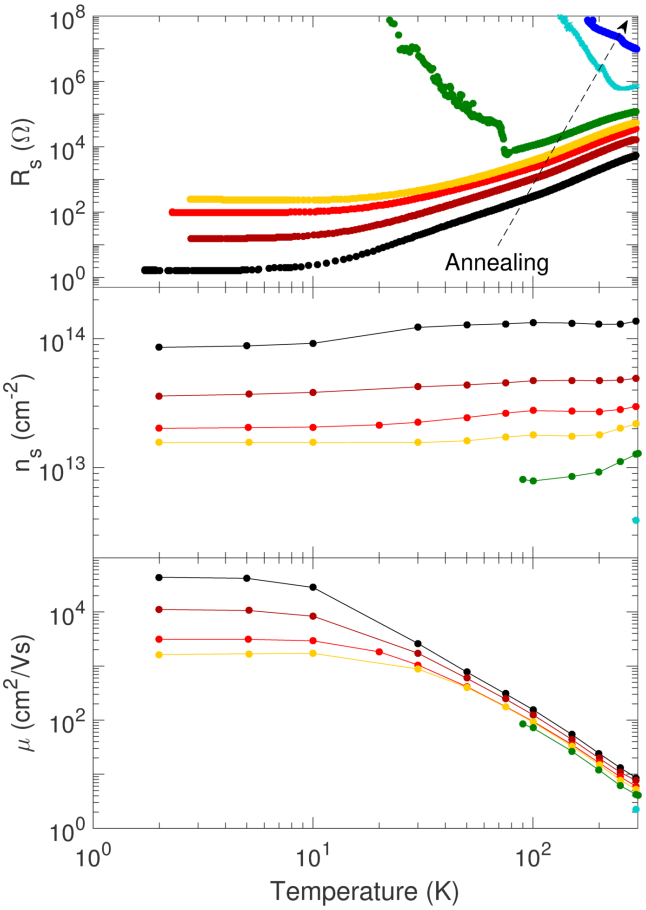

Figure 5.2 – Temperature dependent transport properties
Sheet resistance (R_s), carrier density (n_s) and mobility (μ) as a function of temperature for a PLD-grown GAO/STO heterostructure with varying initial states obtained by post-annealing in pure oxygen at $\sim 200\,^\circ C$ for 2-8 hours. The figure is adapted from Article [XXIII].

5.1 Origin of charge carriers

The origin of the interface conductivity in LAO/STO is still debated, but valuable insight can be gained by investigating STO-based heterostructures beyond LAO/STO. Studying the thermodynamic ground state of the conducting STO-based heterostructures and their sensitivity to oxygen annealing is particularly useful.

5.1.1 Annealing and high-temperature equilibrium conductance

The transition from metallic to insulating GAO/STO by annealing in oxygen (see Figure 5.2) hints towards electrons originating from oxygen vacancies. Further insight was gained by high temperature equilibrium conductance (HTEC) measurements comparing STO and STO-based heterostructures capped with polar and non-polar films [XII]. The study also included the interesting case of the GAO/STO heterostructures where the polarity of GAO was unclear [65, 80]. The heterostructures were heated up to 950 K, and the conductance was measured in equilibrium as a function of the oxygen partial pressure (pO_2). STO without a top film showed the expected V-shaped HTEC characteristics (see Figure 5.3a): At low oxygen pressures, the conductance increases according to $n \propto pO_2^{-1/6}$ as formation of more oxygen vacancies increases the carrier density (n). At high oxygen pressures, the HTEC increases as $n \propto pO_2^{+1/4}$ as oxygen vacancy donors become oxidized and STO becomes acceptor doped.

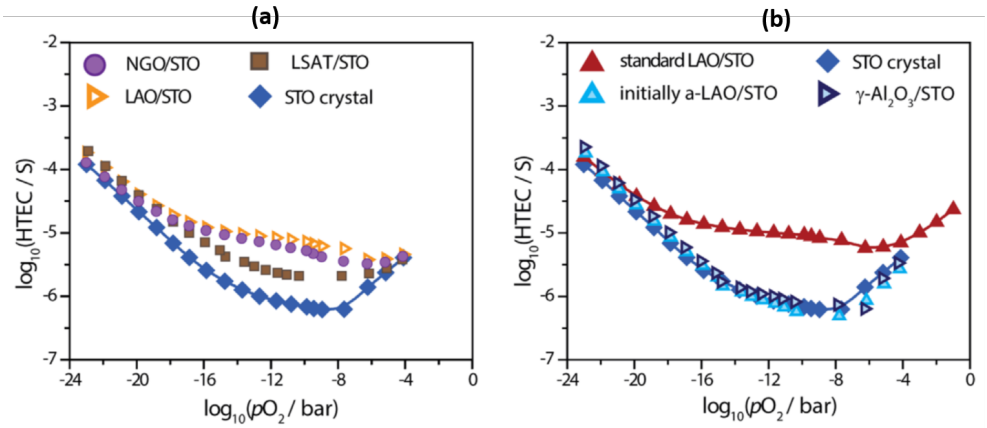

Figure 5.3 – High temperature equilibrium conductance
High temperature equilibrium conductance (HTEC) obtained at 950 K as a function of the oxygen partial pressure (pO_2) for bare STO and STO capped with pulsed laser deposited thin films of $NdGaO_3$ (NGO), (La, Sr)(Al, Ta)O_3 (LSAT), $\gamma - Al_2O_3$, crystalline LAO (standard LAO) and amorphous LAO (initially a-LAO). The figure is adapted from Article [XII].

The characteristic V-shape changed when STO was capped with polar films (LAO, $NdGaO_3$ and $(La, Sr)(Al, Ta)O_3$ (LSAT)). Here, a pressure independent contribution was observed for 10^{-20} bar $< pO_2 < 10^{-6}$ bar, which scaled with the magnitude of the polarity (see Figure 5.3a). At a LAO thickness of 3 u.c. where LAO/STO is insulating, the pressure independent contribution was absent. This was also the case when the nominally non-polar amorphous LAO was grown on STO (see Figure 5.3b), despite some degree of crystallization occurring during the measurements. The pressure independent contribution was therefore attributed to the polarity-induced electron donation. The GAO/STO heterostructure did not exhibit a pressure independent contribution implying that GAO is non-polar and that the conductivity in both amorphous-LAO/STO and GAO/STO is due to thermodynamically unstable oxygen vacancies.

As it will be explained in Section 6.2, an annealing study on GAO/STO further found that removal of carriers by annealing requires an activation energy of 0.5 eV [XIV]. This establishes that the oxygen vacancies are located in STO, as the activation barrier matches that required by oxygen diffusion in STO [XIV].

5.1.2 Oxygen vacancy formation

The oxygen vacancies may be created during the pulsed laser deposition either from bombardment effects when the energetic plasma particles hit the surface or from a movement of oxygen from STO to GAO. The former is, however, unlikely to be the dominant pathway to obtain conductivity based on two arguments: First, low-energetic deposition techniques (MBE and ALD) also form conducting interfaces at GAO/STO [70, 71]. Second, deposition of e.g. $La_{7/8}Sr_{1/8}MnO_3$ thin films do not induce conductivity despite the plasma species arriving with similar energies [37]. These findings can be understood by considering oxygen movement from STO to GAO (see Figure 5.4) described with a redox reaction taking place across the interface:

$$\gamma\text{-}Al_2O_{3-\delta}/SrTiO_3 \longrightarrow Al_2O_{3-\delta+x}/SrTiO_{3-x} \qquad \text{(R5.1)}$$

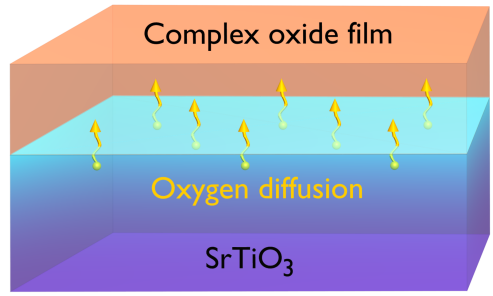

Figure 5.4 – Oxygen diffusion mechanism
Schematic drawing depicting the formation of oxygen vacancies in STO by diffusion of oxygen from STO to the oxygen deficient top film.

If the reaction is thermodynamically favorable, as expected for GAO/STO but not $La_{7/8}Sr_{1/8}MnO_3$/STO, the reaction reduces the oxidation state of titanium (Ti^{4+}) as electrons are introduced in STO. A prerequisite for the oxygen movement is the deposition of an oxygen deficient film, which explains the decrease in conductivity observed upon raising the oxygen background pressure, as the interaction between oxygen and the plasma plume causes oxidation of the plasma plume [75]. The thermodynamics of the redox reaction is simplified greatly by crudely assuming that the species arrive as metals on STO during growth and that interface effects can be neglected [81, 82]:

$$SrTiO_3 + Me \longrightarrow SrTiO_{3-x} + MeO_x \tag{R5.2}$$

The energy required to remove oxygen from bulk STO (250 kJ/mol) can then be compared with the tabulated energy gains of oxidizing various metals as shown in Figure 5.5. Here, Reaction R5.2 is thermodynamically favorable for metals with heat of oxide formation below -250 kJ/mol (below the red line). Interestingly, it is found that when STO is capped with oxide films containing metal atoms with high oxygen affinity (Ca, La, Sr, Hf, Zr, Al and Ti) metallic interfaces are obtained, as realized in LAO/STO [37], STO/STO [37], $CaZrO_3$/STO [IV], $CaHfO_3$/STO [66] and Al_2O_3/STO [34, 73]. In contrast, if the oxide films contain metal atoms where the heat of oxide formation is close to that of STO (Mn, Co, Fe and Cr), insulating interfaces are found as in the case of $La_{7/8}Sr_{1/8}MnO_3$/STO [37], $LaCrO_3$/STO [83], $LaCoO_3$/STO [84] and $LaFeO_3$/STO [85, 86] under typical deposition conditions. Overall, the simple description thus provide a powerful guideline for designing conducting STO-based heterostructures based on oxygen vacancy formation in STO.

5.1.3 Oxygen movement

The redox reaction has kinetic limitations as movement of oxygen across the interface is required. The redox reaction has been proposed to be enhanced kinetically in the Cabrera-Moth theory [88]: If the work function of the metal is lower than that of STO (5.2 eV), electrons gain energy by moving from the metal to STO (see Figure 5.5). The electron transfer produces an electric field, which accelerates the transfer of oxygen ions across the interface. In addition, the kinetic energy needed for the redox reaction is supplied by the thermal energy at a given deposition temperature and the kinetic energy of the incoming species in physical vapor depositions. For atomic layer deposition where only the thermal energy contributes, the conductivity at the a-AO/STO interface decreased with a lowering of the deposition temperature until 200 °C where insulating interfaces were observed [32]. For pulsed laser deposition, however, the GAO/STO interface can be conducting even for room temperature deposition due to the high-energetic plasma species [68]. The plasma species can be slowed down by collision with the background gas leading to the metal-to-insulator transition observed when a background argon pressure is increased from 10^{-2} to 10^{-1} mbar for deposition of amorphous STO on a crystalline STO substrate [75].

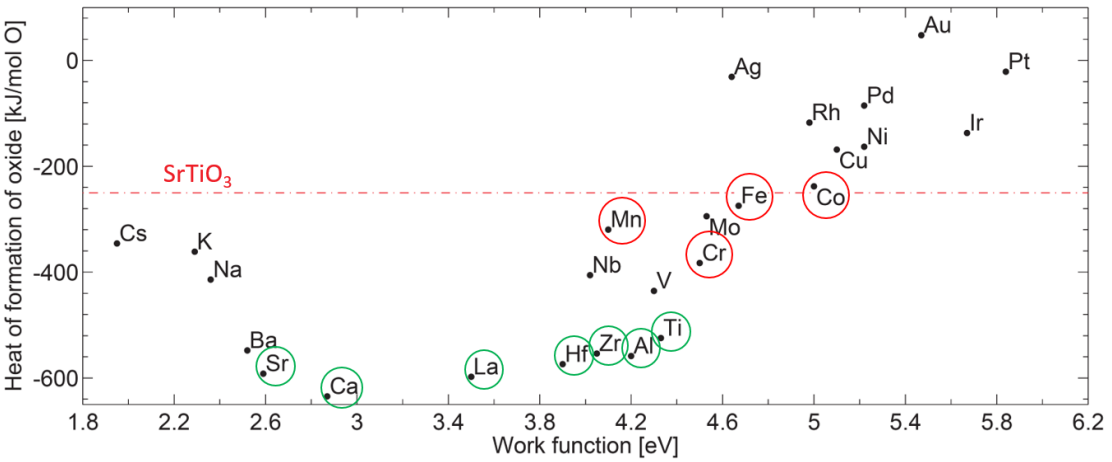

Figure 5.5 – Heat of formation for oxidizing metals
Heat of formation for oxidizing metals as a function of the metal work function. For comparison, the heat of oxide formation for STO is $\Delta H_f^\circ(STO) = -250\,kJ/mol\ O$, which is marked by the horizontal dashed line. Transfer of a neutral oxygen from the bulk of $SrTiO_3$ to the metal is energetically favorable if $\Delta H_f^\circ(Metal) < \Delta H_f^\circ(STO)$. The green (red) circles indicate whether conducting (insulating) heterostructures are observed when thin films containing the given metal are deposited on STO using PLD. The heat of formation values are obtained from Ref. [87].

5.1.4 Polarity

The conductivity of both the a-AO/STO and GAO/STO heterostructures therefore originates from oxygen vacancies in STO, whereas a polarity-induced electron donation from GAO to STO is absent despite GAO has been considered polar [80]. A possible solution to this apparent paradox is presented in Article [XV]. In LAO the polarity is fixed by the crystal structure and if left uncompensated it causes a potential build-up of 0.94 V/a_{LAO} where a_{LAO} denotes the lattice constant in LAO (see Figure 5.6a and f). The intrinsic aluminum vacancies present in GAO, however, provide a degree of freedom for changing the polarity according to the vacancy distribution. If the aluminum vacancies are homogeneously distributed solely in either octahedral or tetrahedral layers, the potential build-up is $7.1\,eV/a_{GAO} \approx 3.5\,eV/a_{LAO}$ or $4.8\,eV/a_{GAO} \approx 2.4\,eV/a_{LAO}$, respectively (see Figure 5.6c, d and f). GAO with these distributions therefore classify as a type 3 polar material similar to LAO, which is associated with a substantial surface energy if left uncompensated [89]. If the aluminum vacancies instead are distributed inhomogeneously among the octa- and tetrahedral layers, certain GAO thicknesses allow for non-polar GAO films. An aluminum distribution leading to the thinnest non-polar GAO film (1 u.c.) possible is shown in Figure 5.6e. The distribution gives a type 2 polarity where non-zero inter-

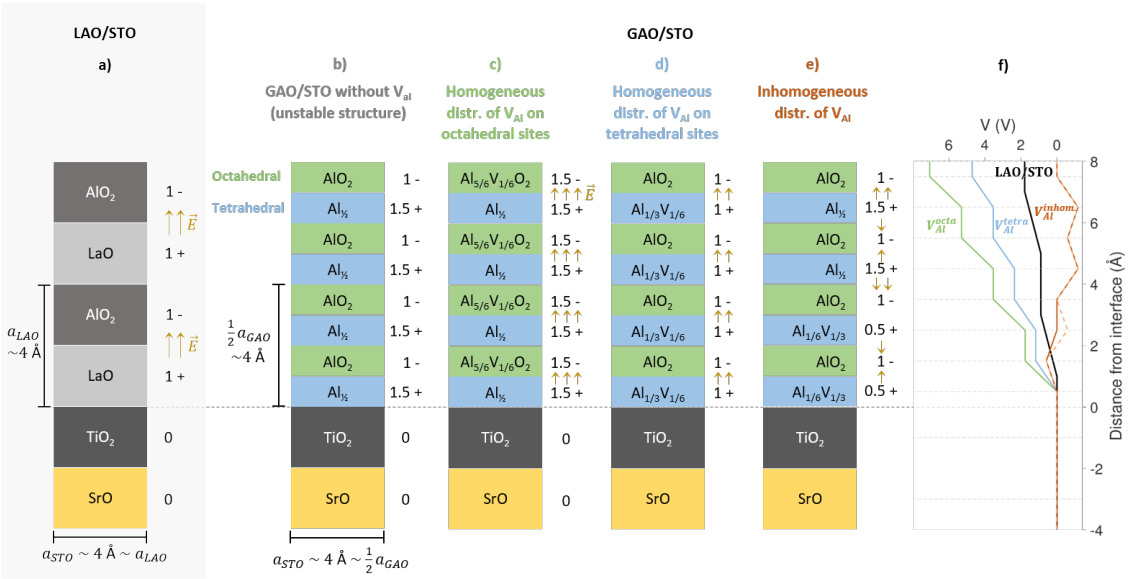

Figure 5.6 – Polarity in GAO
Schematic view of the atomic (001) planes in LAO/STO (a) and GAO/STO (b-e) in addition to the calculated potential build-up of the uncompensated polar films (f). Formal valence states are used to define the charges of the planes given in units of $e/(a_{\mathrm{STO}}^2)$ where e is the elementary charge and a_{STO} is the STO lattice constant. For GAO/STO the schematics show different aluminum distributions in (b-e). The figure is adapted from Article [XV].

nal dipole moments sum up to a zero net dipole moment resulting in an absence of a polarity build-up and a stabilization of the surface [89]. No aluminum vacancy distributions allow for a type 1 polarity with a complete absence of any dipole moments. Whereas the aluminum vacancy redistribution is a likely cause of the absent GAO polarity, other mechanisms such as defect formation may also explain it.

5.2 Transport of charge carriers

Having established the origin of the charge carriers, we discuss their transport through the lattice. When an oxygen vacancy is formed, two electrons are released to the lattice. Several x-ray photoemission and electron energy loss spectroscopy studies reveal that the electrons are located on the titanium ions where they occupy 3d-states in the near-interface region of STO [32, 65, 68, 70, 71, 80]. Here, part of the electrons are placed in localized in-gap states whereas the remaining electrons delocalize along the interface and form conductivity [XX]. At low temperatures the

electrons may even form superconductivity as observed in a-AO/$SrTiO_3$ below ≈200 mK [74].

5.2.1 Band diagram and electron confinement

A band bending causes the conduction band to cross the Fermi level close to the interface and form a quantum well where the conducting electrons reside (see Figure 5.7). The quantum well was measured to be approximately 600 meV deep with a width of 1.5 nm using hard x-ray photoemission spectroscopy (HAXPES) on a GAO/STO sample with a carrier density of $\approx 5 \cdot 10^{14}$ cm^{-2}. A similar analysis on GAO/STO deposited at 20, 400 and 600 °C suggests a more confined electron gas at higher deposition temperatures [68].

Various other studies confirm that the electron gas is confined in the vicinity of the interface as inferred from infrared ellipsometry [VII], scanning superconducting quantum interference device (SQUID) [XXVI], off-axis electron holography [76], electron energy loss spectroscopy [76] and angle-dependent Shubnikov-de Haas oscillations [65]. An example is presented in Figure 5.8 where the electron depth profile is deduced by fitting the infrared Berreman mode using a Drude model [VII]. The fit to the Berreman mode produced a total carrier density matching well with the Hall carrier density ($\sim 10^{13}$ cm^{-2}) in addition to a spatial confinement of the electron gas of 7-8 nm.

5.2.2 Band symmetry

The degeneracy of the titanium 3d bands are lifted in STO due to crystal field splitting, where the titanium ions are located at the center of an octahedral with each

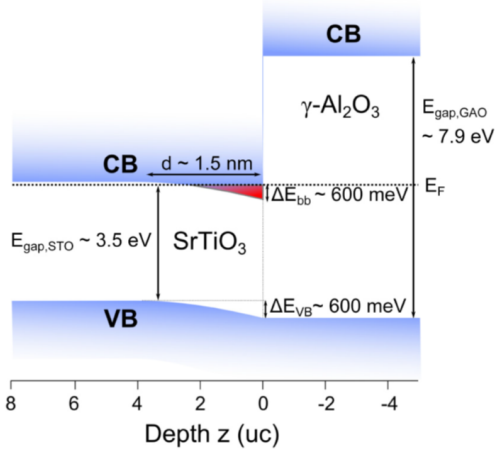

Figure 5.7 – Band diagram of GAO/STO
Band diagram at the pulsed laser deposited GAO/STO heterointerface inferred from hard x-ray photoemission spectroscopy (HAXPES). The sheet carrier density of the sample is $4.7 \cdot 10^{14}$ cm^{-2} as determined by the Ti^{3+} content spectroscopically. The figure is adapted from Ref. [80].

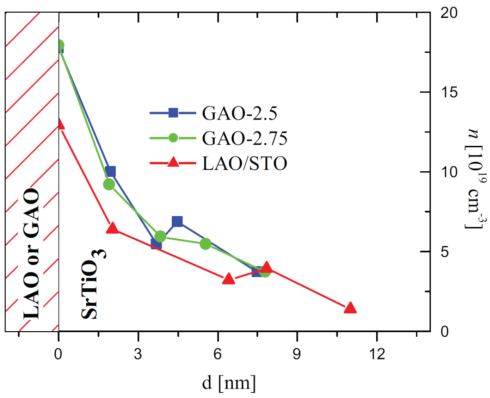

Figure 5.8 – Electron depth profile
Three-dimensional carrier density n inferred from infrared measurements on the Berreman mode as a function of distance d from the PLD-grown LAO/STO or GAO/STO interface. Here, the carrier densities of the GAO/STO are $n_s^{Hall} \approx 6 - 10 \cdot 10^{13}$ cm^{-2} *and* $n_s^{IR} \approx 6 \cdot 10^{13}$ cm^{-2} *as inferred from Hall and optical measurements. The figure is adapted from Article [VII].*

corner composed of oxygen ions. This causes a lowering of the t_{2g} bands (d_{xy}, d_{xz} and d_{yz}) relative to the e_g bands (d_{z^2} and $d_{x^2-y^2}$) [79]. Breaking the symmetry at the (001) surface of STO or the LAO/STO-based interfaces causes the bands to split further with d_{xy} lowered relative to d_{xz} and d_{yz} [62, 79]. In addition, quantum confinement of the electron gas may result in replica bands of d_{xy}, d_{xz} and d_{yz} [62]. The d_{xy} bands with small band effective masses are thus populated first, and by further increasing the electron density a Liftshitz transition occurs when the d_{xz} and d_{yz} bands become occupied [90]. The Lifshitz transition is accompanied with e.g. the emergence of non-linear Hall coefficients [90], a maximum in the superconducting transition temperature [90], large spin-orbit coupling [90] and gate-tunable band positions [91]. For GAO/STO the relative position of the 3d-bands has to date only been reported using x-ray linear dichroism [92] and transport measurements [XXI] with seemingly contradicting conclusions.

In the former, linearly polarized x-rays were used to probe the symmetry and position of the 3d-bands directly [92]. Contrary to LAO/STO and STO (001) surfaces, deposition of GAO on the (001) surface of STO was found to lower the d_{xz} and d_{yz} bands relative to d_{xy} (see Figure 5.9a). The band reordering was attributed to the atomic structure at the interface thereby making GAO/STO an interesting system to probe potential differences in e.g. electron pairing relative to LAO/STO and STO surfaces [51]. The band positions were further found to be tunable by applying compressive or tensile strain to STO by growing GAO/STO epitaxially on substrates with smaller ($NdGaO_3$) or larger ($TbScO_3$) lattice parameters, respectively (see Figure 5.9b and c).

In the latter study, ionic liquid gating was used to tune the carrier density revealing a Lifshitz transition occurring where non-linear Hall coefficients emerge and Rashba spin-orbit coupling becomes enhanced [XXI]. The similarity with LAO/STO suggests a similar band structure with d_{xy} located at a lower energy than d_{xz} and d_{yz} in

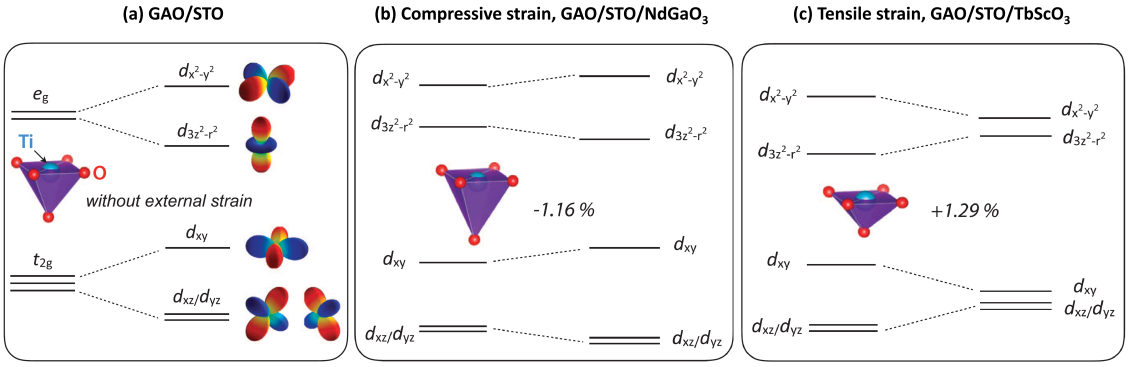

Figure 5.9 – Band symmetry of GAO/STO
(a) Relative position of the Ti-derived bands of the PLD-grown GAO/STO heterostructure determined from resonant soft x-ray linear dichroism. (b-c) Relative position of the Ti-derived bands when GAO/STO is deposited on $NdGaO_3$ or $TbScO_3$ substrates with a 1.16% smaller or 1.29% larger lattice constant than STO, respectively. The figure is adapted from Ref. [92].

contrast to what was found in the x-ray study. The ionic liquid gating is discussed further in the next chapter. In order to resolve this apparent paradox, the k-resolved electronic band structure of GAO/STO was measured using resonant soft x-ray photoemission spectroscopy with preliminary results showing only little or no energy splitting between the d_{xy} and d_{xz}/d_{yz} bands [XXX].

CHAPTER 6

Controlling the carrier density

The ability to control the carrier density is vital for the operation and optimization of electronic components as well as for fundamental scientific research. This is particularly true for STO-based systems where numerous properties, such as the superconductivity [50, 93], magnetism [49, 94] and spin-orbit interaction [53] can be tuned by the carrier density. Strategies for controlling the carrier density during or after the deposition can be designed by using the knowledge of how the free carriers are created. Variation in the deposition conditions, gentle post-annealing, electrostatic gating and light exposure can be used as tuning knobs for varying the carrier density on the macro- or nanoscale.

6.1 Deposition

The carrier density can be controlled during the deposition by countering or promoting the redox reaction leading to the conductivity in the GAO/STO heterostructure (Reaction R5.1). The control pathways are dependent on the deposition technique used, but in general the carrier density can be tuned by several orders of magnitude by a careful control of those deposition parameters that cause insulator-to-metal transitions. A few such parameters are universal for all deposition techniques: First, an insulator-to-metal transition occurs for all techniques when the GAO thickness is increased, and a careful control of the thickness therefore determines the resulting carrier density (see Figure 6.1a-c). Second, by controlling the deposition temperature, the carrier density can be tuned by changing the thermal energy required for activating the oxygen diffusion (see Figure 6.1a). In addition, for pulsed laser deposition the oxygen deposition pressure is a crucial parameter, which, at high deposition temperatures, can change the GAO/STO heterostructure from being insulating to causing conductivity throughout the STO crystal with a thickness of 0.5 mm [XXIII]. A similar tendency for the carrier density to increase upon lowering the oxygen deposition pressure was also observed with electron beam evaporation [34]. For atomic layer deposition, introduction of water and the precursor exposure time are important process parameters to control the resulting carrier density [71].

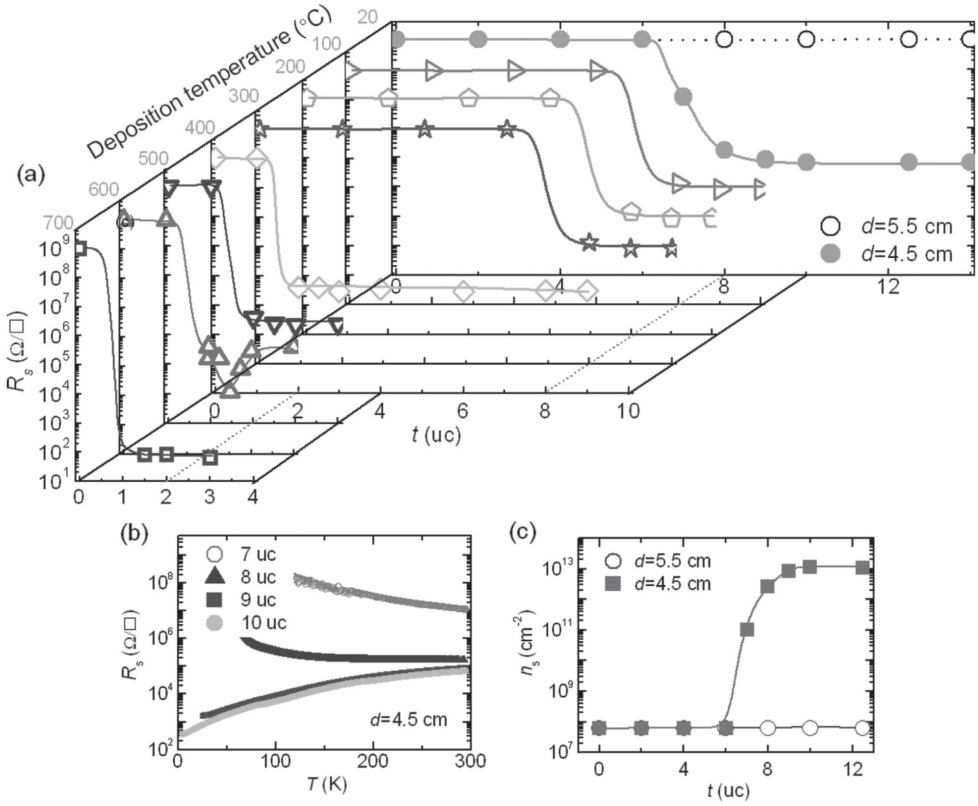

Figure 6.1 – Carrier density control via deposition
(a) Sheet resistance (R_s) of the GAO/STO interface with GAO grown with varying thicknesses (t) using pulsed laser deposition at temperatures ranging from 20 to 700 °C. For room temperature deposition, a target-to-substrate distance of d = 5.5 cm results in insulating interfaces, whereas conducting interfaces are formed for d = 4.5 cm. All sheet resistance measurements are performed at room temperature. (b) The temperature dependent sheet resistance for GAO/STO deposited at room temperature with various GAO thicknesses. (c) Carrier density (n_s) as a function of GAO thickness with both the deposition and Hall measurements performed at room temperature. The figures are adopted from Ref. [68].

6.2 Annealing

As described in the previous chapter, annealing in oxygen has been used to turn conducting interfaces insulating in order to confirm that the charge carriers originate from oxygen vacancies. Careful oxygen annealing at low temperatures ($\leq 300°C$) with *in-situ* measurements of the sheet conductance, however, allows for a fine control of the interface state without suffering from sample-to-sample variations [XIV] (see Figure 6.2a). As the change in conductance is primarily due to decreasing the itinerant electron density (rather than the electron mobility), this allows for a systematic study of a wider range of carrier densities (see Figure 6.2b) than usually possible with conventional electrostatic gating as discussed next. Besides donating itinerant electrons, oxygen vacancies also play an important role in numerous other aspects such as acting as electron scattering sites [95] and providing magnetic moments to STO [17, 96], which renders oxygen vacancy defect control a useful tool.

The mechanism underpinning the carrier density decrease during annealing has been studied by measuring the rate of sheet conductance decrease as a function of temperature [XIV]. From an Arrhenius-plot it was found that two distinct processes occur simultaneously at different rates, but interestingly the processes shared the same activation energy of 0.5 eV (see Figure 6.2c). This activation energy matches well with the energy barrier of 0.5-0.6 eV for oxygen diffusion in STO [97, 98]. By comparing amorphous-LAO/STO and GAO/STO annealed in oxygen and nitrogen, the processes were identified. The first fast process was attributed to an oxygen vacancy redistribution within STO that effectively caused an increase in the carrier localization (see Figure 6.2d). When the oxygen vacancies depth profile reached a quasi-equilibrium after the redistribution, this process ceased and the decrease in carrier density became dominated by the slower refilling of oxygen vacancies by molecular oxygen. Contrary to amorphous-LAO, GAO acts as an oxygen blocking layer preventing oxidation to occur through GAO, and oxidation therefore occurs through STO (see Figure 6.2e). This oxygen migration occurs over distances much longer than the initial redistribution thus causing the much lower carrier density decay rate despite similar activation energies.

6.3 Electrostatic gating

A convenient way to change the carrier density is through electrostatic gating. An electric field has been applied to the a-AO/STO and GAO/STO interface using a gate separated from the interface either by a solid dielectric [IX,XIV] [34, 99] or an ionic liquid [XXI]. The gating experiments have been performed at temperatures ranging from 4 K to room temperature revealing a large temperature dependence of the gate response.

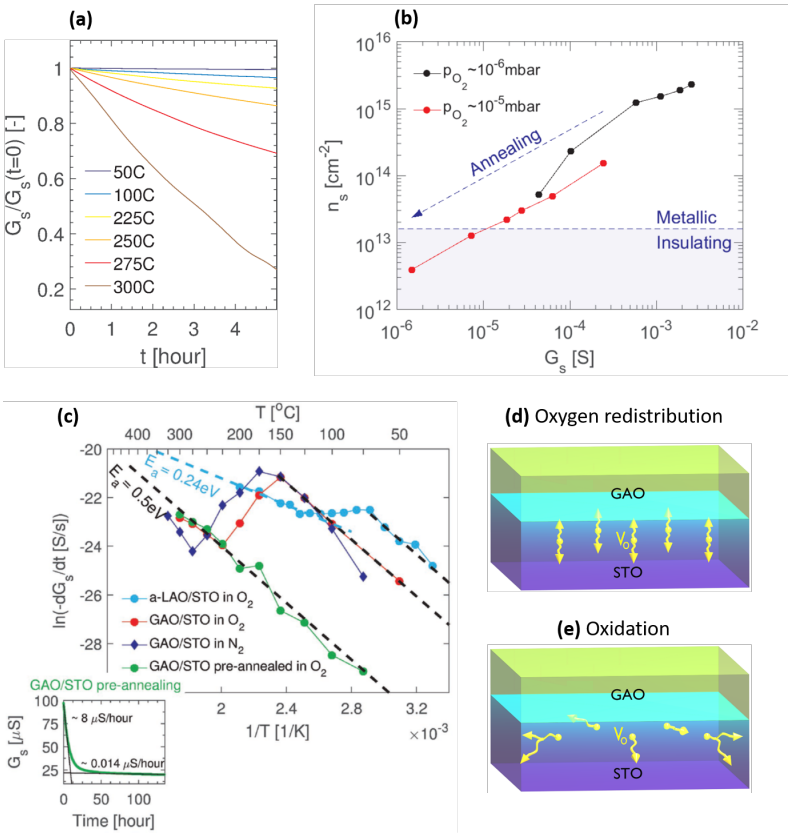

Figure 6.2 – Carrier density control through annealing
(a) Time evolution of the normalized sheet conductance (G_s) in PLD-grown GAO/STO measured in situ at temperatures ranging from 50 to 300 °C in 1 bar oxygen. (b) Carrier density (n_s) measured at room temperature as a function of sheet conductance for different resistive states obtained by annealing GAO/STO at 200 °C in 1 bar oxygen. Data from two GAO/STO heterostructures prepared at oxygen pressures of 10^{-5} and 10^{-6} mbar are shown. (c) Arrhenius-plot of the rate of conductance change (dG_s/dt) for various temperatures for GAO/STO and amorphous-LAO/STO samples annealed in oxygen or nitrogen. Activation barriers of 0.5 and 0.24 eV are marked with black and blue dashed lines, respectively. Pre-annealing GAO/STO at 150 °C for 140 h causes the initial process to saturate (see inset) leaving the second process observable in the Arrhenius plot at low temperatures. (d-e) Proposed mechanisms for the carrier density change resulting from a combination of oxygen vacancy redistribution and oxidation. The figures are adopted from Article [XIV].

6.3.1 Room temperature backgating

Due to its simplicity, backgating is often used to change the carrier density by applying a potential relative to the interface conductivity using a metal located below STO. Applying positive or negative backgate potentials may result in a large increase or decrease in the sheet resistance at the GAO/STO interface by virtue of changing the free carrier density (see inset of Figure 6.3a). At room temperature the bipolar switching of the resistance has both a fast and slow contribution. The fast contribution is generally small and occurs in less than a second. It is attributed to a volatile accumulation or depletion of electrons from the grounded metal contacts in line with the traditional field effect [IX] [99]. The slow contribution is non-volatile with a pronounced memory effect lasting for hours after the backgate potential has been turned off [IX]. As discussed later, this contribution is likely to be related to oxygen vacancy movement.

At a typical STO thickness of 0.5 mm, the capacitance is too small to cause a large change in the sheet resistance of highly conducting interfaces with $R_s < 10\ \mathrm{k}\Omega$ (see Figure 6.3a). However, by preparing the samples with a high initial resistance using either the deposition or annealing approach described in the previous sections, large resistance changes of around three orders of magnitude can be obtained in both GAO/STO [IX] and a-AO/STO [99]. Whereas a large sample-to-sample variation is generally observed (Figure 6.3a), the resistive changes within one sample can be remarkably reproducible over a large number of switching cycles (Figure 6.3b). The general behavior of the resistive switching is similar to that observed in amorphous-LAO/STO and LAO/STO [42, 100].

6.3.2 Temperature-dependent backgating

The temperature-dependence of the resistive switching has been probed in a-AO/STO by monitoring the resistance increase when the backgate potential is changed from +30 V to -30V at temperatures ranging from 10 to 50 °C (see Figure 6.4a). A pronounced temperature sensitivity is observed where the resistive switching occurs on a timescale of hours at 10 °C, whereas it is highly accelerated at 50 °C and occurs on a timescale of a few minutes. A similar behavior was also observed for amorphous-LAO/STO [100]. Plotting an Arrhenius plot of the doubling time t_{x2}, defined as $R_s(t_{x2})/R_s(t = 0) = 2$, reveals an energy barrier of 0.7 eV, in reasonable agreement with the oxygen diffusion barrier (see inset of Figure 6.4a). The room temperature resistance control also enabled driving samples from a metallic to an insulating state. More than a 7 orders of magnitude change in the low-temperature resistance was observed when cooling down the sample with various room temperature resistive states (see Figure 6.4b). A similarly large change could be induced by applying moderate backgate potentials of ±30 V at 4 K (see Figure 6.4c). This was achieved by tuning the initial resistive state of the sample to a desired level before the cool-down using the back-gate at room temperature.

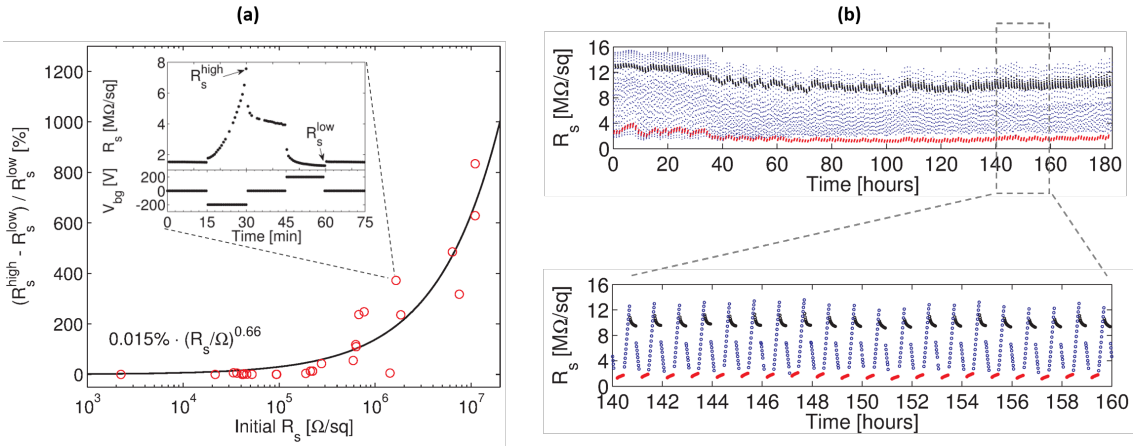

Figure 6.3 – Room temperature backgate-induced resistive switching.
(a) The relative change between high-resistive (R_s^{high}) and low-resistive (R_s^{high}) states of the GAO/STO interface conductivity as a function of the initial sheet resistance (R_s) for various samples. The inset shows the change of the interface sheet resistance between high and low-resistive states for a typical sample when changing the backgate potential from V_{bg} = 0 V → -200 V → 0 V → 200 V → 0 V with each voltage applied for 15 min. All samples have been measured with the same backgate profile. (b) Example of the reproducibility of the backgate-induced resistive switching over 180 cycles using the same backgate profile. Measurements are done in van der Pauw geometry on a GAO/STO sample grown by PLD. The figures are adopted from Article [IX].

The thermal activation implies that the microscopic origin of the non-volatile resistive switching is intimately coupled to the electromigration of oxygen vacancies. Under negative applied backgate voltages, oxygen ions migrate towards the interface whereas oxygen vacancies dilute into STO where they cause a lower resistivity. This possibly occurs due to carrier localization resulting from a lack of percolation path. When the backgate potential is turned off, the oxygen vacancies slowly diffuse back towards their equilibrium distribution. Applying a positive backgate potential reverses the situation and causes the vacancies to accumulate at the interface leading to a high conductivity. The mechanism based on oxygen vacancy electromigration is supported by several studies on other STO-based systems [100–103].

6.3.3 Ionic liquid gating

A prominent feature of the conductivity at the GAO/STO heterostructure is the possibility to obtain a high carrier density. As it will be shown in the two subsequent chapters, interesting properties such as high electron mobility and colossal magnetore-

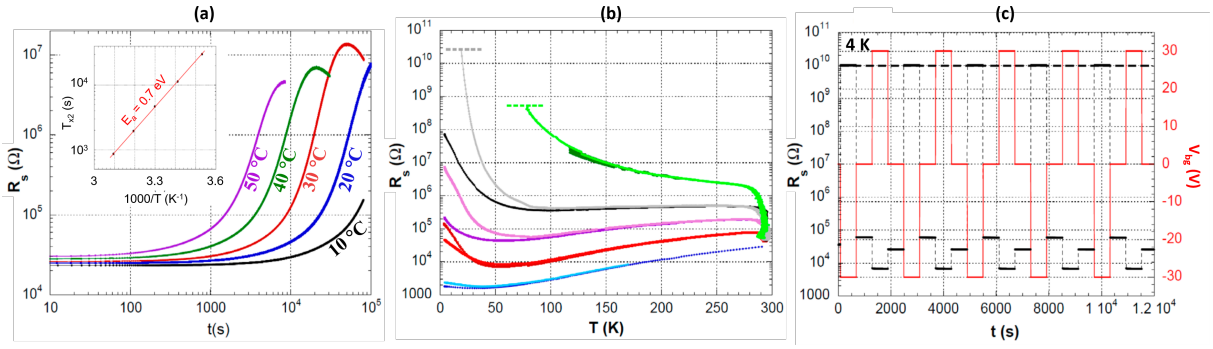

Figure 6.4 – Temperature dependent backgate-induced resistive switching. *(a) Equilibrating the sample with a backgate potential of V_{bg} = 30 V and subsequently applying V_{bg} = -30 V causes an increase in the resistance (R_s), which is measured at temperatures between 10 and 50 °C. The time it takes for the resistance to reach twice the initial value (t_{x2}) is presented as an Arrhenius plot in the inset from which an activation barrier of 0.7 eV is extracted. (b) Resistance as a function of temperature at various resistive states obtained by changing the room temperature resistance using V_{bg} = -30 V until the desired state is reached (near-vertical part of the curves around 300 K). In all cases the cool-down is done with V_{bg} = 0 V except for the red curve where V_{bg} = -30 V. The different resistive states are marked with different colors, and dark and light shades represent cool-down and warm-up, respectively. (c) The resistance of the sample is raised from 30 to 60 kΩ using $V_{bg} < 0$ V at room temperature, and the sample is subsequently cooled down to 4K. Here, the resistance (black curve) is measured at different applied backgate voltages (red curve). Horizontal dashed lines are used for the measurement limit, which in (c) is 10^{10} Ω for (c). The measurements are done in a two-terminal geometry on a sample with a-AO deposited on STO using electron beam evaporation. The figures are adopted from Ref. [34].*

sistance emerge at the states with a high carrier density and low resistance (≈ 1 kΩ). Unfortunately, backgating with a few hundred volts will generally have a minor effect on such high-density samples. Electric double layer gating, where the electric field is applied to the electron gas through ionic liquids or organic electrolytes, is a promising pathway to circumvent this limitation as it allows for a large change in the carrier density. Several studies report the use of this technique for STO and a carrier density tuning in excess of 10^{14} cm^{-2} has been demonstrated [104–108].

The electric double layer gating was performed for GAO/STO in the setup shown in Figure 6.5a [XXI]. The GAO/STO interface conductivity was first patterned into a Hall bar using the protocol from Article [XVI] where an $LaMnO_3$ hard mask was used to only form conductivity in areas not covered by $LaMnO_3$. An ionic gel with a freezing point of 230 K was then applied on the GAO surface. At room temperature

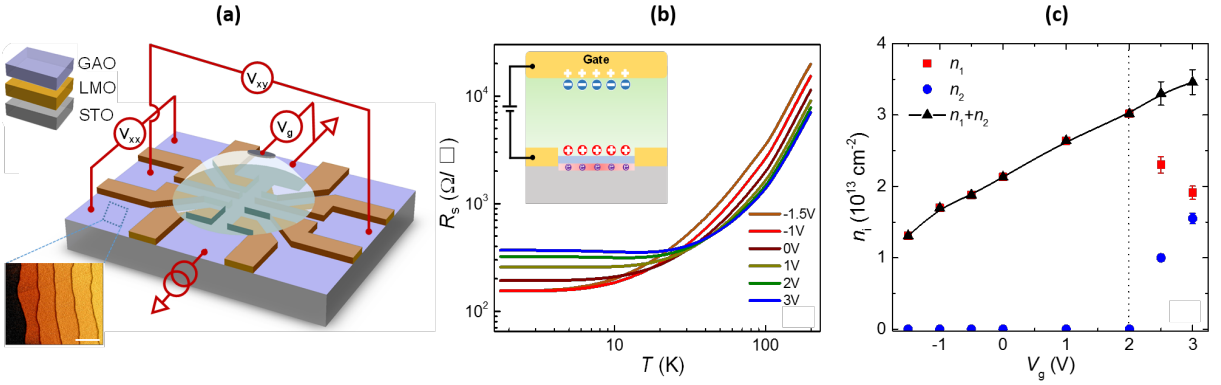

Figure 6.5 – Electric double layer gating of GAO/STO.
(a) Schematic figure of the electric double layer transistor setup where the PLD-grown GAO/STO interface conductivity is patterned into a Hall bar and controlled with a gate potential applied through an ionic liquid. The inset shows an atomic force microscope image of the GAO/STO surface revealing atomically flat terraces with 0.4 nm height separation. (b) Sheet resistance (R_s) as a function of temperature (T) for gate potentials ranging from -1.5 V to 3 V. The inset shows the operation of the electric double layer transistor where a positive gate potential polarizes the liquid ions and effectively accumulates electrons at the GAO/STO interface. (c) Sheet carrier densities for the first band (n_1) and second band (n_2) with varying gate potential (V_g) as obtained from a two-band fit of the non-linear Hall coefficient. The figures are adopted from Article [XXI].

the ions are mobile and applying a positive gate potential accumulates negative ions near the gate whereas positive ions and electrons accumulate on the GAO surface and GAO/STO interface, respectively (see inset of Figure 6.5b). As the sample was cooled down below 230 K, the ions froze in the preformed configuration. Varying the gate potential from -1.5 to 3 V resulted in an accumulation of electrons at the GAO/STO interface and hence a lower sheet resistance at 200 K (see Figure 6.5b). Cooling down the sample to 2 K, however, resulted in the highest resistance being observed for a gate voltage of 3 V. This resistance inversion was caused by the low-temperature mobility decreasing by a factor 6 from $V_g = -1.5$ to 3 V thus outweighing the gain in the carrier density. Accumulating electrons at high positive gate voltages additionally led to emergence of a Kondo-like resistance upturn for $V_g \geq 2$ V at low temperatures (see Figure 6.5b), weak antilocalization arising from Rashba spin-orbit coupling and non-linear Hall coefficients [XXI]. The latter could be described satisfactorily using a two-band model as generally employed for LAO/STO above a critical carrier density of $1.6 \cdot 10^{13}$ cm^{-2} [90]. The total amount of carriers increased monotonously with the gate as expected, however above a critical carrier density of $3 \cdot 10^{13}$ cm^{-2}, occupation of the second band started to take place with a concomitant depopulation of the first

band (see Figure 6.5c). This was observed for LAO/STO as well [91]. The many similarity with LAO/STO suggests that the bandstructure is similar in which the first band has d_{xy} symmetry whereas the second bands are d_{xz}/d_{yz}, in contrast to what was inferred using linearly polarized x-rays [92].

6.3.4 Writing of nanoscale conductivity

A non-volatile change in the resistance has been successfully demonstrated on the nanoscale for LAO/STO by applying electric fields with a conducting atomic force microscopy (c-AFM) tip [43, 47]. Here, the LAO/STO was prepared in an insulating state by depositing LAO with a thickness slightly below the critical thickness for inducing metallic conductivity. Scanning on the LAO/STO surface with a biased c-AFM tip was then found to induce conductivity locally at the interface in areas below where the tip has been scanning. The same procedure can also create conducting lines with nanoscale resolution in GAO/STO [XIV]. Similar to LAO/STO, a highly conducting GAO/STO heterostructure does not allow for inducing a notable conductance change upon scanning at the GAO surface with the biased c-AFM tip (see Figure 6.6). As described in Section 6.2, the conducting GAO/STO sample can be conveniently tuned into an insulating state using annealing, thus avoiding the need for a careful thickness control. Annealing GAO/STO at 150 °C for 3 hours in air using a simple laboratory hot plate enabled c-AFM writing of conducting circuits composed of conducting lines with widths of ≈50 nm. Reversing the voltage on the c-AFM tip resulted in erasing the conducting lines.

The nanowire writing is similar to LAO/STO and is likely to be caused by the same underlying mechanism studied by Bi et al [109]: For LAO/STO the writing has been shown possible only when water is present in the atmosphere. During the writing process water molecules are therefore expected to dissociate into OH^- and H^+ on the thin film surface with OH^- becoming selectively removed by the positively biased AFM tip. This would leave a trail of positively charged H^+ behind on the surface, which induces electrons at the interface.

6.4 Light exposure

Exposing STO-based systems to light has been shown to change the resistance [55, 110–113]. The photo-induced carriers are also observed in a-AO/STO [34] and GAO/STO [IX], albeit this has to date been studied sparsely. An example is given in Figure 6.7, where light exposure is causing the GAO/STO resistance to decrease by a factor of 2 as well as lowering the relative switching between high and low-resistive states from $(R_s^{high} - R_s^{low})/R_s^{low} = 300\%$ to 40%.

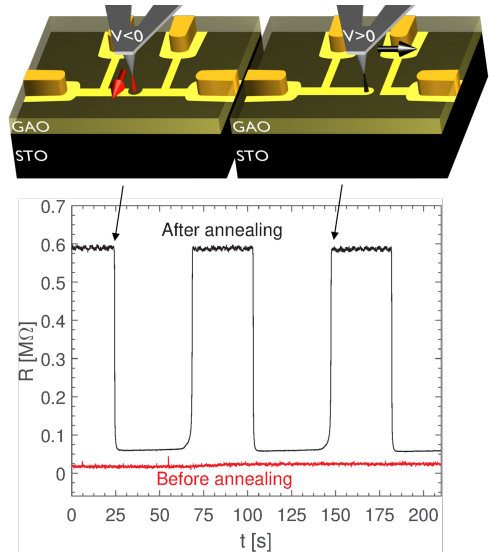

Figure 6.6 – Writing of nanoscale conductivity.
4-probe resistance (R) measured at room temperature as a function of time (t) during writing and erasing of conducting lines. The writing/erasing is done on a PLD-grown GAO/STO heterostructure before and after annealing on a hot plate at 150 °C for 3 hours in ambient conditions. The writing (erasing) is achieved by applying a positive (negative) voltage on a conducting atomic force microscopy tip, which is then moved across the surface of GAO/STO in order to write (cut) a conducting line at the interface. An abrupt increase (decrease) in the measured resistance is seen when the conducting line connects (disconnects) the four gold contacts as depicted in the schematic drawings. The figure is adopted from Article [XIV].

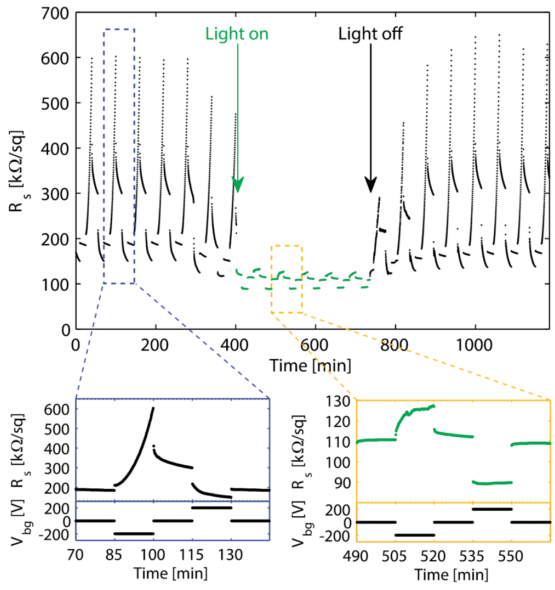

Figure 6.7 – Light exposure and electrostatic gating.
Sheet resistance (R_s) of PLD-grown GAO/STO as a function of time when the backgate is cycled using $V_{bg} = 0 \rightarrow -200 \rightarrow 0 \rightarrow +200 \rightarrow 0$ V. At $t \approx 400$ min the sample is exposed to light from a fluorescent tube, which causes a decrease in both the sheet resistance and the switching ability. The decrease in resistance at $t = 300 - 400$min is due to a small leakage of light to the sample. The figure is adopted from Article [IX].

6.5 Comparison

The palette of methods to control the carrier density and defects is useful for tuning and studying the properties of GAO/STO. In most cases, electrostatic gating is preferable as it often allows for a fast tuning of the carrier density in-situ. Backgating, however, may result in hysteresis in the electronic properties (see Figure 6.4) as well as affecting the spatial extent of the electron gas [114] and the tetragonal domain structure in STO [57]. In addition, a continuous application of a gate potential is impractical for optimizing devices and carrying out some studies such as synchrotron-based measurements. Controlling the carrier density by varying the deposition conditions or performing post-annealing can tune the sample to a (quasi-)permanent state, but at the expense of a longer fabrication time in addition to a potentially poor reproducibility. In addition, both oxygen vacancy donors and electrons are tuned simultaneous, which may be desirable for some purposes, but not all. Combining electrostatic gating with annealing in principle allows for thorough studies separating electronic effects from properties originating from oxygen vacancy. Magnetic ordering in LAO/STO is for instance proposed to originate from localized magnetic moments, possibly stemming from oxygen vacancies, which couples to the itinerant electrons [94]. Combining annealing with electrostatic gating may thus facilitate the separate control of localized magnetic moments and itinerant electrons. Oxygen vacancies also both act as mobility-limiting scattering sites and electron donors, and thus controlling the density and position of oxygen vacancies and electrons should allow for both an enhancement of the mobility and a deeper understanding of the scattering.

CHAPTER 7

Electron mobility

The carrier mobility is defined as the ratio between the drift velocity of the carriers (v_{drift}) and the electric field (E), i.e. $\mu = v_{\text{drift}}/E$. The tireless quest for enhancing the mobility in electronic materials has been motivated by its importance in realizing quantum phenomena as well as fast devices where electrons respond quickly to applied voltages. The high mobility is generally obtained in clean materials with few defects limiting the drift velocity, which also allows for the phase coherent and ballistic movement of electrons over long distances that has enabled the discovery of new mesoscopic physics [115]. A remarkable property of the GAO/STO heterostructure is the high mobility reported to be up to 140,000 cm^2/Vs at 2 K [65]. The high mobility exceeds the mobility of 22,000 cm^2/Vs observed in bulk STO at 2 K [95] as well as other high-mobility STO-based systems such as amorphous-LAO/$\text{La}_{7/8}\text{Sr}_{1/8}\text{MnO}_3$/STO with 70,000 cm^2/Vs at 2 K [V] and STO/SrCuO_2/LAO/STO with 50,000 cm^2/Vs at 2 K [116]. A review of the mobility in oxides can be found in Article [XXIV]. The highest mobility in GAO/STO is to date only obtained using pulsed laser deposition of GAO on STO with optimized deposition parameters. Despite the mobility is significantly lower than in $\text{Al}_x\text{Ga}_{1-x}\text{As}$/GaAs with a mobility of $36 \cdot 10^6$ cm^2/Vs at 0.36 K [117] and $\text{Mg}_x\text{Zn}_{1-x}\text{O}$/ZnO with $1.3 \cdot 10^6$ cm^2/Vs at 0.1 K [7], it remains remarkable considering the high effective mass and defect level in STO [XXIII]. The high mobility of GAO/STO may also be combined with the plethora of attractive properties exhibited by STO and STO-based heterostructures with an aim of designing new devices and exploring new physics [XXVIII]. The high mobility was originally discovered by Chen et al [65] and the dominant scattering mechanisms at temperatures ranging from 2 to 300 K were further investigated in Article [XXIII]. In the following, I will describe the current state and understanding of the mobility in GAO/STO:

7.1 Temperature dependence of the mobility

In Article [XXIII] the temperature dependence of the GAO/STO electron mobility was well described by three contribution added according to the Matthiessen rule:

$$\frac{1}{\mu(T)} = \frac{1}{\mu(T \to 0\ \text{K})} + \frac{1}{AT^{-2}} + \frac{1}{\mu_{LO}(T)} \tag{7.1}$$

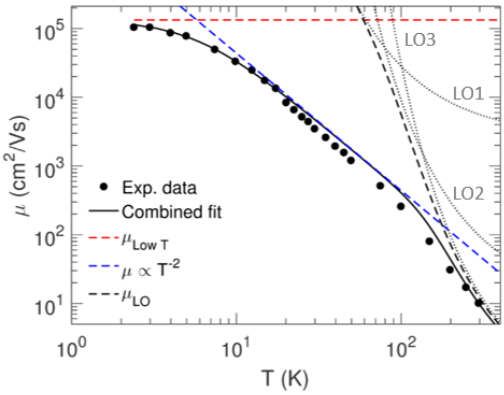

Figure 7.1 – Temperature dependence of the mobility. *Temperature dependence of the electron mobility in PLD-grown GAO/STO including fits using Eq. 7.1. LO1-3 refer to scattering from longitudinal optical phonon mode 1-3, whereas LO is the sum calculated using the Matthiessen rule. The figure is adapted from Article [XXIII].*

Here, the first term describes the temperature-independent mobility contribution dominating at temperatures typically below 5 K. The second term contributes to the mobility with an approximate T^{-2} scaling at intermediate temperatures (5 K $< T <$ 150 K) and can be attributed to electron-electron scattering [118–121]. The third term causes a deviation from the T^{-2} scaling at $T >$ 150 K due to scattering of longitudinal optical (LO) phonons. Three longitudinal optical phonon modes exist in the cubic phase of STO, but only the LO3 phonon mode determines the mobility for 150 K $< T <$ 300 K as this mode has the strongest electron-phonon coupling (α). The scattering contribution from the longitudinal optical phonons is derived by Low and Pines [122]:

$$\mu_{LO} = \frac{\hbar e}{2\alpha\hbar\omega_{LO} m_b} \left(\frac{m_b}{m_p}\right)^3 f(\alpha) \exp\left(\frac{\hbar\omega_{LO}}{k_B T}\right) \tag{7.2}$$

using the elementary charge (e), phonon frequency (ω_{LO}), polaron mass (m_p), bare effective mass (m_b) and a function f that increases monotonically and slowly from 1 to 1.35 as α increases from 0 to 6 [122]. When an electron moves through an ionic lattice, its charge creates a local lattice distortion that effectively enhances the electron mass through polaron formation. If the electron is confined in two dimensions at the interface, this polaron effective mass can be described by $m_p = m_b(1 + (\pi/8)\alpha + 0.1272\alpha^2)$ [123].

The fit of Eq. 7.1 to a high-mobility sample is satisfactory as shown in Figure 7.1 using the electron-electron interaction coefficient A and the low-temperature mobility as free parameters. The contribution from the longitudinal optical phonons was described solely using literature values [XXIII]. In the following, the scattering mechanisms limiting the mobility at room and low temperatures will be discussed following the Articles [XX,XXIII].

7.2 Room temperature mobility

Obtaining a high electron mobility at room temperature is important for device realization. However, STO typically obtains a modest room temperature mobility of 1-10 cm^2/Vs [24, 95, 118, 124, 125] with GAO/STO being no exception (see Figure 7.2). The as-deposited mobility varies greatly from sample to sample, however, by systematically decreasing the carrier density in a single sample using annealing, a positive correlation is found between the mobility and carrier density. High room temperature mobilities of up to 12 cm^2/Vs can thus generally be obtained at carrier densities above 10^{14} cm^{-2}. The underlying reason for this can be understood by noting that the dominant scattering mechanism at room temperature is longitudinal optical phonon scattering according to Eq. 7.2. Here, the only strong carrier density dependence enters via the electron-phonon coupling α, i.e. $\mu(\alpha(n_s))$ [XXIII]. The mobility is monotonously increasing as α is lowered from 4 to 1 (see inset of Figure 7.2), and the mobility can therefore be converted to the corresponding value of the electron-phonon coupling as presented in the lower part of Figure 7.2. From here it can be deduced that the largest mobilities are obtained when lowering the electron-phonon coupling. This occurs at high carrier densities due to an electronic screening of the electron-phonon interaction [10]. Interestingly, this treatment allows for determining the polaron effective mass of the electron, which decreases from 1.9 to $1.4m_e$ as the electron-phonon coupling is screened.

7.3 Low temperature mobility

The mobility increases by up to four orders of magnitude when the temperature is lowered from 300 to 2 K. Contributing factors are the large increase in the dielectric constant and the rapidly decreasing influence of the electron-phonon scattering. At low temperatures STO-based heterostructures generally obtain a high mobility at low carrier densities [126] & [XXIV,XVIII], however, GAO/STO is fundamentally different from this with a positive correlation observed between the mobility and carrier density (see Figure 7.3). The optimized deposition parameters for obtaining high mobility was observed to vary widely from one PLD chamber to another, however, in both cases the mobility increased roughly as $\mu \sim n_s^{1.5}$ up to the maximum value exceeding 100,000 cm^2/Vs obtained at $n_s(\mu_{\max}) \sim 5 \cdot 10^{14}$ cm^{-2} [XXIII]. GAO/STO obtained an increasing character of bulk three-dimensional conductivity at $n_s \gg n_s(\mu_{\max})$ resulting, in the extreme case, in an equal resistance measured at the back and front of the STO substrate for $n_s(\mu_{\max}) \sim 3 \cdot 10^{15}$ cm^{-2}. In this case, the entire 0.5 mm thick STO substrate can be perceived as a homogeneously conducting sheet with a three-dimensional carrier concentration of $n_s/0.05\text{cm} = 6 \cdot 10^{16}$ cm^{-3}. Consequently, the mobility decreases to ∼20,000 cm^2/Vs consistent with bulk conducting STO where donors are distributed throughout the substrate [45].

The current flow in GAO/STO samples with varying mobility and carrier densities

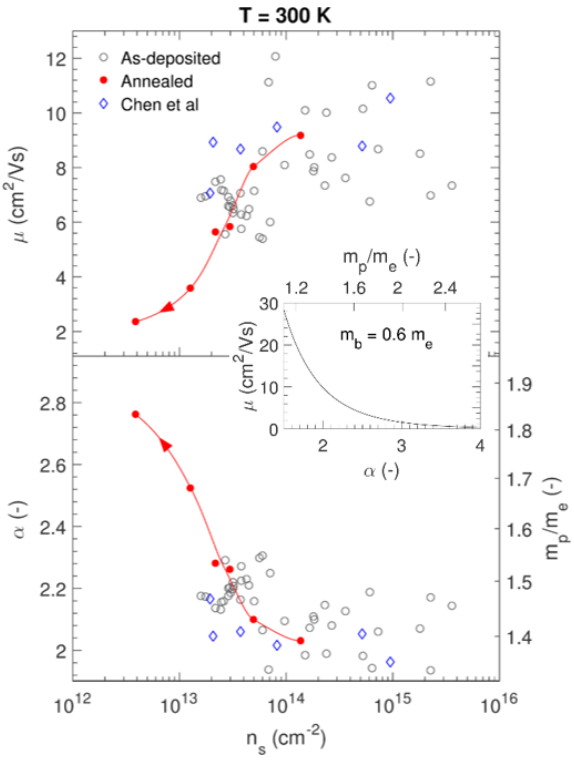

Figure 7.2 – Room temperature mobility.
Room temperature mobility (μ), electron-phonon coupling (α) and polaron effective mass enhancement (m_p/m_e) as a function of carrier density (n_s) in PLD-grown GAO/STO heterostructures. The inset shows the relationship between μ, α and m_p/m_e according to Eq. 7.2 assuming a bare band effective mass of $m_b = 0.6m_e$ and a two-dimensional polaron mass $m_p = m_b(1 + (\pi/8)\alpha + 0.1272\alpha^2)$. The figure is adapted from Article [XXIII] with part of the data taken from Chen et al [65].

was further studied using a scanning superconducting quantum interference device (SQUID). The scanning SQUID sensitively measured the magnetic flux entering a 1.8 µm large pick-up loop located at the end of a flexible scanning probe [127, 128]. The current flow was detected by passing an alternating current through the sample, which created a magnetic field measured by the SQUID with a lock-in technique. Scanning along the sample surface with the scanning probe thus produced a magnetic flux map revealing the current flow in the sample (see Figure 7.3). For $n_s \leq 1 \cdot 10^{14}$ cm^{-2} the stripy modulations were observed in the current flow similar to what has been seen in LAO/STO [129]. The stripes stem from a change in the conducting properties across the different tetragonal domains in STO formed below 105 K [57, 129]. Interestingly, the stripes are no longer observed for $n_s \geq 5 \cdot 10^{14}$ cm^{-2}. This is likely due to (i) a larger degree of bulk conductivity whereby the current can bypass specific surface domains or (ii) large carrier densities which screen potential steps across the domain walls and eventually render the changes in the conducting properties small compared to the overall large conductivity.

In Section 6.2 it was presented that annealing can result in a decrease in the carrier density firstly by redistributing oxygen vacancies to a location more prone to

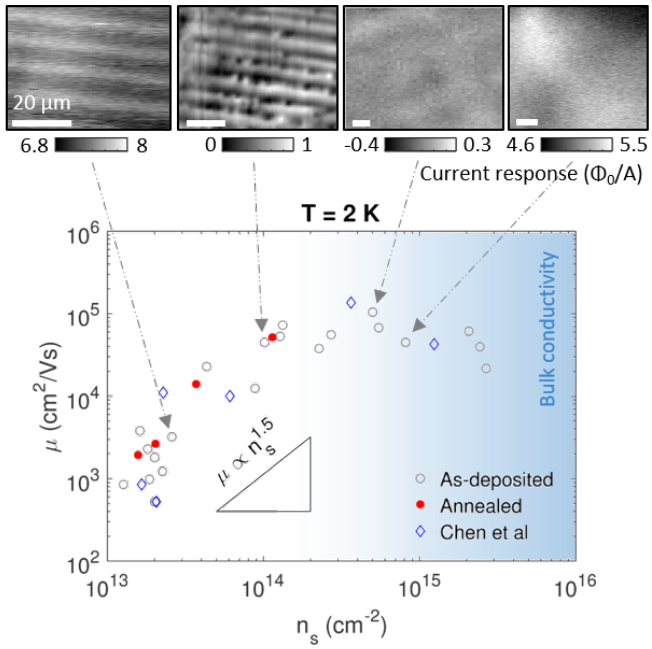

Figure 7.3 – Lower temperature mobility.
Mobility (μ) as a function of carrier density (n_s) measured at 2 K for as-deposited and post-annealed PLD-grown GAO/STO. Scanning SQUID images of the magnetic field created by the current flow in various samples are shown on the top. The absolute value of the current response measurements depends on the location on the sample and cannot be compared between different samples. The figure is adapted from Article [XXIII] with part of the data taken from Chen et al [65].

localization and secondly by oxidation. Very gentle annealing either by prolonged room temperature storage or exposure to elevated temperatures ($\sim$ 100 °C) can, however, also be used to enhance the conductance and mobility at low temperature without changing the carrier density (see Figure 7.4). As the electrical properties at room and elevated temperatures remained constant, this process was invisible by the method described in Section 6.2. The mobility enhancement in absence of a carrier density change was attributed to a change in the scattering landscape by an oxygen vacancy redistribution with little or no change in the charge localization. Oxygen vacancy properties were further examined using resonant soft x-ray photoemission spectroscopy and density functional theory (DFT) calculations [XX]. Oxygen vacancies located at the interface were found to have a lower formation energy and a deeper in-gap state compared to oxygen vacancies a few nanometers into STO (see Figure 7.5a). The deeper in-gap state was absent in LAO/STO and using DFT calculations it was found to originate from the different atomic arrangement at the GAO/STO

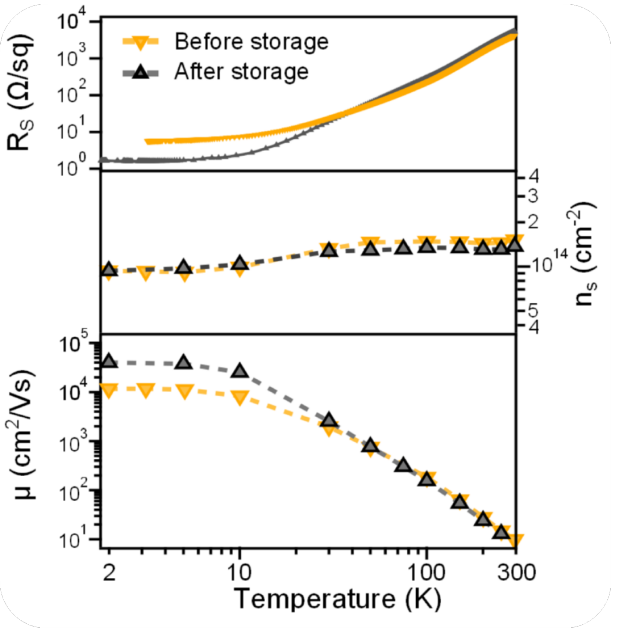

Figure 7.4 – Mobility enhancement through annealing.
Temperature dependence of the sheet resistance (R_s), carrier density (n_s) and mobility (μ) of PLD-grown GAO/STO before and after storing the sample for 6 months in a vacuum desiccator at room temperature. Similar mobility enhancements have been observed by annealing GAO/STO in 1 bar oxygen at ∼100 °C. The figure is adapted from Article [XX].

interface.

The high electron mobility in GAO/STO was attributed to an electron-donor separation in Refs. [XX,XXIII] as outlined in Figure 7.5b. In this view, the oxygen vacancy donors preferentially form at the GAO/STO interface due to the broken symmetry, whereas the electrons spread out deeper into STO thereby causing a lower scattering from the positively charged donors. Mobilities exceeding those observed in bulk conducting STO can thus be expected in analogy with the increased mobility in modulation doped structures. Interestingly, a $\mu \sim n_s^{1.5}$ behavior has also been observed in modulation doped structures owing to (i) predominant small-angle scattering as the Fermi surface expands [130] and (ii) increased electronic screening of ionized scattering sites [115]. The predominant small-angle scattering is supported by the large ratio of 6 between the Hall mobility and quantum mobility, whereas the scanning SQUID current flow images may show an efficient electronic screening at high carrier densities. A delicate balance is further expected to exist between oxygen vacancies located at the interface and deeper into STO. This supports that (i) the high mobility is only formed in a narrow deposition parameter window and (ii) the mobility can be enhanced as oxygen vacancies redistribute during a low temperature annealing. In this view, electromigration of oxygen vacancies may thus be used to further enhance the mobility.

Despite the data suggest that an electron-donor separation underlies the high mobility

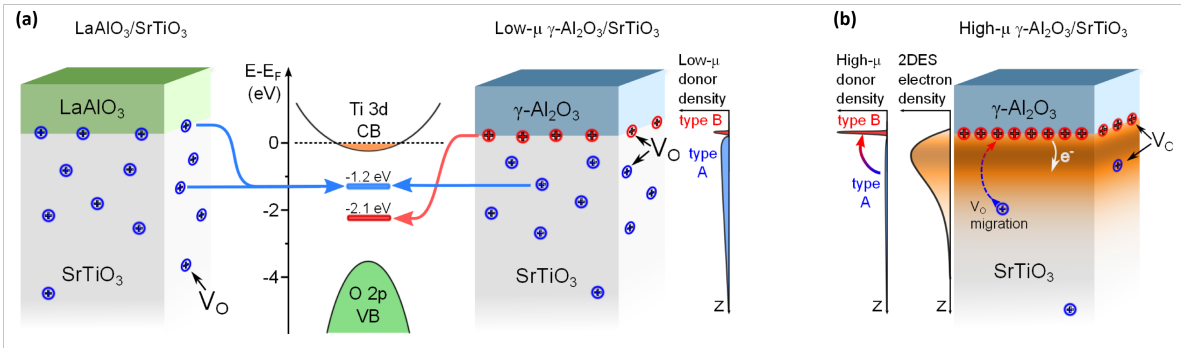

Figure 7.5 – Oxygen vacancies and high electron mobility.
(a) Schematics of the in-gap state produced by oxygen vacancies with different locations in LAO/STO and GAO/STO. Oxygen vacancies at the GAO/STO interface are found to produce a deep in-gap state located -2.1 eV from the conduction band (CB). (b) Proposed model for the high mobility where oxygen vacancies are preferentially formed at the GAO/STO interface whereas the electrons distribute deeper into STO effectively causing an electron-donor separation. The figure is adapted from Article [XX].

in GAO/STO, further studies on the electron and oxygen vacancy depth profiles are needed. It is of particular interest to study whether conducting electrons are found at the interface TiO_2-layer despite the large amount of oxygen vacancies, symmetry breaking and the Al diffusion from the GAO film into the first 1-2 unit cells of STO [65]. The latter is relevant as Al-doping of STO thin films has been observed to cause an increase in the bandgap of 0.3 eV, which is likely to be caused by shifting the conduction band to higher energies [131]. In addition, detailed DFT calculations and a systematic study of how the ratio between Hall and quantum mobility depends on the carrier density might shed more light on the origin of the high mobility.

CHAPTER 8

Colossal magnetoresistance

Magnetic sensors serve as vital components in numerous technologies including position monitoring and high-density information storage [132]. Magnetoresistive sensors provide a cost-efficient way of determining the magnetic field by typically applying a constant current and sensing the magnetic field using the voltage output [133]. The key descriptor is therefore the magnetoresistance (MR) defined as the relative change in the resistance upon application of a magnetic field:

$$\mathrm{MR} = \frac{R(B) - R(B = 0\ \mathrm{T})}{R(B = 0\ \mathrm{T})} \tag{8.1}$$

The magnetoresistance has geometrical and physical (intrinsic) contributions [132]. The geometrical contribution arises from the Lorentz force and manifests itself as a change in the magnetoresistance when varying the geometry e.g. by repositioning contacts or reshaping the active material. The physical contribution is intrinsic to materials and material combinations such as manganites [134] and magnetic multilayers [135]. The physical contribution is to date most widely used for designing sensors and it may originate from, e.g., changing the band structure, carrier density or spin configuration by the magnetic field.

8.1 Characterization of the magnetoresistance

The high mobility in GAO/STO heterostructures coexists with pronounced changes in the sheet resistance upon application of a transverse magnetic field [XXVIII]. In absence of a magnetic field the sheet resistance decreases by more than four orders of magnitude as high-mobility samples are cooled from 300 to 2 K (see Figure 8.1a). When a magnetic field is applied perpendicular to the interface, the sheet resistance deviates from the zero-field behavior below ~ 100 K, obtains a minimum at ~ 50 K and increases at lower temperatures (see Figure 8.1a). The field-induced increase in the sheet resistance causes a colossal magnetoresistance exceeding 80,000% at 2 K and 15 T (see Figure 8.1b) The values obtained in GAO/STO far exceed those

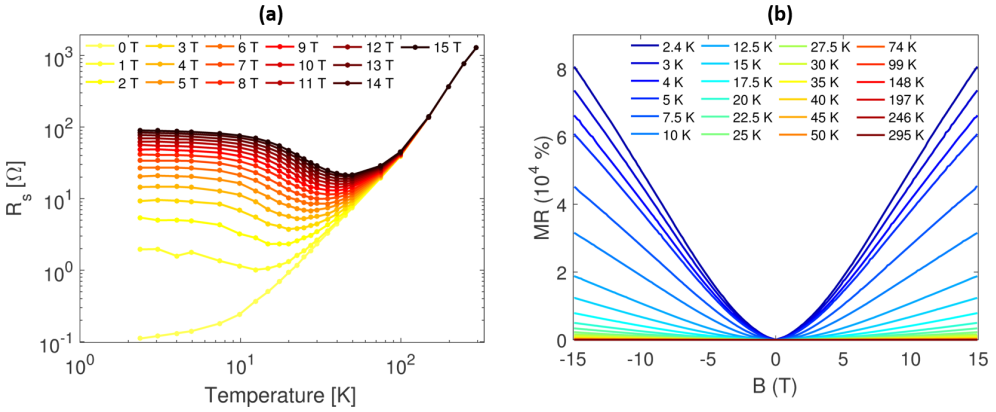

Figure 8.1 – Magnetoresistance in GAO/STO
(a) Temperature dependence of the sheet resistance (R_s) with applied magnetic fields ranging from 0 to 15 T. (b) Magnetoresistance ($MR = (R_s(B) - R_s(0))/R_s(0)$) as a function of the magnetic field (B) at various temperatures. In both cases the sheet resistance is measured in van der Pauw geometry with the magnetic field applied perpendicular to the PLD-grown GAO/STO interface. The figure is adapted from the unpublished Article [XXVIII].

otherwise considered to be the largest positive colossal magnetoresistance reported in any oxide [136]. At room temperature the magnetoresistance is decreased by six orders of magnitude and values of around 0.1% are typically obtained. The magnetoresistance increases as $\sim B^2$ at low magnetic fields as expected from the Lorentz magnetoresistance, however, at large magnetic field the magnetoresistance increases linearly with no sign of saturation.

8.2 Geometric contribution

The magnetoresistance is observed to have a significant geometrical contribution as observed when changing the contact configuration from a van der Pauw geometry to a linear geometry (see Figure 8.2a-b). Consistent sheet resistances are found using the two geometries in absence of an applied magnetic field, which validates the two different strategies for measuring the resistance. However, the magnetoresistance is highly influenced by the geometry. For this sample, the magnetoresistance is ∼60,000% at 2 K and 15 T in the van der Pauw geometry, but it decreases to ∼10,000% in the linear geometry. A noticeable difference is also the sheet resistance peak at $T \approx 8$ K in the van der Pauw geometry, which changes to a minimum in the linear geometry. Interestingly, 8 K is also found to be a characteristic temperature for the magnetic ordering in GAO/STO as discussed in the next chapter.

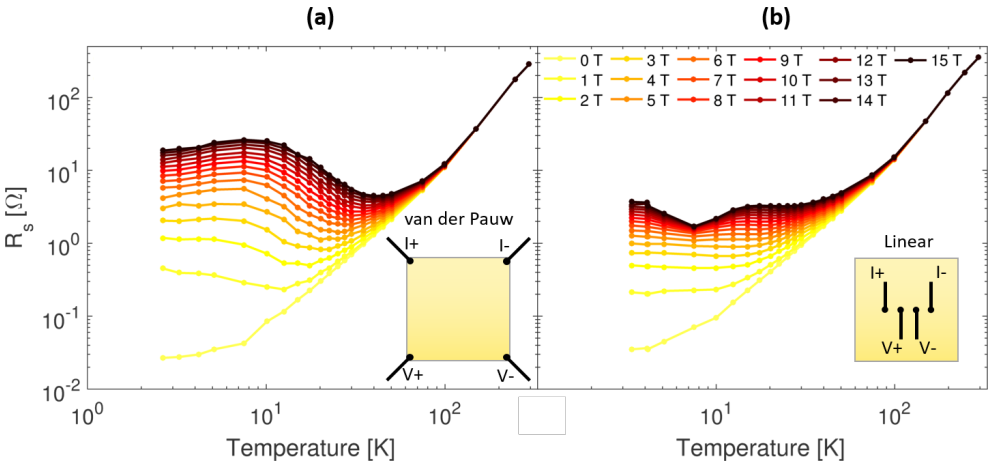

Figure 8.2 – Geometrical dependence of the magnetoresistance.
Temperature dependence of the sheet resistance (R_s) under various applied transverse magnetic fields when a PLD-grown GAO/STO heterostructure is contacted in van der Pauw geometry (a) or linear geometry (b). In the van der Pauw geometry, the bonds are places at the corners of the 5 mm x 5 mm GAO/STO, whereas the linear geometry has 4 bonds spaced with 900 µm on a line in the center of the sample. The figures are adopted from the unpublished Article [XXVIII].

8.3 Extraordinary magnetoresistance

The response of the magnetoresistance to the contact configuration opens up the possibility for geometric optimization. In 2000 the extraordinary magnetoresistance was discovered based on the geometric contribution in metal/semiconductor hybrid systems [137]. Here, a circular sample of Te-doped InSb with a mobility of 45500 cm^2/Vs was filled with a circle of Ti/Pt/Au in the middle, similar to the lower schematic drawing in Figure 8.3a. This enhanced the room temperature magnetoresistance from less than 1,000% at 5 T without the metal to 750,000% in the metal/semiconductor hybrid device with an optimized metal circle radius. The large increase in the magnetoresistance was due a dramatic change in the current flow of the sample when applying a magnetic field. At $B = 0$ T the majority of the current flows through the metal (see Figure 8.3b) leading to a low resistance. At $B > 0$ T the Lorentz force deflects the current away from the metallic area, and a high resistance is therefore obtained. Following the original discovery, additional geometric optimizations and materials have been investigated [132] including the numerical modeling of the Hall bar-like metal inclusion in InSb with a large enhancement of the magnetoresistance (see Figure 8.3). The physics can be described in two dimensions using the conductivity matrix relating

the current density ($\vec{j}$) and the electric field ($\vec{E}$):

$$\begin{bmatrix} j_x \\ j_y \end{bmatrix} = \frac{\sigma_0}{1+(\mu B)^2} \begin{bmatrix} 1 & -\mu B \\ \mu B & 1 \end{bmatrix} \cdot \begin{bmatrix} E_x \\ E_y \end{bmatrix} \tag{8.2}$$

where $\frac{\sigma_0}{1+(\mu B)^2}$ is the Lorentz magnetoconductance described using the zero-field conductance σ_0. The magnetic field causes a non-zero current to flow perpendicular to the electric field. If the conductivity of the metal far exceeds that of the semiconductor, the metal boundaries can be considered equipotential and the electric field is thus perpendicular to the boundaries, which can, e.g., be assigned to the x-direction, $|\vec{E}| = E_x$. From Eq. 8.2, the ratio between the deflected current and the current flowing into the metal is thus: $j_y/j_x = \mu B$. The current is therefore efficiently expelled in the presence of a magnetic field in high-mobility samples. The magnetoresistance of GAO/STO has not yet been enhanced by designing oxide/metal hybrid structures, but this is planned for future work. The GAO/STO heterostructure is a promising material choice for this due to: (i) the proven ability to significantly change the magnetoresistance using the geometry, (ii) the large electron mobility, (iii) the positive sign of both the GAO/STO magnetoresistance and the metal/oxide enhancement and (iv) the large, non-saturating magnetoresistance already found in as-deposited GAO/STO in absence of metal inclusions.

8.4 Origin of the magnetoresistance

The MR $\propto B^2$ observed at low magnetic fields in as-deposited GAO/STO is likely to originate from the classical Lorentz magnetoresistance. The Lorentz magnetoresistance saturates at high magnetic fields and a cross-over to a linear, non-saturating magnetoresistance is observed for some materials such as GAO/STO, silver chalcogenides ($Ag_{2+\delta}Se$ and $Ag_{2+\delta}Te$) [139], indium antimonide [140] and silicon [141]. The linear magnetoresistance is often explained by the current flow in an inhomogeneously conducting material. In the presence of a magnetic field, the Lorentz force may cause a large change in the current flow in the vicinity of inhomogeneities with high or low resistance [142, 143] in a similar fashion as for the metal inclusions discussed previously. Such current redistributions were shown numerically to cause a positive and linear magnetoresistance without saturation using the classical Lorentz force [142, 143]. A similar non-saturating magnetoresistance can have a quantum mechanically origin in the so-called extreme quantum limit where (i) distinguishable quantum levels are formed from electron orbits with frequency ω_c and (ii) all electrons populate the lowest quantum level [140]. This requires $\hbar\omega_c > k_B T$, $\hbar\omega_c > E_F$ and $\mu B > 1$ [140]. However, the large Fermi energy of $E_f \sim 600$ meV in GAO/STO (see Figure 5.7) far exceeds $\hbar\omega_c$ making the classical mechanism the most likely origin of the linear magnetoresistance. The inhomogeneities are likely to be induced by the deposition or stemming from the tetragonal domain formation in STO below 105 K. It should be mentioned that an asymmetric scattering caused by the spin/orbit coupling

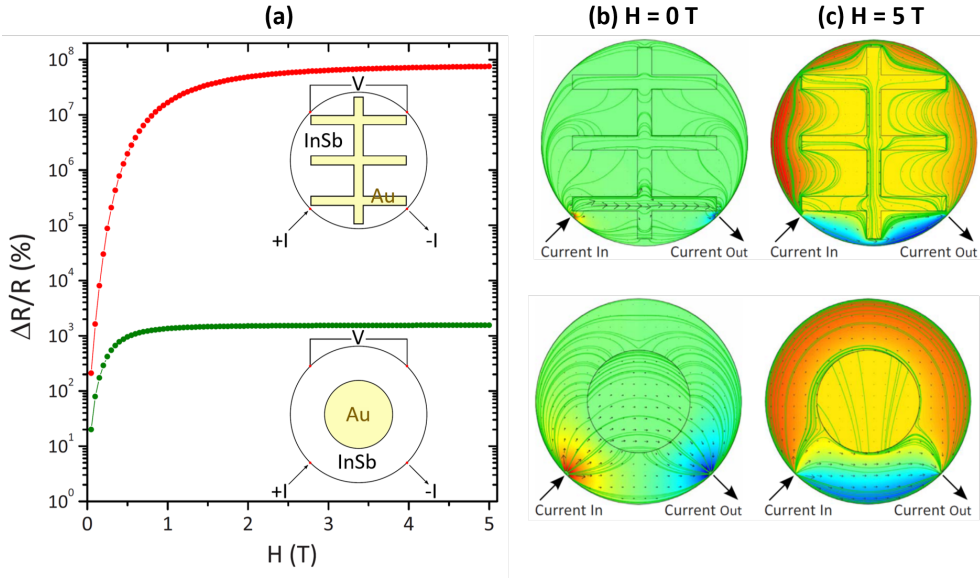

Figure 8.3 – Geometrically enhanced extraordinary magnetoresistance
(a) Magnetoresistance ($\Delta R/R$) as a function of the magnetic field (H) calculated for two different InSb/Au semiconductor/metal hybrid configurations using a numerical model. (b) The calculated electrostatic potential in absence and presence of a magnetic field for the two configurations given in (b). The figure is adapted from Ref. [138].

in GAO/STO may also be significant in understanding the large magnetoresistance and current deflections. This asymmetric scattering is discussed further in the next chapter.

CHAPTER 9

Magnetism

One of the most remarkable discoveries in LAO/STO was the emergence of magnetism between the two insulators that were generally considered non-magnetic [36]. The discovery opened up the possibility to couple the spin, charge and lattice degrees of freedom with a potential of realizing new devices and functionalities by the coupling. This initiated a large interest in the magnetic phase leading to the discovery of coexisting superconductivity and magnetism [48, 144] as well as the observation of magnetism in bulk STO [17, 18] and other STO-based heterostructures such as LAO/$EuTiO_3$/STO [145]. Magnetism was also found in a-AO/STO using torque magnetometry measurements [146]. Later, a strain-tunable magnetic state was found to coexist with the colossal magnetoresistance and high mobility in GAO/STO as observed with magnetotransport measurements and scanning SQUID [XXVI]:

9.1 Torque magnetometry measurements

In torque magnetometry a magnetic field is applied to a sample fixed to a flexible cantilever. If the sample contains a magnetic moment $\vec{m}$, the magnetic field causes a torque $\vec{\tau}$ on the sample, $\vec{\tau} = \vec{m} \times \vec{B}$, which is measured as a deflection of the cantilever. If the magnetic field is homogeneous, the technique is only sensitive to the component of the magnetization perpendicular to the magnetic field. This leaves the technique largely insensitive to dia- and paramagnetism, but highly sensitive to magnetic order or anisotropies that counteract aligning the magnetization along the magnetic field. The technique was used to probe the coexistence of magnetism and superconductivity in pulsed laser deposited LAO/STO [144] and the presence of magnetism in atomic layer deposited a-AO/STO [146]. The angle-dependent torque measurements of a-AO/STO is shown in Figure 9.1a. Applying the magnetic field perpendicular to the interface was found to result in no detectable in-plane magnetization $\vec{M}_{\parallel}$, whereas no conclusion could be made on the out-of-plane component $\vec{M}_{\perp}$ as $\vec{B} \parallel \vec{M}_{\perp}$. Rotating the field gradually from out-of-plane to in-plane results in a measurable torque until the field is aligned in-plane and a vanishing torque is again measured. The angle-dependent torque measurements suggest that the interface causes an anisotropy which favors in-plane magnetization. The torque is in this case given by $\tau = M_{\parallel}(B)B\cos(\phi)$ where ϕ is the angle between the magnetic field and the axis perpendicular to the interface. In this case, the in-plane magnetization can be extracted from the torque

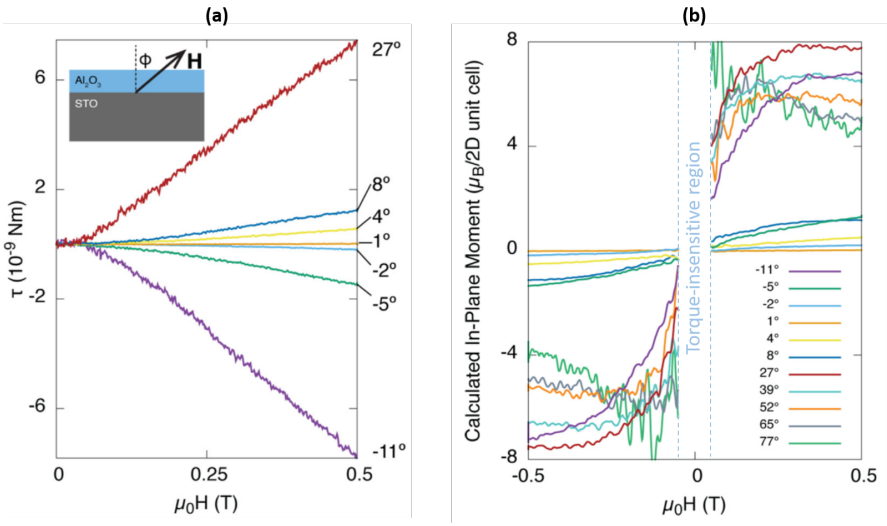

Figure 9.1 – Torque magnetometry measurements of a-AO/STO
(a) The magnetotorque (τ) of atomic layer deposited a-AO/STO as a function of a magnetic field ($\mu_0 H$) aligned at different angles ϕ with respect to the interface normal. (b) The in-plane magnetization inferred from the torque measurements as a function of magnetic field. The torque magnetometry loses sensitivity at low magnetic fields, and magnetization data are therefore not shown here. The figure is adapted from [146].

(see Figure 9.1b). At $B < 50$ mT, the technique loses sensitivity, however, at 50 mT $< B$ the in-plane magnetization increases until it saturates at $5 - 8\mu_B/a_{\mathrm{STO}}^2$ at $B \approx 250$ mT. The saturation magnetization was one order larger than in LAO/STO [144] and is unlikely to result from a single atomic layer, but rather to span multiple atomic layers. No hysteresis or coercivity was observed in any of the measurements on a-AO/STO and the torque signal was found to be unchanged up to the maximum probed temperature of 30 K.

9.2 Magnetotransport measurements

Linear Hall coefficients serve as a valuable tool for extracting carrier densities whereas deviations from the linearity are often used to deduce the band structure and magnetism. In high-mobility GAO/STO, the Hall coefficient is linear for $T > 40$ K revealing, for the sample presented in Figure 9.2a, a high carrier density of $n_s \sim 6 \cdot 10^{14}$ cm^{-2}. For $T < 40$ K, pronounced non-linearities arise without hysteresis. Here, the slope of the Hall coefficient, $|dR_{xy}/dB|$, increases at high magnetic fields, opposite to the S-shaped non-linearities observed in LAO/STO that are explained by

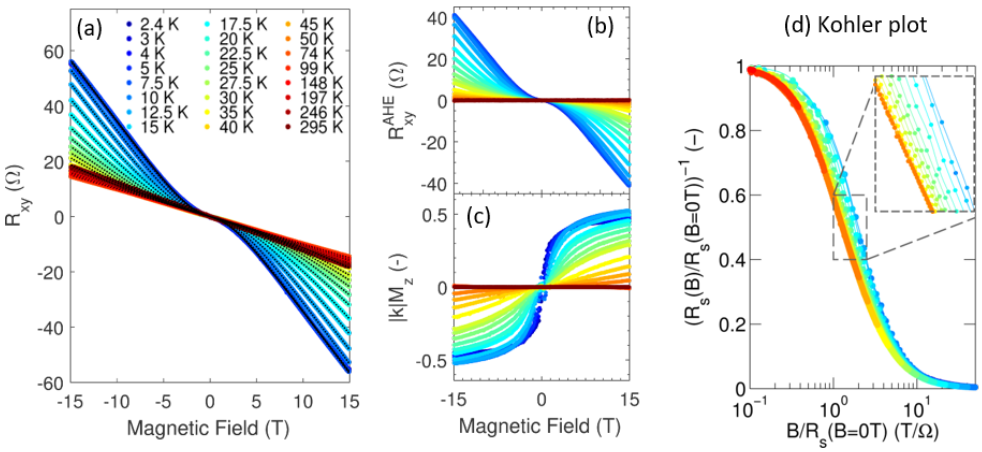

Figure 9.2 – Magnetotransport measurements of GAO/STO
(a) Hall coefficient (R_{xy}) as a function of the magnetic field applied perpendicular to the interface of pulsed laser deposited GAO/STO. Non-linearities are observed below 40 K. (b) Anomalous Hall coefficient (R_{xy}^{AHE}) obtained from R_{xy} by subtracting the ordinary Hall effect determined from the low-field slope of the Hall coefficient. (c) The component of the magnetization perpendicular to the interface (M_z) multiplied by a constant k as described in the main text. (d) Kohler plot of the magnetoresistance showing deviations from Kohler's rule below 40 K. The figure is adapted from Article [XXVI].

conductivity in two n-type bands with d_{xy} and d_{xz}/d_{yz} character [90]. If the Hall curvature in GAO/STO was due to two-band conductivity, it would entail a coexistence of a large number of electrons and holes, which was reject in Article [XXVI]. Instead, the non-linearity was attributed to the anomalous Hall effect (R_{xy}^{AHE}) arising from an interaction between the itinerant electrons and the component of the magnetization along the interface normal [147], $R_{xy}^{AHE} = R_s^{AHE} M_z$. It was further found that the anomalous Hall prefactor (R_s^{AHE}) scales linearly with the sheet resistance (R_s) [XXVI], leading to the following expression

$$R_{xy} = R_{xy}^{OHE} + R_{xy}^{AHE} = -\frac{1}{en_s}B + kR_s(B,T)M_z(B,T) \tag{9.1}$$

where n_s is the sheet carrier density and k is a coefficient describing the coupling strength between the magnetization and the Hall resistance. The linearity is expected in the skew scattering mechanism [147] where the presence of a spin-orbit coupling, allowed by the broken lattice symmetry at the GAO/STO interface, causes an asymmetric scattering of the electrons and a build-up of a Hall voltage. Indeed, the weak anti-localization observed during ionic liquid gating of the GAO/STO heterostructure evidences the presence of a spin-orbit coupling [XXI]. As the main feature

of the non-linear Hall effect is due to the anomalous Hall effect, the ordinary Hall effect is described using the sheet carrier density with a one band model for simplicity, although the data cannot exclude the presence of a second band with a low carrier density. This is consistent with both the depopulation of d_{xy} carriers at high carrier densities and the lowest-lying bands being the high-density d_{xz}/d_{yz} bands as discussed in Section 5.2.2, which both suggest that the majority of carriers populate bands with d_{xz}/d_{yz} symmetry.

At high magnetic fields, the sheet resistance increases linearly with the magnetic field, which, remarkably, results in a non-saturating anomalous Hall effect up to at least 15 T (see Figure 9.2b). The usual extraction of the carrier density from the slope of the Hall coefficient at high magnetic fields is therefore invalid as it includes contributions from both the ordinary and anomalous Hall effect. The carrier densities can be most accurately determined at low magnetic fields, as the sheet resistance is small with a vanishing slope at $B \approx 0$ T leading to a small anomalous Hall contribution. As seen in Figure 9.2a, the low-field slope of the Hall coefficient is temperature independent and hence $n_s \sim 6 \cdot 10^{14}$ cm^{-2} at all temperatures. This is consistent with the temperature independent carrier density deduced optically from the infrared Berreman mode similar to that presented in Figure 5.8. This way of extracting the carrier density was used when describing the mobility ($\mu = 1/en_sR_s$) in Chapter 7. The mobility of the sample shown in Figure 9.2 is $\approx$100,000 cm^2/Vs at 2 K.

By extracting $kM_z = (R_{xy} - R_{xy}^{OHE})/R_s$ the component of the magnetization parallel to the transverse magnetic field was inferred to start to saturate at $\sim$2 T for temperatures below 8 K (see Figure 9.2c). Increasing the temperature opposes the alignment up to $T \sim 40$ K where the magnetization is no longer detectable. Concomitant with the appearance of non-linear Hall coefficients, the magnetoresistance also starts to show deviations from Kohler's rule for $T < 40$ K (see Figure 9.2d). Kohler's rule holds for most materials and states that the resistance ratio $R_s(B,T)/R_s(B = 0\text{ T},T)$ is some function f of $B/R_s(B = 0\text{ T},T)$ [148]:

$$\frac{R_s(B,T)}{R_s(B=0\text{ T},T)} = F(\omega_c\tau_s) = f\left(\frac{B}{R_s(B=0\text{T},T)}\right) \tag{9.2}$$

Kohler's rule results from the magnetic field entering the semi-classical Boltzmann equation as the product of the cyclotron frequency and scattering life time, $\omega_c\tau_s = eB\tau_s/m^*$ with m^* being the effective mass and $\tau_s \propto R_s^{-1}$. Deviations from Kohler's rule may have various origins [149], however, in the case of GAO/STO deviations are expected as Kohler's rule do not include the reduction of the scattering when magnetic moments align along the magnetic field, i.e. both ω_c and τ_s depend on B. A similar behavior of the Hall coefficient and the Kohler plots were observed in four samples [XXVI].

9.3 Scanning SQUID measurements

A scanning SQUID was used to further investigate the magnetic state observed in GAO/STO [XXVI]. The scanning SQUID measures the magnetic flux entering a 1.8 µm wide pick-up loop, and produces a two-dimensional map of the flux by scanning the pick-up loop across the sample surface. The measurements are performed in the absence of an externally applied magnetic field and therefore probe the magnetic field originating from a spontaneous magnetic order in the sample. In the case of LAO/STO, such measurements originally showed the presence of ferromagnetic patches [150] and their coexistence with superconductivity [48]. For the GAO/STO heterostructure with transport measurements presented in Figure 9.2, magnetic flux maps revealed striped modulations with a typical magnitude of $\sim 1\ \mathrm{m}\Phi_0$ at 5 K (see Figure 9.3a). Striped modulations in the magnetic flux were observed in four additional GAO/STO heterostructures as well as in LAO/STO (see Figure 9.3b). Contrary to the dispersed ferromagnetic patches, the striped modulations span hundreds of micrometers, which implies a long-range magnetic order. As the magnetic flux escaping a homogeneously magnetized sample will show a homogeneous flux map in the center of the sample, the flux modulations witness a magnetization with spatial inhomogeneities. The striped inhomogeneities were observed along the [010], [110] and [$\bar{1}$10] crystallographic directions of STO. Interestingly, these orientations coincide with the tetragonal domain wall orientations in STO and the stripes in the current flow observed in LAO/STO and GAO/STO as discussed in Section 7.3. Using the scanning-SQUID to measure the current flow in ac mode and the magnetic signal in dc mode, the magnetic modulations were shown to be located at the same locations where the current flow is modulated due to the domain walls.

Thermally cycling the sample to room temperature resulted in significant changes of the magnetic landscape where [010] oriented stripes with a modulation amplitude of $\sim 0.6\ \mathrm{m}\Phi_0$ converted into very weak [110] orientated stripes with a modulation amplitude close to the noise level (see Figure 9.3d). When the temperature was raised gradually from 5 K, the flux modulations monotonically decreased in size until their disappearance at around 40 K (see Figure 9.3e). This is strikingly analogous to the absence of the magnetic signature in Hall and magnetoresistance measurements in GAO/STO and magnetoresistance measurements in LAO/STO [151, 152]. The temperature also roughly marks an anomaly of the STO substrate where its quantum paraelectric transition causes the dielectric constant to diverge [20]. Cooling the GAO/STO heterostructure to 5 K reintroduced the magnetic modulations without noticeable changes in size or location.

A few studies report magnetism in the STO substrate even in the absence of a top film [17, 18], and the influence of the GAO film was therefore probed by measuring a STO substrate with the same history as the GAO/STO, except that no deposition was performed. Importantly, this STO substrate was heated up to the deposition temperature of 650 °C in an oxygen pressure of 10^{-5} mbar without inducing macroscopic

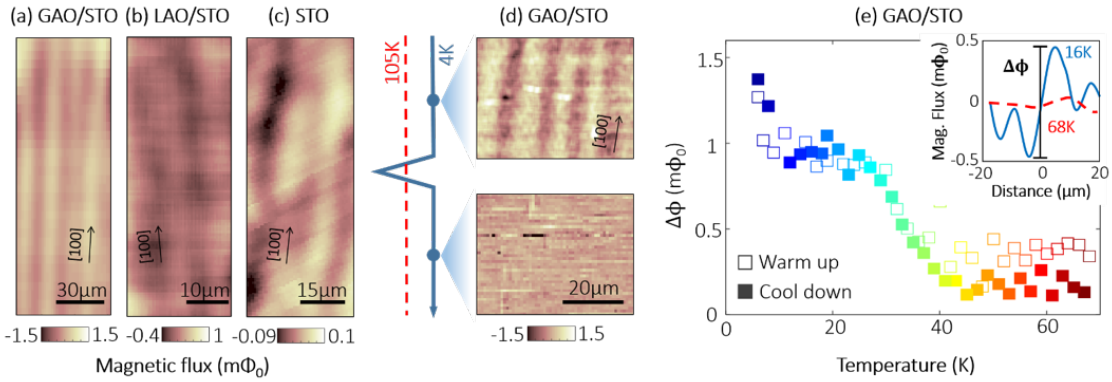

Figure 9.3 – Striped magnetization in GAO/STO
(a-c) Large area scan showing magnetic stripes in GAO/STO (a), LAO/STO (b) and STO (c) samples. The PLD grown GAO/STO sample was also used to obtain the magnetotransport data presented in 9.2. (d) The same location imaged in two subsequent scans on GAO/STO before and after thermal cycling the sample above 105 K (the structural transition temperature of STO). (d) Temperature dependence of the peak-to-peak modulation amplitude ($\Delta\Phi$) *in GAO/STO defined in the inset during warm up and cool down. The modulations disappear as the temperature increases to 40 K, and reappears without noticeable hysteresis during the subsequent cool down below 40 K. In all cases, the magnetic flux is offset by the average value of the scan. The figure is adapted from Article [XXVI].*

electrical conductivity. Also here, magnetic modulations with a similar shape were observed (see Figure 9.3c), with a change in the magnetic landscape when performing thermal cycling up to room temperature [XXVI].

9.4 Strain-tunable magnetism

A particularly interesting feature of the striped magnetic modulations observed in GAO/STO is the tunability under small applied forces [XXVI]. When locally applying a force of 56 nN on the GAO/STO surface using the scanning SQUID probe, the temperature dependence of the magnetic modulations changed markedly (see Figure 9.4a-b). Instead of the gradual decrease of the modulation strength observed up to 40 K, sharp, stripy features emerged when a force of 56 nN is applied. The features start to emerge around 10 K and the flux modulations are increased by a factor of four when reaching 16 K. Figure 3b shows that the sharp features are only obtained after contacting the sample surface with the probe, and the features become monotonically stronger when increasing the applied force. Interestingly, in all cases, the original magnetic landscape without the sharp magnetic modulations could be

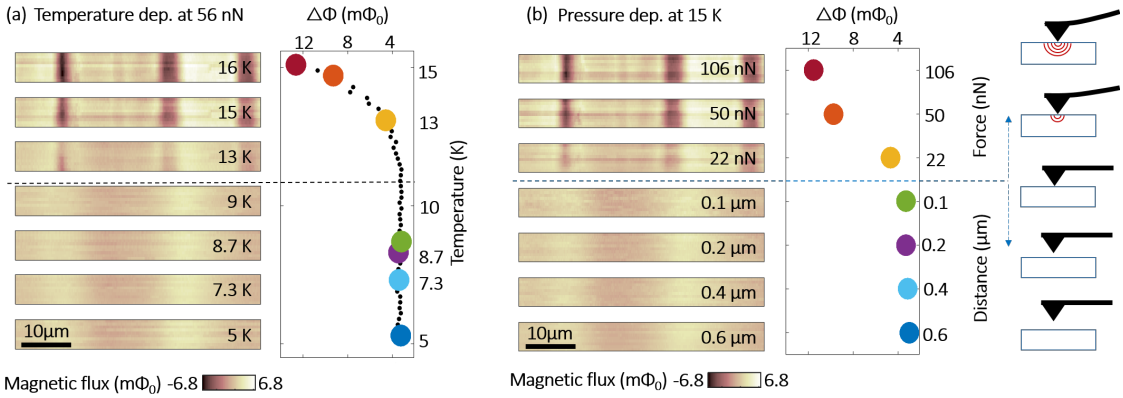

Figure 9.4 – Strain-tunable magnetization in GAO/STO
(a) Spatial modulation in the magnetic flux as function of temperature while pushing the tip of the SQUID tip into the sample with a force of 56 nN. Above ∼10 K the magnetic modulations become very sharp and the peak-to-peak modulation amplitude ($\Delta\Phi$) *increases monotonically with temperature. (b) Magnetic modulations at a fixed temperature of 15 K as the SQUID tip approaches the GAO/STO sample. When the SQUID reaches the sample, sharp magnetic modulations emerge. Further lowering the SQUID results in applying a stronger external force to the sample, which causes an increase in the peak-to-peak modulation amplitude. The force is measured capacitatively via the deflection of the SQUID cantilever. In all cases, the magnetic flux is offset by the average value of the scan. The figure is adapted from Article [XXVI].*

restored without hysteresis by lowering the temperature or removing the force.

Inspired by the stress dependence, the influence of internal strain on the magnetic landscape was also probed. It was found that detectable magnetic modulations similar to those presented in e.g. Figure 9.3a appeared particularly at locations where the tetragonal domain structure in STO was complex such as at the end of needle domains. In addition, modulations were also observed more strongly in the vicinity of areas expected to exhibit strain such as close to the sample border or around a scratch introduced on the surface of one sample. Besides containing high strain, these areas are also expected to have the largest amount of defects such as oxygen vacancies.

The magnetic susceptibility was found to be vanishing or slightly diamagnetic below 5 K with a conversion to paramagnetism with a dramatic increase in intensity above ~ 8 K (see Figure 9.5a). Interestingly, this temperature also appeared in the analysis of the anomalous Hall effect. The characteristic magnetic field (B_c) for the emergence of the anomalous Hall effect can be described by the half width at half maximum of the bell-shaped (dR_{xy}/dB). Below ~ 8 K, the characteristic field was

temperature independent, consistent with reports on NGO/STO[153] and as expected if an ordered state prevents the magnetization to be induced or aligned along the field (see Figure 9.5a). At higher temperatures, B_c increased linearly upon raising the temperature pointing towards a behavior similar to paramagnetism where the alignment of magnetic moments is countered by thermal fluctuations.

9.5 Mechanism

Characteristic temperatures of ∼8 K and ∼40 K were observed in the independent transport measurements and the SQUID imaging of GAO/STO. This gives three different temperature regimes in which the magnetic state was proposed to have different behavior [XXVI]:

1. Below 8 K, the GAO/STO heterostructure is in an ordered state, which manifests itself in soft or no modulations in the magnetization. This state is characterized primarily by a diamagnetic response (negative magnetic susceptibility) when applying small magnetic fields of ±1 mT. Applying a temperature-independent characteristic magnetic field of $B_c \sim 2.5$ T breaks the order and align the magnetic moments perpendicular to the interface, which causes the anomalous Hall effect. At these temperatures, a local application of external forces up to 122 nN has no effect on the ordered state.
2. Above 8 K, the thermal energy leaves the magnetic order more sensitive to breakage. This is supported by the increase in the paramagnetic susceptibility under a small applied force of 56 nN suggesting a gradual release of previously ordered magnetic moments into a paramagnetic state. The alignment of the paramagnetic moments with the magnetic field is countered by thermal fluctuations resulting in a linear increase of B_c with temperature. The fragile magnetic order above 8 K is highly sensitive to externally applied forces, and stronger magnetic modulations can be induced here. This points towards a delicate balance between the intrinsic order and a ferromagnetic order, where the applied pressure can shift the balance towards the ferromagnetic order. The ferromagnetic order is likely to arise from magnetic moments produced by oxygen vacancies [17, 96]. This is supported by the vast number of oxygen vacancies in GAO/STO as well as the localized in-gap states formed by the oxygen vacancies as explained in Chapter 5. The intrinsic order may e.g. be a spiral magnetic order [154] or an electron pair state [51] with an expected diamagnetic response to small magnetic fields. Interestingly, a pressure-sensitive transition from a spiral order to a ferromagnetic order has been predicted by a polar distortion in STO where titanium ions are displaced relative to the oxygen ions [154]. Such a polarity-induced ferromagnetic order may also explain why the magnetic stripes

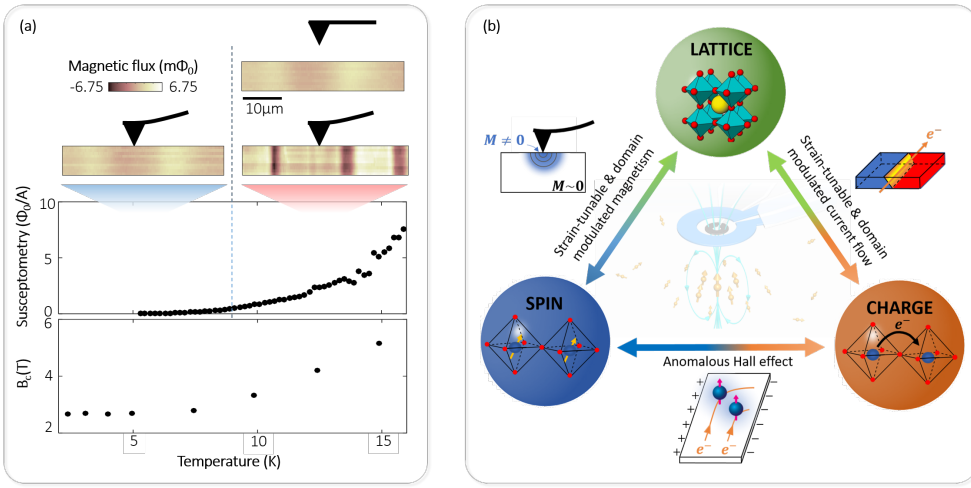

Figure 9.5 – Coupling of lattice, strain and charge
(a) Temperature dependence of the magnetic properties in PLD-grown GAO/STO showing (i) emergence of sharp magnetic features above 10 K upon application of an external force, (ii) an increase in the magnetic susceptibility with an onset of 8 K and (iii) the characteristic field B_c, defined as the half width at half maximum of dR_{xy}/dB from Figure 9.2a, undergoing a change from temperature-independent to linearly increasing with temperature at 8 K. (b) An intimate coupling between the lattice, spin and charge degrees of freedom in GAO/STO. The magnetic state is closely coupled to the lattice as revealed by applying external forces locally to the sample with the scanning probe. The tetragonal domain formation also causes local lattice distortions, which both favor ferromagnetic order and modulates the charge current. The charge current is, in turn, scattered asymmetrically by the magnetic moments, giving rise to the anomalous Hall coefficient. The figure is adapted from Article [XXVI].

(even in absence of an external force) are parallel to the domain walls in STO, as the domain walls have been observed to be polar [23].

3. Above ~ 40 K, all signatures of magnetism from the anomalous Hall effect, magnetoresistance and scanning SQUID vanish in GAO/STO, consistent with the disappearance of striped current modulation in LAO/STO [129] as well as some of the observations of magnetism in LAO/STO [151, 152]. This coincides reasonably well with the emergence of polar domain walls only below ~ 50 K [23], again hinting towards the influence of STO polarity.

9.6 Coupling lattice, spin and charge

The magnetic measurements presented in this chapter witness an intimate coupling between the lattice, spin and charge degrees of freedom (see Figure 9.5b). The charge transport through the lattice is highly affected by magnetic moments producing a spin/orbit-driven asymmetric scattering of the electrons as well as the lattice domain formation giving rise to current modulations. The lattice also influences the magnetic phase of GAO/STO both through the domain formation and pressure-induced changes. Recent unpublished experiments from the group of Beena Kalisky at Bar-Ilan University show that applying external forces using an identical SQUID probe can change the polar state at the ferroelastic domain walls of STO. In combination with the present observations, it seems likely that an exciting multiferroic state awaits to be discovered, which features a coexisting and strain-tunable ferroelectric, ferroelastic and ferromagnetic order.

CHAPTER 10

Perspective

The previous chapters have outlined the discovery of various appealing properties in GAO/STO along with the progress in understanding these. Despite GAO/STO exhibits at range of interesting properties, it remains far less studied than the benchmark LAO/STO heterostructure. In some cases, however, properties like the emergence of the interface conductivity are better understood in GAO/STO. In other cases, the properties are far from well-understood or remain completely unexplored. This chapter serves as my personal view on interesting directions for future research:

10.1 Mobility enhancement

As described in Section 7.3, the high electron mobility at low temperatures is proposed to originate from an electron-donor separation, but further investigations are needed to verify this. The mobility has, to some extent, been optimized through deposition parameter variations, but post-deposition mobility enhancements on high-mobility GAO/STO have only been proven on a proof-of-concept level using post-annealing (Figure 7.4). Other pathways to enhance the mobility remain unexplored such as attempting to (i) electromigrate oxygen vacancies in the presence of a transverse electric field at elevated temperatures to change the oxygen vacancy depth profile, (ii) electrostatically gate high-mobility samples or (iii) apply compressive strain to the interface.

10.2 Extraordinary magnetoresistance

As explained in Section 8.3, the high mobility and colossal positive magnetoresistance make GAO/STO an interesting candidate for realizing extraordinary magnetoresistance in oxide/metal hybrid devices. Important aspects for realizing such an enhancement are the optimization of the metal geometry, minimization of the oxide/metal contact resistance and avoidance of degrading the intrinsic GAO/STO properties with the metal patterning. Studying the magnetic field dependence of the current distribution in unpatterned GAO/STO and oxide/metal hybrid devices may further give a better understanding of the positive magnetoresistance observed in these systems.

10.3 Controllable polarity

An interesting prediction from the discussion of the GAO polarity in Section 5.1.4 is the potential for tuning the polarity in GAO thin films by electromigration of aluminum ions. For instance, at a GAO thickness of 1 u.c., only a few aluminum vacancy distributions lead to non-polar GAO films [XV]. These distributions are characterized by having the aluminum vacancies close to the STO surface, and an electromigration of vacancies towards the GAO surface may thus render GAO polar. This is likely to require elevated temperatures and/or prolonged application of an electric field across the GAO thin film using a top-gate or ionic liquid gate.

10.4 Band perspective

Seemingly conflicting conclusions regarding the band ordering in GAO/STO were reported as explained in Section 5.2.2. Reconciliation of these conclusions is of great interest as the band ordering is vital for understanding the electronic properties. In particular, if the d_{xz}/d_{yz} are located at a lower energy than d_{xy}, GAO/STO is an interesting model system for probing band structure effects. For LAO/STO the population of d_{xy} prior to d_{xz} and d_{yz} is suggested to be a determining factor for the resulting ferromagnetic/antiferromagnetic exchange coupling [94], spin-orbit coupling [90], superconducting phase [90], electron pairing in absence of superconductivity [51] and band splitting [91]. Using a STO-based model system with the first available bands being d_{xz}/d_{yz} rather than d_{xy} allows for studying such band-based hypotheses. In addition, if the four-fold rotational symmetry around the interface normal can be broken, e.g. by applying uniaxial strain along the [100] direction, splitting of d_{xz} and d_{yz} may lead to reducing the electron gas dimensionality from 2D to 1D owing to the directionality of the d_{xz}/d_{yz} orbitals.

10.5 Interface symmetry breaking

The anomalous band structure and the deeper oxygen vacancy in-gap state are likely examples of the unique impact the symmetry breaking at the spinel/perovskite interface has. This, however, remains largely unexplored and other effects such as a modified Rashba spin-orbit coupling may also be revealed.

10.6 Separating the effect of defects and electrons

Combining electrostatic gating and annealing results in a particular versatile tuning of the GAO/STO heterostructure through systematic variations of defects, donors and free charge carriers. As discussed in Section 6.5, this may enable the separate tuning of oxygen vacancies providing localized magnetic moments and the itinerant

electrons that exchange couple to the localized magnetic moments. Control of the magnetoresistance and electron mobility may also be obtained.

10.7 Strain engineering

Application of external strain adds an additional tuning knob to the control of the GAO/STO functionalities. It is of great interest to see if strain can induce room temperature multiferroicity in STO, metal-insulator transitions, changes in the band structure, enhancement of the electron mobility/magnetoresistance and control of the STO domain formation with a concomitant control of magnetism and current flow. Various strategies may be used to perform strain analysis such as straining GAO/STO mechanically with a strain device or epitaxially by growing GAO/STO on substrates with different lattice constants as shown in Section 5.2.2. Preliminary results are obtained in this thesis by mechanically straining undoped and Nb-doped STO while measuring the overall deformation, lattice expansion and effect on the bandstructure. In addition, strain-dependent transport measurements and scanning-SQUID measurements are under preparation.

10.8 Numerical modeling

The above perspectives can be performed experimentally, however, detailed numerical modeling of the GAO/STO is also needed to reach a deeper understanding of the heterostructure. In particular, it may shed light on the influence of the aluminum interdiffusion into the first 1-2 unit cells of STO [65] and the enlarged carrier density observed when depositing either 2.5 or $\sim$3.5 u.c. GAO on STO at 600-650 °C (see Figure 5.1 and 6.1).

CHAPTER 11

Conclusion

The epitaxial and non-isomorphic growth of spinel GAO on perovskite STO breaks the lattice symmetry and results in a confined electron gas at the interface. The conductivity originates from migration of oxygen from STO to GAO, which produces oxygen vacancy donors and itinerant electrons in the interface-near region of STO. The electron density can be tuned by deposition control, post-annealing in oxygen, electrostatic gating and light exposure. The electrons can be highly mobile at low temperatures with mobilities exceeding 100,000 cm^2/Vs, presumably caused by an electron-donor separation. Post-annealing can result in an enhancement of the low-temperature mobility, whereas the room temperature mobility is limited by the electron-phonon scattering and can be enhanced by screening of the electron-phonon coupling. The high mobility is found to coexist with a magnetic order and a colossal positive magnetoresistance of up to 80,000%. The colossal magnetoresistance is likely to stem from inhomogeneities in the conductivity, and it was shown to contain a controllable geometric contribution paving the way for designing extraordinary magnetoresistance in oxide/metal hybrid devices. The magnetism is modulated along the tetragonal domain walls of STO and can be tuned by externally applied forces. The most important conclusions from each chapter are summarized graphically in Figure 11.1. Here, my own key contributions to the various conclusions are marked with an underlined reference to the appropriate paper, whereas supportive contributions to well-established conclusions are marked with a reference without underlining.

Many of the functionalities observed in the GAO/STO originate from an intimate link between the lattice, spin and charge degrees of freedom in the GAO/STO heterostructure. Future research might exploit this to discover additional phenomena such as a multiferroic state where ferroelasticity, ferroelectricity and ferromagnetism all coexist and can be tuned with strain. STO and STO-based systems prove, once again, to be exciting multifunctional material platforms that truly require '*a thorough knowledge of all of solid state physics*' [16].

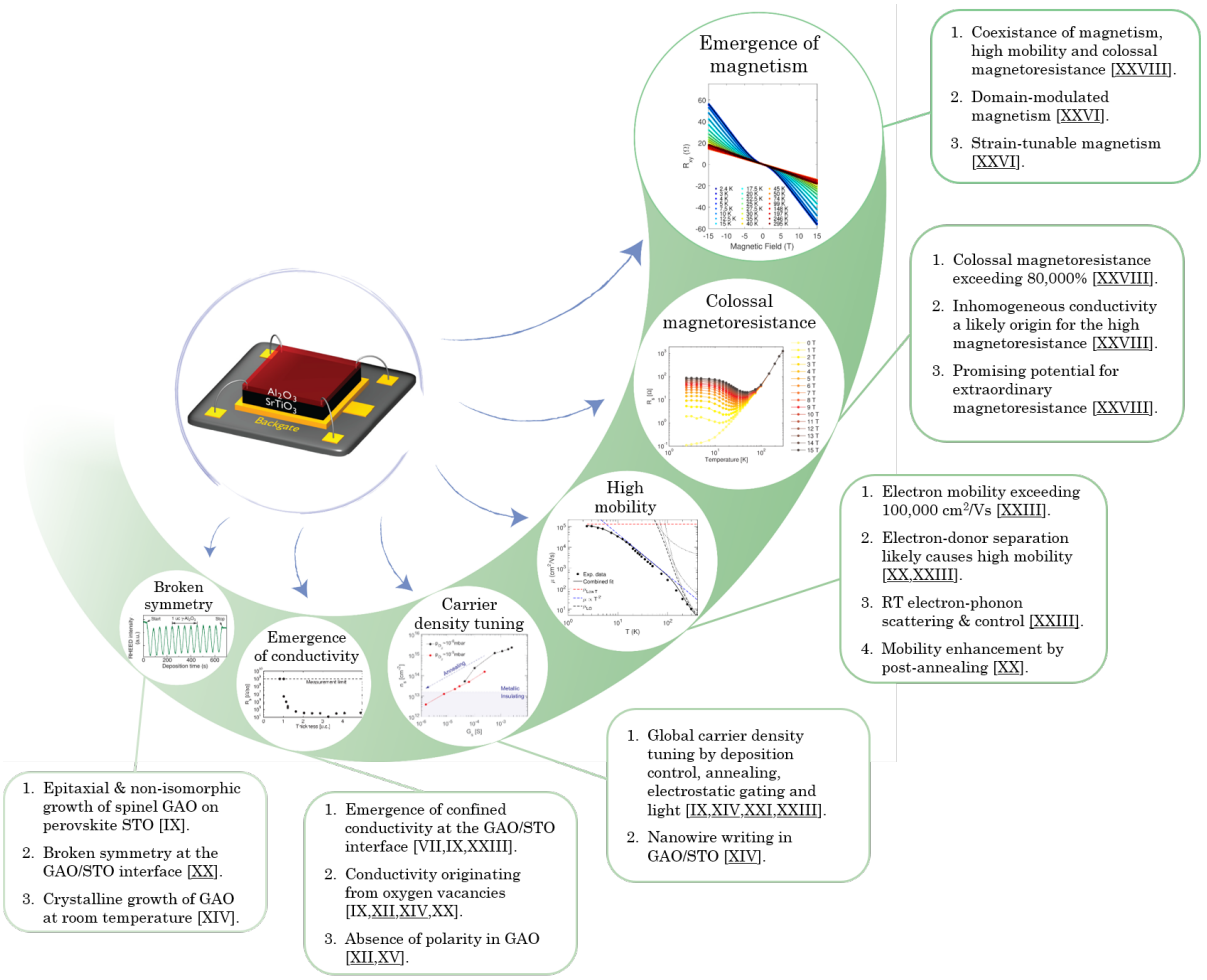

Figure 11.1 – Versatile properties of GAO/STO

An overview of the most prominent observations in the GAO/STO heterostructure discussed in this thesis. My own contributions to each observation is indicated by reference to the respective articles. Underlined references mark key contributions to the observation, whereas references without underlining indicate supportive, non-crucial contributions.

APPENDIX A

List of publications

The following articles are published, submitted or under preparation during the course of this PhD project. For easier reference, the status of the articles has been updated in 2018 after the end of the PhD project. The articles are divided into different sections based on their status and content. The roman numbers enumerate the scientific articles in chronological order and they are used as references in the main text.

A.1 Articles submitted or under preparation

XXX **D. V. Christensen**, A. Chikina, Y. Z. Chen, M. Radovic, N. Pryds, V. N. Strocov. The electronic structure of the γ-Al_2O_3/$SrTiO_3$ heterostructure. Under preparation for *Physical Review Materials* (2018).

XXIX **D. V. Christensen**. The multifunctional γ-Al_2O_3/$SrTiO_3$ heterostructure. Review article under preparation for *Advanced Electronic Materials* (2017).

XXVIII **D. V. Christensen**, A. Smith, Y. Z. Chen, and N. Pryds. Coexistence of colossal magnetoresistance, magnetism and high electron mobility in oxide heterostructures. Under preparation for *Nature Physics* (2018).

XXVII Y. L. Gan, M. von Soosten, Y. Zhang, H. R. Zhang, Z. C. Zhong, W. Niu, **D. V. Christensen**, T. S. Jespersen, B. G. Shen, J. R. Sun, N. Pryds, and Y. Z. Chen. Diluted Oxide Interfaces with Tunable Ground States. Under review in *Advanced Materials* (2018).

A.2 Published peer-reviewed articles related to the PhD project

XXVI **D. V. Christensen**, Y. Frenkel, A. Smith, Y. Z. Chen, L. Klein, N. Pryds, and B. Kalisky. Strain tunable magnetism at ferroelastic domain walls. Accepted by *Nature Physics* (2018).

XXIV **D. V. Christensen**, F. Trier, and N. Pryds. Electron Mobility in Oxide Heterostructures. *Journal of Physics D: Applied Physics* 9, 054004 (2018).

XXIII **D. V. Christensen**, Y. Frenkel, P. Schütz, F. Trier, R. Claessen, B. Kalisky, A. Smith, Y. Z. Chen, and N. Pryds. Electron mobility in γ-Al_2O_3/$SrTiO_3$. *Physical Review Applied* 9, 054004 (2018).

XXII Y. Zhang, Y. L. Gan, W. Niu, K. Norrman, X. Yan, **D. V. Christensen**, M. von Soosten, H. Zhang, B. G. Shen, N. Pryds, J. R. Sun, and Y. Z. Chen. Tuning the Two-Dimensional Electron Gas at Oxide Interfaces by Ti-O Configuration. *ACS Applied Materials and Interfaces* 10, 1434 (2018).

XXI W. Niu, Y. Zhang, Y. L. Gan, **D. V. Christensen**, M. von Soosten, E. J. G. Suárez, A. Riisager, X. Wang, Y. Xu, R. Zhang, N. Pryds, and Y. Z. Chen. Giant tunability of the two-dimensional electron gas at the interface of γ-Al_2O_3/$SrTiO_3$. *Nano Letters* 17, 6878 (2017).

XX P. Schütz, **D. V. Christensen**, V. Borisov, F. Pfaff, P. Scheiderer, L. Dudy, M. Zapf, J. Gabel, Y. Z. Chen, N. Pryds, V. A. Rogalev, V. N. Strocov, C. Schlueter, T.-L. Lee, H. O. Jeschke, R. Valentí, M. Sing, and R. Claessen. Microscopic origin of the mobility enhancement at a spinel/perovskite oxide heterointerface revealed by photoemission spectroscopy. *Physical Review B* 96, 161409 (2017).

XVIII F. Trier, K. V. Reich, **D. V. Christensen**, Y. Zhang, H. L. Tuller, Y. Z. Chen, B. I. Shklovskii, and N. Pryds. Universality of electron mobility in $LaAlO_3$/$SrTiO_3$ and bulk $SrTiO_3$. *Applied Physics Letters* 111, 092106 (2017).

XVII E. D. K. G. Prawiroatmodjo, M. Leijnse, F. Trier, Y. Chen, **D. V. Christensen**, M. von Soosten, N. Pryds, and T. S. Jespersen. Transport and excitations in a negative-U quantum dot at the $LaAlO_3$/$SrTiO_3$ interface. *Nature Communications* 8, 395 (2017).

XVI W. Niu, Y. L. Gan, Y. Zhang, **D. V. Christensen**, M. von Soosten, X. Wang, Y. Xu, R. Zhang, N. Pryds, and Y. Z. Chen. Suppressed carrier density for the patterned high mobility two-dimensional electron gas at γ-Al_2O_3/$SrTiO_3$ heterointerfaces. *Applied Physics Letters* 111, 021602 (2017).

XV **D. V. Christensen**, and A. Smith. Is γ-Al_2O_3 polar? *Applied Surface Science* 423, 887 (2017).

XIV **D. V. Christensen**, M. von Soosten, F. Trier, T. S. Jespersen, A. Smith, Y. Z. Chen, and N. Pryds. Controlling the Carrier Density of $SrTiO_3$–based Heterostructures with Annealing. *Advanced Electronic Materials*, 1700026 (2017).

XIII Y. Z. Chen, Y. L. Gan, **D. V. Christensen**, Y. Zhang, and N. Pryds. Effect of Sr-doping of $LaMnO_3$ spacer on modulation-doped two-dimensional electron gases at oxide interfaces. *Journal of Applied Physics* 121, 095305 (2017).

XII F. Gunkel, S. Hoffmann-Eifert, R. A. Heinen, **D. V. Christensen**, Y. Z. Chen, N. Pryds, R. Waser, and R. Dittmann. Thermodynamic Ground States of Complex Oxide Heterointerfaces. *ACS Applied Materials and Interfaces* 9, 1086 (2017).

XI F. Trier, G. E. D. K. Prawiroatmodjo, Z. Zhong, **D. V. Christensen**, M. von Soosten, A. Bhowmik, J. M. G. Lastra, Y. Z. Chen, T. S. Jespersen, and N. Pryds. Quantization of Hall resistance at the metallic interface between an oxide insulator and $SrTiO_3$. *Physical Review Letters* 117, 096804 (2016).

IX **D. V. Christensen**, F. Trier, M. von Soosten, G. E. D. K. Prawiroatmodjo, T. S. Jespersen, Y. Z. Chen, and N. Pryds. Electric field control of the γ-$Al_2O_3/SrTiO_3$ interface conductivity at room-temperature. *Applied Physics Letters* 109, 021602 (2016).

VIII G. E. D. K. Prawiroatmodjo, F. Trier, **D. V. Christensen**, Y. Z. Chen, N. Pryds, and T. S. Jespersen. Evidence of weak superconductivity at the room-temperature grown $LaAlO_3/SrTiO_3$ interface. *Physical Review B* 93, 184504 (2016).

VII M. Yazdi-Rizi, P. Marsik, B. P. P. Mallett, A. Dubroka, **D. V. Christensen**, Y. Z. Chen, N. Pryds, and C. Bernhard. Infrared ellipsometry study of the confined electrons in a high-mobility γ-$Al_2O_3/SrTiO_3$ heterostructure. *EPL Europhysics Letters* 113, 47005 (2016).

VI F. Trier, G. E. D. K. Prawiroatmodjo, M. von Soosten, **D. V. Christensen**, T. S. Jespersen, Y. Z. Chen, and N. Pryds. Patterning of high mobility electron gases at complex oxide interfaces. *Applied Physics Letters* 107, 191604 (2015).

V Y. Z. Chen, F. Trier, T. Wijnands, R. J. Green, N. Gauquelin, R. Egoavil, **D. V. Christensen**, G. Koster, M. Huijben, N. Bovet, S. Macke, F. He, R. Sutarto, N. H. Andersen, J. A. Sulpizio, M. Honig, G. E. D. K. Prawiroatmodjo, T. S. Jespersen, S. Linderoth, S. Ilani, J. Verbeeck, G. Van Tendeloo, G. Rijnders, G. A. Sawatzky, and N. Pryds. Extreme mobility enhancement of two-dimensional electron gases at oxide interfaces via charge-transfer-induced modulation doping. *Nature Materials* 14, 801 (2015).

IV Y. Z. Chen, F. Trier, T. Kasama, **D. V. Christensen**, N. Bovet, Z. I. Balogh, H. Li, K. T. S. Thydeìn, W. Zhang, S. Yazdi, P. Norby, N. Pryds, and S. Linderoth. Creation of High Mobility Two-Dimensional Electron Gases via Strain Induced Polarization at an Otherwise Nonpolar Complex Oxide Interface. *Nano Letters* 15, 1849 (2015).

I F. Trier, S. Amoruso, **D. V. Christensen**, A. Sambri, Y. Z. Chen, X. Wang, E. Stamate, R. Bruzzese, and N. Pryds. Controlling the conductivity of amorphous $LaAlO_3/SrTiO_3$ interfaces by in-situ application of an electric field during fabrication. *Applied Physics Letters* 103, 031607 (2013).

A.3 Other published peer-reviewed articles

XXV U. Hira, L. Han, K. Norrman, **D. V. Christensen**, N. Pryds, and F. Sher. High-temperature thermoelectric properties of Na- and W-Doped $Ca_3Co_4O_9$ system. *RSC Advances* 8, 12211 (2018).

XIX N. G. Pham, H. Li, and **D. V. Christensen**. Joining of half-Heusler and bismuth tellurides for segmented thermoelectric generators. *Journal of Electronic Materials* 47, 701 (2017).

X L. Han, **D. V. Christensen**, A. Bhowmik, S. B. Simonsen, L. T. Hung, E. Abdellahi, Y. Z. Chen, N. V. Nong, S. Linderoth, and N. Pryds. Scandium-doped zinc cadmium oxide as a new stable n-type oxide thermoelectric material. *Journal of Materials Chemistry A* 4, 12221 (2016).

III P. H. Ngan, **D. V. Christensen**, G. J. Snyder, L. T. Hung, S. Linderoth, N. V. Nong, and N. Pryds. Towards high efficiency segmented thermoelectric unicouples. *Physica Status Solidi A* 211, 9 (2014).

II R. Bjørk, **D. V. Christensen**, D. Eriksen, and N. Pryds. Analysis of the internal heat losses in a thermoelectric generator. *International Journal of Thermal Sciences* 85, 12 (2014).

A.4 Popular scientific articles

D **D. V. Christensen**. Gennemsigtige Ledende Materialer. *Dansk Magisterforening*, www.dm.dk/FagligUdvikling/FagOgForskning/NatSundOgMiljoe/GennemsigtigeLedendeMaterialer (2016).

C **D. V. Christensen**. Nanokys skaber forbindelser. *Dansk Magisterforening*, www.dm.dk/FagligUdvikling/FagOgForskning/NatSundOgMiljoe/Nanokys (2016).

B **D. V. Christensen**, and F. Trier. When insulators become electronics. *ScienceNordic*. http://sciencenordic.com/when-insulators-become-electronics (2013). English translation of 'Når isolatorer bliver til elektronik'.

A **D. V. Christensen**, and F. Trier. Når isolatorer bliver til elektronik. *Videnskab·dk*. http://videnskab.dk/miljo-naturvidenskab/nar-isolatorer-bliver-til-elektronik (2013).

A.5 Author contributions

An overview of my contributions to the articles published, submitted or under preparation during the course of this PhD project is given in Figure **??**. Here, '√' indicates my contributions, '%' indicates that the given contribution is not relevant for the article and empty boxes indicate that the task was undertaken by a co-author.

	Detailed data discussion	Data analysis	Transport measurements	SQUID/ARPES measurements	Sample preparation	Manuscript writing	Manuscript revision	Numerical modeling
XXX	√	√	%	√	√	√	√	%
XXIX	√	√	%	%	%	√	√	%
XXVIII	√	√	√	%	√	√	√	%
XXVII	√	√		%		√	√	%
XXVI	√	√	√	√	√	√	√	√
XXV	√	√	√	%			√	%
XXIV	√	√	%	%	%	√	√	%
XXIII	√	√	√	√	√	√	√	%
XXII	√	√		%			√	%
XXI	√	√		%			√	%
XX	√	√	√		√		√	
XIX	√			%		√	√	√
XVIII	√	√	√	%			√	
XVII	√	√		%			√	
XVI	√			%			√	%
XV	√	√	%	%	%	√	√	√
XIV	√	√	√	%	√	√	√	%
XIII	√			%			√	%
XII	√			%	√	%	√	%
XI	√	√		%			√	
X	√		√	%			√	%
IX	√	√	√	%	√	√	√	%
VIII	√			%			√	%
VII	√	√	√	%	√		√	
VI	√	√		%			√	%
V	√	√		%			√	%
IV	√			%			√	%
III	√	√	%	%	%	√	√	√
II	√	√	%	%	%		√	√
I	√	√	√	%	√	√	√	√
D	%	%	%	%	%	√	√	%
C	%	%	%	%	%	√	√	%
B	%	%	%	%	%	√	√	%
A	%	%	%	%	%	√	√	%

Figure A.1 – Overview of author contributions

APPENDIX B

Selected articles

The following contains selected articles supporting the writing of the PhD thesis. For a full list of publications, the reader is referred to Appendix A. The supplementary material is not appended for the articles where it is of little relevance for the thesis, and I refer to the homepage of the publisher for obtaining these.

IV

ARTICLE

Y. Z. Chen, F. Trier, T. Kasama, **D. V. Christensen** *et al*
Creation of High Mobility Two-Dimensional Electron Gases via Strain Induced Polarization at an Otherwise Nonpolar Complex Oxide Interface
Nano Letters 15, 1849 (2015)

Springtime at Risø campus
Photo: DTU

NANO LETTERS

Letter

pubs.acs.org/NanoLett

Creation of High Mobility Two-Dimensional Electron Gases via Strain Induced Polarization at an Otherwise Nonpolar Complex Oxide Interface

Yunzhong Chen,*[,†] Felix Trier,[†] Takeshi Kasama,[‡] Dennis V. Christensen,[†] Nicolas Bovet,[§] Zoltan I. Balogh,[‡] Han Li,[†] Karl Tor Sune Thydén,[†] Wei Zhang,[†] Sadegh Yazdi,[‡] Poul Norby,[†] Nini Pryds,[†] and Søren Linderoth[†]

[†]Department of Energy Conversion and Storage, Technical University of Denmark, Risø Campus, 4000 Roskilde, Denmark

[‡]Center for Electron Nanoscopy, Technical University of Denmark, 2800 Lyngby, Denmark

[§]Nano-Science Center, Department of Chemistry, University of Copenhagen, 2100 Copenhagen, Denmark

Supporting Information

ABSTRACT: The discovery of two-dimensional electron gases (2DEGs) in $SrTiO_3$-based heterostructures provides new opportunities for nanoelectronics. Herein, we create a new type of oxide 2DEG by the epitaxial-strain-induced polarization at an otherwise nonpolar perovskite-type interface of $CaZrO_3/SrTiO_3$. Remarkably, this heterointerface is atomically sharp and exhibits a high electron mobility exceeding 60 000 $cm^2\ V^{-1}\ s^{-1}$ at low temperatures. The 2DEG carrier density exhibits a critical dependence on the film thickness, in good agreement with the polarization induced 2DEG scheme.

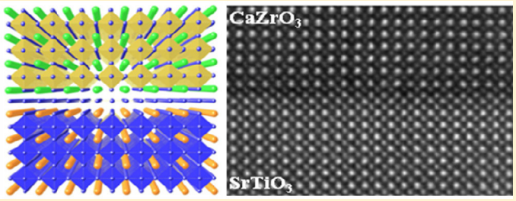

KEYWORDS: *Complex oxide interfaces, oxide electronics, two-dimensional electron gases, strain induced polarization*

Atomically engineered complex oxide heterostructures exhibit a variety of exotic interfacial properties because of strong interactions among the spin, charge, and orbital freedoms as well as lattice vibrations. One particular example is the emergence of high mobility two-dimensional electron gases (2DEGs) at the interface between two oxide insulators,[1,2] one of which is $SrTiO_3$ (STO), the basis material of oxide electronics. These complex oxide 2DEGs consist of strongly coupled electrons and give rise to a rich set of physical phenomena,[3−5] for example, superconductivity,[6,7] magnetism,[8,9] and tunable metal−insulator transitions on nanoscale,[10,11] providing new opportunities for nanoelectronics and mesoscopic physics.[3−5] To date, the creation of complex oxide 2DEGs can mainly be divided into three groups: (1) electronic reconstruction resulting from the polar discontinuity at a polar−nonpolar oxide interface. Such interfacial polar discontinuity requires the presence of a polar oxide, which consists of alternating positively and negatively charged sublayers, epitaxially grown on nonpolar STO, such as $LaAlO_3/SrTiO_3$ (LAO/STO);[1] (2) creation of oxygen vacancies at the bare STO surface or in STO-based heterostructures having interfacial redox reactions,[12−15] such as vacuum cleaved STO[12−14] or the system of amorphous-$LaAlO_3/SrTiO_3$ (*a*-LAO/STO);[15] (3) 2DEGs by delta doping of STO, typically sandwiching a Nb- or La-doped STO thin layer between two nondoped STO layers.[16] Among these, the polarity issue, particularly in the LAO/STO system, has drawn the most attention due to the possibility of an intrinsic doping of STO by electronic reconstruction without the typical disorder caused by chemical doping.[17] However, to compensate the interfacial polar discontinuity, competing mechanisms have often been proposed to occur and obscure the sought-after electronic reconstruction.[18−20] For example, the formation of oxygen vacancies and/or the occurrence of cation intermixing have been shown to play important roles in these STO-based 2DEGs systems.[18,19] To achieve full understanding of complex oxide 2DEGs and to further improve their physical properties such as carrier mobilities, it is necessary to explore perovskite interfaces where competing mechanisms can be isolated distinctly. In this vein, it is nontrivial to investigate the isopolar or nonpolar perovskite heterostructures. Compared to polar oxide interfaces, the isopolar or nonpolar interfaces can not only avoid the intrinsic polar discontinuity issue at the interface[21] but also avoid the possible cation intermixing induced charge compensation mechanisms through formation of donor−acceptor antisite defect pairs.[20]

Besides interfacial polar discontinuity, spontaneous and/or piezoelectric polarizations have been found to result in high-mobility 2DEGs in both traditional semiconductor materials

Received: December 2, 2014
Revised: February 10, 2015
Published: February 18, 2015

DOI: 10.1021/nl504622w
Nano Lett. 2015, 15, 1849−1854

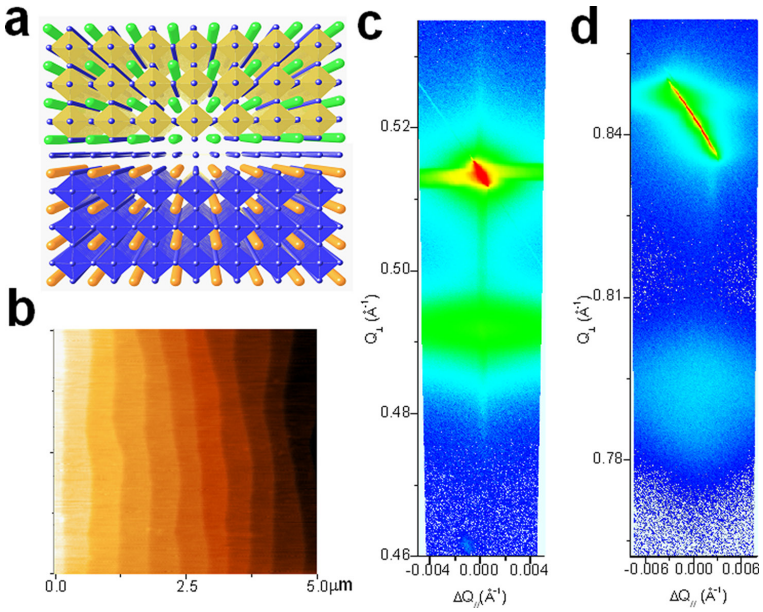

Figure 1. Atomically flat epitaxially grown perovskite-type interface of CZO/STO. (a) Sketch of the CZO/STO heterostructure. (b) AFM image (5 μm × 5 μm) of a 50 uc CZO/STO heterostructure showing an atomically smooth surface. (c,d) XRD-RSM measurements in the vicinity of the (002) and ($\bar{1}$03) perovskite Bragg peaks for the CZO/STO heterostructure.

such as III−V semiconductor AlGaN/GaN compound heterostructures[22] and the binary oxide heterostructures of ZnMgO/ZnO.[23,24] In these systems, 2DEGs carriers normally originate from the ionized surface donor state. The spontaneous and/or piezoelectric polarization in the top film provides the driving force to collect the electrons in the quantum well.[22−24] Though the spontaneous and/or piezoelectric polarizations of ferroelectric oxides have been used to control the physical properties of 2DEGs at the LAO/STO interface,[25,26] their role as the origin for formation of complex oxide 2DEGs has not been reported previously, to the best of our knowledge. Herein, we report for the first time a high mobility 2DEG at an otherwise nonpolar perovskite-type interface of (001) $CaZrO_3$/STO (CZO/STO) via strain induced polarization, as demonstrated in Figure 1a. In contrast to the polar nature of LAO films,[1] the formal valence states of CZO can be assigned as Ca^{2+}, Zr^{4+}, and O^{2-}, in the simple ionic limit. Therefore, the (001) CZO consists of alternating charge neutral stacks of $(Ca^{2+}O^{2-})^0$ and $(Zr^{4+}O^{2-}{}_2)^0$, similar to the case of nonpolar (001) STO. Nevertheless, we find that compressive strain can induce an electric polarization in the CZO epitaxial thin films, consistent with previous reports.[27,28] Remarkably, such strain induced polarization could well account for the 2DEGs at our CZO/STO heterointerface, as demonstrated by a critical dependence of the interfacial conduction on the CZO film thickness. Moreover, the nominally nonpolar CZO/STO interface gives rise to an extremely high electron mobility exceeding 60 000 $cm^2\ V^{-1}\ s^{-1}$ at 2 K, which is among one of the highest mobilities achieved for perovskite-type interfaces.[2,29,30] These findings provide new opportunities for oxide electronics.

The CZO (pseudocubic a = 4.012 Å)[31] exhibits a good lattice match with STO (a = 3.905 Å). Their lattice mismatch is +2.67%, comparable to the mismatch of −2.79% in the LAO/STO system, where the positive and negative values indicate a compressive and tensile strain in the epitaxial film, respectively. Under optimized conditions, the CZO films deposited by pulsed laser deposition (PLD) can be epitaxially grown on the (001) TiO_2-terminated STO substrates within a layer-by-layer two-dimensional growth mode, as confirmed by the presence of periodic intensity oscillations of the reflection high-energy electron diffraction (RHEED) pattern monitored in situ during film growth (Supporting Information, Figure S1). Both RHEED intensity oscillations and sharp RHEED patterns can persist up to a film thickness over 50 unit cells (uc), suggesting high quality film growth. A terrace surface of the grown heterostructure is detected by atomic force microscopy (AFM), which shows a regular step height of 0.4 nm (Figure 1b). High-resolution X-ray diffraction (XRD) further confirms the epitaxial growth of the (001) CZO film on the (001)-oriented STO, without the presence of any impurity phases. The XRD reciprocal space map (RSM) measurements in the vicinity of the (002) and ($\bar{1}$03) perovskite Bragg peaks, as demonstrated in Figure 1c,d, respectively, give direct evidence that the films are under compressive biaxial strain, as expected.

We further investigated the atomic structure and interface chemistry of our CZO/STO heterostructures by an aberration corrected scanning transmission electron microscopy (STEM) in combination with electron energy-loss spectroscopy (EELS). Figure 2a shows a high-angle annular dark field (HAADF) STEM image of a CZO/STO sample with the CZO layer of approximately 50 uc (~20 nm). The CZO film is found to be coherent with the STO substrate with no obvious defects or dislocations at the interface. The averaged line profiles (Figure 2b) across the interface indicate that most of the cation interdiffusion is confined to within 1−2 unit cells on either side

DOI: 10.1021/nl504622w
Nano Lett. 2015, 15, 1849−1854

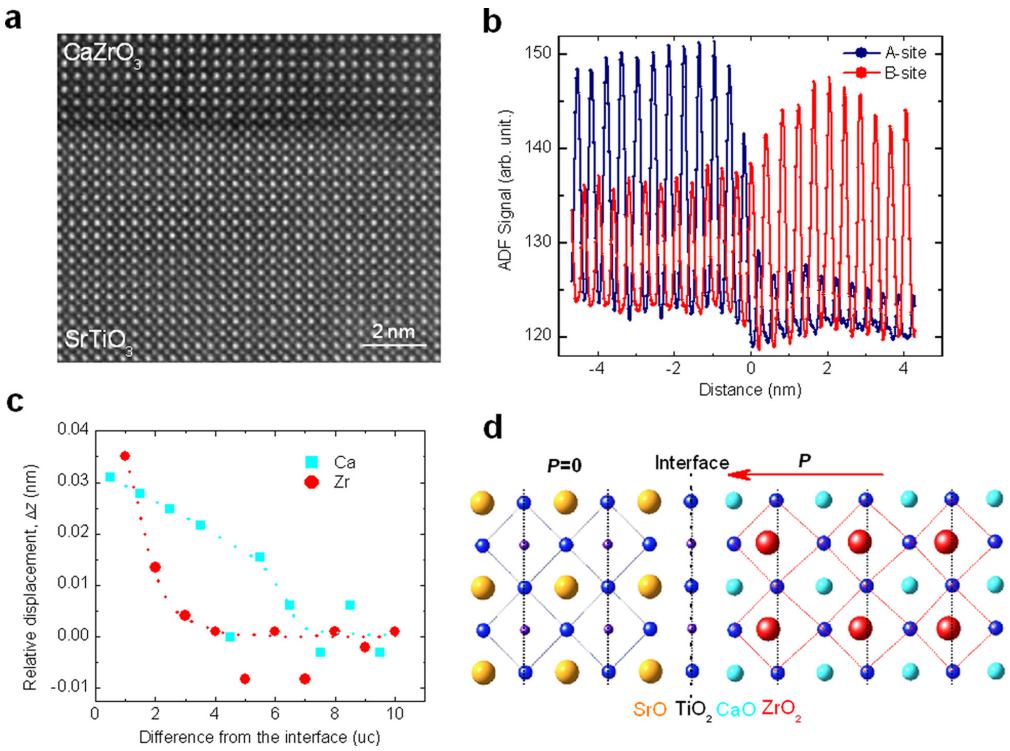

Figure 2. Sharp interface of the compressively strained CZO/STO heterostructure. (a) HAADF-STEM image across the CZO/STO heterointerface. (b) Averaged line profiles across the interface (A = Sr, Ca; B = Ti, Zr). (c) Relative lattice distortion of cations in the CZO film in the vicinity of interface. (d) Sketch for the strain induced polarization due to the lattice distortion near the interface. The dotted lines are a guide to the eye.

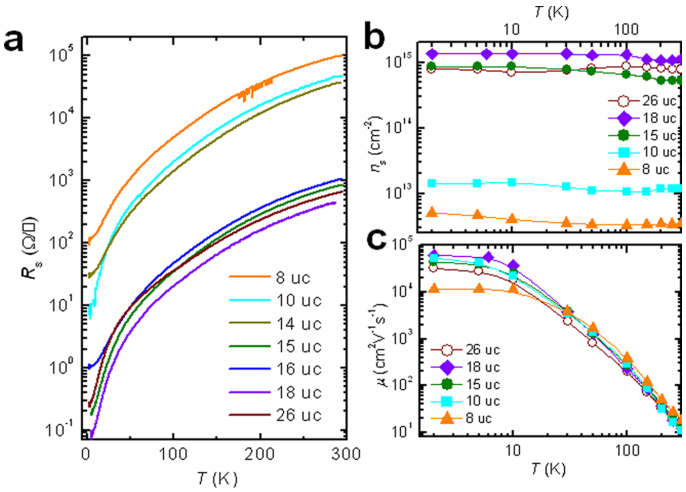

Figure 3. Highly mobile conduction at CZO/STO heterointerfaces. (a–c) Temperature dependence of sheet resistance, R_s, carrier density, n_s, and mobility, μ, respectively. Most of the samples exhibit a large μ exceeding 20 000 cm^2 V^{-1} s^{-1} at 2 K, despite the dramatic difference in n_s.

of the interface, much sharper than the spinel/perovskite interface of GAO/STO grown under similar conditions.[2] The CZO/STO interface is therefore among one of the sharpest hitherto-investigated perovskite-type oxide interfaces.[18,32,33]

DOI: 10.1021/nl504622w
Nano Lett. 2015, 15, 1849−1854

Further STEM investigations indicate that the epitaxial CZO film is strained compressively on STO with $a \approx b \approx 3.905$ Å and $c \approx 4.124$ Å, consistent with the XRD data shown in Figure 1. In a similar zirconate system of $SrZrO_3/SrTiO_3$, the compressive strain has been reported to result in ferroelectricity in its superlattices.[27] Theoretical calculations by first-principle density functional theory indicate that such strain induced polarization originates from a lattice distortion, which is characterized by a prediction that all the cations move toward the interface with the Zr^{4+} exhibiting the largest relative displacement.[28] Therefore, we also investigated the lattice distortion of our CZO films in the vicinity of the interface. Remarkably, compared to the $CaZrO_3$ film that is more than 10 uc away from the interface, we observed unambiguously that both the Ca^{2+} and Zr^{4+} cations move toward the interface in the first 7 uc CZO layers. As shown in Figure 2c, the Zr^{4+} cation in the first ZrO_2 sublayer exhibits the largest relative movement of 0.035 nm to the interface, while such trend degrades quickly in the very beginning 3 unit cells of CZO films. In contrast, the displacement of the Ca^{2+} cations persists up to the first 7 uc layers. The above lattice displacement implies a polarization pointing toward the interface, given that there is a negligible lattice distortion for the oxygen sublattice as illustrated in Figure 2d.

The stoichiometric CZO and STO are both band gap insulators, with the energy band gap of 4.1 and 3.2 eV, respectively. Nevertheless, we measured highly mobile metallic conduction at the epitaxial CZO/STO heterointerface. Figure 3a shows the typical temperature-dependent sheet resistance, R_s, for our CZO/STO heterostructures at different film thickness, t. All of our CZO/STO heterostructures show good metallic behavior as long as the CZO film thickness t is higher than 6 uc. Note that the samples are highly insulating at $t \leq 6$ uc. This rules out the possibility of thermal reduction of STO as a contribution to the interface conduction.[34] This critical thickness $t_c = 6$ uc (~2.4 nm) for the occurrence of interface conduction is slightly higher than that of the LAO/STO interface ($t_c \approx 1.6$ nm).[35] However, in distinct contrast to the LAO/STO system, where the carrier density normally exhibits a carrier freezing out behavior at $T = 100$ K, the CZO/STO system exhibits an almost constant carrier density as a function of temperature (Figure 3b), similar to the high mobility spinel/perovskite GAO/STO interface.[2,36] Moreover, the CZO/STO system distinguishes from the other complex oxide 2DEGs by two characteristic properties: First, we observe two jumps in the carrier density (Figures 3b and 4a) upon increasing film thickness. Besides the occurrence of interface conduction at around $t_c = 6$ uc for the insulator–metal transition, we observed another unexpected conduction jump in the carrier density by more than 40 times at t =15 uc, from approximately $n_s = 0.4–2.0 \times 10^{13}$ cm^{-2} at $t \leq 14$ uc to $n_s = 0.4–1.1 \times 10^{15}$ cm^{-2} at $t \geq 15$ uc. Second, despite the strong dependence of n_s on t, most of the CZO samples show very high electron mobilities much larger than 20 000 cm^2 V^{-1} s^{-1} at 2 K (the bulk mobility of STO),[37] regardless of the CZO film thickness (Figure 3c). For example, we obtained a $\mu = 5.3 \times 10^4$ cm^2 V^{-1} s^{-1} and $\mu = 6.1 \times 10^4$ cm^2 V^{-1} s^{-1} at 2 K for samples with $t = 10$ uc and $t = 18$ uc, respectively, which represents the record mobility for perovskite-type interfaces and are also among the highest mobilities for complex oxide interfaces (Supporting Information, Table S1).[2,29,30]

The metallic conduction at the nominally nonpolar CZO/STO heterointerface is remarkable since two of the most

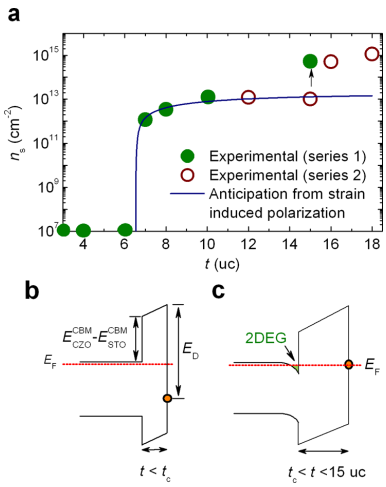

Figure 4. Sketch of the formation of oxide 2DEG by strain-induced polarization. (a) Thickness-dependent sheet carrier density. (b,c) Band alignment before and after the formation of 2DEG, respectively, at the CZO/STO heterointerface.

discussed conduction mechanisms for the polar LAO/STO interface, intrinsic polar discontinuity and La-doping induced n-type conduction, are both ruled out here. However, besides the presence of strain-induced polarization in the CZO epitaxial thin films, the CZO/STO heterointerface meets also the thermodynamic criterion for interfacial redox reaction: the B site metal (Zr for CZO system) locates in the region of the formation heat of metal oxide, $\Delta H_f^O < -350$ kJ/mol of O, and the work function of the metals, 3.75 eV < φ < 4.4 eV.[38] The redox reaction at the interface of STO-based heterostructures can result in oxygen vacancy-dominated metallic conduction.[15] To explore the role of oxygen vacancies in the CZO/STO heterostructures, we performed angle-resolved X-ray photoelectron spectroscopy (XPS) measurements. Generally, the presence of oxygen vacancies in these STO-based oxide 2DEG heterostructures is indicated by the fact that the content of 3d electrons, Ti^{3+} on the STO side, deduced by XPS measurements is much larger than the carrier density obtained from transport measurements.[2,15] Remarkably, in dramatic difference with both crystalline LAO/STO[39] and GAO/STO systems,[2] negligible Ti^{3+} signal in the $2p_{3/2}$ core-level spectra is detected in our CZO/STO heterostructures at $t \leq 14$ uc (Supporting Information, Figure S2). This strongly suggests that the content of oxygen vacancies in our CZO/STO samples is negligible for $t \leq 14$ uc (approximately the detection limit of XPS). Such conclusion is further supported by the fact that all our samples can survive the postannealing in 1 bar pure O_2 at 100 °C for over 5 h (Supporting Information, Figure S3), with no obvious change in the interface conduction. Therefore, the 2DEG at the CZO/STO ($t \leq 14$ uc) interface results predominantly from the strain induced polarization, P_{CZO}, in the CZO films. Note that although the content of the oxygen vacancies in the CZO/STO ($t \leq 14$ uc) is strongly suppressed, the 2DEG carriers originating from the polarization-induced electronic reconstruction still locate preferably on the STO side in the region proximate to the interface. This is confirmed by our observation that the e_g/t_{2g} ratio of the $L_{2,3}$ edge in the EELS spectra of STO

DOI: 10.1021/nl504622w
Nano Lett. 2015, 15, 1849–1854

is decreased close to the interface with respect to the ones further in the bulk STO (Supporting Information, Figure S4). The polarization in the epitaxial CZO films could result from the relative displacements of the cations and anions under compressive strain, as shown in Figure 2d. If we assume a constant polarization, P_{CZO}, in the CZO film, this polarization will lead to the presence of a macroscopic electric field $E_{CZO} = P_{CZO}/\varepsilon_0\varepsilon_{CZO}$ across CZO films (ε_{CZO} is the relative permittivity of CZO), which will bend the electronic bands. As illustrated in Figure 4b, for ultrathin CZO films with a thickness below t_c, the ionized donor surface states, which are sufficiently deep and below the conduction band of CZO with an energy E_D, lie far below the conduction band of STO. In this case, no 2DEG is formed. Increasing the CZO film thickness normally lifts the surface donor states. At the critical thickness, the surface donor energy reaches the bottom of the conduction band for STO, as demonstrated in Figure 4c. Electrons, coming from the occupied surface donor states, are then transferred to the empty conduction band of STO at the interface, creating the 2DEG. Until all the surface states are empty, in the ideal case, the Fermi level remains at the donor energy, while more and more electrons are transferred with increasing the film thickness. This simple electrostatic model not only explains the formation of 2DEG in CZO/STO but also yields the following expression of the critical barrier thickness, t_c:

$$t_c = [E_D - (E_{CBM}^{CZO} - E_{CBM}^{STO})]\varepsilon_0\varepsilon_{CZO}/eP_{CZO} \quad (1)$$

where, E_{CBM}^{CZO} and E_{CBM}^{STO} are the conduction band minima (CBM) of CZO and STO, respectively. For $t > t_c$, the 2DEG density as a function of the CZO film thickness can be given by[22]

$$en_s = P_{CZO}/(1 - t_c/t) \quad (2)$$

Figure 4a summarized the CZO/STO sheet carrier density n_s as a function of t. Note that the abrupt enhancement in n_s at $t >$ 15 uc is probably due to the formation of large content of oxygen vacancies on the STO side due to interfacial redox reactions. This concern is supported by the facts that there is measurable conduction at the back side of the STO substrates when $t >$ 15 uc and that we observed an additional decay in sheet conduction resulting from oxygen absorption at the initial process for the postannealing in pure O_2 at 150 °C of a t = 22 uc sample (Supporting Information, Figure S3b). For this reason, we fitted eq 2 only to $t <$ 15 uc. A least-squares fit was achieved for $P_{CZO} = 2.3 \times 10^{13}$ e/cm^2 and t_c = 6.5 uc. The deduced value of $P_{CZO} = 2.3 \times 10^{13}$ e/cm^2 = 3.5 μC cm^{-2} is in good agreement with the experimentally determined values for a comparable compressively strained 40 uc $SrZrO_3/SrTiO_3$ bilayer-heterostructure.[27] In short, the strain induced polarization model can fit well the critical thickness dependence of the sheet carrier density for CZO/STO heteostructures and can explain largely the metallic conduction at the nominally nonpolar perovskite interface between the two band insulators, when the content of oxygen vacancies is negligible. It is noteworthy that the deduced polarization of P_{CZO} = 3.5 μC cm^{-2} in CZO/STO ($t \leq$ 14 uc) is much lower than that expected at the polar LAO/STO interface, $P_{LAO} = e/2a_{LAO}^2$ = 55.8 μC cm^{-2}. It, therefore, might be tantalizing to determine why the two different perovskite-type interfaces exhibit similar sheet carrier densities.

In conclusion, we have discovered a 2DEG at the sharp perovskite-type interface of CZO/STO with very high electron mobility exceeding 60 000 cm^2 V^{-1} s^{-1} at 2 K. The sheet carrier density of the 2DEG exhibits a critical thickness dependence, suggesting the polarization induced electronic reconstruction dominates the interface conduction. The strain-induced polarization can provide new avenues to explore high mobility 2DEGs at complex oxide interfaces.

Methods. *Sample Growth and Characterizations.* The $CaZrO_3$ (CZO) films were grown on (001) TiO_2-terminated $SrTiO_3$ (STO) substrates (5 × 5 × 0.5 mm^3 with miscut less than 0.2°) by pulsed laser deposition (PLD) in an oxygen atmosphere of ~10^{-4} mbar with the film growth process monitored by *in situ* RHEED. During ablation, a KrF laser (λ = 248 nm) with a repetition rate of 1 Hz and laser fluence of 1.5 J cm^{-2} was used. The target−substrate distance was fixed at 5.6 cm. The growth temperature was fixed at 600 °C. A CZO ceramic pellet produced by Spark plasma sintering (SPS) was used as the target. Layer-by-layer two-dimensional growth of CZO films was optimized by RHEED oscillations with a growth rate of approximately 75 pulses per unit cell (0.05 Å/s) (Supporting Information, Figure S1a). After deposition, the sample was cooled under the deposition pressure with a rate of 15 °C/min to room temperature (below 30 °C). All samples are extremely stable at room temperature and can survive the annealing in 1 bar of pure O_2 at 100 °C for over 5 h.

Electrical characterization was made mainly using a 4-probe Van der Pauw method with ultrasonically wire-bonded aluminum wires as electrodes. For all samples, the Hall resistance is linear with respect to magnetic field (0−2 T). The high resolution XRD measurements were performed on a Rigaku Smartlab system.

STEM and EELS Analysis. Aberration-corrected STEM measurements were performed by an FEI Titan 80-300ST TEM equipped with a high brightness Shottky emitter (XFEG) and a Gatan Image Filter (Tridiem). High-angle annular dark field (HAADF) images were acquired at 300 kV, where the probe size, convergence angle and HAADF inner collection angle were 0.8−1.0 Å, 17.3 mrad, and 71.9 mrad, respectively. For EELS in the STEM, an accelerating voltage of 120 kV (probe size of 1.5−2.0 Å) and the spectrum imaging technique were used to avoid changes in the specimen induced by the electron beam during acquisition. Spectrum images consisting of 40 ten-analysis-point lines parallel to the interface were acquired, and an increment of 0.28 nm to the next line was used. Each spectrum with an energy resolution of 0.9 eV was obtained at a dispersion of 0.1 eV/pixel for 0.2−0.4 s. Then the spectra along the lines were summed to increase signal-to-noise ratio.

X-ray Photoelectron Spectroscopy (XPS) Measurement. The XPS measurements were performed in a Kratos Axis UltraDLD instrument, using a monochromatic Al Ka X-ray source with photon energy of 1486.6 eV. This leads to a kinetic energy of Ti 2p electrons of roughly 1025 eV. According to the NIST database (NIST Standard Reference Database 71, version 1.2), the electron escape depth is approximately 22 Å in STO at this kinetic energy. The pass energy used for the high resolution scan was 20 eV. The detection angle of the electrons varied between 0° and 60° with respect to the sample normal.

■ ASSOCIATED CONTENT

Supporting Information

Supplemental table and figures. This material is available free of charge via the Internet at http://pubs.acs.org.

DOI: 10.1021/nl504622w
Nano Lett. 2015, 15, 1849−1854

AUTHOR INFORMATION

Corresponding Author

*E-mail: yunc@dtu.dk. Phone: +45 4677 5614.

Notes

The authors declare no competing financial interest.

ACKNOWLEDGMENTS

The authors gratefully acknowledge the discussions with G. A. Sawatzky, T. S. Jespersen, L. P. Yu, N. Balke, and the technical assistance from J. Geyti, M. Søgaard, and K. V. Hansen. Funding from the Danish Agency for Science, Technology and Innovation is acknowledged.

REFERENCES

(1) Ohtomo, A.; Hwang, H. Y. *Nature* **2004**, *427*, 423.
(2) Chen, Y. Z.; Bovet, N.; Trier, F.; Christensen, D. V.; Qu, F. M.; Andersen, N. H.; Kasama, T.; Zhang, W.; Giraud, R.; Dufouleur, J.; Jespersen, T. S.; Sun, J. R.; Smith, A.; Nygård, J.; Lu, L.; Büchner, B.; Shen, B. G.; Linderoth, S.; Pryds, N. *Nat. Commun.* **2013**, *4*, 1371.
(3) Mannhart, J.; Schlom, D. G. *Science* **2010**, *327*, 1607.
(4) Miletto Granozio, F.; Koster, G.; Rijnders, G. *MRS Bull.* **2013**, *38*, 1017.
(5) Sulpizio, J. A.; Ilani, S.; Irvin, P.; Levy, J. *Annu. Rev. Mater. Sci.* **2014**, *44*, 117.
(6) Reyren, N.; Thiel, S.; Caviglia, A. D.; Fitting Kourkoutis, L.; Hammerl, G.; Richter, C.; Schneider, C. W.; Kopp, T.; Ruetschi, A.-S.; Jaccard, D.; Gabay, M.; Muller, D. A.; Triscone, J.-M.; Mannhart, J. *Science* **2007**, *317*, 1196.
(7) Richter, C.; Boschker, H.; Dietsche, W.; Fillis-Tsirakis, E.; Jany, R.; Loder, F.; Kourkoutis, L. F.; Muller, D. A.; Kirtley, J. R.; Schneider, C. W.; Mannhart, J. *Nature* **2013**, *502*, 528.
(8) Brinkman, A.; Huijben, M.; Van Zalk, M.; Huijben, J.; Zeitler, U.; Maan, J. C.; Van der Wiel, W. G.; Rijnders, G.; Blank, D. H. A.; Hilgenkamp, H. *Nat. Mater.* **2007**, *6*, 493.
(9) Lee, J.-S.; Xie, Y. W.; Sato, H. K.; Bell, C.; Hikita, Y.; Hwang, H. Y.; Kao, C.-C. *Nat. Mater.* **2013**, *12*, 703.
(10) Irvin, P.; Neazey, J. P.; Cheng, G. L.; Lu, S. C.; Bark, C. W.; Ryu, S.; Eom, C. B.; Levy, J. *Nano Lett.* **2013**, *13*, 364.
(11) Chen, Y. Z.; Zhao, J. L.; Sun, J. R.; Pryds, N.; Shen, B. G. *Appl. Phys. Lett.* **2010**, *97*, 123102.
(12) Santander-Syro, A. F.; Copie, O.; Kondo, T.; Fortuna, F.; Pailhes, S.; Weht, R.; Qiu, X. G.; Bertran, F.; Nicolaou, A.; Taleb-Ibrahimi, A.; Le Fevre, P.; Herranz, G.; Bibes, M.; Reyren, N.; Apertet, Y.; Lecoeur, P.; Barthelemy, A.; Rozenberg, M. J. *Nature* **2011**, *469*, 189.
(13) Meevasana, W.; King, P. D. C.; He, R. H.; Mo, S.-K.; Hashimoto, M.; Tamai, A.; Songsiriritthigul, P.; Baumberger, F.; Shen, Z.-X. *Nat. Mater.* **2011**, *10*, 114.
(14) Plumb, N. C.; Salluzzo, M.; Razzoli, E.; Månsson, M.; Falub, M.; Krempasky, J.; Matt, C. E.; Chang, J.; Schulte, M.; Braun, J.; Ebert, H.; Minár, J.; Delley, B.; Zhou, K.-J.; Schmitt, T.; Shi, M.; Mesot, J.; Patthey, L.; Radović, M. *Phys. Rev. Lett.* **2014**, *113*, 086801.
(15) Chen, Y. Z.; Pryds, N.; Kleibeuker, J. E.; Sun, J. R.; Stamate, E.; Koster, G.; Shen, B. G.; Rijnders, G.; Linderoth, S. *Nano Lett.* **2011**, *11*, 3774.
(16) Kozuka, Y.; Kim, M.; Ohta, H.; Hikita, Y.; Bell, C.; Hwang, H. Y. *Appl. Phys. Lett.* **2010**, *97*, 222115.
(17) Hesper, R.; Tjeng, L. H.; Heeres, A.; Sawatzky, G. A. *Phys. Rev. B* **2000**, *62*, 16046.
(18) Chambers, S. A.; Engelhard, M. H.; Shutthanandan, V.; Zhu, Z.; Droubay, T. C.; Qiao, L.; Sushko, P. V.; Feng, T.; Lee, H. D.; Garfunkel, E.; Shah, A. B.; Zuo, J.-M.; Ramasse, Q. M. *Surf. Sci. Rep.* **2010**, *65*, 317.
(19) Kalabukhov, A.; Gunnarsson, R.; Börjesson, J.; Olsson, E.; Claeson, T.; Winkler, D. *Phys. Rev. B* **2007**, *75*, 121404.
(20) Yu, L. P.; Zunger, A. *Nat. Commun.* **2014**, *5*, 5118.
(21) Kleibeuker, J. E.; Zhong, Z.; Nishikawa, H.; Gabel, J.; Müller, A.; Pfaff, F.; Sing, M.; Held, K.; Claessen, R.; Koster, G.; Rijnders, G. *Phys. Rev. Lett.* **2014**, *113*, 237402.
(22) Ibbetson, J. P.; Fini, P. T.; Ness, K. D.; DenBaars, S. P.; Speck, J. S.; Mishra, U. K. *Appl. Phys. Lett.* **2000**, *77*, 250.
(23) Tampo, H.; Shibata, H.; Maejima, K.; Yamada, A.; Matsubara, K.; Fons, P.; Kashiwaya, S.; Niki, S.; Chiba, Y.; Wakamatsu, T.; Kanie, H. *Appl. Phys. Lett.* **2008**, *93*, 202104.
(24) Tsukazaki, A.; Ohtomo, A.; Kita, T.; Ohno, Y.; Ohno, H.; Kawasaki, M. *Science* **2007**, *315*, 1388.
(25) Bark, C. W.; Felker, D. A.; Wang, Y.; Zhang, Y.; Jang, H. W.; Folkman, C. M.; Park, J. W.; Baek, S. H.; Zhou, H.; Fong, D. D.; Pan, X. Q.; Tsymbal, E. Y.; Rzchowski, M. S.; Eom, C. B. *Proc. Natl. Acad. Sci. U.S.A.* **2011**, *108*, 4720.
(26) Kim, S.-I.; Kim, D.-H.; Kim, Y.; Moon, S. Y.; Kang, M.-G.; Choi, J. K.; Jang, H. W.; Kim, S. K.; Choi, J.-W.; Yoon, S.-J.; Chang, H. J.; Kang, C.-Y.; Lee, S.; Hong, S.-H.; Kim, J.-S.; Baek, S.-H. *Adv. Mater.* **2013**, *25*, 4612.
(27) Tsurumi, T.; Harigai, T.; Tanaka, D.; Nam, S.-M.; Kakemoto, H.; Wada, S.; Saito, K. *Appl. Phys. Lett.* **2004**, *85*, 5016.
(28) Yang, K.; Wang, C. L.; Li, J. C.; Zhao, M. L.; Wang, X. Y. *Solid State Commun.* **2006**, *139*, 144.
(29) Huijben, M.; Koster, G.; Kruize, M. K.; Wenderich, S.; Verbeeck, J.; Bals, S.; Slooten, E.; Shi, B.; Molegraaf, H. J. A.; Kleibeuker, J. E.; van Aert, S.; Goedkoop, J. B.; Brinkman, A.; Blank, D. H. A.; Golden, M. S.; van Tendeloo, G.; Hilgenkamp, H.; Rijnders, G. *Adv. Funct. Mater.* **2013**, *23*, 5240.
(30) Xie, Y. W.; Bell, C.; Hikita, Y.; Harashima, S.; Hwang, H. Y. *Adv. Mater.* **2013**, *25*, 4735.
(31) Mathews, M. D.; Mirza, E. B.; Momin, A. C. *J. Mater. Sci. Lett.* **1991**, *10*, 305.
(32) Cantoni, C.; Gazquez, J.; Miletto Granozio, F.; Oxley, M. P.; Varela, M.; Lupini, A. R.; Pennycook, S. J.; Aruta, C.; di Uccio, U. S.; Perna, P.; Maccariello, D. *Adv. Mater.* **2012**, *24*, 3952.
(33) Nakagawa, N.; Hwang, H. Y.; Muller, D. A. *Nat. Mater.* **2006**, *5*, 204.
(34) Herranz, G.; Basletic, M.; Bibes, M.; Carretero, C.; Tafra, E.; Jacquet, E.; Bouzehouane, K.; Deranlot, C.; Hamzic, A.; Broto, J.-M.; Barthelemy, A.; Fert, A. *Phys. Rev. Lett.* **2007**, *98*, 216803.
(35) Thiel, S.; Hammerl, G.; Schmehl, A.; Schneider, C. W.; Mannhart, J. *Science* **2006**, *313*, 1942.
(36) Chen, Y. Z.; Bovet, N.; Kasama, T.; Gao, W. W.; Yazdi, S.; Ma, C.; Pryds, N.; Linderoth, S. *Adv. Mater.* **2014**, *26*, 1462.
(37) Tufte, O. N.; Chapman, P. W. *Phys. Rev.* **1967**, *155*, 796.
(38) Chen, Y. Z.; Pryds, N.; Sun, J. R.; Shen, B. G.; Linderoth, S. *Chin. Phys. B* **2013**, *22*, 116803.
(39) Sing, M.; Berner, G.; Goβ, K.; Müller, A.; Ruff, A.; Wetscherek, A.; Thiel, S.; Mannhart, J.; Pauli, S. A.; Schneider, C. W.; Willmott, P. R.; Gorgoi, M.; Schäfers, F.; Claessen, R. *Phys. Rev. Lett.* **2009**, *102*, 176805.

DOI: 10.1021/nl504622w
Nano Lett. 2015, 15, 1849−1854

V

ARTICLE

Y. Z. Chen, F. Trier, T. Wijnands, R. J. Green, N. Gauquelin, R. Egoavil, **D. V. Christensen** *et al.*
Extreme mobility enhancement of two-dimensional electron gases at oxide interfaces via charge-transfer-induced modulation doping
Nature Materials 14, 801 (2015)

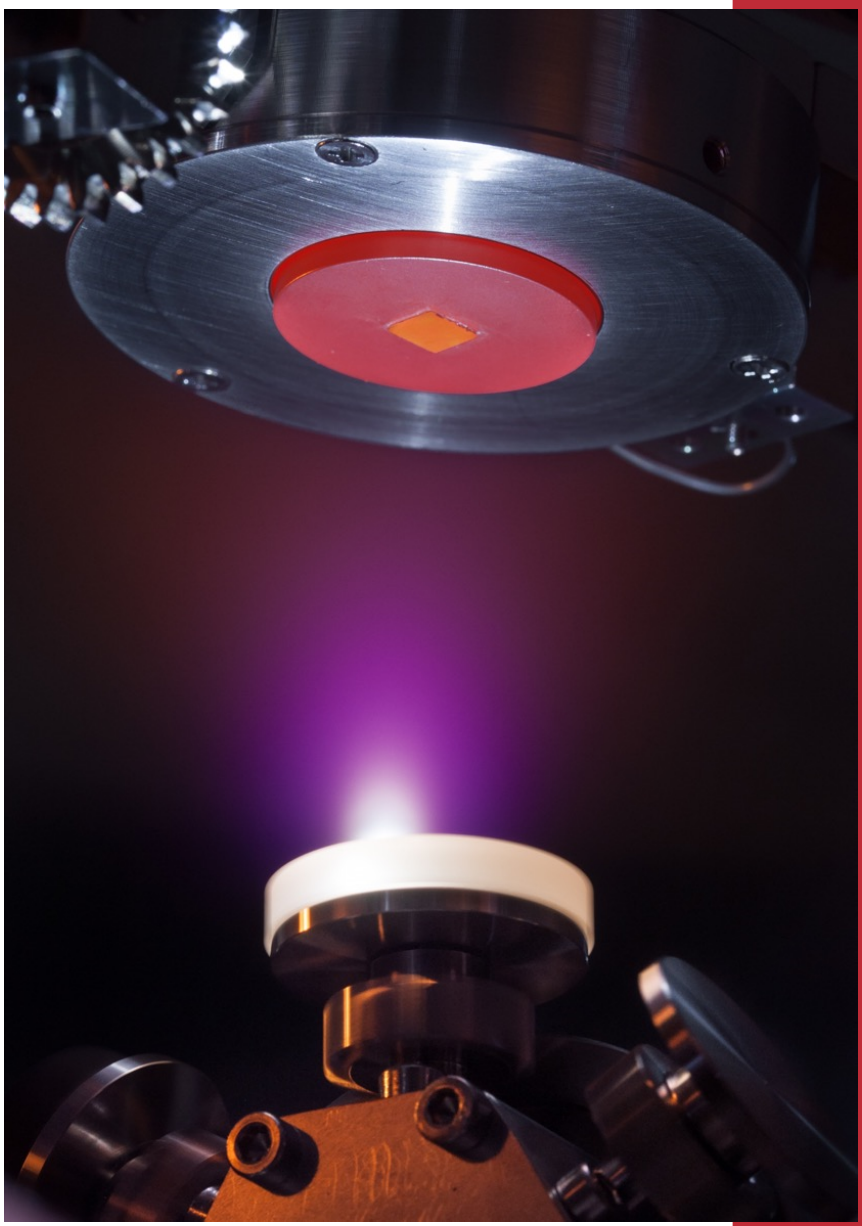

Pulsed laser deposition in action
Photo: Adam Andersen Læssøe and Dennis Valbjørn Christensen

nature materials

ARTICLES

PUBLISHED ONLINE: 1 JUNE 2015 | DOI: 10.1038/NMAT4303

Extreme mobility enhancement of two-dimensional electron gases at oxide interfaces by charge-transfer-induced modulation doping

Y. Z. Chen[1]*, F. Trier[1], T. Wijnands[2], R. J. Green[3,4], N. Gauquelin[5], R. Egoavil[5], D. V. Christensen[1], G. Koster[2], M. Huijben[2], N. Bovet[6], S. Macke[3,7], F. He[8], R. Sutarto[8], N. H. Andersen[9], J. A. Sulpizio[10], M. Honig[10], G. E. D. K. Prawiroatmodjo[11], T. S. Jespersen[11], S. Linderoth[1], S. Ilani[10], J. Verbeeck[5], G. Van Tendeloo[5], G. Rijnders[2], G. A. Sawatzky[3] and N. Pryds[1]

Two-dimensional electron gases (2DEGs) formed at the interface of insulating complex oxides promise the development of all-oxide electronic devices. These 2DEGs involve many-body interactions that give rise to a variety of physical phenomena such as superconductivity, magnetism, tunable metal–insulator transitions and phase separation. Increasing the mobility of the 2DEG, however, remains a major challenge. Here, we show that the electron mobility is enhanced by more than two orders of magnitude by inserting a single-unit-cell insulating layer of polar $La_{1-x}Sr_xMnO_3$ ($x = 0$, 1/8, and 1/3) at the interface between disordered $LaAlO_3$ and crystalline $SrTiO_3$ produced at room temperature. Resonant X-ray spectroscopy and transmission electron microscopy show that the manganite layer undergoes unambiguous electronic reconstruction, leading to modulation doping of such atomically engineered complex oxide heterointerfaces. At low temperatures, the modulation-doped 2DEG exhibits Shubnikov–de Haas oscillations and fingerprints of the quantum Hall effect, demonstrating unprecedented high mobility and low electron density.

One of the most important developments in semiconductors, both from the viewpoint of fundamental physics and for the purpose of developing new devices, has been the realization of 2DEGs in heterointerfaces based on Si or on III–V compounds. The quality of the material hosting the 2DEG is quantified predominantly by its carrier mobility, which is limited owing to the scattering of electrons by ionized impurities, particularly at low temperatures[1,2]. The usage of the so-called modulation-doping technique, artificially separating the electrons from the ionized impurities by inserting a spacer at the interface, has significantly increased the carrier mobility of 2DEGs in semiconductor heterostructures[1–3]. This led not only to the realization of high-electron-mobility field-effect transistors but also to the discovery of the fractional quantum Hall effect in 2DEG samples of unprecedented structural perfection[4].

The enhancement of 2DEG carrier mobilities at complex oxide interfaces, by contrast, remains rather challenging[5–19]. So far, one of the most investigated complex oxide 2DEGs is based on interfacing epitaxial LAO and STO (*c*-LAO/STO), where both electronic reconstruction[5,20,21] and ion transfer across the interface[22,23] can make important contributions to the conduction. In a different but related system, the interface between disordered LAO and STO (*d*-LAO/STO) created at room temperature holds a 2DEG resulting from interfacial redox reactions[24–26]. Both types of STO 2DEGS exhibit a distinct electronic feature: the interfacial charge carriers (t_{2g} electrons) come in two species, d_{xy} and d_{xz}/d_{yz} (z is perpendicular to the 2D layers)[27–30]. The d_{xy} component accounts for most of the 2DEG charge. They reside at or in the immediate proximity of the interface, but they exhibit a rather low mobility. In contrast, d_{xz} or d_{yz} electrons naturally extend further away from the interface and amount to only a small fraction of the 2DEG population. Yet, their mobilities reach much higher values than that of the d_{xy} states[27–30].

So far, there are experimental indications that decreasing the charge carrier density could enhance the electron mobility[16–19]. However, experiments to control the charge carriers have mainly focused either on controlling processes at the surface of the heterostructures or simply reducing the contributions of defect dopants such as oxygen vacancies[16–19]. Considering the electronic structure as well as the inherent lack of long-range translational symmetry in the *d*-LAO/STO system, which could give rise to random potentials across the interface leading to low mobilities[24], in this study, we performed investigations to tackle both the issues of suppressing the charge carrier density as well as improving the interface order by introducing an additional layer at the interface of *d*-LAO/STO. The buffer layer is designed to serve three purposes: to reduce the 2DEG carrier density by selecting a material which

[1]Department of Energy Conversion and Storage, Technical University of Denmark, Risø Campus, 4000 Roskilde, Denmark. [2]Faculty of Science and Technology and MESA+ Institute for Nanotechnology, University of Twente, 7500 AE Enschede, The Netherlands. [3]Quantum Matter Institute, Department of Physics and Astronomy, University of British Columbia, Vancouver, British Columbia V6T 1Z1, Canada. [4]Max Planck Institute for Chemical Physics of Solids, Nöthnitzerstraße 40, 01187 Dresden, Germany. [5]EMAT, University of Antwerp, Groenenborgerlaan 171, 2020 Antwerp, Belgium. [6]Nano-Science Center, Department of Chemistry, University of Copenhagen, 2100 Copenhagen, Denmark. [7]Max Planck Institute for Solid State Research, Heisenbergstraße 1, 70569 Stuttgart, Germany. [8]Canadian Light Source, Saskatoon, Saskatchewan S7N 2V3, Canada. [9]Department of Physics, Technical University of Denmark, 2800 Lyngby, Denmark. [10]Department of Condensed Matter Physics, Weizmann Institute of Science, 76100 Rehovot, Israel. [11]Center for Quantum devices, Niels Bohr Institute, University of Copenhagen, 2100 Copenhagen, Denmark. *e-mail: yunc@dtu.dk

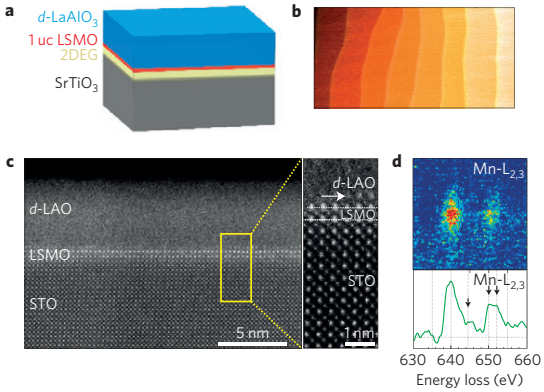

Figure 1 | Atomically engineered complex oxide interfaces with a single-unit-cell manganite buffer layer. a, Sketch of the single-unit-cell LSMO-buffered *d*-LAO/STO heterostructures. **b**, AFM image (2.5 μm × 5 μm) of a 20 nm *d*-LAO/1-uc LSMO (x=1/8)/STO heterostructure showing an atomically smooth surface. **c**, HAADF-STEM images of an 8 nm *d*-LAO/1-uc LSMO (x=1/8)/STO heterostructure. The brighter two LaO layers (marked with white dotted lines) determine the 1-uc LSMO layer. The occasional LaO islands (indicated by the white arrow) probably result from intrinsic epitaxial crystallization of LAO at the disordered/crystalline interface during room-temperature film growth. **d**, Spatially resolved Mn $L_{2,3}$ EELS spectra confirm the confinement of the LSMO buffer layer at the interface. The L_3 peak position at 640 eV and the L_2 features indicated by arrows are characteristic of Mn^{2+} states, in good agreement with other spectroscopic results (Fig. 3). More details are presented in the Supplementary Information (Supplementary Figs 2–4).

can trap electrons in a controlled manner and therefore enhance the carrier mobility; to improve the interfacial order; and to act as a separating layer between the conducting layer and its source(s) of doping. Most perovskite oxides that have a prominent characteristic of a lower Fermi level compared to STO 2DEGs can be good candidates.

Here, we report a 2DEG mobility enhancement of more than two orders of magnitude in *d*-LAO/STO obtained by inserting a single-unit-cell (uc) buffer layer of manganite[31], $La_{1-x}Sr_xMnO_3$ (LSMO, x = 0, 1/8 and 1/3), at the interface, as illustrated in Fig. 1a. As it will become clear, this leads to an unexpected modulation-doping scheme of the complex oxide 2DEG, and results in a very high 2DEG mobility, exceeding 70,000 $cm^2\,V^{-1}\,s^{-1}$ at 2 K. The fact that the final step to create these complex oxide 2DEGs occurs at room temperature, offers a notable advantage of improved compatibility with the established lithography of semiconductor microfabrication to pattern oxide interfaces[19,32]. This opens new opportunities for oxide nanoelectronic devices such as tunnel junctions and high-mobility field-effect transistors[33].

Our samples were grown at room temperature on TiO_2-terminated single-crystal STO substrates by pulsed laser deposition (see Methods). For the buffered sample, an epitaxial LSMO layer was first deposited at 600 °C and 1×10^{-4} mbar of O_2, then slowly cooled to room temperature at the approximate deposition pressure (10^{-5}–10^{-4} mbar) before switching to *d*-LAO deposition *in situ*. The LSMO layer with a thickness of 1 uc was accurately controlled by monitoring *in situ* reflection high-energy electron diffraction (RHEED) intensity oscillations under optimized condition of layer-by-layer epitaxial film growth mode (Supplementary Information and Supplementary Fig. 1). For all samples, with the *d*-LAO film thickness up to 20 nm, atomic force microscopy (AFM) images show regular surface terraces with a step height of 0.4 nm (Fig. 1b), similar to that of the original STO substrate and indicating uniform film growth. Representative samples were investigated further by scanning transmission electron microscopy (STEM). Figure 1c shows high-angle annular dark-field (HAADF) STEM images of a LSMO-buffered (x = 1/8) sample with a *d*-LAO layer of approximately 8.0 nm. The room-temperature-deposited and unannealed LAO film is found to be disordered or amorphous-like, and the nominally 1-uc LSMO film is found to be coherently grown on the STO substrate with no detectable defects or dislocations at the LSMO/STO interface. We observe what is likely to be an intrinsic crystallization of the LaO sublayer in close proximity to the LSMO buffer layer during room-temperature film growth of LAO (Supplementary Information and Supplementary Figs 2–4). The first layer of the subsequent *d*-LAO might be partially crystallized in the form of islands, according to the contrast differences within this layer, but accurate quantification of the amorphous/crystalline ratio from such a projected image remains open[34,35]. The further investigation of chemical composition across the interface by electron energy-loss spectroscopy (EELS) confirms the interfacial confinement of Mn, as well as limited cation intermixing within 0.8 nm (Supplementary Information and Supplementary Figs 2 and 4). Note that EELS spectra at the Mn-$L_{2,3}$ edge indicate a much reduced manganese valence compared to the nominal Mn^{3+}/Mn^{4+} of bulk LSMO (Fig. 1d). Furthermore, the possibility of La-doping of STO-induced interface conduction is ruled out here, because all our LSMO/STO heterostructures with LSMO up to 4 uc are highly insulating without the growth of the capping *d*-LAO layer.

The presence of the LSMO buffer layer is found to have a strong impact on the transport properties of the *d*-LAO/STO structure. First, when the buffer layer thickness, t, is increased from 1 uc to 2 uc, a metal-to-insulator transition is observed (Fig. 2a,b)—that is, the buffered heterostructures become highly insulating when $t \geq 2$ uc (see also Supplementary Information and Supplementary Fig. 5). Second, in the case with a single-unit-cell buffer layer, the transport behaviour of these room-temperature-created STO-based heterostructures is improved greatly. Figure 2c–e shows the typical electrical transport properties of *d*-LAO/STO interfaces with and without the single-unit-cell LSMO buffer layer. The unbuffered *d*-LAO/STO interface shows a good metallic behaviour with an electron density, n_s, of approximately 1.2×10^{14} cm^{-2} at 300 K. However, on cooling, it always exhibits a carrier freeze-out effect at $T \leq 100$ K, with an activation energy of 5–10 meV (ref. 26), indicating the presence of localized electrons. This results in a low electron mobility, μ, of approximately 600 $cm^2\,V^{-1}\,s^{-1}$ at 2 K. In contrast, all LSMO-buffered samples exhibit a nearly temperature-independent n_s as well as a striking decrease in sheet resistance, R_s, of about three to four orders of magnitude during cooling. This suggests the removal of localized electrons and improved metallic conduction by the insertion of LSMO layers. Furthermore, all metallic LSMO-buffered samples exhibit a strongly suppressed n_s in the range 3.4×10^{12} cm^{-2} to 2.7×10^{13} cm^{-2} (0.005–0.040 electrons per uc), nearly independent of x. With respect to electron mobility, more than 30 samples have been grown with high mobilities exceeding 10,000 $cm^2\,V^{-1}\,s^{-1}$ at 2 K, which is more than ten times higher than the mobilities of unbuffered samples. Representatively, at 2 K, a $n_s = 6.9 \times 10^{12}$ cm^{-2}, μ = 16,000 $cm^2\,V^{-1}\,s^{-1}$, a $n_s = 1.7 \times 10^{13}$ cm^{-2}, μ = 73,000 $cm^2\,V^{-1}\,s^{-1}$ and a $n_s = 1.8 \times 10^{13}$ cm^{-2}, μ = 8,800 $cm^2\,V^{-1}\,s^{-1}$, are obtained for x = 0, 1/8 and 1/3, respectively. The very high electron mobility of 73,000 $cm^2\,V^{-1}\,s^{-1}$ is larger than any yet-reported mobilities for 2DEGs based on the LAO/STO system[7–18].

Our subsequent spectroscopic measurements reveal marked electronic reconstruction in the LSMO-buffered samples. First, different from the unbuffered *d*-LAO/STO sample, where the 2DEG is coupled strongly to a large content of oxygen vacancies extending more than 3 nm deep into STO (ref. 24), all buffered samples show

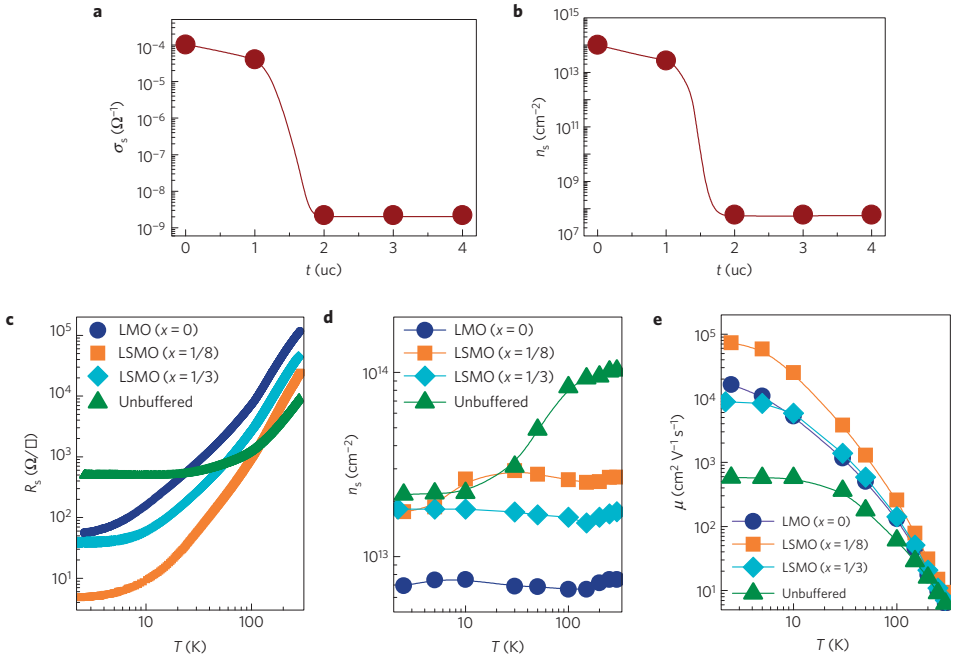

Figure 2 | Electronic properties of *d*-LAO (8.5 nm)/STO heterostructures with and without LSMO ($x = 0, 1/8,$ and $1/3$) buffer layers. a,b, Sheet conductance σ_s (**a**) and carrier density n_s (**b**) as a function of the buffer layer thickness, t, for LSMO-buffered (x=1/8) *d*-LAO/STO heterostructures. All data were obtained at room temperature. **c**–**e**, Temperature dependence of sheet resistance R_s (**c**), carrier density n_s (**d**) and mobility μ(**e**). The unbuffered *d*-LAO/STO always shows a carrier freeze-out at around 100 K, whereas the buffered samples exhibit a remarkable temperature-independent n_s and a large μ, often exceeding approximately 10,000 cm^2 V^{-1} s^{-1} at 2 K. The lines are guides to the eye.

a rather low content of Ti^{3+}, far below the detection limit of our *in situ* X-ray photoelectron spectroscopy (XPS) measurements (Supplementary Information and Supplementary Fig. 6). This suggests a much reduced carrier density and/or oxygen vacancies compared to the unbuffered sample, consistent with the transport measurements (Fig. 2c–e). Similar results are also detected by our spatially resolved EELS measurements, which discover a nearly perfect Ti^{4+} for the LMO-buffered case and some remaining Ti^{3+} confined exclusively to the first two unit cells (~0.8 nm) of STO in the LSMO-buffered ($x = 1/8$) case (Supplementary Information and Supplementary Fig. 7). Second, both *in situ* XPS (Supplementary Fig. 6) and EELS spectra (Fig. 1d and Supplementary Fig. 7) data show an unambiguous signature of Mn^{2+} in the buffer layer, which appears only when the *d*-LAO film is thicker than 2 nm (Supplementary Fig. 6). The lowering of the Mn valence and its impact on the 2DEG carriers in the buffered samples are further determined by synchrotron-radiation-based resonant X-ray reflectivity (RXR) (Supplementary Information and Supplementary Fig. 8), which can probe buried interfaces and thin layers with extremely high sensitivity.

Figure 3a,b shows reflectivity measurements across the Ti and Mn $L_{2,3}$ resonances, respectively, for both the unbuffered and the LSMO-buffered ($x = 1/8$) samples. The overall shapes of the spectra across the Ti $L_{2,3}$ resonance (Fig. 3a) are indicative of the Ti^{4+} in the STO, with distinct stronger e_g peaks relative to the t_{2g} peaks at both the L_3 (~460 eV) and L_2 (~466 eV) edges for the unbuffered sample. This confirms the stronger presence of Ti^{3+} (that is, occupied 2DEG t_{2g} states) in the unbuffered sample, as independently determined by both XPS and EELS. The enhancement near the e_g peak as a response to the 2DEG is also found in resonant photoemission spectra from *c*-LAO/STO samples[36]. In strong agreement with the EELS and XPS spectra, the RXR scan across the Mn resonance (Fig. 3b) also reveals the presence of Mn^{2+} in the buffer layer. Remarkably, an X-ray absorption spectra (XAS) calculation based on a theoretical cluster model (Supplementary Information and Supplementary Table 1), which can be comparable to the experimental RXR spectra, finds that the experimental spectrum is due to the presence of almost entire Mn^{2+}, exhibiting a relatively weak e_g–t_{2g} crystal field splitting energy about one half in magnitude of that in MnO (ref. 37). This presence of nearly entire Mn^{2+} indicates an extremely high concentration of reconstructed electrons of ~1 *e*/uc in the LSMO buffer layer, much higher than the deduced n_s of the 2DEG (Fig. 2). This implies that the reconstructed electrons at the Mn^{2+} site are mostly trapped as expected, whereas the 2DEG carriers stay on the Ti site, as in the case of the unbuffered sample. Moreover, the buffered samples show a total amount of reconstructed electrons (~1.005–1.040 e per uc square area) much higher than that of the unbuffered sample (typically below 0.5 e per uc square area[24]). This marked difference probably comes from the polarity of the LSMO buffer layer and the *d*-LAO film. Note that, although without any detectable long-range translational symmetry, the *d*-LAO locally could contain AlO_6 octahedra that are similar to the local bonding units in *c*-LAO. Moreover, the polarity of *d*-LAO can be tuned by an external dipole[38]. Therefore, it is reasonable that the polar nature of the LSMO buffer layer is inherited or even enhanced in the *d*-LAO system, and that the polarization-catastrophe-induced electronic reconstruction[20] can adequately explain the electron sources in the buffered sample. We further confirmed that reduction of the LSMO buffer layer during the *d*-LAO deposition hardly occurs, as indicated by another control experiment: an insulating behaviour and negligible signature of Mn^{2+} was detected when the bilayer of *d*-LAO/LSMO was grown on a $(LaAlO_3)_{0.3}$ $(Sr_2AlTaO_6)_{0.7}$ substrate under exactly the same conditions as the buffered *d*-LAO/STO

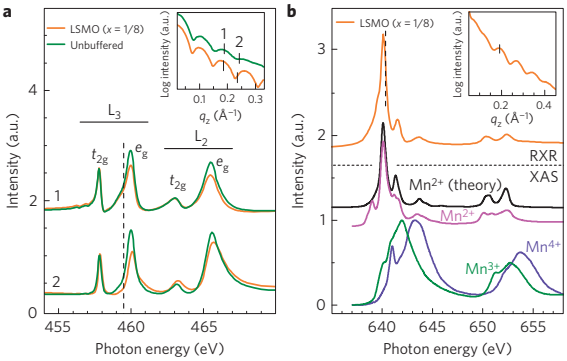

Figure 3 | Electronic reconstructions in *d*-LAO/STO heterostructures. **a**,**b**, RXR fixed-momentum measurements with photon energies scanned across the Ti and Mn $L_{2,3}$ edges, respectively. The insets show momentum scans at fixed energies of 459.5 eV and 640.3 eV for Ti and Mn, respectively, as indicated by the vertical dashed lines. Vertical bars in the insets show the specific momentum values used for the RXR measurements. The interference fringes are primarily defined by the *d*-LAO layer thickness (8.5 nm). Mn X-ray absorption spectra (XAS) of reference materials MnO (Mn^{2+}), $LaMnO_3$ (Mn^{3+}) and $SrMnO_3$ (Mn^{4+}) (ref. 47) are shown in **b** for comparison, as well as a calculated spectrum of Mn^{2+}.

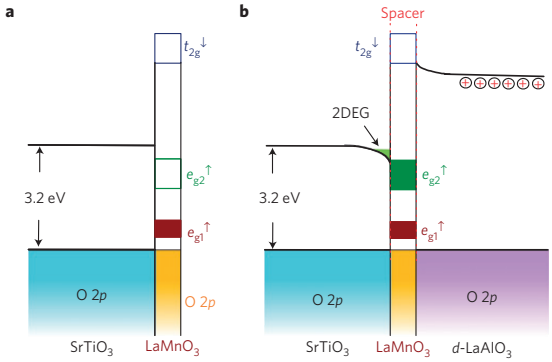

Figure 4 | Modulation doping of STO-based heterostructures. **a**,**b**, Schematic band diagram of LMO-buffered *d*-LAO/STO before (**a**) and after (**b**) the *d*-LAO deposition. Given the alignment of O 2*p* bands when STO and LMO come into contact, Ti 3*d* bands are higher than the empty or partially filled e_g bands of LSMO, as illustrated in **a**. Therefore, reconstructed electrons coming from the positively ionized donors will be transferred first to the LSMO buffer layer. The formation of the 2DEG occurs only after the presence of Mn^{2+} (when *d*-LAO is thicker than 3.2 nm), as shown in **b**.

sample, consistent with the previous report[39]. Note that we cannot rule out the possibility that some oxygen vacancies might be present in the buffer layer owing to its oxygen-deficient growth environment (mainly for $x = 1/8$ and $1/3$), although their amount is expected to be small, as determined by XPS before the *d*-LAO deposition (Supplementary Information and Supplementary Fig. 6). Owing to this possible presence of oxygen vacancies in the buffer layer, it becomes challenging to compare the buffered samples with different Sr content (x), which also suffer from various strain effects. Nevertheless, by comparing all the buffered samples with the unbuffered one, we can conclude unambiguously that the manganite buffer layer prevents the reduction of STO and induces a remarkable electronic reconstruction: most of the interfacial electrons, which otherwise stay on Ti, are transferred to Mn and become highly trapped.

The effective electron absorption by LSMO in the buffered *d*-LAO/STO results from the unique band alignment of the manganite–titanate perovskite interface. The undoped $LaMnO_3$ (LMO) is a charge-transfer insulator. Its electronic configuration of the Mn *d* electrons is $t_{2g}^3 e_g^1$. Generally, a static Jahn–Teller distortion lifts the degeneracy in the e_g level, splitting it into e_{g1} and e_{g2} levels, with the energy separation between e_{g1} and the empty e_{g2} levels being about 1.9 eV (ref. 40). The substitution of La^{3+} by Sr^{2+} ions produces holes in the e_g orbitals which are strongly hybridized with oxygen 2*p* states. As the doping level x is increased, a downward shift of the Fermi level position is expected. On the other hand, the Fermi level of the STO 2DEG is close to that of Nb-doped STO. When manganites are grown epitaxially on the titanate, the interfacial barrier height (Φ_B) between the slightly electron-doped STO and the LSMO is determined to be increased from approximately 0.5 eV to 1.0 eV when x increases from 0 to 0.5 (refs 41,42). Therefore, the Ti 3*d* bands of STO are always higher than the empty or partially filled e_g bands of LSMO, given the alignment of O 2*p* bands when they come into contact, as illustrated in Fig. 4a. In this vein, during the formation of 2DEG in buffered samples, electrons, which originate from positively ionized donors on the *d*-LAO side, will be first transferred to the Mn sublattice before filling the electronic shell of Ti ions. This scenario is consistent with the fact that Mn^{2+} becomes detectable already at an *d*-LAO film thickness of 2.0 nm (Supplementary Fig. 6), much before the critical thickness for occurrence of interface conduction, ~3.2 nm for the $x = 1/8$ buffered sample (Supplementary Fig. 5). Moreover, the above electron-transfer process is expected to modulate the band alignment significantly at buffered *d*-LAO/STO interfaces. Taking the LMO buffer layer as an example, transferred electrons will completely fill the first empty subband ($e_{g2}^{\uparrow}$) of LMO (Fig. 4a). This results in a non-trivial consequence that the bottom of the conduction band ($t_{2g}^{\downarrow}$) of the reconstructed buffered layer becomes higher than that of the capping *d*-LAO (Fig. 4b). Consequently, the LSMO buffer layer, remaining highly insulating both before and after electron transfer, could act as a spacer as introduced in the modulation-doped semiconductor heterostructures (Supplementary Information and Supplementary Fig. 9)[1,3]. It spatially separates the 2DEG electrons (on the STO side) and the ionized donors (on the *d*-LAO side). Therefore, the buffered samples exhibit a much higher mobility. Interestingly, such band alignment of the buffered sample, particularly the filling of the e_g subbands by charge transfer, is strongly supported by our spatially resolved EELS spectra at the O–K edges (Supplementary Information and Supplementary Figs 10 and 11). Moreover, the electronic reconstruction scheme is also consistent with the insulating nature of the buffered sample when the LSMO buffer layer is increased to 2 uc (Fig. 2a,b): The total amount of reconstructed electrons resulting from interface polarity is expected to be constant regardless of the LSMO thickness. When the buffer layer is thicker than 1 uc, the reconstructed electrons can not fully fill the empty subbands of LSMO, therefore there will be no electrons transferred to the STO conduction bands and, thus, no formation of 2DEGs.

Finally, it is noteworthy that the combination of high mobility and low carrier density of our modulation-doped 2DEGs may enable the observation of the quantum Hall effect. Here, the electrons in our modulation-doped 2DEGs with a true 2D Fermi surface—that is, constant density of states (DOS) as a function of energy—and a sufficiently high mobility form extended edge states at high magnetic fields. At these fields the DOS becomes discretized into separate Landau levels with an integer filling factor. For 2DEGs with a sufficiently low carrier density these Landau levels become experimentally resolvable at available fields and low temperatures.

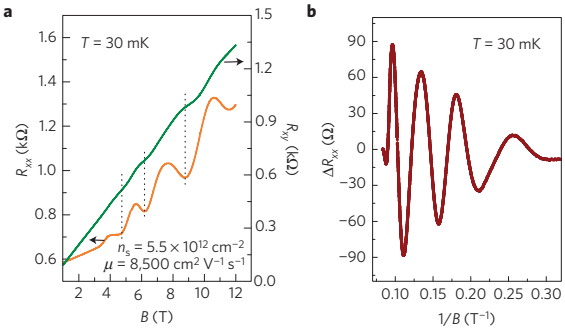

Figure 5 | Quantum oscillations at modulation-doped oxide interfaces. **a**, Longitudinal resistance, R_{xx}, and Hall resistance, R_{xy}, as a function of magnetic field B normal to the sample surface. R_{xx} exhibits Shubnikov–de Hass (SdH) quantum oscillations with minima at the same positions as the plateau-like structures in R_{xy}, indicating the observation of the quantum Hall effect. **b**, Amplitude of the SdH oscillations, ΔR_{xx}, shows $1/B$ periodicity, which is dominated by single-band conduction with an oscillation frequency of approximately 21 T.

Figure 5a shows transport measurements at $T = 30$ mK of the longitudinal resistance, R_{xx}, and the transverse resistance, R_{xy}, as a function of magnetic field (B) applied perpendicular to a Hall-bar sample with $n_s = 5.5 \times 10^{12}$ cm^{-2}. Despite a relatively reduced electron mobility in our patterned oxide interface, presumably due to the processing, R_{xx} shows clear Shubnikov–de Haas (SdH) oscillations[43]. By subtracting a magnetoresistance background, the oscillations are periodic in $1/B$ and dominated by a single oscillation frequency, as shown in Fig. 5b. This behaviour is similar to other STO-based conduction heterostructures with extremely high mobility[6,44]. At fields where R_{xx} shows a minimum (indicated by vertical dashed lines), there is a corresponding reduction of the R_{xy} slope consistent with the initial formation of quantized Hall plateaux[45]. The observation of quantum Hall-like structure in our 2DEG further supports the feasibility of our modulation-doping approach and establishes the quality of our samples. Detailed analysis of the density-, temperature- and angle-dependence of the quantum Hall results will be presented elsewhere[46].

In conclusion, the LSMO buffer layer not only significantly suppresses the oxygen vacancies on the STO side but also results in modulation doping in buffered d-LAO/STO, which remains underexploited at complex oxide interfaces[10]. As most of complex oxide 2DEGs possess a similar electronic structure[27–30], the charge-transfer-induced modulation doping discussed here is expected to be a universal phenomenon, and it could result in a plethora of exotic physical phenomena.

Methods

Methods and any associated references are available in the online version of the paper.

Received 5 August 2014; accepted 22 April 2015; published online 1 June 2015

References

1. Kroemer, H. Nobel Lecture: Quasielectric fields and band offsets: Teaching electrons new tricks. *Rev. Mod. Phys.* **73,** 783–793 (2001).
2. Schlom, D. G. & Pfeiffer, L. N. Oxide electronics: Upward mobility rocks! *Nature Mater.* **9,** 881–883 (2010).
3. Dingle, R., Stormer, H. L., Gossard, A. C. & Wiegmann, W. Electron mobilities in modulation-doped semiconductor heterojunction superlattices. *Appl. Phys. Lett.* **33,** 665–667 (1978).
4. Tsui, D. C., Stormer, H. L. & Gossard, A. C. Two-dimensional magnetotransport in the extreme quantum limit. *Phys. Rev. Lett.* **48,** 1559–1562 (1982).
5. Ohtomo, A. & Hwang, H. Y. A high-mobility electron gas at the $LaAlO_3/SrTiO_3$ heterointerface. *Nature* **427,** 423–426 (2004).
6. Chen, Y. Z. *et al.* A high-mobility two-dimensional electron gas at the spinel/perovskite interface of γ-$Al_2O_3/SrTiO_3$. *Nature Commun.* **4,** 1371 (2013).
7. Mannhart, J. & Schlom, D. G. Oxide interfaces: An opportunity for electronics. *Science* **327,** 1607–1611 (2010).
8. Miletto Granozio, F., Koster, G. & Rijnders, G. Functional oxide interfaces. *Mater. Res. Soc. Bull.* **38,** 1017–1023 (2013).
9. Hwang, H. Y. *et al.* Emergent phenomena at oxide interfaces. *Nature Mater.* **11,** 103–113 (2012).
10. Stemmer, S. & Allen, S. J. Two-dimensional electron gases at complex oxide interfaces. *Annu. Rev. Mater. Sci.* **44,** 151–171 (2014).
11. Reyren, N. *et al.* Superconducting interfaces between insulating oxides. *Science* **317,** 1196–1199 (2007).
12. Brinkman, A. *et al.* Magnetic effects at the interface between non-magnetic oxides. *Nature Mater.* **6,** 493–496 (2007).
13. Lee, J-S. *et al.* Titanium d_{xy} ferromagnetism at the $LaAlO_3/SrTiO_3$ interface. *Nature Mater.* **12,** 703–706 (2013).
14. Cen, C. *et al.* Nanoscale control of an interfacial metal–insulator transition at room temperature. *Nature Mater.* **7,** 298–302 (2008).
15. Ariando, *et al.* Electronic phase separation at the $LaAlO_3/SrTiO_3$ interface. *Nature Commun.* **2,** 188 (2011).
16. Huijben, M. *et al.* Defect engineering in oxide heterostructures by enhanced oxygen surface exchange. *Adv. Funct. Mater.* **23,** 5240–5248 (2013).
17. Caviglia, A. D. *et al.* Two-dimensional quantum oscillations of the conductance at $LaAlO_3/SrTiO_3$ interfaces. *Phys. Rev. Lett.* **105,** 236802 (2010).
18. Xie, Y. W., Bell, C., Hikita, Y., Harashima, S. & Hwang, H. Y. Enhancing electron mobility at the $LaAlO_3/SrTiO_3$ interface by surface control. *Adv. Mater.* **25,** 4735–4738 (2013).
19. Chen, Y. Z. *et al.* Room temperature formation of high-mobility two-dimensional electron gases at crystalline complex oxide interfaces. *Adv. Mater.* **26,** 1462–1467 (2014).
20. Hesper, R., Tjeng, L. H., Heeres, A. & Sawatzky, G. A. Photoemission evidence of electronic stabilization of polar surfaces in K3C60. *Phys. Rev. B* **62,** 16046 (2000).
21. Jang, H. W. *et al.* Metallic and insulating oxide interfaces controlled by electronic correlations. *Science* **331,** 886–889 (2011).
22. Chambers, S. A. *et al.* Instability, intermixing and electronic structure at the epitaxial $LaAlO_3/SrTiO_3$(001) heterojunction. *Surf. Sci. Rep.* **65,** 317–352 (2010).
23. Kalabukhov, A. *et al.* Effect of oxygen vacancies in the $SrTiO_3$ substrate on the electrical properties of the $LaAlO_3/SrTiO_3$ interface. *Phys. Rev. B* **75,** 121404(R) (2007).
24. Chen, Y. Z. *et al.* Metallic and insulating interfaces of amorphous $SrTiO_3$-based oxide heterostructures. *Nano Lett.* **11,** 3774–3778 (2011).
25. Christensen, D. V. *et al.* Controlling interfacial states in amorphous/crystalline $LaAlO_3/SrTiO_3$ heterostructures by electric fields. *Appl. Phys. Lett.* **102,** 021602 (2013).
26. Chen, Y. Z., Pryds, N., Sun, J. R., Shen, B. G. & Linderoth, S. High-mobility two-dimensional electron gases at oxide interfaces: Origins and opportunities. *Chin. Phys. B* **22,** 116803 (2013).
27. Gabay, M. Triscone, J-M. Oxide heterostructures: Hund rules with a twist. *Nature Phys.* **9,** 610–611 (2013).
28. Delugas, P. *et al.* Spontaneous 2-dimensional carrier confinement at the n-type $SrTiO_3/LaAlO_3$ interface. *Phys. Rev. Lett.* **106,** 166807 (2011).
29. Son, W. J., Cho, E., Lee, B., Lee, J. & Han, S. Density and spatial distribution of charge carriers in the intrinsic n-type $LaAlO_3$-$SrTiO_3$ interface. *Phys. Rev. B* **79,** 245411 (2009).
30. Berner, G. *et al.* Direct k-space mapping of the electronic structure in an oxide–oxide interface. *Phys. Rev. Lett.* **110,** 247601 (2013).
31. Huijben, M. *et al.* Critical thickness and orbital ordering in ultrathin $La_{0.7}Sr_{0.3}MnO_3$ films. *Phys. Rev. B* **78,** 094413 (2008).
32. Shibuya, K., Ohnishi, T., Lippmaa, M., Kawasaki, M. & Koinuma, H. Single crystal $SrTiO_3$ field-effect transistor with an atomically flat amorphous $CaHfO_3$ gate insulator. *Appl. Phys. Lett.* **85,** 425–427 (2004).
33. Cen, C., Thiel, S., Mannhart, J. & Levy, J. Oxide nanoelectronics on demand. *Science* **323,** 1026–1030 (2009).
34. Mkhoyan, K. A., Maccagnano–Zacher, S. E., Kirkland, E. J. & Silcox, J. Effects of amorphous layers on ADF-STEM imaging. *Ultramicroscopy* **108,** 791–803 (2008).
35. Van Aert, S., Chang, L. Y., Bals, S., Kirkland, A. I. & Van Tendeloo, G. Effect of amorphous layers on the interpretation of restored exit waves. *Ultramicroscopy* **109,** 237–246 (2009).

36. Cancellieri, C. *et al.* Interface Fermi states of $LaAlO_3/SrTiO_3$ and related heterostructures. *Phys. Rev. Lett.* **110,** 137601 (2013).
37. Haverkort, M. W., Zwierzycki, M. & Andersen, O. K. Multiplet ligand-field theory using Wannier orbitals. *Phys. Rev. B* **85,** 165113 (2012).
38. Wachtel, E. & Lubomirsky, I. Quasi-amorphous inorganic thin films: Non-crystalline polar phases. *Adv. Mater.* **22,** 2485–2493 (2010).
39. Ferguson, J. D. *et al.* Epitaxial oxygen getter for a brownmillerite phase transformation in manganite films. *Adv. Mater.* **23,** 1226–1230 (2011).
40. Jung, J. H. *et al.* Determination of electronic band structures of $CaMnO_3$ and $LaMnO_3$ using optical-conductivity analyses. *Phys. Rev. B* **55,** 15489 (1997).
41. Sawa, A. *et al.* Fermi level shift in $La_{1-x}Sr_xMO_3$ (M=Mn, Fe, Co, and Ni) probed by Schottky-like heteroepitaxial junctions with $SrTi_{0.99}Nb_{0.01}O_3$. *Appl. Phys. Lett.* **90,** 252102 (2007).
42. Chen, Y. Z. *et al.* Charge ordering transition near the interface of the (011)-oriented $La_{1-x}Sr_xMnO_3$ (x∼1/8) films. *Appl. Phys. Lett.* **93,** 152515 (2008).
43. Shubnikov, L. W. & de Haas, W. J. Magnetische Widerstandsvergrösserung in Einkristallen von Wismut bei tiefen Temperaturen. *Proc. R Neth. Acad. Arts Sci.* **33,** 130–133 (1930).
44. Son, J. *et al.* Epitaxial $SrTiO_3$ films with electron mobilities exceeding 30,000 $cm^2 V^{-1} s^{-1}$. *Nature Mater.* **9,** 482–484 (2010).
45. Klitzing, K. v., Dorda, G. & Pepper, M. New methods for high-accuracy determination of the fine-structure constant based on quantized Hall resistance. *Phys. Rev. Lett.* **45,** 494–497 (1980).
46. Trier, F. *et al.* Quantum Hall effect at a $SrTiO_3$-based heterointerface: Evidence of a multiple quantum well nature (in the press).
47. Burnus, T. *et al.* Local electronic structure and magnetic properties of $LaMn_{0.5}Co_{0.5}O_3$ studied by x-ray absorption and magnetic circular dichroism spectroscopy. *Phys. Rev. B* **77,** 125124 (2008).

Acknowledgements

The authors gratefully acknowledge discussions with J. Mannhart, J. R. Sun and B. G. Shen, and technical assistance from J. Geyti, L. Han, K. V. Hansen, S. Upadhyay, C. Olsen and A. Jellinggaard. This work was funded by the European Union (EU) Council under the 7th Framework Program (FP7) grant number NMP3-LA-2010-246102 IFOX, by funding from the European Research Council (ERC) under FP7, ERC grant No. 246791—COUNTATOMS and ERC Starting Grant 278510 VORTEX. The Qu-Ant-EM microscope was partly funded by the Hercules Fund from the Flemish Government. The authors acknowledge also financial support from EU under FP7 under a contract for an Integrated Infrastructure Initiative. Reference No. 312483-ESTEEM2. Funding from the Fund for Scientific Research Flanders is acknowledged for FWO project G.0044.13N ('Charge ordering'). Funding from the Danish Agency for Science, Technology and Innovation, and the Lundbeck Foundation are acknowledged. The Center for Quantum Devices is supported by the Danish National Research Foundation. The Canadian work was supported by NSERC and the Max Planck-UBC Centre for Quantum Materials. Some experiments for this work were performed at the Canadian Light Source, which is funded by the Canada Foundation for Innovation, NSERC, the National Research Council of Canada, the Canadian Institutes of Health Research, the Government of Saskatchewan, Western Economic Diversification Canada, and the University of Saskatchewan.

Author contributions

Y.Z.C.: concept design, film growth, transport measurements, data analysis, interpretation and writing of the manuscript. The contributions of other authors are as follows. Transport measurements and analysis: D.V.C., N.H.A., M.Huijben, J.A.S., M.Honig and S.I.; STEM and EELS measurements and analysis: N.G., R.E., J.V. and G.V.T.; XPS measurements and analysis: T.W., G.K., M.Huijben, G.R. and N.B.; RXR measurements and analysis: R.J.G., S.M., F.H., R.S. and G.A.S.; SdH measurements: F.T., G.E.D.K.P. and T.S.J.; Data discussion: N.P. and S.L. All authors extensively discussed the results and the manuscript.

Additional information

Supplementary information is available in the online version of the paper. Reprints and permissions information is available online at www.nature.com/reprints. Correspondence and requests for materials should be addressed to Y.Z.C.

Competing financial interests

The authors declare no competing financial interests.

Methods

Sample growth and transport measurements. All heterostructures were grown on TiO_2-terminated $SrTiO_3$ (STO) substrates ($5 \times 5 \times 0.5\,mm^3$ with miscut less than 0.2°) by pulsed laser deposition (PLD) in an oxygen atmosphere of $\sim 10^{-4}$ mbar, with the film growth process monitored by *in situ* RHEED. During ablation, a KrF laser ($\lambda = 248$ nm) with a repetition rate of 1 Hz and laser fluence of $1.5\,J\,cm^{-2}$ was used. The target–substrate distance was fixed at 5.6 cm. For disordered $LaAlO_3$ (d-LAO) films deposited at room temperature at 10^{-5}–10^{-4} mbar, a single-crystalline LAO target was used. For the buffered $La_{1-x}Sr_xMnO_3$ (LSMO, $x = 0, 1/8, 1/3$) layers, sintered LSMO ceramics were used as targets. The growth temperature of LSMO was fixed at 600 °C. Layer-by-layer two-dimensional growth of LSMO films was optimized by RHEED oscillations with a growth rate of approximately 50 pulses per unit cell ($\sim 4.8\,Å\,min^{-1}$, Supplementary Information and Supplementary Fig. 1a). For each buffered sample, after the epitaxial growth of monolayer LSMO, the sample was cooled under the deposition pressure at a rate of $15\,°C\,min^{-1}$ to room temperature (below 30 °C, in 5–6 h) before the subsequent d-LAO film deposition *in situ* (Supplementary Fig. 1d). Note that *in situ* annealing of our samples at 80 °C in 10^{-2} mbar oxygen pressure results in insulating samples, indicating that the ionized donors may be strongly coupled to oxygen vacancies at the sample surface.

Electrical characterization was made mainly using a four-probe Van der Pauw method with ultrasonically wire-bonded aluminium wires as electrodes. Samples patterned in a Hall-bar configuration also showed similar enhanced electron mobilities. All buffered samples exhibit linear Hall resistance in magnetic fields.

Quantum transport measurements were performed on a patterned Hall-bar device ($W = 70\,\mu m$, $L = 300\,\mu m$) in a dilution refrigerator at 30 mK with magnetic fields up to 12 T using a standard lock-in technique.

STEM and EELS analysis. Transmission electron microscopy studies were performed at room temperature using the Qu–Ant–EM microscope, which is an aberration-corrected scanning transmission electron microscope (STEM), FEI Titan3 80–300 operated at an acceleration voltage of 200 kV, equipped with a high-brightness field-emission electron source (X-FEG) and a high-resolution electron energy-loss spectrometer. Cross-sectional cuts of the samples grown under the optimum condition described above were prepared using a dual-beam focused ion beam (FIB) instrument. For HAADF imaging, a probe size of approximately 1 Å with a convergence angle of 24 mrad, and an HAADF inner collection angle of 140 mrad were used. For electron energy-loss spectroscopy (EELS) in STEM, the collection angle was set to 36 mrad. Owing to the very high sensitivity of the d-LAO layer, the challenge for atomically resolved EELS and STEM imaging of the heterostructures is to minimize radiation damage resulting in recrystallization of the d-LAO layer. This was taken care of through the use of a very low electron dose for both STEM imaging and EELS spectroscopy (<40 pA). The acquisition time for EELS could not be set to more than 0.05 s/pixel, with a step size of 0.2 Å/pixel, resulting in rather low signal-to-noise ratio and making it very difficult to extract the small signal of Mn from the spectrum image. Two-dimensional spectrum images were acquired with STEM–EELS to investigate the spatial distribution of the elements within the sample. To improve the signal-to-noise ratio (SNR) in the EELS spectra (mainly on the Mn signal), principal components analysis (PCA) was applied. This analysis technique is a powerful tool to reduce the noise from STEM–EELS data, which enables one to extract the fundamental chemical information[48,49]. The elemental maps were generated by subtracting and integrating the corresponding core-loss excitation edge for each chemical element and are presented in Supplementary Figs 2a and 4a. Another way to improve the SNR in the EELS spectra is as follows: using the raw data, after subtraction of the corresponding power law background, EELS spectra on each line are summed and the result is plotted as a function of the vertical direction of the spectrum image (growth direction). The edges are then plotted as a contour plot in a colour scale, as shown in Supplementary Figs 2b and 4b, giving direct insight into compositional and electronic structure changes at atomic resolution.

***In situ* X-ray photoelectron spectroscopy (XPS) measurement.** For the study using angular-resolved XPS, a series of samples were first grown by PLD. Subsequently, the samples were transferred to the XPS chamber while keeping them under ultrahigh vacuum (below 1×10^{-9} mbar). The XPS chamber (Omicron Nanotechnology GmbH) had a base pressure below 1×10^{-10} mbar. The measurements were done using a monochromatic Al Kα (XM 1000) X-ray source and an EA 125 electron energy analyser. All spectra were acquired in the constant analyser energy (CAE) mode. A CN 10 charge neutralizer system was used to overcome the charging effect in the LSMO/STO heterostructures. For each measurement, the filament current, emission current and beam energy were optimized to minimize the full-width at half-maximum (FWHM) of the peaks. For analysing the Ti $2p_{3/2}$ peaks, a Shirley background was subtracted and the spectra were normalized on the total area below the Ti peaks ([Ti] = [Ti4+] + [Ti3+] = 100%). To investigate the dependence of interface states on the film thickness of d-LAO, the XPS measurement was performed after each 2 nm deposition of d-LAO.

Synchrotron radiation resonant X-ray reflectivity (RXR) experiments. The RXR measurements were performed using an in-vacuum four-circle diffractometer at the Resonant Elastic and Inelastic X-ray Scattering (REIXS) 10ID-2 beamline of the Canadian Light Source (CLS) in Saskatoon, Canada[50]. The beamline has a flux of 5×10^{12} photon/s and photon energy resolution $\Delta E/E$ of $\sim 10^{-4}$. The base pressure of the diffractometer chamber was kept lower than 10^{-9} torr. The samples were aligned with their surface normal in the scattering plane. All data reported here were collected at room temperature (293 K) with σ-polarized light (polarization perpendicular to the scattering plane). The measurements were carried out in the specular reflection geometry with either constant photon energies or constant momentum transfer across Ti $L_{2,3}$ resonances ($\sim$450–470 eV) and Mn $L_{2,3}$ resonances ($\sim$635–660 eV). The experimental geometry is depicted in Supplementary Fig. 8.

References

48. Watanabe, M., Okunishi, E. & Ishizuka, K. Analysis of spectrum-imaging datasets in atomic-resolution electron microscopy. *Microsc. Anal.* **23,** 5–7 (2009).
49. Keenan, M. R. & Kotula, P. G. Accounting for poisson noise in the multivariate analysis of ToF-SIMS spectrum images. *Surf. Interface Anal.* **36,** 203–212 (2004).
50. Hawthorn, D. G. *et al.* An in-vacuum diffractometer for resonant elastic soft x-ray scattering. *Rev. Sci. Instrum.* **82,** 073104 (2011).

VII

ARTICLE

M. Yazdi-Rizi, P. Marsik, B.P.P. Mallett, A. Dubroka, **D.V. Christensen** *et al.*
Infrared ellipsometry study of the confined electrons in a high-mobility γ-Al_2O_3/$SrTiO_3$ heterostructure
EPL Europhysics Letters 113, 47005 (2016)

Springtime at Risø campus
Photo: DTU

A Letters Journal Exploring the Frontiers of Physics

February 2016

EPL, **113** (2016) 47005 www.epljournal.org
doi: 10.1209/0295-5075/113/47005

Infrared ellipsometry study of the confined electrons in a high-mobility γ-Al_2O_3/$SrTiO_3$ heterostructure

M. Yazdi-Rizi[1], P. Marsik[1], B. P. P. Mallett[1], A. Dubroka[2], D. V. Christensen[3], Y. Z. Chen[3], N. Pryds[3] and C. Bernhard[1]

[1] *University of Fribourg, Department of Physics and Fribourg Center for Nanomaterials Chemin du Musée 3, CH-1700 Fribourg, Switzerland*
[2] *Department of Condensed Matter Physics, Faculty of Science and Central European Institute of Technology, Masaryk University - Kotlářska 2, 61137 Brno, Czech Republic*
[3] *Department of Energy Conversion and Storage, Technical University of Denmark, Risø Campus 4000 Roskilde, Denmark*

received on 17 February 2016; accepted by M. Potemski on 3 March 2016
published online 14 March 2016

PACS 78.20.-e – Optical properties of bulk materials and thin films
PACS 78.67.-n – Optical properties of low-dimensional, mesoscopic, and nanoscale materials and structures
PACS 78.30.-j – Infrared and Raman spectra

Abstract – With infrared ellipsometry we studied the response of the confined electrons in γ-Al_2O_3/$SrTiO_3$ (GAO/STO) heterostructures in which they originate predominantly from oxygen vacancies. From the analysis of a so-called Berreman mode, that develops near the highest longitudinal optical phonon mode of $SrTiO_3$, we derive the sheet carrier density, N_s, the mobility, μ, and the depth profile of the carrier concentration. Notably, we find that N_s and the shape of the depth profile are similar as in $LaAlO_3$/$SrTiO_3$ (LAO/STO) heterostructures for which the itinerant carriers are believed to arise from a polar discontinuity. Despite an order of magnitude higher mobility in GAO/STO, as obtained from transport measurements, the derived mobility in the infrared range exhibits only a twofold increase. We interpret this finding in terms of the polaronic nature of the confined charge carriers in GAO/STO and LAO/STO which leads to a strong, frequency-dependent interaction with the STO phonons.

Introduction. – The observation that highly mobile electrons can be created at the interface between the nominal band-insulators $SrTiO_3$ (STO) and $LaAlO_3$ (LAO) with $\Delta_{gap}^{STO} = 3.2\,eV$ and $\Delta_{gap}^{LAO} = 5.6\,eV$, respectively, has initiated intense research activities on LAO/STO heterostructures [1]. Meanwhile, it has been demonstrated that functional field effect devices can be made from these oxide heterostructures [2] which even allow one to tune a superconductor to insulator quantum phase transition at very low temperatures [3]. A major unresolved question concerns the origin of these confined charge carriers and the conditions for obtaining a high mobility. The explanations range from i) an electronic reconstruction due to the polar discontinuity at the LAO/STO interface which gives rise to a transfer of 1/2 e charge per STO unit cell (corresponding to a sheet carrier density of $N_s = 3.3 \times 10^{14}\,cm^{-2}$), ii) an intermixing of La and Sr cations across the interface [4], to iii) the creation of oxygen vacancies which may be stabilized near the interface by space charge effects [5]. While the polar discontinuity scenario (i) has obtained a great deal of attention, more recently the focus has shifted toward the oxygen vacancies (iii). In particular, it has been demonstrated that an electron gas can be created in the absence of a polar discontinuity, for example at the LAO/STO (110) interface [6], with amorphous LAO cap layers [7,8], and even with a γ-Al_2O_3 (GAO) top layer which has a spinel structure. The results reported in ref. [9] suggest that both the oxygen vacancies and the polar discontinuity can be the source of mobile electrons that are confined near the surface of STO. Notably, the highest mobility reported to date has been achieved in GAO/STO heterostructures for which oxygen vacancies seem to be at the heart of the interfacial electrons [10,11]. This raises the question

about the differences in the dynamical properties of the interfacial electrons and also of the concentration depth profiles in these different kinds of heterostructures. In GAO/STO the latter has so far only been determined at room temperature using X-ray photoelectron spectroscopy (XPS) [10,12]. The depth distribution of the confined electrons at low temperature, where the dielectric constant of STO is much larger and the electron mobility strongly enhanced, is yet unknown. Some of us have previously shown for the case of LAO/STO that this information can be obtained with infrared ellipsometry [13]. Here we present a similar ellipsometry study of GAO/STO.

Sample growth and characterization. – Two GAO/STO heterostructures with GAO layer thicknesses of 2.5 and 2.75 unit cells (in the following they are denoted as GAO-2.5 and GAO-2.75) have been grown by pulsed laser deposition (PLD) on singly TiO_2-terminated (001) STO crystals with a repetition rate of 1 Hz and a laser fluence of 2.5 J cm^{-2}, and monitored by *in situ* high-pressure RHEED [10]. During the deposition at 600 °C, the static oxygen pressure was kept constant at 10^{-4} mbar. After the deposition, the sample was cooled down to room temperature at the deposition pressure without any further post oxygen annealing. The samples have been studied with standard dc Hall transport measurements. The obtained values for the sheet carrier density, N_s, and the mobility, μ, are shown in fig. 1. The infrared ellipsometry measurements have been performed with a home-built setup that is equipped with a He flow cryostat and attached to a Bruker 113V Fast Fourier spectrometer as described in ref. [14]. The data have been taken at 10 K in rotating analyser mode, with and without a static compensator based on a ZnSe prism. Almost identical data (not shown) have been obtained by using a rotating compensator with a ZnSe prism. The angle of incidence of the light was set to 75°. Special care was taken to avoid photo-doping effects by shielding the sample against visible and UV light [15]. The measurements have been performed under identical conditions first on the GAO/STO heterostructures and, right afterwards, on a bare STO substrate that serves as a reference.

Experimental results. – Infrared ellipsometric spectra contain valuable information about the properties of the electrons that are confined at the interface of the GAO/STO heterostructure. The most instructive feature is due to a so-called Berreman mode that occurs in the vicinity of the plasma frequency of the highest longitudinal optical (LO) phonon mode [16,17] which in STO is located at $\omega_{LO}(\mathrm{STO}) \approx 788\,\mathrm{cm}^{-1}$ [18]. It is an electronic plasma mode that originates from a charging of the interfaces due to the dynamical accumulation of the itinerant charge carriers. It occurs under an oblique angle of incidence of the light if the polarization of the electric field, E, is parallel to the plane of incidence (p-polarization) and thus has a finite normal component with respect to the interfaces. The corresponding reflection coefficient, r_p, exhibits

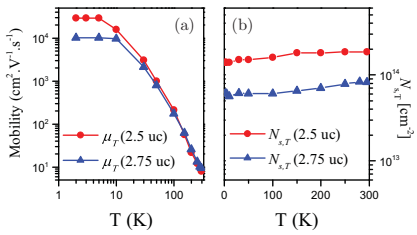

Fig. 1: (Colour online) Temperature dependence of (a) the mobility, μ, and (b) the sheet carrier density, $N_{s,T}$, as obtained from dc transport measurements on the GAO/STO samples with a GAO layer thickness of 2.5 and 2.75 unit cells (uc).

a characteristic structure in the vicinity of the LO plasma frequency, ω_{LO}. The Berreman mode is conveniently presented and analyzed in terms of the difference spectrum of the ellipsometric angle, $\Psi = \arctan(r_p/r_s)$, of the heterostructure with respect to the bare STO substrate, $\Delta\Psi = \Psi(\mathrm{sample}) - \Psi(\mathrm{STO})$. In the following we discuss primarily the data on the sample GAO-2.5 since virtually identical results (within the accuracy of our technique) have been obtained for the sample GAO-2.75 (see figs. 2(a) and (b)). The spectrum of $\Delta\Psi$ shown in fig. 2(a) reveals two major features. The broad peak with a maximum near 956 cm^{-1} corresponds to the Berreman mode. It has been previously pointed out that the difference in frequency between this maximum and $\omega_{LO}(\mathrm{STO})$ is a measure of the plasma frequency of the itinerant electrons, ω_{pl} [13]. The intensity of this peak is determined by the overall sheet carrier density and its broadening by the mobility (or the inverse scattering rate). For the case of LAO/STO it was shown that this peak has a strongly asymmetric shape which provides additional information about the depth profile of the carrier concentration [13]. For the LAO/STO system the carrier density is highest next to the interface and decreases rather rapidly toward the bulk of STO over a length scale of about 11 nm. The second feature is a fairly sharp and pronounced minimum around $\omega^{dip} \approx 865\,\mathrm{cm}^{-1}$ that occurs slightly above $\omega_{LO}(\mathrm{STO})$ when the real part of the dielectric function of STO matches the one of the ambient such that the interface becomes fully transparent. As was outlined in ref. [19] and ref. [13], this dip feature contains contributions from the out-of-plane and the in-plane components of the dielectric function. The in-plane contribution arises from the Drude-like response of the itinerant electrons which leads to a reduction of ε_1 (865 cm^{-1}) and, given a low mobility and thus large scattering rate, an increase of ε_2 (865 cm^{-1}). The strength of this dip is a measure of the overall carrier density N_s, it is rather insensitive to the details of the depth distribution of the itinerant carriers (since the penetration depth of the infrared light is about one micrometer). It is also not sensitive to the in-plane mobility of the carriers, unless it is very low such that the Drude peak in ε_2 is very

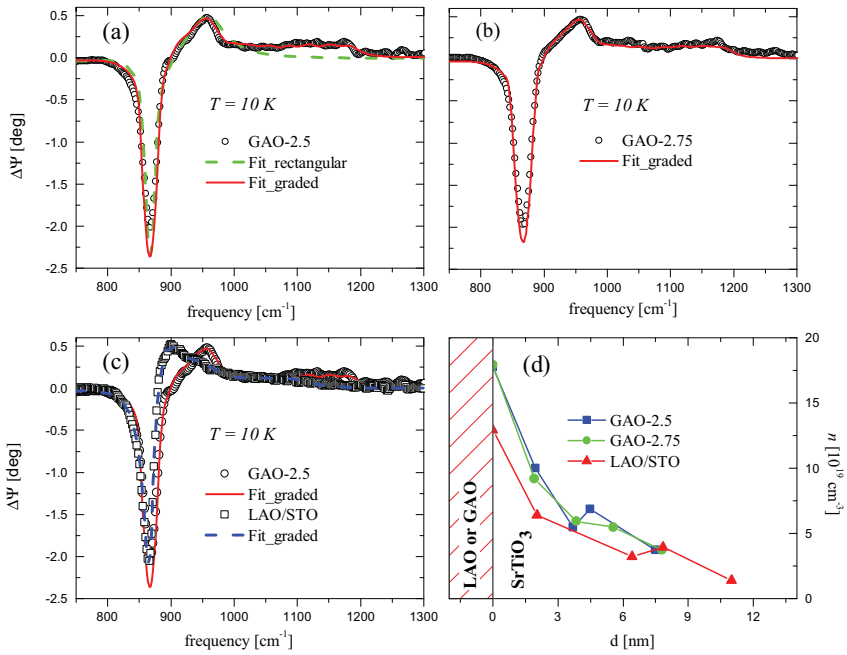

Fig. 2: (Colour online) (a) and (b) Difference spectrum of the ellipsometric angle, $\Delta\Psi = \Psi(\text{GAO/STO}) - \Psi(\text{STO})$, showing the Berreman mode above the highest LO phonon mode of STO for samples GAO-2.5 and GAO-2.75, respectively. The experimental data (open symbols) are compared with the fits with an isotropic model using a rectangular carrier concentration profile (dashed line) and a graded profile (solid line), respectively. (c) Comparison of the data and fit of GAO-2.5 with the experimental data on LAO/STO (symbols) and the best fit with a graded profile (dashed line) as reproduced from ref. [13]. (d) Comparison of the depth profile of the carrier concentration, n, as obtained from the fits with the graded potential.

Table 1: Parameters obtained from the best fit with an isotropic Drude response and a graded potential of the confined charge carriers at 10 K. The parameters for LAO/STO have been reproduced from ref. [13].

	N_s (cm^{-2})	μ (cm^2/Vs)	d (nm)
LAO/STO	5.4×10^{13}	34	11
GAO/STO - 2.5 uc	6.2×10^{13}	74	7.5
GAO/STO - 2.75 uc	6.0×10^{13}	63	7.7

broad and extends to the dip feature. We start by analyzing the ellipsometric spectra with the same model that was used in ref. [13] for the LAO/STO heterostructures. Figure 2(a) shows for GAO-2.5 the measured spectrum of $\Delta\Psi$ (symbols) at 10 K and the best fits using either a block-like potential with a constant (dashed line) or a graded profile of the concentration of the confined carriers (solid line). In the latter case, the thickness parameter, d, corresponds to the total width of the region over which the carriers are distributed. The graded profile provides a significantly better fit to the data. It reproduces the main features, like the pronounced dip around 865 cm^{-1}, the maximum around 955 cm^{-1} and, especially, the long tail toward higher frequency which is terminated by a step-like feature around 1186 cm^{-1}. Figure 2(b) shows the corresponding data and fit for GAO-2.75 which are very similar to the ones of GAO-2.5. Figure 2(c) shows a comparison with the data of GAO-2.5 and the best fit with the graded profile for the LAO/STO heterostructure [13]. The obtained depth profiles for GAO/STO (squares) and the LAO/STO (triangles) heterostructures are displayed in fig. 2(d). The derived values for the sheet carrier density N_s, the mobility, μ, and the total thickness of the conducting layers, d, are listed in table 1. To allow for a direct comparison, we assumed the same value of the effective mass, $m^* = 3.2\ m_e$, (m_e is the free electron mass) as in ref. [13]. First of all, we notice that the obtained sheet carrier density from this infrared experiment

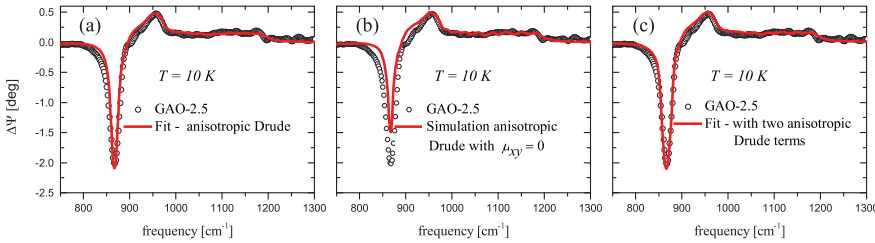

Fig. 3: (Colour online) Fitting of the difference spectrum $\Delta\Psi = \Psi(\mathrm{GAO/STO}) - \Psi(\mathrm{STO})$ with anisotropic Drude models. (a) Fit using a single anisotropic Drude term with μ_{xy} as fit parameter and the remaining parameters fixed to the values obtained from the isotropic fit as shown in fig. 2 and table 1. (b) Simulation of only the contribution of the out-of-plane component, *i.e.* for $\mu_{xy} = 0\,\mathrm{cm}^2/\mathrm{Vs}$. (c) Fit using two unidirectional Drude terms, one for the out-of-plane response with $\mu_z = 74\,\mathrm{cm}^2/\mathrm{Vs}$ and $\mu_{xy} = 0\,\mathrm{cm}^2/\mathrm{Vs}$ and the other for the in-plane response with $\mu_z = 0\,\mathrm{cm}^2/\mathrm{Vs}$ and $\mu_{xy} > 0\,\mathrm{cm}^2/\mathrm{Vs}$.

of $N_s(IR) \approx 6.2 \times 10^{13}\,\mathrm{cm}^{-2}$ and $6.0 \times 10^{13}\,\mathrm{cm}^{-2}$ for GAO-2.5 and GAO-2.75 compare indeed rather well to the ones of the dc Hall transport measurements at 10 K of $N_{s,T} \approx 1.4 \times 10^{14}\,\mathrm{cm}^{-2}$ and $5.7 \times 10^{13}\,\mathrm{cm}^{-2}$, respectively. Secondly, we remark that the larger thickness of the conducting layer of $d = 7.5\,\mathrm{nm}$, as compared to the one deduced from XPS measurements at room temperature of $d = 0.9\,\mathrm{nm}$ [10,12], can be understood in terms of the increase of the dielectric constant of STO at low temperature which leads to enhanced screening and thus a weaker confinement of the electrons. A similar difference between the thicknesses deduced from the infrared measurements at 10 K [13] and XPS [20] and scanning probe measurement at room temperature [21] was previously observed for LAO/STO. Overall, it is rather striking that despite the supposedly different origin of the confined electrons, oxygen vacancies in GAO/STO and the polar discontinuity in LAO/STO, respectively, the values of N_s and the shape of the depth profile are similar for both systems. The only main differences with respect to LAO/STO concern the thickness, d, which is somewhat reduced, and the mobility of the charge carriers, which is nearly doubled. The higher mobility enhances the visibility of the characteristic features of the Berreman mode such as the peak and, especially, the step-like edge that terminates the high-energy tail at $1185\,\mathrm{cm}^{-1}$. The latter is a measure of the maximal plasma frequency next to the interface. Note that the obtained mobility is still orders of magnitude lower than the values deduced from dc transport measurements [10]. Also, the factor of three difference in the dc mobility at 10 K of the samples GAO-2.5 and GAO-2.75 (see fig. 1) is not reflected in the value of the infrared mobility. A corresponding discrepancy between the values of the mobility obtained from dc transport and from Berreman mode in the infrared was observed for LAO/STO where it was explained in terms of the different frequency scales that are probed by the dc transport and the optical experiment. The charge carriers in bulk STO are indeed well known to have a polaronic character [22] with a strongly enhanced inelastic scattering rate in the frequency range of the Berreman mode. Our infrared data therefore suggest that the confined carriers in both GAO/STO and LAO/STO have a similar polaronic character.

While this isotropic model accounts for the main features of the Berreman mode, it fails to describe some details of the $\Delta\Psi$ curve. In particular, it overestimates the depth of the dip feature at $865\,\mathrm{cm}^{-1}$. In the following we show for the example of the GAO-2.5 samples that the fitting can be further improved by allowing for an anisotropic mobility of the charge carriers along the out-of-plane and the in-plane directions, *i.e.* $\mu_z \neq \mu_{xy}$. It is well indeed known that the confined electrons at the STO interface may originate from different bands derived from the Ti t_{2g} orbitals which have an anisotropic dispersion behavior. As was discussed in the previous paragraph, the peak of the Berreman mode is governed by the out-of-plane component of the dielectric function to which the electrons in the d_{xz}- and d_{yz}-related bands provide the major contribution since they are dispersive along the z-direction. The contribution of the d_{xy}-related bands is expected to be less important, since their z-axis conductivity arises mainly from transitions between the different subbands [18]. On the other hand, it can be expected that the electrons with d_{xy} character govern the Drude-like response along the in-plane direction which makes a major contribution to the dip feature at $865\,\mathrm{cm}^{-1}$. Figure 3(a) shows the best fit with an anisotropic Drude model, for which the mobility along the in-plane direction, μ_{xy}, was allowed to vary, whereas μ_z and N_s as well as the depth profile where kept fixed at the values obtained with the isotropic model. This anisotropic model provides a better description of the dip feature than the graded isotropic model in fig. 2(a). However, it yields an unreasonably low value of $\mu_{xy} = 5\,\mathrm{cm}^2/\mathrm{Vs}$ in view of the very high mobility that has been deduced from the dc measurements in ref. [10]. As a next step, we therefore allowed for two Drude components to account independently for the out-of-plane response (with $N_{s,z}$, $\mu_z > 0$ and $\mu_{xy} = 0$) and the in-plane response (with $N_{s,xy}$, $\mu_{xy} > 0$ and $\mu_z = 0$), respectively. The parameters $N_{s,xy}$ and μ_{xy} were allowed to vary, whereas $N_{s,z}$ and μ_z as well as the depth profile of

Table 2: Parameters obtained from the best fit to the data of GAO-2.5 using an anisotropic Drude response of the confined charge carriers along the out-of-plane (z) and the in-plane (xy) directions. Details are described in the text.

	N_s (cm^{-2}) for z-direction	N_s (cm^{-2}) for xy-direction	μ_{xy} ($\mathrm{cm}^2/\mathrm{Vs}$)
Single-component model	6.2×10^{13}	–	5
Two-component model	6.2×10^{13}	4.6×10^{13}	> 30

the carrier concentration were fixed to the ones obtained from the isotropic model. The contribution of only the z-component, which has been singled out by setting $\mu_{xy} = 0\,\mathrm{cm}^2/\mathrm{Vs}$, is shown by the red line in fig. 3(b). It confirms that the Berreman mode, *i.e.* the region above the dip where $\Delta\Psi > 0$, is indeed governed by the z-component whereas the in-plane component mainly affects the dip feature. Note that the fitting is not sensitive to the depth profile of the in-plane component. Therefore, we used for the in-plane component a block-like depth profile with a thickness of 7.5 nm. The best fit shown in fig. 3(c) yields a lower in-plane value of $N_{s,xy} = 4.6 \times 10^{13}\,\mathrm{cm}^{-2}$ and a larger mobility of $\mu_{xy} > 30\,\mathrm{cm}^2/\mathrm{Vs}$. According to the discussion in the previous paragraph, the fitting only yields a lower limit for the in plane mobility since it looses sensitivity when the Drude peak becomes too narrow. The fit in fig. 3(c) provides a satisfactory description of the experimental data that could not be significantly improved by allowing additional parameters to vary. A corresponding anisotropic fitting procedure for the LAO/STO heterostructure is not reported here since the broadening of the characteristic features of the Beremann mode, due to the lower electron mobility of LAO/STO, makes the distinction between the out-of-plane and the in-plane components more difficult and rather unreliable.

We have thus obtained the following information about the high-mobility electrons in GAO-2.5. From the analysis of the Berreman mode in the range where $\Delta\Psi > 0$, we derived the parameters of the z-axis component of the response of the carriers with $N_{s,z} = 6.2 \times 10^{13}\,\mathrm{cm}^{-2}$ and $\mu_z = 75\,\mathrm{cm}^2/\mathrm{Vs}$ and determined the shape of the graded depth profile of the carrier concentration which has a thickness of $d = 7.5\,\mathrm{nm}$. In comparison, we have obtained only limited information about the in-plane response. The latter is mostly based on the analysis of the dip feature around $865\,\mathrm{cm}^{-1}$ and yields $N_{s,xy} = 4.6 \times 10^{13}\,\mathrm{cm}^{-2}$ and a lower limit for the in-plane mobility of $\mu_{xy} > 30\,\mathrm{cm}^2/\mathrm{Vs}$ (see table 2). The width and the shape of the depth profile of the carriers that are mobile in the lateral direction along the interface could not be determined. The comparison with the LAO/STO heterostructures thus yields very similar values of N_s and the same characteristic, asymmetric shape of the depth profile. The main difference concerns the somewhat higher mobility of the confined electrons and the reduced thickness of their distribution near the interface. The reduced thickness of the conducting layer likely reflects a somewhat larger magnitude of the confining potential (that is consistent with the slightly larger value of N_s) rather than a reduced strength of the dielectric screening in STO. The latter would require a hardening of the soft mode in STO that results from defects and compressive strain which both are expected to be stronger in LAO/STO than in GAO/STO. The twofold increase of the mobility in GAO/STO, as compared to the one in LAO/STO, is still much smaller than the corresponding increase of the dc mobility as obtained from the transport measurements which amounts to more than an order of magnitude. Furthermore, despite a threefold difference in the dc mobility of the samples GAO-2.5 and GAO-2.75, the mobility values obtained from the analysis of the Berreman mode are comparable. These trends can be understood in terms of the polaronic nature of the electrons in STO which leads to a strong inelastic interaction with the lattice in the frequency range of the Berreman mode. Apparently, this polaronic coupling is less sensitive to defects and strain than the elastic scattering processes that governs the dc mobility.

Summary. – With infrared ellipsometry we have studied the so-called Beremann mode in GAO/STO heterostructures which arises from the itinerant charge carriers that are confined to the interface. We analyzed the Beremann mode with the same model that was previously used in ref. [13] for LAO/STO heterostructures and found that both kinds of samples have a similar sheet carrier densities and asymmetric shapes of the depth profile of the carrier concentration, although the main origin of the confined carriers is supposed to be different, *i.e.* oxygen vacancies in GAO/STO and a polar discontinuity in LAO/STO. The most significant differences concern the mobility of the charge carriers, which is twice higher in GAO/STO, and the thickness of the depth profile of the confined electrons which is somewhat redcued. The stronger carrier confinement in the GAO/STO heterostructure may be the result of a larger confining potential [12]). The observed twofold increase of the mobility deduced from the Berreman mode is still much smaller than the one of the dc mobility which is more than tenfold. This can be understood in terms of a polaronic nature of the confined electrons in STO (similar to the one in bulk STO [22]).

* * *

The work at the University of Fribourg has been supported by the Schweizerische Nationalfonds (SNF)

through the grant No. 200020-153660. The work at Muni was supported by the project CEITEC (CZ.1.05/1.1.00/02.0068). Funding from the Danish Agency for Science, Technology and Innovation (4070-00047B) is also acknowledged.

REFERENCES

[1] Mannhart J. *et al.*, *MRS Bull.*, **33** (2008) 1027.
[2] Cen C. *et al.*, *Science*, **323** (2009) 1026.
[3] Caviglia A. D. *et al.*, *Nature*, **456** (2008) 624.
[4] Willmott P. R. *et al.*, *Phys. Rev. Lett.*, **99** (2007) 155502.
[5] Kalabukhov A. *et al.*, *Phys. Rev. B*, **75** (2007) 121404.
[6] Herranz G. *et al.*, *Sci. Rep.*, **2** (2012) 758.
[7] Chen Y. Z. *et al.*, *Nano Lett.*, **11** (2011) 3774.
[8] Lee S. W. *et al.*, *Nano Lett.*, **12** (2012) 4775.
[9] Liu Z. Q. *et al.*, *Phys. Rev. X*, **3** (2013) 021010.
[10] Chen Y. Z. *et al.*, *Nat. Commun.*, **4** (2013) 1371.
[11] Kormondy K. J. *et al.*, *J. Appl. Phys.*, **117** (2015) 095303.
[12] Schütz P. *et al.*, *Phys. Rev. B*, **91** (2015) 165118.
[13] Dubroka A. *et al.*, *Phys. Rev. Lett.*, **104** (2010) 156807.
[14] Bernhard C. *et al.*, *Thin Solid Films*, **455** (2004) 143.
[15] Kozuka Y. *et al.*, *Phys. Rev. B*, **76** (2007) 085129.
[16] Berreman D. W. *et al.*, *Phys. Rev.*, **130** (1963) 2193.
[17] Humlíček J. *et al.*, *Appl. Phys. Lett.*, **69** (1996) 2581.
[18] Rössle M. *et al.*, *Phys. Rev. B*, **88** (2013) 104110.
[19] Park S. Y. *et al.*, *Phys. Rev. B*, **87** (2013) 205145.
[20] Sing M. *et al.*, *Phys. Rev. Lett.*, **102** (2009) 176805.
[21] Basletic M. *et al.*, *Nat. Mater.*, **7** (2008) 621.
[22] van Mechelen J. L. M. *et al.*, *Phys. Rev. Lett.*, **100** (2008) 226403.

IX

ARTICLE

D. V. Christensen, *et al.*
Electric field control of the γ-Al_2O_3/$SrTiO_3$ interface conductivity at room-temperature
Applied Physics Letters 109, 021602 (2016)

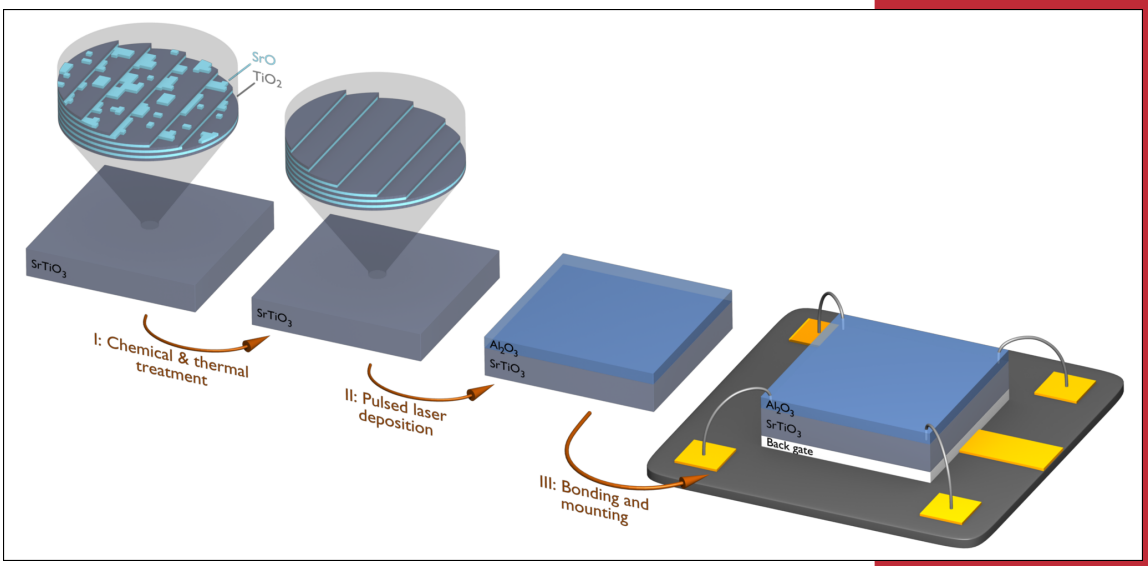

Experimental procedure
Figure: Dennis Valbjørn Christensen

APPLIED PHYSICS LETTERS **109**, 021602 (2016)

Electric field control of the γ-Al_2O_3/$SrTiO_3$ interface conductivity at room temperature

D. V. Christensen,[1,a] F. Trier,[1] M. von Soosten,[1] G. E. D. K. Prawiroatmodjo,[2] T. S. Jespersen,[2] Y. Z. Chen,[1] and N. Pryds[1]
[1]*Department of Energy Conversion and Storage, Technical University of Denmark, Risø Campus, DK-4000 Roskilde, Denmark*
[2]*Niels Bohr Institute, Center for Quantum Devices, University of Copenhagen, DK-2100 Copenhagen Ø, Denmark*

(Received 20 April 2016; accepted 27 June 2016; published online 11 July 2016)

Controlling interfaces using electric fields is at the heart of modern electronics. The discovery of the conducting interface between the two insulating oxides $LaAlO_3$ (LAO) and $SrTiO_3$ (STO) has led to a number of interesting electric field-dependent phenomena. Recently, it was shown that replacing LAO with a spinel γ-Al_2O_3 (GAO) allows a good pseudo-epitaxial film growth and high electron mobility at low temperatures. Here, we show that the GAO/STO interface resistance, similar to LAO/STO, can be tuned by orders of magnitude at room temperature using the electric field of a backgate. The resistance change is non-volatile, bipolar, and can be tuned continuously rather than being a simple on/off switch. Exposure to light significantly changes the capabilities to tune the interface resistance. High- and low-resistive states are obtained by annihilation and creation, respectively, of free *n*-type carriers, and we speculate that electromigration of oxygen vacancies is the origin of the tunability. *Published by AIP Publishing*. [http://dx.doi.org/10.1063/1.4955490]

Controlling interface properties using electric fields is at the heart of modern electronics and fundamental research. In particular, the interface properties between the two band insulators $LaAlO_3$ (LAO) and $SrTiO_3$ (STO) can be controlled dramatically with electric fields: Applying an electric field with a sample-wide backgate can change the sheet resistance reversibly by three orders of magnitude at room temperature,[1,2] whereas applying a voltage on an atomic force microscope tip allows for drawing conducting lines with nanometer widths.[3] At low temperatures, electric fields can induce superconductivity,[4] greatly modify the electronic,[5,6] magnetic,[7] and topographic[6] landscape of the heterostructure, as well as enhance the electron mobility.[8]

In the wake of the pioneering LAO/STO heterostructure, several other STO-based oxide heterostructures have been discovered. In particular, the heterostructure made by depositing Al_2O_3 on the perovskite STO is rather promising. Amorphous Al_2O_3 has previously been deposited on $SrTiO_3$ using, e.g., atomic layer deposition,[9,10] resulting in conducting interfaces. A few studies report an electric field control of these amorphous-Al_2O_3/STO interfaces at room temperature: In Ref. 11, a top-gated field effect transistor was reported, and Ref. 10 briefly considers the change of interface resistance using the electric field from a backgate. However, growing crystalline Al_2O_3 in the spinel γ-phase (GAO) using pulsed laser deposition (PLD) has been demonstrated[12] to result in a superior pseudo-epitaxial growth—even at room temperature[13]—along with an electron mobility exceeding 140 000 $cm^2/V\,s$ at 2 K. As for the case of LAO/STO, the *n*-type conductivity in GAO/STO occurs through the 3*d* states of the titanium ions on the STO side near the interface,[12] and the two systems are expected to share electronic properties. To date, however, this potential of GAO/STO remains unexplored.

Here, we report the electric field control of the GAO/STO interface using a sample-wide backgate. The electric field control occurs at room temperature, is highly light sensitive, and shows similarities to previous reports on LAO/STO.[14]

Crystalline GAO/STO heterostructures were grown by PLD on TiO_2-terminated STO substrates, which were prepared by first immersing STO in water (20 min at 70 °C)[15] followed by selective etching in an acid solution (H_2O:HCl:HNO_3 = 16:3:1, 20 min at 70 °C).[16] The substrates were then annealed at 1000 °C for 1 h in 1 bar pure oxygen. Thin films of GAO (0–5 unit cells) were deposited on STO at 650 °C using PLD with a 248 nm KrF laser operating at 1 Hz and a fluency of ~3.5 J/cm^2. The growth rate was determined by reflective high-energy electron diffraction (RHEED) with 4 oscillations corresponding to the growth of 1 unit cell GAO (0.8 nm),[12] thus allowing for sub-unit cell control of the GAO thickness. The heating, deposition, and cooling of the samples were performed at a background oxygen pressure of 10^{-5} mbar without the post-annealing step, which is often used to reduce oxygen vacancies in STO.[17] The samples were mounted with conductive silver paste on a chip carrier with a sample-wide gold backgate where a voltage can be applied relative to the interface. Ultrasonic wedge bonding of 20 μm thick aluminum wires was used to contact the interface electrically in the van der Pauw geometry, allowing for the sheet resistance, carrier density, and mobility to be determined (see Figure 1(a)). Reproducible but nonlinear current/voltage (*I*/*V*)-curves were observed for some samples with high sheet resistance ($\gg$1 MΩ/sq) due to a resistance change induced by the probing voltage applied

[a]Author to whom correspondence should be addressed. Electronic mail: dechr@dtu.dk

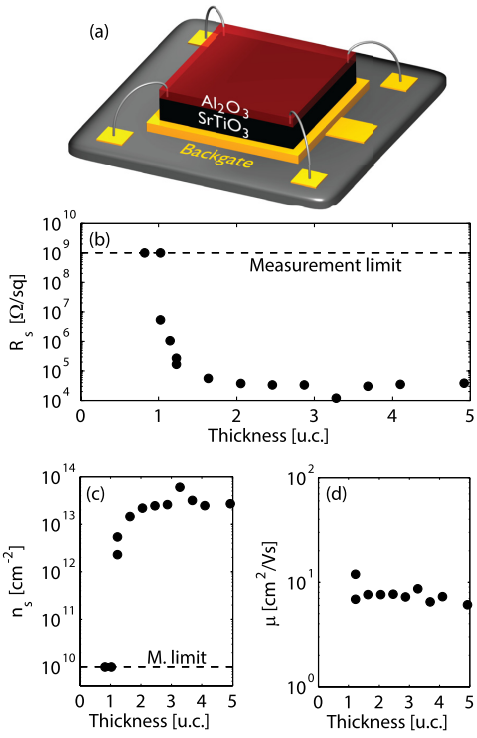

FIG. 1. (a) Schematic figure of the sample. (b) The sheet resistance (R_s) of the γ-Al_2O_3/$SrTiO_3$ heterostructure as a function of the thickness of the γ-Al_2O_3 layer reveals a critical thickness of ~1.5 unit cells above which the heterostructure becomes conducting. The conductivity is accompanied with an increase in (c) the free carrier density, n_s, whereas (d) the carrier mobility, μ, stays largely constant.

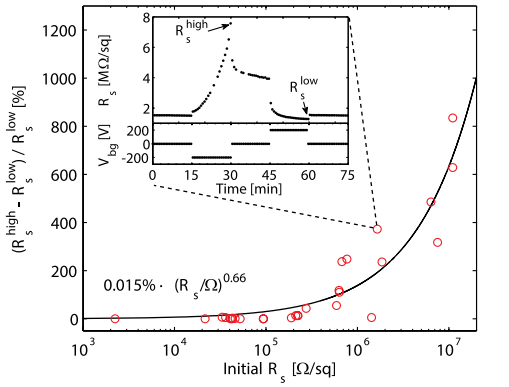

FIG. 2. The relative change between high- and low-resistive states ($R_s^{high} - R_s^{low}$)/R_s^{low} as a function of the initial sheet resistance (R_s) for a number of samples. The dependence roughly follows a power law. The inset shows the change of the interface sheet resistance between high and low-resistive states for a typical sample when changing the backgate potential from $V_{bg} = 0$ V → −200 V → 0 V → 200 V → 0 V with each voltage applied for 15 min. All samples have been measured with the same backgate profile.

along the interface. In the following, we focus on the change in the resistance induced solely by the backgate potential and only report results with linear *I*/*V*-curves. When not noted otherwise, the samples were stored in darkness for >24 hours before measurements, and the leakage current through the 0.5 mm thick STO was at least two orders of magnitude smaller than the probing current applied to the interface.

Deposition of less than ~1.5 unit cells (1.2 nm) of GAO on STO resulted in insulating heterostructures (Figure 1). Metallically conducting interfaces were induced when exceeding the 1.5 u.c. critical thickness of GAO as a result of introducing free *n*-type carriers at the interface. By carefully varying the deposited thickness, the sheet resistance can be controlled by several orders of magnitude. For samples with low sheet resistance (<500 kΩ/sq), no or very limited resistive switching is observed (Figure 2). For heterostructures with high resistances, the interface can generally be turned into a more conductive state by applying a positive backgate potential (V_{bg}) at room temperature (see inset of Figure 2) without an electroforming process, which is often needed for enabling resistive switching.[18] Setting $V_{bg} < 0$ V drives the interface into a high-resistive state, thus qualifying it as being a bipolar change in conductance.

The change in the resistance has generally both a volatile and nonvolatile component: The volatile component changes the resistance faster than the data acquisition rate used here and is observed as a sudden jump in the sheet resistance in the inset of Figure 2 when the backgate potential is turned on or off. The fast change suggests that the volatile component is purely electronic in character, i.e., an accumulation or a depletion of electrons induced by the backgate. The non-volatile component is observed as a slower change in the resistance both when the backgate potential is turned on and off. In particular, it ensures that a sample placed in a high- or low-resistive state by the backgate potential remains in that state for several hours after returning to $V_{bg} = 0$ V. This is apparent from the inset of Figure 2 and emphasized in Figure S1 in the supplementary material[19] where the high- or low-resistive states are still separable 16 h after setting $V_{bg} = 0$ V. The non-volatile decay in GAO/STO can be described by a superposition of two exponential functions with a slow (~250–300 min) and medium slow (~30–45 min) time constant (Figure S1[19]), revealing that non-volatile decays are composed of two coexisting processes with different time constants. This is different from reports[2] on amorphous LAO grown at room temperature on STO where the decay in a similar setup followed a single exponential function with decay rates of 10–30 min. Previous reports on amorphous-Al_2O_3/STO do not allow for such a comparison.[10,11]

Although a sizeable sample-to-sample variation is observed (Figure 2), which probably stems from the extreme sensitivity of the interface conductivity to GAO thicknesses close to the critical thickness, cycling the backgate potential periodically for a *single* sample can result in remarkably consistent results. An example of this is shown in Figure 3 where a $V_{bg} = 0$ V → −200 V → 0 V → 200 V cycle is repeated for more than a week with each backgate voltage applied for 15 min. A significant separation between the low-resistive (1.5 ± 0.5 MΩ/sq) and high-resistive (11.0 ± 1.1 MΩ/sq)

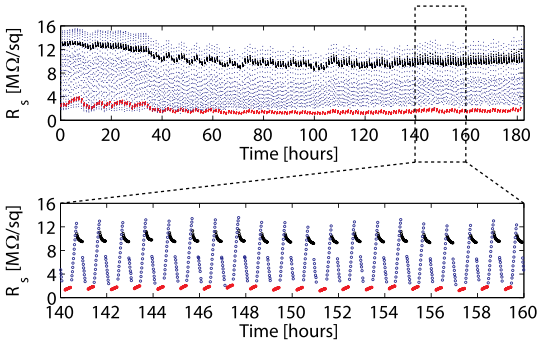

FIG. 3. The sheet resistance is measured when cycling the backgate potential using 0 V → −200 V → 0 V → 200 V with each step lasting 15 min. The lower panel shows a highlight of a selected part. The quasi-stable high- and low-resistive states obtained when returning to $V_{bg} = 0$ V after applying ±200 V are marked with black and red, respectively.

states is observed in all 180 cycles with the mean value of the high-resistive states being more than 17 standard deviations away from the low-resistive state. Continuous cycling of the interface resistance gradually results in more self-consistent results (see Figure 3) as it decreases the hysteresis observed especially in virgin samples.

A continuum of resistive states rather than simple on and off states is obtainable by controlling the backgate potential or the duration at which the field is applied. Varying the backgate potential results in an exponential change of the interface conductance where several resistive states can be obtained (Figure 4(a)). Measuring noise-free Hall resistances in high-resistive samples during the application of an electric field is challenging, but the trends reveal that a change in the conductance (ΔG_s) is a result of a change in carrier density (Δn_s) rather than mobility. A simple capacitive charging of the interface would then entail a fast change in the carrier density that is approximately linear with the backgate potential as $\Delta G_s \propto \Delta n_s = \Delta V_{bg} C/e$, with $C \approx 5\,\mu\text{F/m}^2$ being the parallel plate capacitance per unit area and e being the elementary charge. Contrary to this, the exponential relationship observed here points towards the electric field lowering the energy of the activation barrier that needs to be overcome to enable the change in the resistance. An example of using the duration at which the backgate potential is applied to achieve a continuum of resistive states is shown in Figure 4(b). The continuous application of $V_{bg} = -200$ V increases the sample resistance by more than three orders of magnitude from $\sim 10^6$ to 10^9 Ω/sq in 1.5 h. Subsequent application of +200 V on the backgate returns the sample into a low-resistive state with a sheet resistance slightly lower than the initial state. Previous reports on LAO/STO traces the sheet resistance with applied gate using either a single exponential[2] or a Curie-von Schweidler law.[14] The latter is used[14] to describe a change in the resistance that requires overcoming a distribution of energy barriers rather than a single energy barrier, but here neither can be used to fit the results.

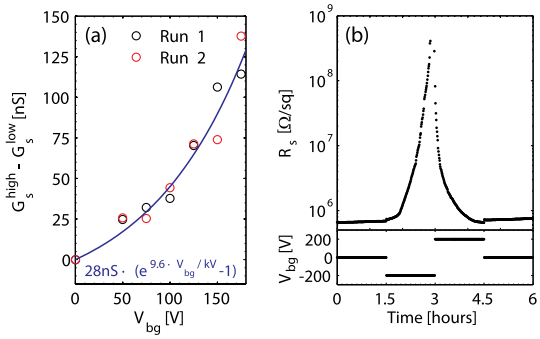

FIG. 4. (a) The backgate potential was varied in steps from $V_{bg} = 0$ to 180 V by cycling the backgate potential 5 times for each V_{bg} using the profile 0 V → $-V_{bg}$ → 0 V → $+V_{bg}$ with one cycle lasting 60 min. The conductance difference between the high- and low-conductive states ($G_s^{high} - G_s^{low}$) was extracted from the fifth cycle for each V_{bg} to reduce the effect of hysteresis. The set of measurements was repeated to verify consistency (run 1 and 2), and all data were fitted with an exponential function, $G_s^{high} - G_s^{low} = 28$ nS × (exp (9.6 × V_{bg} kV^{-1}) − 1). (b) Applying the backgate potential for longer times (here 1.5 h) results in a continuous resistance change of more than 3 orders of magnitude. Data points with non-linear *I*/*V*-curves occurring frequently in the highly insulating state (≫0.1 GΩ/sq) are not shown.

High-resistive GAO/STO interfaces are found to be light sensitive with a proof-of-concept shown in Figure 5 using the light of a fluorescent tube. When exposing the sample to the white light during a switching sequence, three distinct features are observed: First, the sheet resistance with $V_{bg} = 0$ V decreases from 230 to 130 kΩ/sq. After the sample is returned to a dark environment, the sample resistance is returned to its initial level after around 2 hours. This is consistent with the persistent photoinduced carriers observed in LAO/STO.[20,21] Second, the relative resistive switching between the high and low resistive states decreases from $(R_s^{high} - R_s^{low})/R_s^{low} = 3$ to

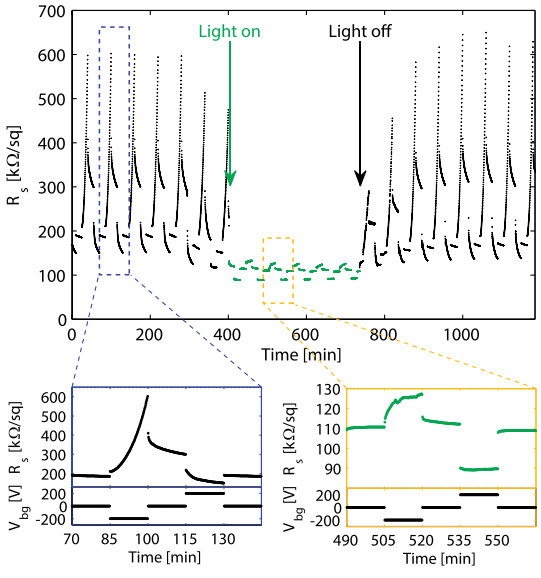

FIG. 5. Cycling the backgate potential using $V_{bg} = 0$ V → −200 V → 0 V → 200 V with each step lasting 15 min reveals that both the sheet resistance (R_s) and its resistive switching capabilities are very dependent on whether the sample is placed in the dark or in light. A slight leakage of light occurred when preparing to expose the sample to light, which is observed as a small drop in resistance seen between 300 min and 400 min. The lower panel highlights a single cycle without and with the sample exposed to light.

0.4. As the sample becomes more conducting when exposed to light, a decrease in the resistive switching abilities is expected (Figure 2). Third, the changes in resistance in a dark environment are non-volatile, whereas the changes are highly accelerated in light and reach saturation within several minutes (Figure 5).

The combined effect of light and a backgate potential has previously been reported for LAO/STO,[14] where the response to the backgate was also observed to be slow in the dark and much faster during illumination. Contrary to what is observed here, the relative resistance change was enhanced due to the high-resistive state becoming more resistive mainly as a result of a pronounced lowering of the carrier mobility. The authors found a threshold energy ($\sim$1.4 eV) needed for the light enhanced gating effect, which matches oxygen vacancy in-gap states in STO, and attributed the resistance change to an illumination-accelerated electromigration of oxygen vacancies.

Several studies relate the resistive switching in STO-based structures to an electromigration of oxygen vacancies.[2,14,18,22] The resistive switching observed here is qualitatively very similar to that observed in other STO based heterostructures, suggesting the same underlying mechanism in GAO/STO. This is consistent with the non-volatile character, non-linear backgate response, and large sample-to-sample variation. In this picture, $V_{bg} > 0$ V drives oxygen vacancies towards the GAO/STO interface, where the electric field lines terminate, leading to a high local concentration of oxygen vacancies and a high conductivity. By setting $V_{bg} = 0$ V, the oxygen vacancies slowly migrate back to a quasi-equilibrium state. The migration can be accelerated by applying $V_{bg} < 0$ V, which dilutes the oxygen vacancies at the interface and results in a high-resistive state. The migration pathways of the oxygen vacancies may not be fully reversible resulting in the observed hysteresis. The top film primarily serves as an oxygen absorber during the PLD in order to achieve the right concentration of oxygen vacancies in STO. The criteria for designing conducting STO-based interfaces, by creating oxygen vacancies in STO via redox reactions with the top film,[23] are thus also expected to be applicable for creating interfaces with resistive switching properties. Replacing GAO with yttrium-stabilized zirconia (YSZ),[22] $CaHfO_3$,[24] or STO[22] is thus predicted to yield interfaces with a similar possibility to change resistances with electric fields. Some detailed differences may, however, exist due to the different top layers, leading to possible differences in the kinetics and energetics of the oxygen vacancies located right at the interface. In particular, previous annealing experiments on GAO/STO suggest that oxygen vacancies are stabilized at the interface.[12] Two different time constants may thus be expected corresponding to electromigration of oxygen vacancies, which are located at the interface or deeper into STO, consistent with the two time constants observed during the decay in Figure S1.[19] The second time constant may also arise from other sources such as a difference in strain and dislocations when growing GAO instead of amorphous LAO.

The γ-Al_2O_3/$SrTiO_3$ interface has been shown to exhibit a clear change in the resistance over several orders of magnitude when a potential is applied on the backgate. Preparing the interface to have a high, initial resistance greatly enhances the resistive switching capabilities. A range of similarities to the resistive switching in LAO/STO is observed, but a closer analysis reveals differences such as a dual-component retention compared to the single-exponential retention observed for amorphous-LAO/STO.

[1]S. Thiel, G. Hammerl, A. Schmehl, C. W. Schneider, and J. Manhart, Science **313**, 1942 (2006).
[2]D. V. Christensen, F. Trier, Y. Z. Chen, A. Smith, J. Nygård, and N. Pryds, Appl. Phys. Lett. **102**, 021602 (2013).
[3]C. Cen, S. Thiel, G. Hammerl, C. W. Schneider, K. E. Andersen, C. S. Hellberg, J. Mannhart, and J. Levy, Nat. Mater. **7**, 298 (2008).
[4]A. D. Caviglia, S. Gariglio, N. Reyren, D. Jaccard, T. Schneider, M. Gabay, S. Thiel, G. Hammerl, J. Mannhart, and J.-M. Triscone, Nature **456**, 624 (2008).
[5]B. Kalisky, E. M. Spanton, H. Noad, J. R. Kirtley, K. C. Nowack, C. Bell, H. K. Sato, M. Hosoda, Y. Xie, Y. Hikita, C. Woltmann, G. Pfanzelt, R. Jany, C. Richter, H. Y. Hwang, J. Mannhart, and K. A. Moler, Nat. Mater. **12**, 1091 (2013).
[6]M. Honig, J. A. Sulpizio, J. Drori, A. Joshua, E. Zeldov, and S. Ilani, Nat. Mater. **12**, 1112 (2013).
[7]F. Bi, M. Huang, S. Ryu, H. Lee, C.-W. Bark, C.-B. Eom, P. Irvin, and J. Levy, Nat. Commun. **5**, 5019 (2014).
[8]C. Bell, S. Harashima, Y. Kozuka, M. Kim, B. G. Kim, Y. Hikita, and H. Y. Hwang, Phys. Rev. Lett. **103**, 226802 (2009).
[9]S. W. Lee, Y. Liu, J. Heo, and R. G. Gordon, Nano Lett. **12**, 4775 (2012).
[10]J. Delahaye and T. Grenet, J. Phys. D: Appl. Phys. **45**, 315301 (2012).
[11]K. Ueno, I. H. Inoue, H. Akoh, M. Kawasaki, Y. Tokura, and H. Takagi, Appl. Phys. Lett. **83**, 1755 (2003).
[12]Y. Z. Chen, N. Bovet, F. Trier, D. V. Christensen, F. M. Qu, N. H. Andersen, T. Kasama, W. Zhang, R. Giraud, J. Dufouleur, T. S. Jespersen, J. R. Sun, A. Smith, J. Nygård, L. Lu, B. Büchner, B. G. Shen, S. Linderoth, and N. Pryds, Nat. Commun. **4**, 1371 (2013).
[13]Y. Z. Chen, N. Bovet, T. Kasama, W. W. Gao, S. Yazdi, C. Ma, N. Pryds, and S. Linderoth, Adv. Mater. **26**, 1462 (2014).
[14]Y. Lei, Y. Li, Y. Z. Chen, Y. W. Xie, Y. S. Chen, S. H. Wang, J. Wang, B. G. Shen, N. Pryds, H. Y. Hwang, and J. R. Sun, Nat. Commun. **5**, 5554 (2014).
[15]G. Koster, B. Kropman, G. Rijnders, D. Blank, and H. Rogalla, Appl. Phys. Lett. **73**, 2920 (1998).
[16]M. Kareev, S. Prosandeev, J. Liu, C. Gan, A. Kareev, J. W. Freeland, M. Xiao, and J. Chakhalian, Appl. Phys. Lett. **93**, 061909 (2008).
[17]Z. Q. Liu, L. Sun, Z. Huang, C. J. Li, S. W. Zeng, K. Han, W. M. Lü, T. Venkatesan, and Ariando, J. Appl. Phys **115**, 054303 (2014).
[18]R. Waser and M. Aono, Nat. Mater. **6**, 833 (2007).
[19]See supplementary material at http://dx.doi.org/10.1063/1.4955490 for details and fitting of the decays of the high- and low-resistive state.
[20]A. Tebano, E. Fabbri, D. Pergolesi, G. Balestrino, and E. Traversa, ACS Nano **6**, 1278 (2012).
[21]H.-L. Lu, Z.-M. Liao, L. Zhang, W.-T. Yuan, Y. Wang, X.-M. Ma, and D.-P. Yu, Sci. Rep. **3**, 2870 (2013).
[22]K. Szot, W. Speier, G. Bihlmayer, and R. Waser, Nat. Mater. **5**, 312 (2006).
[23]Y. Z. Chen, N. Pryds, J. E. Kleibeuker, G. Koster, J. Sun, E. Stamate, B. Shen, G. Rijnders, and S. Linderoth, Nano Lett. **11**, 3774 (2011).
[24]K. Shibuya, T. Ohnishi, M. Lippmaa, and M. Oshima, Appl. Phys. Lett. **91**, 232106 (2007).

Electric field control of the γ-Al_2O_3/$SrTiO_3$ interface conductivity at room temperature

Supplementary Material

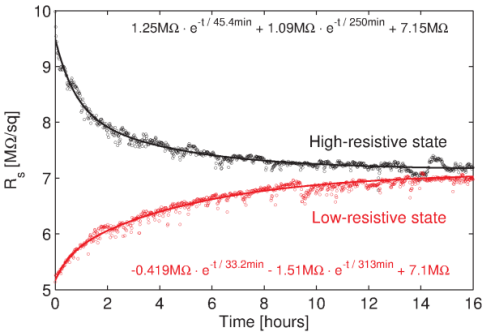

Figure S1: The backgate potential was cycled 8 times to reduce hysteresis using the profile V_{bg} = 0 V → -200 V → 0 V → 200 V with each step lasting 10 min. The 8 periods ended with either -200V or +200V applied at the backgate, and the high-resistive (black) or low-resistive (red) state was hereafter left decaying with V_{bg} = 0 V while measuring the sheet resistance (R_s). Linear least square fits using summed exponential decays are shown as solid lines.

XII

ARTICLE

F. Gunkel, S. Hoffmann-Eifert, R. A. Heinen, **D. V. Christensen** *et al.*
Thermodynamic Ground States of Complex Oxide Heterointerfaces
ACS Applied Materials and Interfaces 9, 1086 (2017)

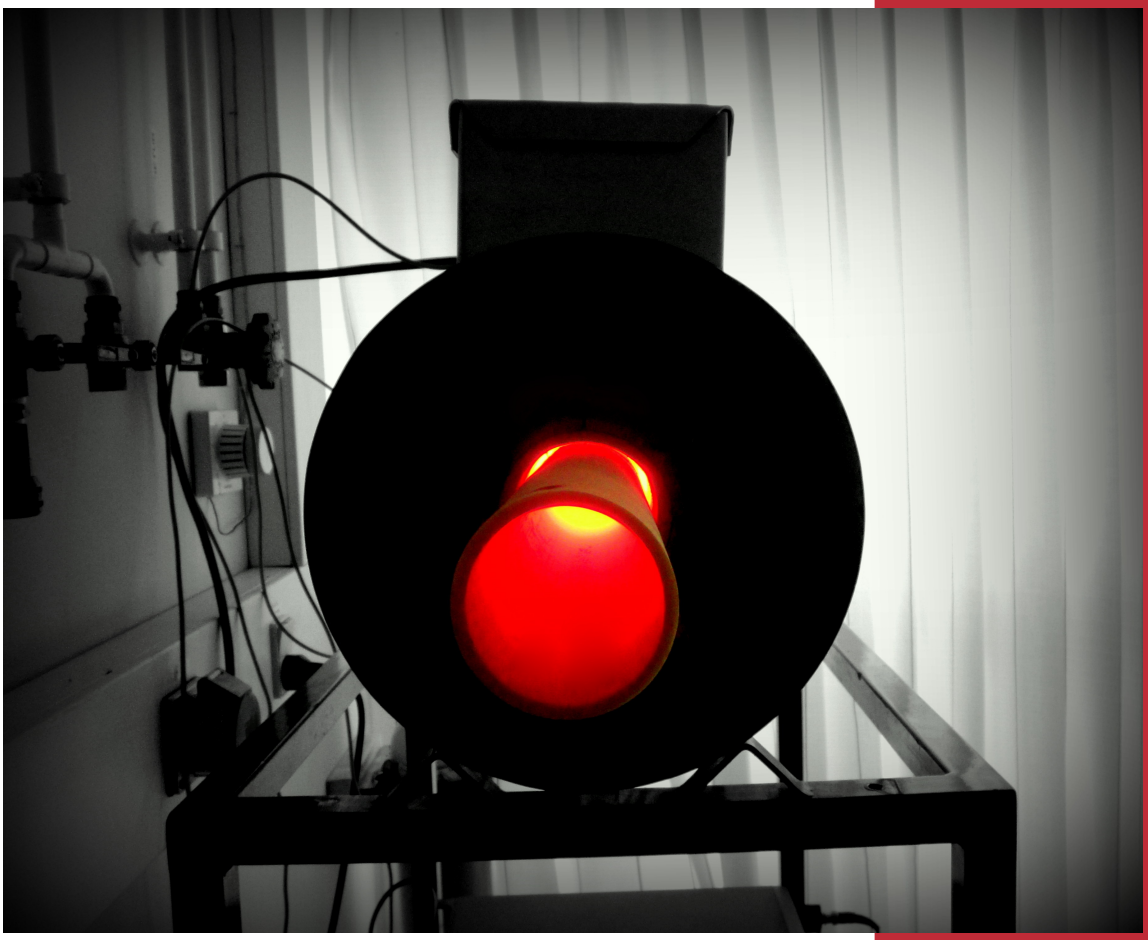

Heated tube furnace
Photo: Dennis Valbjørn Christensen

ACS APPLIED MATERIALS & INTERFACES

Research Article

www.acsami.org

Thermodynamic Ground States of Complex Oxide Heterointerfaces

F. Gunkel,*[,†] S. Hoffmann-Eifert,[‡] R. A. Heinen,[‡] D. V. Christensen,[§] Y. Z. Chen,[§] N. Pryds,[§] R. Waser,[‡] and R. Dittmann[‡]

[†]Institute of Electronic Materials, IWE2, RWTH Aachen University, 52056 Aachen, Germany

[‡]Peter Gruenberg Institute and JARA-FIT, Forschungszentrum Juelich GmbH, 52425 Juelich, Germany

[§]Department of Energy Conversion and Storage, Technical University of Denmark, Risø Campus, 4000 Roskilde, Denmark

ABSTRACT: The formation mechanism of 2-dimensional electron gases (2DEGs) at heterointerfaces between nominally insulating oxides is addressed with a thermodynamical approach. We provide a comprehensive analysis of the thermodynamic ground states of various 2DEG systems directly probed in high temperature equilibrium conductivity measurements. We unambiguously identify two distinct classes of oxide heterostructures: For epitaxial perovskite/perovskite heterointerfaces ($LaAlO_3/SrTiO_3$, $NdGaO_3/SrTiO_3$, and $(La,Sr)(Al,Ta)O_3/SrTiO_3$), we find the 2DEG formation being based on charge transfer into the interface, stabilized by the electric field in the space charge region. In contrast, for amorphous $LaAlO_3/SrTiO_3$ and epitaxial γ-$Al_2O_3/SrTiO_3$ heterostructures, the 2DEG formation mainly relies on the formation and accumulation of oxygen vacancies. This class of 2DEG structures exhibits an unstable interface reconstruction associated with a quenched nonequilibrium state.

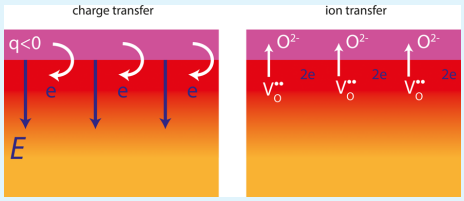

KEYWORDS: *oxide heterointerfaces, 2DEG, defect-chemistry, thermodynamics, interface chemistry*

1. INTRODUCTION

Two-dimensional electron gases (2DEGs) in oxide heterostructures have attracted a significant amount of attention in recent years.[1,2] In particular, the 2DEG at the $LaAlO_3/SrTiO_3$ (LAO/STO) interface has been studied extensively.[3−6] Meanwhile, various material systems including other epitaxial (epi-) perovskite/perovskite interfaces (e.g., $NdGaO_3$/STO (NGO/STO), $LaGaO_3$/STO, etc.),[7−11] amorphous-oxide/perovskite interfaces,[12−14] spinel/perovskite interfaces (γ-Al_2O_3/STO (GAO/STO)),[15] as well as reactive metal/STO interfaces[16,17] have been found to show a similar electron gas. Some of these 2DEGs even seem to exhibit properties superior to the standard LAO/STO case, in particular, enhanced electron mobility.[11,15,18]

Conduction in the prototypical epi-LAO/STO has been ascribed to an interface reconstruction forced by the polarity mismatch occurring at the epitaxial interface of these two materials.[4] In contrast, such a mismatch is absent in the amorphous-LAO/STO (a-LAO/STO) system as it lacks a macroscopic ionic order in the amorphous LAO layer. The apparent contradiction in the fact that both of these systems show an interfacial 2DEG with rather similar properties (in fact, the two systems are often not distinguishable in room temperature electrical measurements) has led to an extensive debate on whether or not the 2DEG formations in all these systems are of a similar nature. It is highly debated if all these oxide heterointerface systems share a similar driving force for 2DEG formation, or if they have to be separated into categories of 2DEGs with fundamentally different chemistry at the interface. If so, it furthermore needs to be clarified how any presumed differences affect the electrical performance of such 2DEG systems.

Here, we tackle these fundamental considerations for various complex oxide interfaces in a direct thermodynamic approach. For this, we directly probe the thermodynamic equilibrium states of oxide heterointerfaces by measuring their conduction contribution at high temperatures ($T \gtrsim 850$ K, allowing thermodynamic equilibration) as a function of oxygen partial pressure (pO_2). Under experimental conditions, the samples are in their electronic-ionic configuration of minimum Gibbs' energy, thus disclosing the fundamental thermodynamic ground states of the system, determined by thermodynamic bounds such as temperature T, oxygen pressure pO_2, and electric field E (Figure 1a). Here, we presume that a thermodynamic ensemble approaches a unique thermodynamic equilibrium state, fully determined at a given temperature and oxygen pressure (Figure 1a). These equilibrium states can in general be probed in a reversible manner; i.e., the same thermodynamic ground state is obtained at a given T, pO_2, and E independent of the history of the sample. In this way, the thermodynamic approach allows us to uncover fundamental sample properties in the absence of nonequilibrium defect contributions, e.g., due to a growth-induced substrate reduction, potentially affecting low temperature measurements. The high temperature equilibrium conductance (HTEC) yields information about the thermal stability of interface reconstruction and 2DEG formation, as

Received: October 6, 2016
Accepted: December 6, 2016
Published: December 6, 2016

DOI: 10.1021/acsami.6b12706
ACS Appl. Mater. Interfaces 2017, 9, 1086−1092

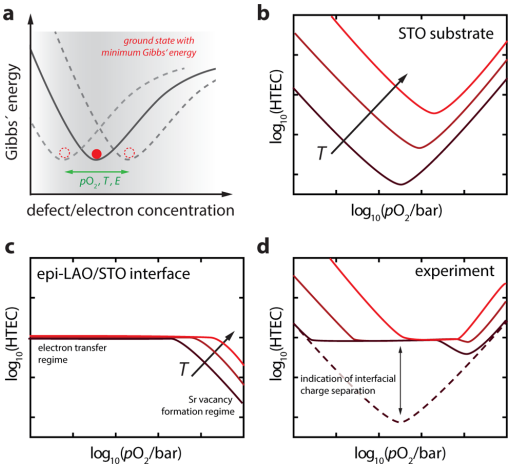

Figure 1. (a) Under experimental conditions, the heterostructure relaxes into the ionic-electronic state of minimum Gibbs' energy determined by external thermodynamic bounds such as temperature T, oxygen pressure pO_2, and electric field E. As a result, the system adjusts the concentration of charge carriers yielding a characteristic HTEC. Schematic illustration (b) of HTEC characteristics of undoped STO single crystals, (c) of the n-type epi-LAO/STO interface, and (d) of the resulting superposition of both characteristics for epi-LAO/STO heterostructure.

well as information about the specific defect structure and chemistry established at a specific interface.[19−21]

At the heart of this experimental approach is the 4-point measurement of the sample's conductance while it is kept in equilibrium with the ambient atmosphere. Typically, high temperatures are supplied in a tube furnace in the range of 850 and 1150 K. The oxygen partial pressure is controlled chemically by actively pumping oxygen in the vicinity of the sample using a yttria-stabilized ZrO_2 oxygen pump. The actual pO_2 is measured by the Nernst potential between sample space and reference atmosphere (air). Technical details regarding the experimental setup can be found in ref 22.

Using this method, we quantify the charge separation emerging in different 2DEG systems in their thermodynamic ground state. We reveal two distinct categories of 2DEG systems, one based on charge transfer driven by electrostatics, and the other based on the formation of excess oxygen vacancies in a kinetically quenched state.

2. RESULTS

The HTEC characteristics of standard epi-LAO/STO heterostructures have been discussed in detail in previous studies.[20,21] Here, we first address the specific impact of growth conditions and layer thickness and then compare the behavior of LAO/STO to those of other complex oxide heterointerfaces. In this way, we are able to reveal the fundamental differences in their conduction behavior and to classify and categorize them with respect to their inherent thermodynamic ground states.

The standard LAO/STO heterointerface is characterized by a thermodynamically stable conductance contribution observable in thermodynamic equilibrium. The total HTEC signal measured for such samples is the superposition of a substrate contribution and the actual interface contribution. The substrate's equilibrium conductivity as a function of pO_2 is determined by the exchange of oxygen between (inherently acceptor-doped) STO and the ambient atmosphere associated with the formation and annihilation of oxygen vacancies.[23] It is characterized by electronic conductivity in reducing conditions, and hole conductivity resulting from band gap excitation in oxidizing conditions. This yields the "V"-shaped conductance characteristic sketched in Figure 1b and discussed well in the literature.[21,24] The interface contribution sketched in Figure 1c exhibits a temperature and pO_2 independent conductance in reducing and moderately oxidizing conditions resulting from electrons being transferred into the interface. In the high pO_2 region, one observes temperature-activated conduction behavior with reduced 2DEG electron density[20] due to the formation of Sr vacancies, becoming the favored charge compensation mechanism in the interface region under these conditions.[19] This ionic charge compensation occurs as a kink in the conductance characteristics,[20] so that the interface signature is not entirely flat in oxidizing conditions (Figure 1c). Hence, from the thermodynamic view, the negative charge transferred into the interface can not only be provided by electrons, but also by ionic defects, in particular Sr vacancies, which provide a negative net charge. (Other ionic defects such as Ti vacancies or Al−Ti-antisite defects may also contribute with a negative net charge. However, their formation is typically hindered by the slow formation kinetics in the investigated temperature regime.[24])

The total measurement signal observed in the experiment refers to the sum of substrate contribution and interface contribution, as sketched in Figure 1d.[20,21] Here, the pO_2 independent region observed at intermediate pO_2 can be identified with electron transfer from the LAO layer into the STO side of the interface.[19−21] (Note that rare-earth doping of STO may result in a similar HTEC signature. However, as we will elaborate, this scenario is unlikely on the basis of the results of this study.) The magnitude of the conductance contribution in this pO_2 region is expected to scale with the amount of charge separated at the interface.

We use this specific interface signature observed in the intermediate pressure range (Figure 1d) as a direct probe of a thermodynamic ground state that involves thermodynamically stable charge separation across the interface.[19] For the sake of clarity, we will limit our discussion on data obtained at a single temperature of 950 K (a typical temperature for fabricating perovskite/perovskite heterointerfaces). Temperature dependent measurements as discussed in previous studies[19−21] reveal consistent results.

Figure 2 shows experimental data obtained for epi-LAO/STO heterostructures with a layer thickness below and above the critical thickness of four unit cells of LAO. Below the critical thickness (here, *three* unit cells of LAO on STO), the LAO/STO heterostructure shows an HTEC characteristic which is identical to the characteristic of an STO single crystal (cf. Figure 1b). Hence, below the critical thickness there is no signature of a thermally stable interface reconstruction proving that only negligible charge separation has occurred. In contrast, above the critical thickness, the behavior of LAO/STO (denoted as "standard") reproduces the behavior sketched in Figure 1d indicating that significant charge separation has occurred at the interface and that this separation is sustained in thermodynamic equilibrium. Hence, the thermodynamic ground states (i.e., the ionic-electronic configuration of minimum Gibbs' energy) change abruptly as the layer thickness

DOI: 10.1021/acsami.6b12706
ACS Appl. Mater. Interfaces 2017, 9, 1086−1092

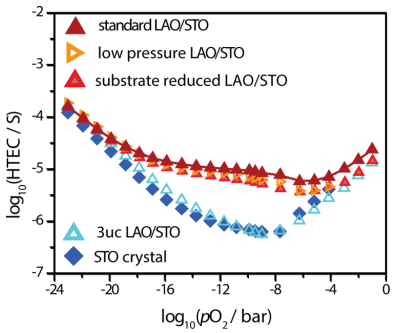

Figure 2. HTEC characteristics obtained at 950 K for epi-LAO/STO above the critical thickness grown at various deposition pressures, as well as for epi-LAO/STO below the critical layer thickness for 2DEG formation. Additionally, we plot the HTEC data obtained for a bare STO substrate reference.

crosses four unit cells. This result indicates a sudden appearance of charge transfer appearing only above this critical thickness. In other words, below four unit cells no charge transfer occurs across the interface, corresponding to zero electric field at the interface penetrating into the STO, yielding a bulk-like ground state of the heterostructure. Above this critical layer thickness, charge is transferred across the interface, in spontaneous response to the increased built-in potential within the polar LAO layer.[4] As a result, a nonzero electric field is established on the STO side of the interface, according to Gauss' law,[19] resulting in the appearance of a thermally stable interface signature in the HTEC experiment. In accordance, we observe similar HTEC behavior for different LAO layer thicknesses above four unit cells. The HTEC results are in good agreement with the behavior observed for epitaxial LAO/STO heterostructures at low temperature.[5] The sudden appearance of the interface signature observed in the HTEC experiment hence refers to a sudden change of E at the interface, yielding a significantly different thermodynamic ground state when traversing the critical layer thickness. On this basis, the HTEC measurements are capable of identifying (and quantifying) the amount of charge transferred into (and separated at) the interface of oxide heterostructures, by comparing the interface conduction contribution with respect to the standard epi-LAO/STO heterostructure (charge transfer $\gtrsim 1 \times 10^{14}$ e/cm^2, as elaborated in ref 20) and the STO single crystal (zero charge transfer).

In Figure 2, we additionally display the HTEC characteristics of epi-LAO/STO heterostructures (above the critical thickness) obtained at different growth conditions. More specifically, we compare the characteristics of samples grown at growth pressures of 1×10^{-3} mbar ("standard") and 4×10^{-5} mbar ("low pressure"), as well as that of a sample grown at even a lower growth pressure of 1×10^{-5} mbar, which clearly shows bulk conductivity arising from a strong reduction of the STO single crystal substrate (i.e., $n_s \approx 1 \times 10^{17}$ cm^{-2}) during growth ("substrate reduced"). While such samples show tremendously different transport behavior at low temperatures,[25−27] the thermodynamic equilibrium experiments reveal a very similar behavior with comparable interface conduction contributions for all of these samples. Judging from the HTEC behavior, this suggest that the charge transfer in all these crystalline samples is the same, independent of the actual growth pressure. In fact, in thermodynamic equilibrium, crystalline interfaces established at different growth conditions seem to be essentially identical (as far as the growth conditions result in a defined growth mode and sufficient crystallinity to allow for a 2DEG formation at all). Even samples that were strongly (bulk-)reduced after the growth establish the same interface signature as samples grown at higher oxygen pressures. Hence, the additional bulk conduction observed at low temperature in such samples is the result of a nonequilibrium process leading to an oxygen-deficient STO substrate during growth. Upon relaxation into thermodynamic equilibrium, this conduction path cancels, while the generic signature of the interface is maintained. Remarkably, the generic interface signatures of all these crystalline LAO/STO samples overlap on a single line. Thus, differences in transport behavior (observed at low temperature)[25−27] are associated with varying thermodynamic states of one and the same generic structure, characterized by a specific ionic defect configuration (that varies with ambient atmosphere, cf. ref 19 and Figure 1a). [Moreover, this explains why differently *annealed* LAO/STO samples show (to a great extent) similar behavior to that of LAO/STO heterostructures *grown* at different pO_2.[26]]

We now turn to alternative material systems other than LAO/STO that show similar 2DEG properties at low temperatures. (Room temperature carrier densities of all samples will be summarized later on.) Figure 3a shows the HTEC characteristics obtained for an NGO/STO hetero-

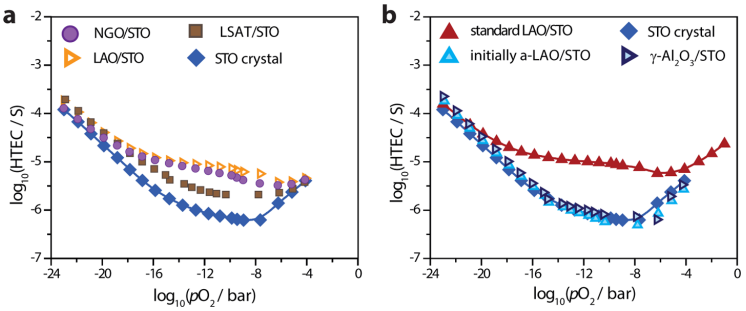

Figure 3. HTEC characteristics at 950 K obtained for (a) epitaxial NGO/STO and LSAT/STO heterostructures and (b) amorphous LAO/STO and epitaxial GAO/STO. For comparison, we plot in both panels data obtained for the STO substrate reference as well as for standard epi-LAO/STO.

DOI: 10.1021/acsami.6b12706
ACS Appl. Mater. Interfaces 2017, 9, 1086−1092

structure in comparison to those of LAO/STO. Both characteristics are remarkably similar (in fact, they almost match), indicating that the generic interface signatures of both systems and thus their thermodynamic ground states established under experimental conditions are the same. The interface reconstruction driven by LAO deposition and the one driven by NGO deposition are nearly identical, involving transfer and separation of a similar amount of charge. This indicates that both interfaces are stabilized by the polar discontinuity at the interface. In this view, both materials, LAO and NGO, share a similar ionic structure with trivalent cations on A- and B-sites. Hence, they require a similar amount of charge transfer[4] resulting in the same thermodynamic equilibrium state, as evident from the identical HTEC characteristics. (Note, however, that NGO/STO suffers from a loss of Ga at elevated temperatures, resulting in a slow degradation of the interface.)[7] The similar HTEC signatures obtained for epi-LAO/STO and NGO/STO moreover indicate that the different magnitude of epitaxial strain in these two systems has only a minor impact on the thermodynamic ground state and defect structure obtained in high temperature equilibrium.

In Figure 3a, we additionally plot the HTEC characteristics obtained for (La,Sr)(Al,Ta)O_3/STO (LSAT/STO) which has been shown to exhibit an interfacial 2DEG, too.[11] In high temperature equilibrium, we find an HTEC characteristic which in the intermediate pO_2 region is shifted significantly toward lower values as compared to LAO/STO and NGO/STO. Thus, the interface conductance contribution (cf. Figure 1c) to the total measurement signal is significantly reduced. Yet, we find conductance values that are significantly higher than those of the bare STO single crystal indicating a finite, nonzero charge transfer into the LSAT/STO interface. Thus, similar to LAO/STO and NGO/STO, LSAT/STO exhibits a thermally stable interface reconstruction driven by charge separation at the interface. The amount of transferred charge can be estimated from the HTEC values using the high temperature electron mobility value reported in ref 24. It is found to be of the order of $(2-3) \times 10^{13}$ e/cm^2. The observed charge separation is thus by a factor of 4−5 smaller than the one observed in LAO/STO. As (in the (100)-direction) LSAT consists of atomic layers that are nominally charged by about ±0.2 electrons per areal unit cell (e/uc^2), a less pronounced polar discontinuity is expected to arise at the LSAT/STO interface requiring (by a factor of 5) less charge to be transferred into the interface as compared to LAO/STO and NGO/STO (with nominal charges of ±1 e/uc^2). This is in excellent agreement with our HTEC experiment. All interface systems discussed in this section thus show thermodynamic ground states consistent with a thermodynamically stable charge transfer across the interface, associated with a nonzero electric field at the interface. (Charge separation implies an electric field at the interface, as these quantities are directly connected via Gauss' law.[19]) The amount of transferred charge scales with the nominal charge of the atomic planes of the capping material.

In contrast to these, if we choose a-LAO/STO as a starting point for the HTEC characterization, we observe a fundamentally different behavior in thermodynamic equilibrium. As shown in Figure 3b, a-LAO/STO does not show a thermally stable signature of interface conduction in high temperature equilibrium. In fact, the HTEC characteristics obtained for a bare STO single crystal and for a-LAO/STO overlap which indicates a zero (or negligible) charge separation at the a-LAO/STO interface and the absence of any stabilizing electric field at this interface. Hence, while after the growth process the a-LAO/STO heterostructure exhibited an electron gas with an electron density of about 2×10^{14} cm^{-2}, the relaxation of the structure into thermodynamic equilibrium resulted in a complete canceling of any interface conduction. In other words, the energetically (thermodynamically) preferred interface does not exhibit a 2DEG. This behavior is observed despite a crystallization process taking place under measurement conditions. In contrast to epitaxial LAO/STO heterostructures, no charge separation occurs during this process, most likely due to imperfect ionic ordering or an incoherent interface achieved during thermal crystallization in contrast to epitaxial growth. Hence, the thermodynamic properties of epi-LAO/STO and initially a-LAO/STO differ fundamentally.

The absence of any thermally stable interface conduction observed in the HTEC experiment indicates that, in contrast to epi-LAO/STO, the 2DEG in a-LAO/STO obtained after growth corresponds to a quenched nonequilibrium state of the system that vanishes upon equilibration. This result is in accordance with the reported disappearance of the 2DEG upon annealing.[12,14,28] Furthermore, the substantially different behavior of a-LAO/STO and epi-LAO/STO emphasizes that the interfacial 2DEG in these systems does not seem to be caused by penetration of La-ions into the substrate caused by the high energetic impingement during the PLD process. In addition, a scenario based on merely growth-induced rare-earth doping in epi-LAO/STO as well as in NGO/STO and LSAT/STO appears unlikely in light of the observed systematic scaling of the HTEC with the nominal ionic charge of the polar perovskite capping layer and the sudden change in the characteristic behavior at the critical layer thickness (here, observed in high temperature equilibrium).

Remarkably, epitaxial GAO/STO shows identical behavior (Figure 3b) as a-LAO/STO. GAO/STO shows no detectable interface contribution in high temperature equilibrium, again indicating a negligible charge transfer into the interface. Thus, similar to a-LAO/STO, the GAO/STO system shows interface conduction unambiguously based on a quenched nonequilibrium state that vanishes during equilibration. This result is rather surprising because, due to its ionic structure, epitaxial GAO may, similar to epitaxial LAO, generate a polar discontinuity at the GAO/STO interface, which may again drive a thermally stable charge separation at the interface. Our study, however, strongly suggests that this is not the case. In fact, from experimental limits we can estimate $\approx 1 \times 10^{12}$ e cm^{-2} to be an upper limit for any thermally stable charge separation in GAO/STO. This value is orders of magnitude smaller than the value expected from the polar discontinuity picture. Hence, similar to a-LAO/STO, GAO/STO is characterized by thermodynamical ground states that do not involve significant charge separation at its interface. There is no indication of a stabilizing electric field evolving at the GAO/STO interface.

3. DISCUSSION

For the prototype 2DEG system, epi-LAO/STO, as well as for NGO/STO and LSAT/STO, we revealed a thermally stable interface reconstruction, while the magnitude of the interface conduction contribution scales with the nominal charge of the atomic layers in the capping material. This strongly suggests that the polar discontinuity at these interfaces forces charge transfer from the polar capping layer into the STO side of the

DOI: 10.1021/acsami.6b12706
ACS Appl. Mater. Interfaces 2017, 9, 1086−1092

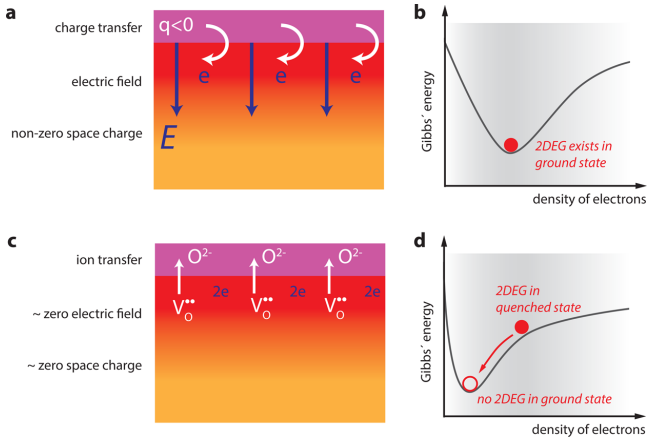

Figure 4. Schematic of the two different conduction mechanisms responsible for interface conduction in oxide heterostructures. (a) Sustained charge separation resulting from electrostatic boundary conditions that stabilize an electric field at the interface. Therefore, (b) an interfacial 2DEG is maintained in thermodynamic equilibrium. (c) Excess oxygen vacancy formation due to ion transfer from the STO substrate into the growing film. This scenario does not imply a thermally stable separation of charge at the interface. In contrast, (d) interface conduction in these systems refers to a quenched nonequilibrium state.

interface (Figure 4a). As a result, one obtains spatial charge separation and a space charge layer associated with an electric field at the interface.[4,19,29] In that case, a thermodynamically stable interface reconstruction takes place involving 2DEG formation and the formation of a specific ionic defect profile in the space charge layer.[19−21] Here, the interfacial 2DEG and its specific ionic defect structure correspond to the energy minimum (Gibbs' energy) of the system (Figure 4b). This is because the electric field emerging at the interface provides an internal driving force for the systems to form a conducting interface that is sustained in thermodynamic equilibrium.[19]

On the other hand, for initially a-LAO/STO and epi-GAO/STO, we showed that any signature of interface conduction vanishes in thermodynamic equilibrium indicating that the interface chemistry in these samples is fundamentally different from the one discussed above. In fact, the 2DEGs in GAO/STO and a-LAO/STO only exist in a quenched nonequilibrium state. This quenched state involves the formation of excess oxygen vacancies on the STO side of the interface during growth, as sketched in Figure 4c. As has been suggested, during growth, oxygen-deficient thin films take up oxygen from the STO substrate, forming oxygen vacancies in this process. As a result, electrons reside on the STO side leading to interface conduction. In this case, charge is not necessarily spatially separated, as both the dopants (here oxygen vacancies) and the mobile charge carriers (electrons) reside on the same side of the interface. The interface region is therefore rather charge neutral, and the depth profile of oxygen vacancies dictates the electron profile in the first place. Thus, the ion transfer (O^{2-} transfer from the STO side into the growing film) does not imply the presence of a significant electric field at the interface. In this scenario, the conducting state does not correspond to the energy-minimized ionic-electronic configuration, and the stabilizing electric field at the interface is absent (even after thermal crystallization). On the contrary, the system is forced into this state due to merely kinetic limitations. Such interfaces do not preserve their 2DEG state when allowed to relax toward equilibrium (Figure 4d). Therefore, from a thermodynamic perspective, these systems need to be categorized as a different type of 2DEG system, clearly distinct from 2DEGs on the basis of electric-field-stabilized charge separation, as observed, e.g., in epitaxially grown LAO/STO heterostructures. For GAO/STO, this result is particularly remarkable as this interface may inherently have the potential for a thermally stable charge transfer, since GAO may be a polar type crystal with nonvanishing electric dipole moment, similar to LAO.[30] Our experiments, however, unambiguously indicate that the main mechanism of conduction at the interface is the formation of oxygen vacancies.

For clarity and to summarize our results, we plot in Figure 5 the room temperature electron density obtained after fabrication for the various material systems discussed in this letter and compare it with the amount of charge separation that is maintained in thermodynamic equilibrium. While the as-grown 2DEG carrier densities can be very similar for, e.g.,

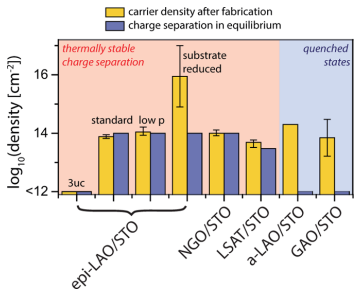

Figure 5. Comparison of the room temperature carrier density obtained from Hall measurements after fabrication of the samples and the amount of thermally stable charge separation probed in the high temperature equilibrium experiments. The HTEC experiments reveal two classes of 2DEG systems characterized by a nonzero (red areas) and zero (blue area) charge separation in their thermodynamic ground states.

DOI: 10.1021/acsami.6b12706
ACS Appl. Mater. Interfaces 2017, 9, 1086−1092

GAO/STO and epi-LAO/STO, the amount of charge separation in the state of minimum Gibbs energy differs by several orders of magnitude. In accordance with this, GAO/STO and a-LAO/STO did show little residual room temperature conductivity after the HTEC experiment, while all other interface systems maintained their 2DEG behavior.

Interestingly, enhanced electron mobility has been reported for GAO/STO as compared to epi-LAO/STO.[15] This may be explained by the fundamental differences in the chemistry of these interfaces (Figure 4): In GAO/STO, the control of the dopant (and thus impurity) concentration and electron density is basically unrestricted. In contrast to that, interfaces that are driven by charge separation such as epi-LAO/STO are restricted by their fixed electrostatic bounds. Therefore, with generation of more dilute electron gases during growth, additional ionic defects (e.g., Sr vacancies as suggested in refs 19, 20) are induced automatically to compensate the missing charge of electrons. Therefore, lower carrier densities are achieved only at an increased density of ionic defects in the near-interface region (partially countercompensated by a widening of the potential well at low temperatures). These additional defects act as additional, if not dominant, scatter centers for electrons in these interfaces.[27] These defects are to great extent absent in GAO/STO where 2DEG formation solely relies on oxygen vacancies. This may yield the enhanced electron mobility.

In summary, we have revealed two distinct categories of conducting oxide heterointerface systems. The first category is based on charge separation across the interface driven by electrostatic boundary conditions. Members of this category are epitaxial LAO/STO, NGO/STO, LSAT/STO, and other systems, such as $NdAlO_3$/STO and $LaGaO_3$/STO, not discussed in detail here. The second category is based on the mere formation of excess oxygen vacancies and a quenched nonequilibrium state. Members of this category are amorphous oxide/STO heterostructures and, remarkably, also epitaxial GAO/STO. Reactive metal/STO interface systems are expected to belong to this category, too. With respect to electronic properties, charge-separation driven oxide interfaces are thermally more stable, as their intrinsic energy minimum promotes the formation of a 2DEG. However, at the same time, this may imply the formation of additional ionic defects in the interface region, as reported before.[19] Therefore, the latter category based on the excess formation of interfacial oxygen vacancies may bear some benefits for reaching high mobility electron samples, with the drawback of requiring a thermally unstable quenched state.

4. EXPERIMENTAL DETAILS

Oxide thin films were grown by RHEED-controlled pulsed laser deposition (PLD) in layer-by-layer growth mode. For epi-LAO deposition, NGO deposition, and LSAT deposition, a growth temperature of 950 K was used at a laser frequency of 1 Hz and a fluence of 1.9 J/cm^2. For deposition of a-LAO, the sample was kept at room temperature during the growth. The deposition pressure was chosen between 1×10^{-3} mbar and 4×10^{-5} mbar. For GAO deposition, a growth temperature of 873 K was used at a laser frequency of 1 Hz and a fluence of 2.0 J/cm^2. The oxygen pressure was set to 1×10^{-4} mbar both during and after film deposition. HTEC experiments were conducted using a custom oxygen pump system based on a ZrO_2 oxygen pump ($850 < T/K < 1100$, $10^{-23} < pO_2/bar < 1$). Electrical contact was made in a four-point geometry by sputtering 100 nm thick Pt pads on top of the 5×10 mm^2 wide samples. The metal pads were then contacted by Pt wires wrapped around the sample ensuring optimum electrical contact throughout the high temperature experiment. Further details can be found in ref 22. Note that all samples investigated in this study are characterized by electronic conductivity (both n-type and p-type).[24] Ionic conductivity contributions in STO are not significant at the given temperature.[21]

AUTHOR INFORMATION

Corresponding Author

*E-mail: gunkel@iwe.rwth-aachen.de.

ORCID

F. Gunkel: 0000-0003-1178-9986

Notes

The authors declare no competing financial interest.

REFERENCES

(1) Hwang, H. Y.; Iwasa, Y.; Kawasaki, M.; Keimer, B.; Nagaosa, N.; Tokura, Y. Emergent Phenomena at Oxide Interfaces. *Nat. Mater.* **2012**, *11*, 103−113.

(2) Schlom, D. G.; Mannhart, J. Oxide Electronics - Interface takes charge over Si. *Nat. Mater.* **2011**, *10*, 168−169.

(3) Ohtomo, A.; Hwang, H. Y. A High-Mobility Electron Gas at the $LaAlO_3$/$SrTiO_3$ Heterointerface. *Nature* **2004**, *427*, 423−426.

(4) Nakagawa, N.; Hwang, H. Y.; Muller, D. A. Why some Interfaces cannot be Sharp. *Nat. Mater.* **2006**, *5*, 204−9.

(5) Thiel, S.; Hammerl, G.; Schmehl, A.; Schneider, C. W.; Mannhart, J. Tunable Quasi-Two-Dimensional Electron Gases in Oxide Heterostructures. *Science* **2006**, *313*, 1942−1945.

(6) Reyren, N.; Thiel, S.; Caviglia, A. D.; Kourkoutis, L. F.; Hammerl, G.; Richter, C.; Schneider, C. W.; Kopp, T.; Ruetschi, A.-S.; Jaccard, D.; Gabay, M.; Muller, D. A.; Triscone, J. M.; Mannhart, J. Superconducting Interfaces Between Insulating Oxides. *Science* **2007**, *317*, 1196−1199.

(7) Gunkel, F.; Skaja, K.; Shkabko, A.; Dittmann, R.; Hoffmann-Eifert, S.; Waser, R. Stoichiometry Dependence and Thermal Stability of Conducting $NdGaO_3$/$SrTiO_3$ Heterointerfaces. *Appl. Phys. Lett.* **2013**, *102*, 71601.

(8) Chen, Y.; Trier, F.; Kasama, T.; Christensen, D. V.; Bovet, N.; Balogh, Z. I.; Li, H.; Thyden, K. T. S.; Zhang, W.; Yazdi, S.; Norby, P.; Pryds, N.; Linderoth, S. Creation of High Mobility Two-Dimensional Electron Gases via Strain Induced Polarization at an Otherwise Nonpolar Complex Oxide Interface. *Nano Lett.* **2015**, *15*, 1849−1854.

(9) Perna, P.; Maccariello, D.; Radovic, M.; di Uccio, U. S.; Pallecchi, I.; Codda, M.; Marre, D.; Cantoni, C.; Gazquez, J.; Varela, M.; Pennycook, S. J.; Granozio, F. M. Conducting Interfaces between Band Insulating Oxides: The $LaGaO_3$/$SrTiO_3$ Heterostructure. *Appl. Phys. Lett.* **2010**, *97*, 152111.

(10) Annadi, A.; Putra, A.; Liu, Z. Q.; Wang, X.; Gopinadhan, K.; Huang, Z.; Dhar, S.; Venkatesan, T.; Ariando. Electronic Correlation and Strain Effects at the Interfaces between Polar and Nonpolar Complex Oxides. *Phys. Rev. B: Condens. Matter Mater. Phys.* **2012**, *86*, 085450.

(11) Huang, Z.; Han, K.; Zeng, S.; Motapothula, M.; Borisevich, A. Y.; Ghosh, S.; L, W.; Li, C.; Zhou, W.; Liu, Z.; Coey, M.; Venkatesan, T.; Ariando. The Effect of Polar Fluctuation and Lattice Mismatch on Carrier Mobility at Oxide Interfaces. *Nano Lett.* **2016**.

(12) Chen, Y.; Pryds, N.; Kleibeuker, J. E.; Koster, G.; Sun, J.; Stamate, E.; Shen, B.; Rijnders, G.; Linderoth, S. Metallic and Insulating Interfaces of Amorphous $SrTiO_3$-Based Oxide Heterostructures. *Nano Lett.* **2011**, *11*, 3774−3778.

(13) Trier, F.; Amoruso, S.; Christensen, D. V.; Sambri, A.; Chen, Y. Z.; Wang, X.; Stamate, E.; Bruzzese, R.; Pryds, N. Controlling the Conductivity of Amorphous $LaAlO_3$/$SrTiO_3$ Interfaces by in-situ Application of an Electric Field during Fabrication. *Appl. Phys. Lett.* **2013**, *103*, 031607.

(14) Liu, Z. Q.; Li, C. J.; Lü, W. M.; Huang, X. H.; Huang, Z.; Zeng, S. W.; Qiu, X. P.; Huang, L. S.; Annadi, A.; Chen, J. S.; Coey, J. M. D.; Venkatesan, T.; Ariando. Origin of the Two-Dimensional Electron Gas

DOI: 10.1021/acsami.6b12706
ACS Appl. Mater. Interfaces 2017, 9, 1086−1092

at $LaAlO_3/SrTiO_3$ Interfaces: The Role of Oxygen Vacancies and Electronic Reconstruction. *Phys. Rev. X* **2013**, *3*, 021010.
(15) Chen, Y. Z.; Bovet, N.; Trier, F.; Christensen, D. V.; Qu, F. M.; Andersen, N. H.; Kasama, T.; Zhang, W.; Giraud, R.; Dufouleur, J.; Jespersen, T.; Sun, J.; Smith, A.; Nygard, J.; Lu, L.; Buechner, B.; Shen, B.; Linderoth, S.; Pryds, N. A High-Mobility Two-Dimensional Electron Gas at the Spinel/Perovskite Interface of γ-$Al_2O_3/SrTiO_3$. *Nat. Commun.* **2013**, *4*, 1371−1376.
(16) Santander-Syro, A. F.; Copie, O.; Kondo, T.; Fortuna, F.; Pailhes, S.; Weht, R.; Qiu, X. G.; Bertran, F.; Nicolaou, A.; Taleb-Ibrahimi, A.; Le Fevre, P.; Herranz, G.; Bibes, M.; Reyren, N.; Apertet, Y.; Lecoeur, P.; Barthelemy, A.; Rozenberg, M. J. Two-Dimensional Electron Gas with Universal Subbands at the Surface of $SrTiO_3$. *Nature* **2011**, *469*, 189−193.
(17) Lee, S. W.; Liu, Y.; Heo, J.; Gordon, R. G. Creation and Control of Two-Dimensional Electron Gas Using Al-Based Amorphous Oxides/SrTiO3 Heterostructures Grown by Atomic Layer Deposition. *Nano Lett.* **2012**, *12*, 4775−4783.
(18) Chen, Y. Z.; Trier, F.; Wijnands, T.; Green, R. J.; Gauquelin, N.; Egoavil, R.; Christensen, D. V.; Koster, G.; Huijben, M.; Bovet, N.; Macke, S.; He, F.; Sutarto, R.; Andersen, N. H.; Sulpizio, J. A.; Honig, M.; Prawiroatmodjo, G.; Jespersen, T. S.; Linderoth, S.; Ilani, S.; Verbeeck, J.; Van Tendeloo, G.; Rijnders, G.; Sawatzky, G. A.; Pryds, N. Extreme Mobility Enhancement of Two-Dimensional Electron Gases at Oxide Interfaces by Charge-Transfer-Induced Modulation Doping. *Nat. Mater.* **2015**, *14*, 801−806.
(19) Gunkel, F.; Waser, R.; Ramadan, A. H. H.; De Souza, R. A.; Hoffmann-Eifert, S.; Dittmann, R. Space Charges and Defect Concentration Profiles at Complex Oxide Interfaces. *Phys. Rev. B: Condens. Matter Mater. Phys.* **2016**, *93*, 245431.
(20) Gunkel, F.; Brinks, P.; Hoffmann-Eifert, S.; Dittmann, R.; Huijben, M.; Kleibeuker, J. E.; Koster, G.; Rijnders, G.; Waser, R. Influence of Charge Compensation Mechanisms on the Sheet Electron Density at Conducting $LaAlO_3/SrTiO_3$-Interfaces. *Appl. Phys. Lett.* **2012**, *100*, 052103.
(21) Gunkel, F.; Hoffmann-Eifert, S.; Dittmann, R.; Mi, S.; Jia, C.; Meuffels, P.; Waser, R. High Temperature Conductance Characteristics of $LaAlO_3/SrTiO_3$-Heterostructures under Equilibrium Oxygen Atmospheres. *Appl. Phys. Lett.* **2010**, *97*, 12103.
(22) Ohly, C.; Hoffmann-Eifert, S.; Guo, X.; Schubert, J.; Waser, R. Electrical Conductivity of Epitaxial $SrTiO_3$ Thin Films as a Function of Oxygen Partial Pressure and Temperature. *J. Am. Ceram. Soc.* **2006**, *89*, 2845−2852.
(23) Smyth, D. M. *The Defect Chemistry of Metal Oxides*; Oxford University Press: New York, 2000.
(24) Moos, R.; Haerdtl, K. H. Defect Chemistry of Donor-Doped and Undoped Strontium Titanate Ceramics Between 1000 Degrees and 1400 Degrees C. *J. Am. Ceram. Soc.* **1997**, *80*, 2549−2562.
(25) Brinkman, A.; Huijben, M.; van Zalk, M.; Huijben, J.; Zeitler, U.; Maan, J. C.; van der Wiel, W. G.; Rijnders, G.; Blank, D. H. A.; Hilgenkamp, H. Magnetic Effects at the Interface Between Non-Magnetic Oxides. *Nat. Mater.* **2007**, *6*, 493−496.
(26) Xu, C.; Bäumer, C.; Heinen, R. A.; Hoffmann-Eifert, S.; Gunkel, F.; Dittmann, R. Disentanglement of Growth Dynamic and Thermodynamic Effects in $LaAlO_3/SrTiO_3$ Heterostructures. *Sci. Rep.* **2016**, *6*, 22410.
(27) Gunkel, F.; Bell, C.; Inoue, H.; Kim, B.; Swartz, A. G.; Merz, T. A.; Hikita, Y.; Harashima, S.; Sato, H. K.; Minohara, M.; Hoffmann-Eifert, S.; Dittmann, R.; Hwang, H. Y. Defect Control of Conventional and Anomalous Electron Transport at Complex Oxide Interfaces. *Phys. Rev. X* **2016**, *6*, 031035.
(28) Trier, F.; Christensen, D.; Chen, Y.; Smith, A.; Andersen, M.; Pryds, N. Degradation of the Interfacial Conductivity in $LaAlO_3/SrTiO_3$ Heterostructures during Storage at Controlled Environments. *Solid State Ionics* **2013**, *230*, 12−15.
(29) Yoshimatsu, K.; Yasuhara, R.; Kumigashira, H.; Oshima, M. Origin of Metallic States at the Heterointerface between the Band Insulators $LaAlO_3$ and $SrTiO_3$. *Phys. Rev. Lett.* **2008**, *101*, 026802.
(30) Schütz, P.; Pfaff, F.; Scheiderer, P.; Chen, Y. Z.; Pryds, N.; Gorgoi, M.; Sing, M.; Claessen, R. Band Bending and Alignment at the Spinel/Perovskite γ-$Al_2O_3/SrTiO_3$ Heterointerface. *Phys. Rev. B: Condens. Matter Mater. Phys.* **2015**, *91*, 165118.

DOI: 10.1021/acsami.6b12706
ACS Appl. Mater. Interfaces 2017, 9, 1086−1092

XIV

ARTICLE

D. V. Christensen, *et al.*
Controlling the Carrier Density of
$SrTiO_3$-based Heterostructures with Annealing
Advanced Electronic Materials, 1700026 (2017)

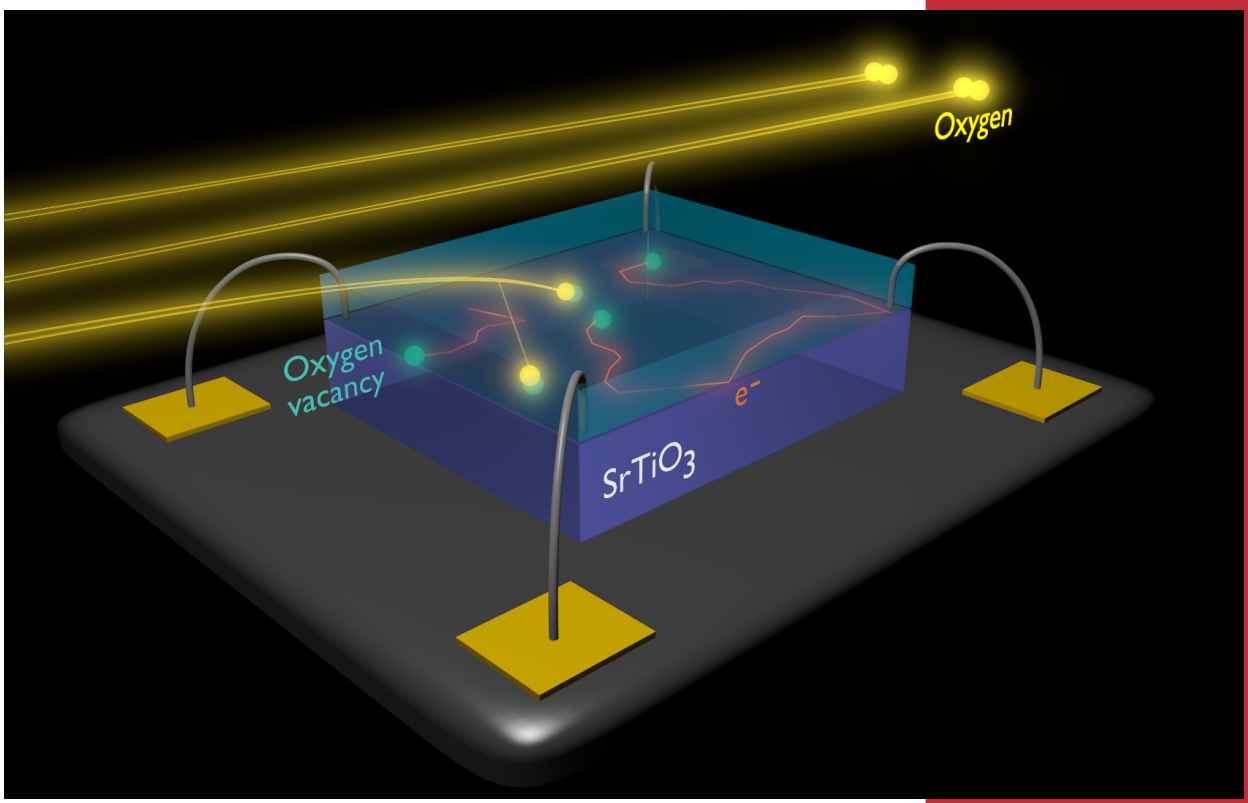

Defect control
Figure: Dennis Valbjørn Christensen

FULL PAPER

Oxide Electronics

ADVANCED ELECTRONIC MATERIALS
www.advelectronicmat.de

Controlling the Carrier Density of $SrTiO_3$-Based Heterostructures with Annealing

Dennis V. Christensen, Merlin von Soosten, Felix Trier, Thomas S. Jespersen, Anders Smith, Yunzhong Chen, and Nini Pryds*

The conducting interface between the insulating oxides $LaAlO_3$ (LAO) and $SrTiO_3$ (STO) displays numerous physical phenomena that can be tuned by varying the carrier density, which is generally achieved by electrostatic gating or adjustment of growth parameters. Here, it is reported how annealing in oxygen at low temperatures ($T < 300$ °C) can be used as a simple route to control the carrier density by several orders of magnitude. The pathway to control the carrier density relies on donor oxidation and is thus applicable to material systems where oxygen vacancies are the dominant source of conductivity. Using STO capped with epitaxial γ-Al_2O_3 (GAO) or amorphous LAO (a-LAO), the pathways for changing the carrier density in the two STO-based cases are identified where oxygen blocking (GAO) and oxygen permeable (a-LAO) films create interface conductivity from oxygen vacancies located in STO near the interface. For a-LAO/STO, the rate limiting step ($E_a = 0.25$ eV) for oxidizing oxygen vacancies is the transportation of oxygen from the atmosphere through the a-LAO film, whereas GAO/STO is limited by oxygen migration inside STO ($E_a = 0.5$ eV). Finally, it is showed how the control of the carrier density enables writing of conducting nanostructures in γ-Al_2O_3/STO by conducting atomic force microscopy.

1. Introduction

Controlling the carrier density in operando or by means of device fabrication plays a key role in modern electronics. Varying the carrier density at the interface between the band insulator $SrTiO_3$ (STO) and a thin film of a second band insulator, $LaAlO_3$ (LAO), grown on top of STO has resulted in a versatile control of many physical phenomena. The carrier density in this system is typically controlled either by varying the sample fabrication process or by electrostatic gating. In the former approach, the carrier density is controlled by the parameters of the LAO growth, where, for instance, increasing the LAO layer thickness above a critical thickness of 4 unit cells[1] or lowering the oxygen growth pressure[2] renders insulating interfaces conducting. In the latter approach, free carriers are induced by electrostatic gating of the conducting interface separated from the gate by a solid dielectric (typically STO or LAO),[1] an electrolyte with mobile ions[3] or a ferroelectric material.[4] Using this approach, the gate-control of a large number of properties has been demonstrated including magnetism,[5] the anomalous Hall effect,[3] superconductivity[6] and spin-orbit coupling.[7]

The two different approaches each have their strengths and weaknesses. In the first approach, the effect of the carrier density on the sample properties is often studied by fabricating a series of samples with a discrete set of carrier densities. This allows for a change in carrier density exceeding 10^{14} cm^{-2}. The process does not allow for in situ control of the carrier density, and the results may be strongly influenced by unwanted sample-to-sample variations related to variations of the sample fabrication process or the STO substrate quality.

In the second approach, the carrier density can be controlled continuously within a single sample during the experiments. The range of the carrier density tuning using conventional back-gating is much smaller than the first approach. A typical induced carrier density when 100 V is applied at room temperature through a 0.5 mm thick STO substrate is less than 10^{12} cm^{-2},[8] which is much lower than typical carrier densities ($n_s > 10^{13}$ cm^{-2}) in as-grown LAO/STO.[1] The use of top-gating or gating through electrolytes can reduce the gate potential while maintaining or increasing the possible range of carrier density tuning. The electrostatic gating has side effects beyond changing the carrier density by a shift in the Fermi energy level. The applied potential adds to the confinement potential of the electrons at the interface and effectively changes their depth distribution.[9] At low temperatures, electrostatic gating has also previously been observed to predominantly alter the electron mobility rather than the carrier density,[9] change the tetragonal domain structure in STO,[10] and result in pronounced hysteresis of the electrical properties.[11] At or above room temperature, electromigration of oxygen may occur in STO.[8,12,13] In

D. V. Christensen, M. von Soosten, Dr. F. Trier, Dr. A. Smith, Dr. Y. Chen, Prof. N. Pryds
Department of Energy Conversion and Storage
Technical University of Denmark
Risø Campus, DK-4000 Roskilde, Denmark
E-mail: dechr@dtu.dk
Dr. T. S. Jespersen
Niels Bohr Institute
Center for Quantum Devices
University of Copenhagen
DK-2100 Copenhagen Ø, Denmark

DOI: 10.1002/aelm.201700026

addition, obtaining a desired electron density through gating requires a continuous application of an electrostatic potential, which may be undesirable in combination with local gating or when designing functional electronic devices.

Understanding the origin of the conducting interface is crucial to predict how the growth parameters should be changed to obtain a desired carrier density. However, the origin of the conductivity in LAO/STO is still debated, with the predominant explanations relying on a potential build-up in the polar LAO,[14,15] or oxygen vacancies in STO.[16] In the wake of the discovery of the LAO/STO heterostructure, several other conducting STO-based interfaces have been fabricated where the origin of the conductivity is less controversially assigned to oxygen vacancies such as STO capped with, e.g., γ-Al_2O_3 (GAO),[17,18] or amorphous LAO (a-LAO).[18,19] In these cases, the top film gathers oxygen from STO during growth which leads to oxygen vacancies and free electrons in the near-interface region of STO. Recent high temperature equilibrium conductance measurements in various oxygen pressures have been used to compare several STO-based heterostructures. The results show that the conductivity disappears in a-LAO/STO and GAO/STO in oxidizing conditions, whereas a conductivity component attributed to the potential build-up persists in epitaxial-LAO/STO.[18] Besides testing if the interface conductivity survives oxidizing conditions, annealing at elevated temperatures in oxygen atmospheres has frequently been used to minimize the effect of oxygen vacancies.

A hitherto largely overlooked possibility is to use a controlled annealing to regulate the free carrier density by refilling oxygen vacancies with oxygen from a reservoir such as an oxygen-containing atmosphere. Here, we report the control of the carrier density and conductivity in GAO/STO and a-LAO/STO using a low-temperature (T < 300 °C) annealing in a 1 bar oxygen environment. As an application of the carrier density control, we show how it can be used to tune GAO/STO into a regime where it is possible to write and erase nanostructures with the biased tip of a conducting atomic force microscope (c-AFM).

2. Results and Discussion

The annihilation or creation of oxygen vacancies in oxidizing or reducing environment can be described by a chemical equation of the form

$$\frac{1}{2}O_2 + V_O^{\cdot\cdot} + 2e' \overset{k}{\rightleftarrows} O_O^x \quad (1)$$

using the Kröger–Vink notation and a rate constant k. Here, the two electrons created by forming an oxygen vacancy can be delocalized and contribute to the conductivity or be localized, e.g., by creating different oxygen vacancy charge states ($V_O^{\cdot}$ or $V_O^{\cdot\cdot}$). The oxygen vacancies created in STO during the growth of a reducing top layer are thermodynamically unstable,[18] but refilling is kinetically hindered at room temperature leading to quasi-stable interfaces. We investigate this oxygen vacancy refilling by measuring the changes in the sheet conductance in situ in an atmosphere of 1 bar pure oxygen while the temperature is increased in steps from room temperature to 350 °C (see the Experimental Section for details). The refilling is highly accelerated by elevating the temperature, with the conductivity of the GAO/STO interface being significantly more stable than a-LAO/STO (see **Figure 1**a,b). Annealing can be used to carefully control the conductance with a time scale of hours at $T \leq 300$ °C, where the movement of the heavier cations (La, Sr, and Ti) is generally frozen.,[20,21] We note, however, that the lighter aluminum may be mobile in GAO below 300 °C owing to the inherent Al vacancies present in GAO.[22] The change in conductivity for 20 °C < T < 300 °C is mainly a result of varying the carrier density (see Figure 1c). The contribution of the carrier mobility change is typically < 10% of the total conductivity change, as the mobility at these temperatures is limited by

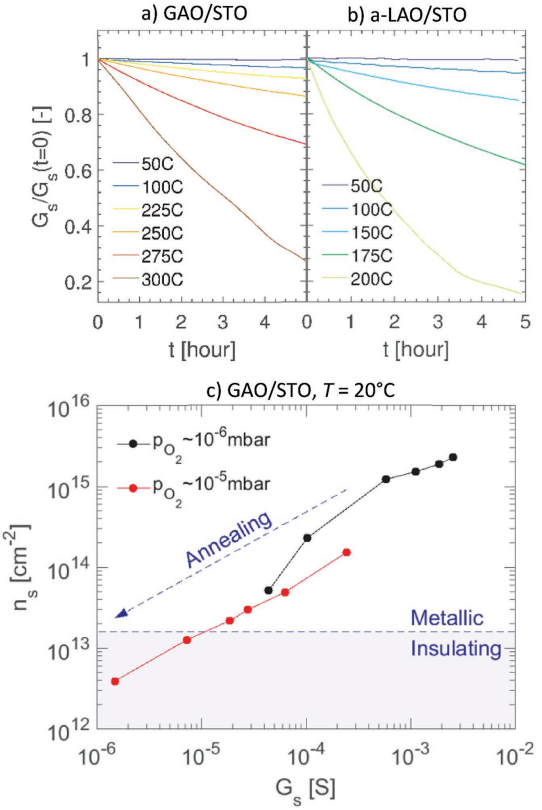

Figure 1. Normalized sheet conductance G_s for a) γ-Al_2O_3/$SrTiO_3$ (GAO/STO) and b) amorphous-$LaAlO_3$/$SrTiO_3$ (a-LAO/STO) measured as a function of time during annealing in 1 bar oxygen. Selected temperatures are chosen which produces comparable annealing traces for the two heterostructures while avoiding large nonlinearities (see discussion in the main text). c) The Hall carrier density, n_s, as a function of the sheet conductance for two GAO/STO samples with different initial carrier densities obtained by varying the oxygen partial pressure (p_{O2}) during growth. The carrier density and sheet conductance is measured at room temperature and in between two measurement points the sample is annealed at ≈200 °C in 1 bar oxygen to induce a carrier density change. The metallic region is defined as the region in carrier densities where $dG_s/dT < 0$ for any temperature T in the interval 2 K < T < 300 K.

ADVANCED SCIENCE NEWS
www.advancedsciencenews.com

ADVANCED ELECTRONIC MATERIALS
www.advelectronicmat.de

optical phonon scattering with only a moderate dependence on the electron density.[23] For a-LAO/STO, the maximum carrier density is typically around 10^{14} cm^{-2} at room temperature,[19] whereas for GAO/STO, carrier densities up to 10^{15} cm^{-2} have been reported.[17] In both cases, the carrier density can easily be controlled without sample-to-sample variations in a large range from the maximum value to a level where the free carriers cannot be measured.

The temperature dependence can be analyzed quantitatively by investigating the thermal activation of the annealing process. We extract the rate of sheet conductance change at each temperature and present it in an Arrhenius plot (see **Figure 2**). While the rate of sheet conductance change is fastest for a-LAO/STO, the activation barrier is 0.5 eV for both a-LAO/STO and GAO/STO at low temperatures. Upon reaching higher temperatures of ≈125 °C during the incremental increase of the temperature, the rates deviate from the straight Arrhenius-type behavior observed at low temperatures. For a-LAO/STO, the activation energy of the thermally activated behavior changes from 0.5 eV at low temperatures (<75 °C) to 0.24 eV at high temperatures (>125 °C). For GAO/STO, the rate decreases dramatically by more than two orders of magnitude and subsequently

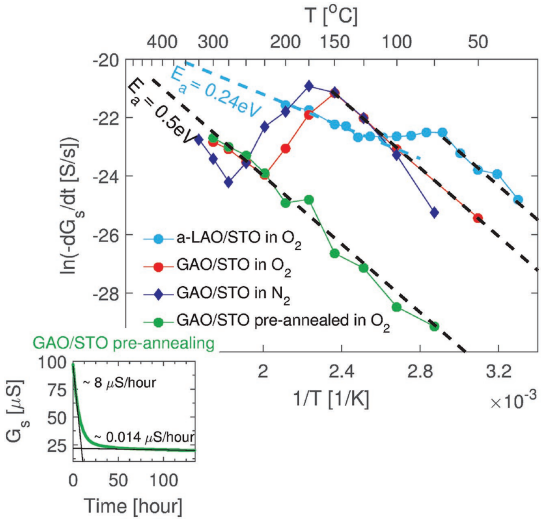

Figure 2. Arrhenius plot of the sheet conductance change (dG_s/dt) measured at various annealing temperatures (T) for GAO/STO and a-LAO/STO in 1 bar nitrogen or oxygen. The rate of conductance change was obtained by stabilizing each temperature for 12 h while measuring the conductance, except for a-LAO/STO where each annealing step was limited to 7 h to resolve the low-temperature behavior below 150 °C before saturation. The Arrhenius plot is shown for three as-grown samples and one preannealed GAO/STO heterostructure. The latter has been subjected to a 140 h preannealing step at 150 °C in 1 bar oxygen prior to measuring the rate of conductance change for the Arrhenius plot. This preannealing saturates the initial degradation process responsible for the high initial conductance change at lower temperatures. The inset shows the sheet conductance as a function of time during this 140 h preannealing; we note that this cannot be fitted satisfactorily by a single exponential function. The parallel black lines correspond to an activation barrier of 0.50 eV, whereas the light blue line represents an activation barrier of 0.24 eV.

reestablishes a regular thermal activation with an activation energy of 0.5 eV. This is consistently reproduced in four GAO/STO samples. Such behavior is typical for the coexistence of two distinct processes where one process (process A) initially is dominant but eventually saturates, thus allowing the observation of a second process (process B). To test this hypothesis, we subject a new as-grown GAO/STO sample to a fixed temperature of 150 °C in 1 bar of oxygen while continuously measuring the sheet conductance (see the inset of Figure 2). The initial rate of sheet conductance change (8 μS h^{-1}) is decreased by more than two orders of magnitude to 0.014 μS h^{-1} after 140 h at 150 °C. Following this preannealing step at 150 °C, the sample is cooled to room temperature and then subjected to an identical stepwise increase in the temperature as previously employed to obtain the Arrhenius plot in Figure 2. Contrary to as-grown GAO/STO, this preannealed GAO/STO now shows a single thermal activation energy during the annealing with E_a = 0.5 eV without a drop in the rate (green circles in Figure 2), and the preannealing is consistent with a saturation of process A.

When GAO/STO heterostructures are subjected to the same stepwise annealing procedure in 1 bar nitrogen rather than 1 bar oxygen, the changes in the initial conductivity at low temperatures are similar (dark blue curve in Figure 2). After saturation, the conductivity change decreases in both annealing environments before it increases again at higher temperatures. The high-temperature annealing rate in nitrogen is, however, smaller than in oxygen by a factor 2–4. Based on this annealing in nitrogen, we conclude that process A and its saturation are independent of the environment.

We furthermore determine the thickness dependence of the conductance change rate ($|dG_s/dt|$) when GAO/STO and a-LAO/STO samples are stored for around two months at room temperature in a standard vacuum desiccator providing a slight vacuum of 0.8 bar. For GAO/STO, the rate is largely independent of the top film thickness (see Figure S1 in the Supporting Information). For a-LAO/STO, the average rate increases almost one order of magnitude when the a-LAO layer is decreased from 5 to 1.5 nm, whereas varying the film thickness only produces a small change if merely the first 12 days are considered. Process A is therefore independent of the top layer thickness whereas process B is highly dependent on the top layer thickness, however, only for the case of a-LAO/STO.

We then attempt to explain the physical origin of the two processes. As the temperature is stabilized at each step, fast (electronic) changes have already occurred before the beginning of each measurement. This includes thermal activation of electrons to the conduction band. Slow ionic movements are therefore suggested to be responsible for the conductivity change reported here. Cation movement generally requires higher activation energy than what is observed here. The energy barriers for moving oxygen in STO[24,25] and GAO[26] are 0.5–0.6 and 1.3 eV, respectively; the energy barrier in a-LAO is to our knowledge unknown, but arguably smaller than the 0.6–0.7 eV for crystalline LAO.[24] We therefore attribute the activation energies of 0.5 eV observed at low temperatures (process A), and, for GAO/STO, at high temperatures (process B) to oxygen movement in STO (black, dashed lines in Figure 2).

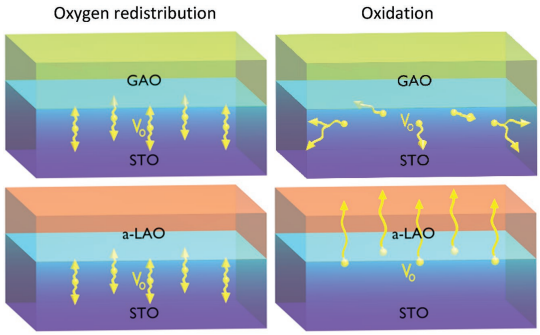

Figure 3. The proposed mechanism for conductance change upon annealing of a-LAO/STO and GAO/STO. Initially, the conductance change is governed by oxygen redistribution (left column), which effectively localizes the electrons. After the oxygen redistribution has reached saturation, oxygen from the atmosphere eliminates oxygen vacancies close to the interface (right column).

Process A is two orders of magnitude faster than process B, which suggests that the initial oxygen movement occurs over short distances. In addition, process A occurs for both a-LAO/STO and GAO/STO and is independent of top layer thickness and annealing atmosphere. It can therefore be attributed to an internal redistribution of oxygen vacancies within STO (see **Figure 3**). During deposition of oxygen deficient thin films, a nonequilibrium vacancy depth distribution is created in STO, which eventually equilibrates during process A leading to the observed saturation. The effect on the conductivity is likely due to a change in the charge localization when oxygen vacancies are redistributed. Localization of charges is often attributed to trapping sites in the vicinity of oxygen vacancies or a lack of a macroscopic percolation path. Using density functional theory, it was for instance deduced that oxygen vacancies at the surface of STO trap electrons in contrast to bulk oxygen vacancies.[27] Movement of oxygen vacancies from the bulk to the surface may thus lower the free carrier density. Electrons can therefore change their state between delocalized and localized with an associated rate constant k'

$$e_{\text{deloc}} \overset{k'}{\rightleftarrows} e_{\text{loc}} \tag{2}$$

This contribution gives $\mathrm{d}n_s/\mathrm{d}t|_{(\text{de})\text{loc}} \propto -k'$.

Process B, however, is different for a-LAO/STO and GAO/STO. In the former case, process B has a low activation energy and the rate increases greatly when the a-LAO thickness is decreased. Consistent with a previous report,[28] we assign the oxygen vacancy refilling in a-LAO/STO preferentially to molecular oxygen dissociating and diffusing through the top film with a rate-limiting energy barrier of 0.24 eV (see Figure 3). For GAO/STO, this process is halted due to the high activation energy for oxygen movement in GAO, and the oxidation occurs through STO instead. Although the pathway is different for a-LAO/STO and GAO/STO, the net result of both oxidation reactions can be described by Equation (1) with a rate constant k giving rise to a contribution $\mathrm{d}n_s/\mathrm{d}t|_{\text{redox}} \propto -k$.

Oxygen vacancies therefore affect the density of itinerant charge carriers by changing the donor density and by localizing charge carriers. The total rate of carrier density change by the two processes can be described by $\frac{\mathrm{d}n_s}{\mathrm{d}t} = \frac{1}{A}\frac{\mathrm{d}N_{\text{total}}}{\mathrm{d}t} = -\frac{1}{A}(f_{\text{deloc}}k + k')$. Here, f_{deloc} denotes the average number of delocalized electrons annihilated when an oxygen vacancy is refilled with oxygen, and the sheet carrier density $n_s = N_{\text{total}}/A$ is defined as the total amount of delocalized electrons (N_{total}) per sample area (A).

Since the change in sheet conductance (G_s) during the annealing at a constant temperature is predominantly caused by a change in the carrier density (n_s) rather than the electron mobility (μ), the measured rate of sheet conductance change at a fixed temperature can then be described by

$$\begin{aligned} -\left.\frac{\mathrm{d}G_s}{\mathrm{d}t}\right|_T &\approx -e\mu\frac{\mathrm{d}n_s}{\mathrm{d}t} = e\mu\frac{1}{A}\left(f_{\text{deloc}}k + k'\right) \\ &= e\mu\frac{1}{A}\left[f_{\text{deloc}}k_0\exp\left(-E_a/k_BT\right) + k_0'\exp\left(-E_a'/k_BT\right)\right] \end{aligned} \tag{3}$$

We assume that the rates can be described by the product of a prefactor (k_0 and k_0') with an exponential term describing the thermal activation balancing the thermal energy (k_BT) with the activation energies (E_a and E_a') of the rate-limiting step in reactions (1) and (2). Using $E_a^{\text{a-LAO}} = 0.24\ \text{eV}$ and $E_a^{\text{GAO}} = E_a'^{\text{GAO}} = E_a'^{\text{a-LAO}} = 0.5\text{eV}$ together with $k_0' \to 0$ as the oxygen vacancy redistribution reaches a quasi-equilibrium, Equation (3) captures the essence of the annealing processes observed in Figure 2.

We note that extracting activation energies is a useful way to deduce the location of the donors. For GAO/STO it has been unclear whether oxygen vacancy donors are located in STO[17,19] or on the GAO surface due to a possible polarity in GAO in analogy with the polar discontinuity model initially proposed for LAO/STO.[15] The activation energy of 0.5 eV for oxidizing oxygen vacancies in GAO/STO, however, implies that oxygen vacancies are predominantly located in STO, consistent with interface redox reactions where the growth of an oxygen deficient film reduces STO.[17,19]

The control of carrier density may be used to enable writing of conducting nanowires in GAO/STO using c-AFM, similar to the nanowire writing demonstrated in LAO/STO.[29,30] Previously, LAO/STO samples for AFM sketching required a careful control of the deposition parameters including a precise LAO thickness of 3.3 unit cells,[30,31] which is just below the critical thickness of ≈4 unit cells for inducing metallic conductivity.[1] Metallic conductivity can then be locally induced at the interface by moving a positively biased c-AFM tip across the surface of LAO, leaving behind conducting lines with widths down to a few nanometers (see the left schematic drawing in **Figure 4**). Preparing the sample in an ideal initial state is challenging due to the abrupt insulator-to-metal transition accompanied with a decrease in the sheet resistance by more than 5 orders of magnitude when increasing the LAO thickness with a single unit cell from 3 to 4 unit cells.[1] Instead, the metal-to-insulator transition can be induced after the deposition using annealing, which may enable c-AFM writing of nanostructures. To simplify the fabrication process, we here use a crystalline

ADVANCED SCIENCE NEWS
www.advancedsciencenews.com

ADVANCED ELECTRONIC MATERIALS
www.advelectronicmat.de

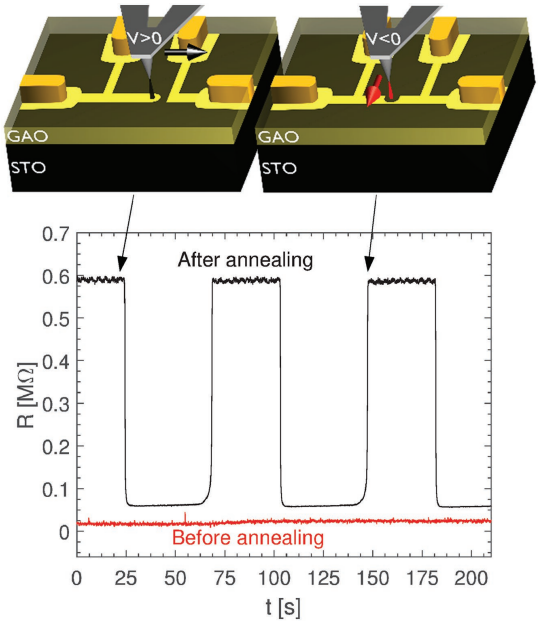

Figure 4. 4-probe resistance (R) measured at room temperature as a function of time (t) during writing and erasing of conducting nanowires before and after annealing on a hot plate at 150 °C for 3 h in ambient conditions. The writing (erasing) is achieved by applying a positive (negative) voltage on a conducting atomic force microscopy tip, which is then moved across the surface of GAO/STO in order to write (cut) a conducting nanowire at the interface connecting four gold contacts as depicted in the schematic drawings.

GAO/STO sample with GAO deposited at room temperature and subsequently annealed on a standard laboratory hot plate in ambient environment.

Prior to the annealing, the GAO/STO interface is metallically conducting, and it is, as expected, not possible to measure a notable conductance change when attempting to write a nanowire between two gold electrodes (see Figure 4). Upon annealing the interface on a hot plate at 150 °C for 3 h, the room temperature resistance of the sample increases by a factor of 30. In this state, nanowires can be efficiently written and erased at room temperature with positive and negative voltages applied to the c-AFM tip, respectively. When connecting the two gold electrodes with a nanowire written with +25 V applied on the tip, the 4-probe resistance between the electrodes decreases one order of magnitude. Subsequent cutting of the wire by applying a negative tip voltage and scanning across the wire returns the resistance to the original value. By correlating the cutting of the wire with the speed of the c-AFM tip, the width of a nanowire is determined to be ≈50 nm. The nanowire is observed to be metallically conducting down to 50 mK, whereas the remaining sample is insulating, thus further increasing the difference in the local resistivity of the nanowire and the background. The low-temperature characterization of the c-AFM written nanostructures will be presented in a future publication. The mechanism underpinning the c-AFM writing has been attributed to dissociation of water on the surface, which effectively donates electrons to the nanowire located at interface.[32] The role of the annealing is expected simply to be to raise the sample resistance to an insulating state where writing can be observed. The annealing strategy thus makes it possible to post process of the interface of GAO/STO with the possibility to stop at a desired point rather than relying on an intricate control of deposition parameters that may depend on the specific sample, growth method, and growth chamber.

We have shown that annealing can be used as a simple way to control the carrier density over many orders of magnitude with no sample-to-sample variation. The approach should be applicable to numerous materials, in particular oxides, where the conductivity either originates primarily from oxygen vacancies or where donor atoms or the material itself changes the electronic properties upon oxidation. Focusing on STO-based samples, the approach can be applied on ion-bombarded[33] or illuminated[34] STO, STO capped with various metal films[35] and STO capped with reducing oxides such as yttrium-stabilized zirconia,[19] amorphous STO[19] or $CaHfO_2$.[36] The carrier density in epitaxial LAO/STO can also be controlled to some extent by annealing, if a postannealing step is not performed after the LAO growth.[28] Differences are, however, expected depending on the capping of STO. First, the route for refilling oxygen vacancies is determined by the kinetics of breaking molecular O_2 bonds on the surface and diffusing oxygen through the thin film. Oxygen blocking layers such as crystalline GAO grown at high temperatures provide a high stability of the interface conductivity whereas a freely exposed STO surface degrades rapidly. Second, the different atomic arrangement at the interface may result in atomic sites located at the interface where oxygen vacancies are stabilized or destabilized.

The carrier density control and dopant engineering using annealing have strengths and weaknesses compared to controlling the carriers by gating or growth. Similar to the growth-induced carrier density change, annealing allows for a large carrier density change, but the low-temperature oxidation minimizes sample-to-sample variations and unwanted side effects such as large changes in the crystallinity. An immediate weakness is that by annealing a sample, the initial state is lost with attempts to reverse the oxidation by reduction being likely to lead to a different state. This has profound implications for reproducing results without suffering from sample-to-sample variation by fabricating a new sample. Second, if oxygen blocking films such as GAO are used, the annealing process can result in some degree of inhomogeneity of the carrier density with the center of the sample being more resilient to annealing due to oxygen diffusion through the sides of STO. Last, whereas the carrier density tuning by annealing is usually easier than the growth approach, gating is often more convenient and allows for real-time tunability during a number of measurements. However, in certain cases leakage current or insufficient carrier density tunability renders gating ineffective. This includes gating of highly conducting samples or gating through a leaking dielectric with free carriers stemming from, e.g., some degree of bulk conductivity, defects or photoinduced carriers in measurements featuring irradiation with X-ray, UV or visible light.

Beyond studying effects of shifting the Fermi energy level, the simultaneous control of the oxygen vacancies and electrons can yield some advantages over gating. Donors constitute scattering sites for electrons, and by controlling the number and distribution of donors, we expect that annealing can enhance the mobility and help identifying the dominant scattering mechanism by comparing theoretical predictions with the dependence of the mobility on the carrier density. This includes classical cases of coexisting electrons and donors,[37] modulation doping,[38] and delta-doping in the low and high density regime.[39] In addition, magnetism in STO and STO-based heterostructures is often suggested to originate in localized magnetic moments on oxygen vacancies,[40] which then could be controlled by careful annealing.

3. Conclusion

We have shown that in those oxides where the conductivity originates from oxygen vacancies, such as a range of STO-based heterostructures, annealing is a powerful procedure for controlling both the Fermi energy level and the donor concentration and distribution. For STO-based heterostructures, the annealing approach provides a hitherto largely overlooked alternative or supplement to traditional approaches to tune the carrier density such as gating and adjustment of growth parameters. We have shown that annealing can enable interface nanowire writing, but the approach may also be particularly interesting for tuning emergent magnetism, enhancing mobility, and studying the metal-to-insulator transition.

4. Experimental Section

GAO/STO heterostructures were prepared using pulsed laser deposition from TiO_2-terminated STO at a temperature of 650 °C as described elsewhere.[41] The same deposition conditions were used for making the a-LAO/STO heterostructures with the exception of depositing LAO on a STO substrate with a temperature of 25 °C instead of 650 °C. For GAO/STO the heating and cooling rate was set to 15 °C min^{-1}, and the samples were cooled immediately after the deposition. If not stated otherwise, the thickness of the GAO film is fixed to ≈3.5 unit cells (2.8 nm), whereas thicker a-LAO films of 16 nm were used to clearly resolve the low-temperature annealing behavior. The heterostructures were electrically connected using wedge wire bonding in van der Pauw geometry, and subjected to annealing at various temperatures in 1 bar oxygen or nitrogen. For the measurements presented in Figures 1a,b, and 2, the temperature was increased in steps from room temperature to 350 °C. At each step, the temperature was stabilized and the sheet conductance was measured in situ. The Hall carrier density and sheet conductivity presented in Figure 1c were measured at room temperature after subjecting the heterostructures to annealing at ≈200 °C in 1 bar oxygen for 2–8 h. The Hall carrier density was deduced from the linear Hall coefficient in magnetic fields up to 15 T. For c-AFM writing, e-beam lithography was used to create resist patterns such that the sample surface was exposed only at areas intended for metal contacts. Argon ion milling was then used to remove 10 nm of GAO and STO, which produced trenches that were filled with titanium (2 nm) and gold (8 nm) to contact the buried electron gas at the GAO/STO interface. A positive voltage applied on the c-AFM tip was used to draw conducting lines from the gold contacts as sketched in Figure 4. To emphasize the simplicity of fabricating interfaces that enable nanowire writing, the GAO film (4 nm) was deposited at room temperature, and the nanowire writing was enabled by annealing on a standard laboratory hot plate in ambient environment.

Supporting Information

Supporting Information is available from the Wiley Online Library or from the author.

Acknowledgements

The authors thank J. Levy, P. Irvin, M. Huang, F. Bi, and M. Kirkendall from University of Pittsburgh, USA, for their valuable help in setting up the c-AFM experiments. The authors also thank J. Geyti from Technical University of Denmark for technical assistance.

Conflict of Interest

The authors declare no conflict of interest.

Keywords

γ-$Al_2O_3/SrTiO_3$, c-AFM nanowires, $LaAlO_3/SrTiO_3$, oxide electronics

Received: January 19, 2017
Revised: May 23, 2017
Published online:

[1] S. Thiel, G. Hammerl, A. Schmehl, C. W. Schneider, J. Manhart, *Science* **2006**, *313*, 1942.
[2] A. Brinkman, M. Huijben, M. van Zalk, J. Huijben, U. Zeitler, J. C. Maan, W. G. van der Wiel, G. Rijnders, D. H. A. Blank, H. Hilgenkamp, *Nat. Mater.* **2007**, *6*, 493.
[3] Y. Lee, C. Clement, J. Hellerstedt, J. Kinney, L. Kinnischtzke, X. Leng, S. D. Snyder, A. M. Goldman, *Phys. Rev. Lett.* **2011**, *106*, 136809.
[4] V. T. Tra, J.-W. Chen, P.-C. Huang, B.-C. Huang, Y. Cao, C.-H. Yeh, H.-J. Liu, E. A. Eliseev, A. N. Morozovska, J.-Y. Lin, Y.-C. Chen, M.-W. Chu, P.-W. Chiu, Y.-P. Chiu, L.-Q. Chen, C.-L. Wu, Y.-H. Chu, *Adv. Mater.* **2013**, *25*, 3357.
[5] F. Bi, M. Huang, S. Ryu, H. Lee, C.-W. Bark, C.-B. Eom, P. Irvin, J. Levy, *Nat. Commun.* **2014**, *5*, 5019.
[6] A. D. Caviglia, S. Gariglio, N. Reyren, D. Jaccard, T. Schneider, M. Gabay, S. Thiel, G. Hammerl, J. Mannhart, J.-M. Triscone, *Nature* **2008**, *456*, 624.
[7] A. D. Caviglia, M. Gabay, S. Gariglio, N. Reyren, C. Cancellieri, J.-M. Triscone, *Phys. Rev. Lett.* **2010**, *104*, 126803.
[8] D. V. Christensen, F. Trier, Y. Z. Chen, A. Smith, J. Nygård, N. Pryds, *Appl. Phys. Lett.* **2013**, *102*, 021602.
[9] C. Bell, S. Harashima, Y. Kozuka, M. Kim, B. G. Kim, Y. Hikita, H. Y. Hwang, *Phys. Rev. Lett.* **2009**, *103*, 226802.
[10] M. Honig, J. A. Sulpizio, J. Drori, A. Joshua, E. Zeldov, S. Ilani, *Nat. Mater.* **2013**, *12*, 1112.
[11] J. Biscaras, S. Hurand, C. Feuillet-Palma, A. Rastogi, R. C. Budhani, N. Reyren, E. Lesne, J. Lesueur, N. Bergeal, *Sci. Rep.* **2014**, *4*, 6788.
[12] J. Delahaye, T. Grenet, *J. Phys. D: Appl. Phys.* **2016**, *49*, 395303.
[13] R. Waser, M. Aono, *Nat. Mater.* **2007**, *6*, 833.
[14] N. Nakagawa, H. Hwang, D. Muller, *Nat. Mater.* **2006**, *5*, 204.
[15] L. Yu, A. Zunger, *Nat. Commun.* **2014**, *5*, 5118.
[16] A. Kalabukhov, R. Gunnarsson, J. Börjesson, E. Olsson, T. Claeson, D. Winkler, *Phys. Rev. B* **2007**, *75*, 121404.

ADVANCED SCIENCE NEWS
www.advancedsciencenews.com

ADVANCED ELECTRONIC MATERIALS
www.advelectronicmat.de

[17] Y. Z. Chen, N. Bovet, F. Trier, D. V. Christensen, F. M. Qu, N. H. Andersen, T. Kasama, W. Zhang, R. Giraud, J. Dufouleur, T. S. Jespersen, J. R. Sun, A. Smith, J. Nygård, L. Lu, B. Büchner, B. G. Shen, S. Linderoth, N. Pryds, *Nat. Commun.* **2013**, *4*, 1371.
[18] F. Gunkel, S. Hoffmann-Eifert, R. A. Heinen, D. V. Christensen, Y. Z. Chen, N. Pryds, R. Waser, R. Dittmann, *ACS Appl. Mater. Interfaces* **2017**, *9*, 1086.
[19] Y. Z. Chen, N. Pryds, J. E. Kleibeuker, G. Koster, J. Sun, E. Stamate, B. Shen, G. Rijnders, S. Linderoth, *Nano Lett.* **2011**, *11*, 3774.
[20] W. H. Rhodes, W. D. Kingery, *J. Am. Chem. Soc.* **1966**, *49*, 521.
[21] R. Meyer, A. F. Zurhelle, R. A. De Souza, R. Waser, F. Gunkel, *Phys. Rev. B* **2016**, *94*, 115408.
[22] S. T. Murphy, B. P. Uberuaga, J. B. Ball, A. R. Cleave, K. E. Sickafus, R. Smith, R. W. Grimes, *Solid State Ionics* **2009**, *180*, 1.
[23] E. Mikheev, B. Himmetoglu, A. P. Kajdos, P. Moetakef, T. A. Cain, C. G. van de Walle, S. Stemmer, *Appl. Phys. Lett.* **2015**, *106*, 062102.
[24] M. Lontsi-Fomena, A. Villesuzanne, J.-P. Doumerc, C. Frayret, M. Pouchard, *Comput. Mater. Sci.* **2008**, *44*, 53.
[25] F. Cordero, *Mater. Sci. Eng., A* **2009**, *77*, 521.
[26] T. Nabatame, T. Yasuda, M. Nishizawa, M. Ikeda, T. Horikawa, A. Toriumi, *Jpn. J. Appl. Phys.* **2003**, *42*, 7205.
[27] H. Choi, J. D. Song, K.-R. Lee, S. Kim, *Inorg. Chem.* **2015**, *54*, 3759.
[28] F. Trier, D. V. Christensen, Y. Z. Chen, A. Smith, M. I. Andersen, N. Pryds, *Solid State Ionics* **2013**, *230*, 12.
[29] C. Cen, S. Thiel, G. Hammerl, C. W. Schneider, K. E. Andersen, C. S. Hellberg, J. Mannhart, J. Levy, *Nat. Mater.* **2008**, *7*, 298.
[30] C. Cheng, S. Thiel, J. Mannhart, J. Levy, *Science* **2009**, *323*, 1026.
[31] C. Cen, D. F. Bogorin, J. Levy, *Nanotechnology* **2010**, *21*, 475201.
[32] F. Bi, D. F. Bogorin, C. Cen, C. W. Bark, J.-W. Park, C.-B. Eom, J. Levy, *Appl. Phys. Lett.* **2010**, *97*, 173110.
[33] J. H. Ngai, Y. Segal, D. Su, Y. Zhu, F. J. Walker, S. Ismail-Beigi, K. Le Hur, C. H. Ahn, *Phys. Rev. B* **2010**, *81*, 241307.
[34] S. M. Walker, F. Y. Bruno, Z. Wang, A. de la Torre, S. Riccó, A. Tamai, T. K. Kim, M. Hoesch, M. Shi, M. S. Bahramy, P. D. C. King, F. Baumberger, *Adv. Mater.* **2015**, *27*, 3894.
[35] Q. Fu, T. Wagner, *J. Phys. Chem. B* **2005**, *109*, 11697.
[36] K. Shibuya, T. Ohnishi, M. Lippmaa, M. Oshima, *Appl. Phys. Lett.* **2007**, *91*, 232106.
[37] A. Verma, A. P. Kajdos, T. A. Cain, S. Stemmer, D. Jena, *Phys. Rev. Lett.* **2014**, *112*, 216601.
[38] D. Monroe, Y. H. Xie, E. A. Fitzgerald, P. J. Silverman, G. P. Watson, *J. Vac. Sci. Technol., B* **1993**, *11*, 1731.
[39] E. H. Hwang, S. D. Sarma, *Phys. Rev. B* **2013**, *87*, 125411.
[40] N. Pavlenko, T. Kopp, E. Y. Tsymbal, G. A. Sawatzky, J. Mannhart, *Phys. Rev. B* **2012**, *85*, 020407.
[41] D. V. Christensen, F. Trier, M. von Soosten, G. E. D. K. Prawiroatmodjo, T. S. Jespersen, Y. Z. Chen, N. Pryds, *Appl. Phys. Lett.* **2016**, *109*, 021602.

Supporting Information

Controlling the Carrier Density of $SrTiO_3$–based Heterostructures with Annealing

Dennis V. Christensen[1,*], Merlin von Soosten[1], Felix Trier[1], Thomas S. Jespersen[2], Anders Smith[1], Yunzhong Chen[1], and Nini Pryds[1]

[1]*Department of Energy Conversion and Storage, Technical University of Denmark, Risø Campus, DK-4000 Roskilde, Denmark*

[2]*Niels Bohr Institute, Center for Quantum Devices, University of Copenhagen, DK-2100 Copenhagen Ø, Denmark*

** Corresponding author – dechr@dtu.dk*

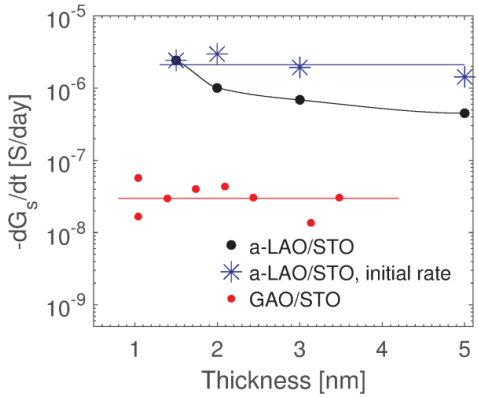

Figure S1: The conductance change (dG_s/dt) in GAO/STO and a-LAO/STO as a function of the thickness of the GAO and a-LAO films when stored for around 2 months in a vacuum desiccator providing a slight vacuum of 0.8 bar. For amorphous-$LaAlO_3$ the initial conductance change from the first 12 days is also shown.

XV

ARTICLE

D. V. Christensen and A. Smith
Is γ-Al_2O_3 polar?
Applied Surface Science 423, 887 (2017)

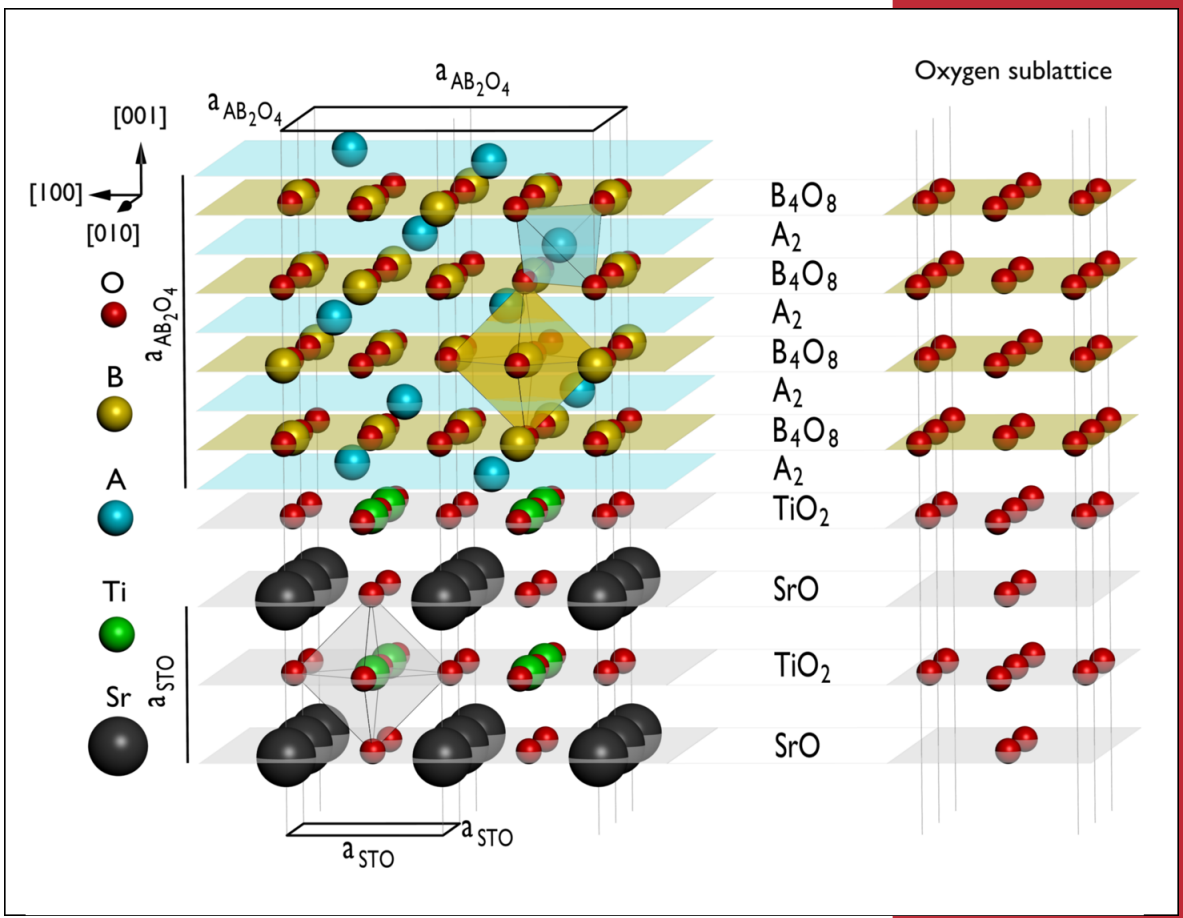

Spinel/perovskite interface
Figure: Dennis Valbjørn Christensen

Applied Surface Science 423 (2017) 887–890

Contents lists available at ScienceDirect

Applied Surface Science

journal homepage: www.elsevier.com/locate/apsusc

Short communication

Is γ-Al_2O_3 polar?

D.V. Christensen*, A. Smith

Department of Energy Conversion and Storage, Technical University of Denmark, Risø Campus, DK-4000 Roskilde, Denmark

ARTICLE INFO

Article history:
Received 13 May 2017
Received in revised form 12 June 2017
Accepted 17 June 2017
Available online 23 June 2017

Keywords:
Polarity
γ-Al_2O_3/$SrTiO_3$
Ferroelectric
Two-dimensional electron gas
Aluminum vacancies
Oxygen vacancies

ABSTRACT

Polarity in thin films and polar discontinuities across an interface plays an important role in determining electronic properties. A key example is the conductivity at the $LaAlO_3$/$SrTiO_3$ (LAO/STO) interface, which is proposed to originate from the polarity of LAO. As a consequence, the conductivity does not disappear when LAO/STO is subjected to highly oxidizing conditions. Substituting LAO with another nominally polar material γ-Al_2O_3 (GAO) results in an interface conductivity which can be destroyed by annealing in oxygen. We investigate this apparent paradox by revisiting the defect spinel atomic structure of GAO. We show that the polarity is dependent on the distribution of aluminum vacancies which are intrinsically present in GAO to ensure charge neutrality. In particular, certain film thicknesses allow for vacancy distributions that make GAO nominally non-polar along the [001] direction. We further propose that electromigration of aluminum vacancies across atomic layers can alter the polarity, making the GAO film effectively act as a ferroelectric.

1. Introduction

Polarity has profound impact on the properties and applications of surfaces, thin films and heterostructures. If left uncompensated, it causes an increase in the electrostatic potential when the thickness of the polar material is increased in the direction of the polarity. The potential build-up may result in atomic restructuring [1], electronic band gradients [2], spontaneous defect formation [2,3] and electron transfer [2]. Surfaces are traditionally classified into three types with respect to their polarity, where type 1 is a non-polar surface with no dipole moment perpendicular to the surface, type 2 has internal dipole moments but no net dipole moment whereas type 3 has a net dipole moment [1]. Type 1 and 2 result in modest surface energies, whereas a type 3 surface has high surface energy and is typically not stable without a substantial reconstruction of the atomic lattice. Such a reconstruction is proposed to be the origin of the conductivity in the type 3/1 heterostructure formed when the polar $LaAlO_3$ (LAO) is grown epitaxially on the TiO_2-terminated (001) surface of nominally non-polar $SrTiO_3$ (STO) [2]. The (001) planes of these ABO_3 perovskites can be viewed as alternating AO_2 and BO layers as depicted in Fig. 2a. If formal valence charges are assigned to the atoms (Sr^{2+}, Ti^{4+}, La^{3+}, Al^{3+}, O^{2-}), STO is non-polar as it is composed of charge neutral atomic planes, whereas planes with an alternating charge density of ±1 elementary charge pr. surface unit cell ($\sigma = \pm e/a_{LAO}^2$) make LAO is polar [2]. If the atomic layers are (crudely) approximated as charged continuous planes, the electric field between the planes becomes $E = \sigma/\varepsilon_r\varepsilon_0$, giving rise to an electrostatic potential build-up ($V(z) = \int_{-\infty}^{z} E(z')\,dz'$), which increases linearly with the LAO thickness (see Fig. 2g). Adopting a dielectric constant of $\varepsilon_r = 24$ for LAO [4], the potential build-up is 0.94 V/a_{LAO}. Above a critical thickness of LAO, it becomes energetically favorable to counter the potential build-up by an electron transfer from the top of LAO to the LAO/STO interface where the resulting mobile electrons cause interface conductivity [2]. This explains the sudden insulator-to-metal transition with increasing LAO thickness observed experimentally [5]. While overly simple, the polarity model has been shown to be qualitatively useful in this [2,6] and other systems [1,7], even if more detailed density-functional based studies are needed to predict the actual density of free carriers resulting from the electron transfer [8].

A recent study compared heterostructures where different non-polar and polar oxide films were grown on STO [9]. By heating up the heterostructures to 950 K and varying the oxygen partial pressure, it was found that at low ($<10^{-20}$ bar) or high ($>10^{-4}$ bar) oxygen pressure, the conductivity of all heterostructures in thermal equilibrium is dominated by oxygen vacancy donors or acceptors in STO, respectively (see Fig. 1). At intermediate partial pressures, however, an oxygen independent contribution to the conductivity

* Corresponding author.
E-mail address: dechr@dtu.dk (D.V. Christensen).

http://dx.doi.org/10.1016/j.apsusc.2017.06.184
0169-4332/

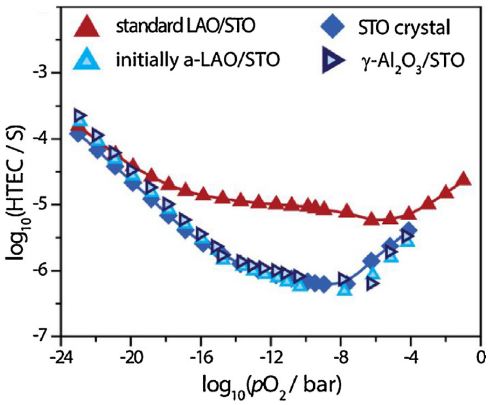

Fig. 1. High temperature equilibrium conductance (HTEC) at 950 K as a function of the oxygen partial pressure, pO_2, for a $SrTiO_3$ (STO) substrate and STO with a high-temperature grown $LaAlO_3$ (LAO), room-temperature grown LAO (a-LAO) or γ-Al_2O_3 film. In all cases, the film thickness exceeds the critical thickness for inducing interface conductivity. Reprinted with permission from Ref. [6]. Copyright 2017, American Chemical Society.

was found only for polar films (LAO, $NdGaO_3$ and (La,Sr)(Al,Ta)O_3 (LSAT)). Results from $NdGaO_3$ and LSAT can be found in Ref. [9]. As this contribution scales with the polarity of the film and is absent below the critical thickness of LAO, it was attributed to the electron transfer to STO due to the potential build-up. Although γ-Al_2O_3 (GAO) is generally considered to be polar [10], the oxygen-independent conductivity contribution was completely absent. This leads to the conclusion that the origin of the conductivity in GAO/STO is thermodynamically unstable interface oxygen vacancies rather than a polarity-induced potential build-up. This conclusion is supported by the observations that the critical thickness for inducing insulator-to-metal transition varies with GAO deposition conditions [11] and that annealing in oxygen at low temperatures (<600 K) destroys the conductivity [12,13] with a characteristic activation energy consistent with oxygen vacancy movement in STO [13]. Here, we aim to explain this apparent paradox by revisiting the atomic structure of GAO. During the process, we identify a pathway that may turn GAO into a material with a tunable polarity.

2. Results and discussion

GAO has a cubic spinel crystal structure. In the general form (AB_2O_4), the cubic spinel unit cell is composed of 32 oxygen atoms, 16 B-site cations placed in an octahedral environment and 8 A-site cations in a tetrahedral environment ($A_8B_{16}O_{32}$). In the case of GAO, Al^{3+} occupies both A and B sites with a unit cell of a_{GAO} = 7.911 Å [14]. By virtue of compatible oxygen sublattices in STO and GAO, pseudo-epitaxial growth with $a_{GAO} \sim 2a_{STO}$ is possible [12]. The (001) planes of GAO can be viewed as alternating $Al_{1/2}$ and AlO_2 layers as depicted in Fig. 2b. In order to obey charge neutrality each spinel unit cell contains on average $2\frac{2}{3}$ aluminum vacancies ($Al_{21}\square_{1/3}O_{32}$), which may be located on sites with octahedral or tetragonal symmetry. Consistent with ref. [10], a homogeneous distribution of aluminum vacancies exclusively on octahedral site gives layers with an alternating charge density of $\sigma = \pm 1.5e/(0.5a_{GAO})^2$ (see Fig. 2c). Assuming a relative dielectric constant of ε_r = 9.5 [4,15,16] we obtain a large potential build-up of 7.1 V/a_{GAO} (see Fig. 2g). A homogeneous distribution on tetrahedral sites gives $\sigma = \pm 1e/(0.5a_{GAO})^2$ and a reduced potential build-up of 4.8 V/a_{GAO} (see Fig. 2d and g). In both cases, the potential build-up is significantly larger than that in LAO due to the lower dielectric constant of GAO. If the rapidly increasing potential in these cases was compensated by the electronic reconstruction, a critical thickness for forming a conducting interface would be expected to be less than one unit cell, taking into account the band alignment of STO and GAO [10]. Experimentally, however, the critical thickness is observed to be around 1.5 unit cells [12,17]. In terms of the polar classification, both distributions lead to a type 3 surface with a non-zero dipole moment and, for a sufficiently thick film, require a substantial reconstruction to stabilize the surface [1]. An inhomogeneous distribution of aluminum vacancies can, however, lead to a very different polarity. There is some evidence for such an inhomogeneous distribution from X-ray studies [18] of single crystal GAO which find that Al is distributed over both octahedral and tetrahedral sites in a ratio 63:37. For a GAO thickness of one unit cell (8 atomic layers), Fig. 2e and f depict two distributions where GAO has no net dipole moment and no monotonously increasing potential.

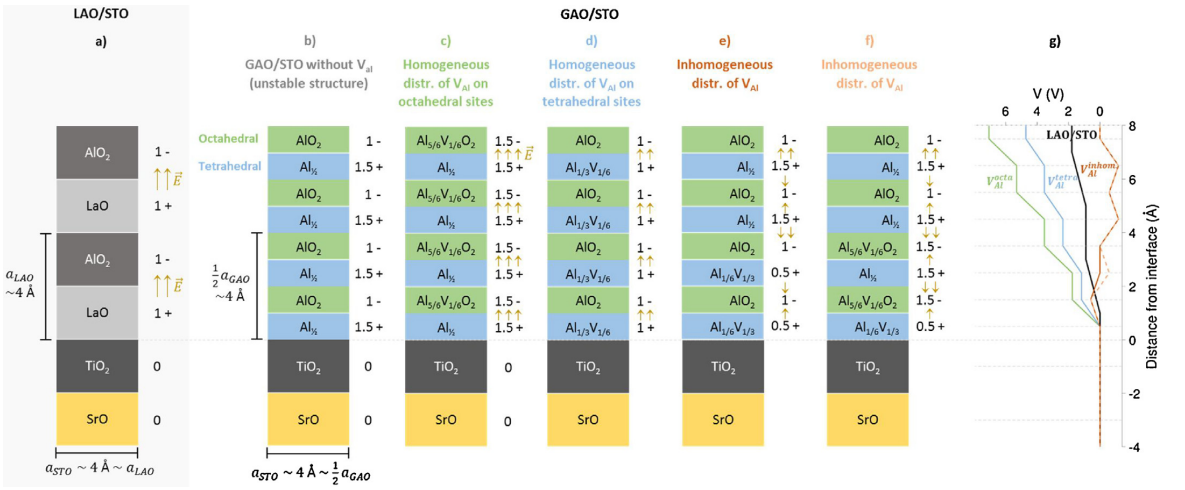

Fig. 2. (a–f) Schematics of the polarity of LAO/STO and GAO/STO viewed along the [001]-direction. For GAO/STO various distributions of aluminum vacancies are considered. (g) The resulting electrostatic potential (V) along the [001] direction for the different systems.

These atomic structures can be classified as type 2 [1]. Note that the distribution of Al between octahedral and tetrahedral sites in Fig. 2f is 0.31, which compares favorably to distribution found in the X-ray study. The electrostatic potential of both solutions remains between −1.2 and 0.6 eV throughout the 8 atomic layers. This is significantly lower than the potential increase from 2.8 to 3.8 eV corresponding to the LAO thickness increase from 3 u.c. to 4 u.c. that causes conductivity in STO [5].

The general condition for non-polarity of a film with M atomic layers, the i'th layer having a charge density of σ_i, can be written as:

$$\sum_{i=1}^{M}(M-2i+1)\sigma_i = 0,$$

subject to the constraint of over-all charge neutrality, $\Sigma_i\sigma_i = 0$. For GAO, we introduce aluminum vacancies (V) in the $Al_{0.5}$ and AlO_2 layers, which can be described as alternating layers of $Al_{x_i}V_{0.5-x_i}$ (i odd; charge $3x_i$) and $Al_{x_i}V_{1-x_i}O_2$ (i even; charge $3x_i - 4$). There are no non-polar solutions for fewer than 8 atomic layers (one unit cell). At a thickness of one unit cell, Fig. 2e and f give two simple non-polar distributions. As the thickness increases, the number of different solutions increases rapidly. The configuration which actually will be realized, will be the kinetically accessible state with the lowest total energy. We will discuss the kinetics and energetics next:

Chen et al. [12] found that each RHEED oscillation detected during the growth of the film corresponds to growing a charge neutral block composed of two atomic layers as depicted in Fig. 2 with a total thickness of ¼ unit cell (2 Å). The charge neutrality entails that each block initially is polar, and diffusion of aluminum vacancies between individual blocks is required to make GAO overall non-polar. The energy barrier for Al diffusion in GAO is lowered by the large number of intrinsic aluminum vacancies and may be as low as 0.6 eV [19]. In a typical pulsed laser deposition, thin GAO films (<10 nm) are deposited at ~900 K at low oxygen background pressures (<10^{-6} bar) where the plasma plume is freely expanding with plasma species arriving at the sample surface with kinetic energies exceeding 10 eV [20]. At such deposition conditions, aluminum is expected to be highly mobile across the entire GAO thickness. Even for films thick enough to hinder a sufficient aluminum diffusion throughout the entire film, GAO can be overall non-polar if diffusion over short distances results in repeating non-polar units such as the one in Fig. 2e or f. The aluminum mobility, however, severely decreases if the deposition temperature is lowered or a less energetic deposition method is used.

Predicting the most thermodynamically stable aluminum vacancy distribution requires careful analysis well beyond the scope of this short communication. The total energy contains contributions from vacancy–vacancy interactions, coordination of vacancy positions (tetragonal vs. octahedral), symmetry breaking from the interface and GAO surface in addition to the energy contribution from the polarity. The high temperature equilibrium conductance measurements, however, directly probe the thermodynamically stable situation experimentally, and the lack of signature of sufficiently polar GAO films makes the non-polar aluminum vacancy contributions likely to be energetically favorable. This is further supported by (i) the lowering of the surface energy by conversion from a type 3 to type 2 polarity [1], (ii) the lack of a polarity signature in the low-temperature annealing [12,13], (iii) the absence of energy shifts in aluminum core levels and the oxygen 2p valence state [10] and (iv) the dependence of the critical GAO thickness on the deposition conditions [11].

An intriguing consequence of this interpretation is that it may be possible to change the polarity by applying electric fields. Considering, e.g., the case with one unit cell GAO presented in Fig. 2e and f, the non-polar solutions are found by locating aluminum vacancies close to STO. If a positive top-gate potential is applied relative to the grounded electron gas at the interface, electromigration of aluminum vacancies towards the GAO surface yield a polar GAO film. In this way, the GAO film may effectively act as a ferroelectric material. The possibility for electromigration at room or slightly elevated temperatures seems likely in the view of frequently reported room temperature electromigration of oxygen vacancies with a similar energy barrier [21,22].

3. Conclusion

In conclusion, we have presented a possible solution for the apparent paradox in which experiments show a lack of the distinguishing features of the polar discontinuity at the GAO/STO interface although GAO is generally considered to be polar. We show that inhomogeneous distributions of aluminum vacancies highly affect the polarity and allow for non-polar GAO films for certain thicknesses. Thus, we have presented a possible resolution of the paradox. However, it should be noted that alternative explanations may also be possible, such as defect formations, and we encourage future studies to clarify the actual structure of the GAO film on STO. In particular, density-functional based calculations will be useful for assessing the relative stability of the configurations considered here.

Acknowledgement

We thank Yunzhong Chen, Nini Pryds, Felix Gunkel and Philipp Schütz for valuable discussions.

References

[1] P.W. Tasker, The stability of ionic crystal surfaces, J. Phys. C: Solid State Phys. 12 (1979) 4977, http://dx.doi.org/10.1088/0022-3719/12/22/036.
[2] N. Nakagawa, H.Y. Hwang, D.A. Muller, Why some interfaces cannot be sharp, Nat. Mater. 5 (2006) 204–209, http://dx.doi.org/10.1038/nmat1569.
[3] L. Yu, A. Zunger, A polarity-induced defect mechanism for conductivity and magnetism at polar–nonpolar oxide interfaces, Nat. Commun. 5 (2014) 5118, http://dx.doi.org/10.1038/ncomms6118.
[4] J. Krupka, R.G. Geyer, M. Kuhn, J.H. Hinken, Dielectric properties of single crystals of Al_2O_3 $LaAl0_3$, $NdGa0_3$, $SrTi0_3$, and MgO at cryogenic temperatures, IEEE Trans. Microw. Theory Tech. 42 (1994) 1886, http://dx.doi.org/10.1109/22.320769.
[5] S. Thiel, G. Hammerl, A. Schmehl, C.W. Schneider, J. Mannhart, Tunable quasi-two-dimensional electron gases in oxide heterostructures, Science 313 (2006) 1942–1945, http://dx.doi.org/10.1126/science.1131091.
[6] Z.Q. Liu, C.J. Li, W.M. Lü, X.H. Huang, Z. Huang, S.W. Zeng, X.P. Qiu, L.S. Huang, A. Annadi, J.S. Chen, J.M.D. Coey, T. Venkatesan, Ariando, origin of the two-dimensional electron gas at $LaAlO_3/SrTiO_3$ interfaces: the role of oxygen vacancies and electronic reconstruction, Phys. Rev. X 3 (2013) 021010, http://dx.doi.org/10.1103/PhysRevX.3.021010.
[7] P. Moetakef, T.A. Cain, D.G. Ouellette, J.Y. Zhang, D.O. Klenov, A. Janotti, C.G. Van de Walle, S. Rajan, S.J. Allen, S. Stemmer, Electrostatic carrier doping of $GdTiO_3/SrTiO_3$ interfaces, Appl. Phys. Lett. 99 (2011) 232116, http://dx.doi.org/10.1063/1.3669402.
[8] Z. Popović, S. Satpathy, R. Martin, Origin of the two-dimensional electron gas carrier density at the $LaAlO_3$ on $SrTiO_3$ interface, Phys. Rev. Lett. 101 (2008) 256801, http://dx.doi.org/10.1103/PhysRevLett.101.256801.
[9] F. Gunkel, S. Hoffmann-Eifert, R.A. Heinen, D.V. Christensen, Y.Z. Chen, N. Pryds, R. Waser, R. Dittmann, Thermodynamic ground states of complex oxide heterointerfaces, ACS Appl. Mater. Interf. 9 (2017) 1086–1092, http://dx.doi.org/10.1021/acsami.6b12706.
[10] P. Schütz, F. Pfaff, P. Scheiderer, Y.Z. Chen, N. Pryds, M. Gorgoi, M. Sing, R. Claessen, Band bending and alignment at the spinel/perovskite γ-$Al_2O_3/SrTiO_3$ heterointerface, Phys. Rev. B 91 (2015) 165118, http://dx.doi.org/10.1103/PhysRevB.91.165118.
[11] Y.Z. Chen, N. Bovet, T. Kasama, W.W. Gao, S. Yazdi, C. Ma, N. Pryds, S. Linderoth, Room temperature formation of high-mobility two-dimensional electron gases at crystalline complex oxide interfaces, Adv. Mater. 26 (1) (2013), http://dx.doi.org/10.1002/adma.201304634.
[12] Y.Z. Chen, N. Bovet, F. Trier, D.V. Christensen, F.M. Qu, N.H. Andersen, T. Kasama, W. Zhang, R. Giraud, J. Dufouleur, T.S. Jespersen, J.R. Sun, A. Smith, J. Nygård, L. Lu, B. Büchner, B.G. Shen, S. Linderoth, N. Pryds, A high-mobility two-dimensional electron gas at the spinel/perovskite interface of

γ-Al_2O_3/$SrTiO_3$, Nat. Commun. 4 (2013) 1371, http://dx.doi.org/10.1038/ncomms2394.

[13] D.V. Christensen, M. von Soosten, F. Trier, T.S. Jespersen, A. Smith, Y.Z. Chen, N. Pryds, et al., Controlling the Carrier Density of $SrTiO_3$–based Heterostructures with Annealing, Adv. Electron. Mater. (2017), http://dx.doi.org/10.1002/aelm.201700026, 1700026.

[14] R.-S. Zhou, R.L. Snyder, Structures and transformation mechanisms of the η, γ and θ transition aluminas, Acta Crystallogr. B 7 (1991) 617–630, http://dx.doi.org/10.1107/S0108768191002719.

[15] S. Guha, E. Cartier, N.A. Bojarczuk, J. Bruley, L. Gignac, J. Karasinski, High-quality aluminum oxide gate dielectrics by ultra-high-vacuum reactive atomic-beam deposition, J. Appl. Phys. 90 (2001) 512–514, http://dx.doi.org/10.1063/1.1373695.

[16] X. He, Z.-X. Tang, B. Zhang, Y. Wu, A new deembedding method in permittivity measurement of ferroelectric thin film material, Prog. Electromagn. Res. Lett. 3 (2008) 1–8, http://dx.doi.org/10.2528/PIERL08011501.

[17] D.V. Christensen, F. Trier, M. von Soosten, G.E.D.K. Prawiroatmodjo, T.S. Jespersen, Y.Z. Chen, N. Pryds, Electric field control of the γ-Al_2O_3/$SrTiO_3$ interface conductivity at room temperature, Appl. Phys. Lett. 109 (2016) 021602, http://dx.doi.org/10.1063/1.4955490.

[18] Ľ. Smrčok, V. Langer, J. Křesťan, γ-Alumina: a single-crystal X-ray diffraction study, Acta Crystallogr. C 62 (2006) i83–i84, http://dx.doi.org/10.1107/S0108270106026850.

[19] S.T. Murphy, B.P. Uberuaga, J.B. Ball, A.R. Cleave, K.E. Sickafus, R. Smith, R.W. Grimes, Cation diffusion in magnesium aluminate spinel, Solid State Ion. 180 (2009) 1–8, http://dx.doi.org/10.1016/j.ssi.2008.10.013.

[20] A. Sambri, D.V. Christensen, F. Trier, Y.Z. Chen, S. Amoruso, N. Pryds, R. Bruzzese, X. Wang, Plasma plume effects on the conductivity of amorphous-$LaAlO_3$/$SrTiO_3$ interfaces grown by pulsed laser deposition in O_2 and Ar, Appl. Phys. Lett. 100 (2012) 231605, http://dx.doi.org/10.1063/1.4727905.

[21] R. Waser, M. Aono, Nanoionics-based resistive switching memories, Nat. Mater. 6 (2007) 833–840, http://dx.doi.org/10.1038/nmat2023.

[22] K. Szot, W. Speier, G. Bihlmayer, R. Waser, Switching the electrical resistance of individual dislocations in single-crystalline $SrTiO_3$, Nat. Mater. 5 (2006) 312–320, http://dx.doi.org/10.1038/nmat1614.

XVI

ARTICLE

W. Niu, Y. Gan, Y. Zhang, **D. V. Christensen** *et al.*
Suppressed carrier density for the patterned high mobility two-dimensional electron gas at γ-Al_2O_3/$SrTiO_3$ heterointerfaces
Applied Physics Letters 111, 021602 (2017)

Wintertime at Risø campus
Photo: Dennis Valbjørn Christensen

APPLIED PHYSICS LETTERS 111, 021602 (2017)

Suppressed carrier density for the patterned high mobility two-dimensional electron gas at γ-Al_2O_3/$SrTiO_3$ heterointerfaces

Wei Niu,[1,2] Yulin Gan,[1] Yu Zhang,[1] Dennis Valbjørn Christensen,[1] Merlin von Soosten,[1] Xuefeng Wang,[2,a)] Yongbing Xu,[2] Rong Zhang,[2] Nini Pryds,[1] and Yunzhong Chen[1,a)]
[1]*Department of Energy Conversion and Storage, Technical University of Denmark, Risø Campus, Roskilde 4000, Denmark*
[2]*National Laboratory of Solid State Microstructures, Collaborative Innovation Center of Advanced Microstructures and School of Electronic Science and Engineering, Nanjing University, Nanjing 210093, China*

(Received 22 May 2017; accepted 27 June 2017; published online 10 July 2017)

The two-dimensional electron gas (2DEG) at the non-isostructural interface between spinel γ-Al_2O_3 and perovskite $SrTiO_3$ is featured by a record electron mobility among complex oxide interfaces in addition to a high carrier density up to the order of $10^{15}\,cm^{-2}$. Herein, we report on the patterning of 2DEG at the γ-Al_2O_3/$SrTiO_3$ interface grown at 650 °C by pulsed laser deposition using a hard mask of $LaMnO_3$. The patterned 2DEG exhibits a critical thickness of 2 unit cells of γ-Al_2O_3 for the occurrence of interface conductivity, similar to the unpatterned sample. However, its maximum carrier density is found to be approximately $3 \times 10^{13}\,cm^{-2}$, much lower than that of the unpatterned sample ($\sim 10^{15}\,cm^{-2}$). Remarkably, a high electron mobility of approximately $3600\,cm^2\,V^{-1}s^{-1}$ was obtained at low temperatures for the patterned 2DEG at a carrier density of $\sim 7 \times 10^{12}\,cm^{-2}$, which exhibits clear Shubnikov-de Haas quantum oscillations. The patterned high-mobility 2DEG at the γ-Al_2O_3/$SrTiO_3$ interface paves the way for the design and application of spinel/perovskite interfaces for high-mobility all-oxide electronic devices. *Published by AIP Publishing.*
[http://dx.doi.org/10.1063/1.4993165]

Two-dimensional electron gases (2DEGs) formed at $SrTiO_3$-based interfaces provide a rich platform for fundamental research and device applications.[1] Their unique properties such as superconductivity,[2] magnetism,[3] high carrier mobility,[4] and sensitivity to light illumination[5] have drawn extensive interest. Among complex oxide interfaces, the isostructural perovskite-type $LaAlO_3$/$SrTiO_3$ (LAO/STO) interface is so far the most investigated system. Nevertheless, although extensive research has been carried out on this system, the typical mobility remains $\sim 1000\,cm^2\,V^{-1}s^{-1}$ or less (at low temperatures). Recently, a new 2DEG was discovered at the non-isostructural interface between perovskite STO and spinel γ-Al_2O_3 (GAO) with compatible oxygen sublattices.[6–10] Remarkably, the GAO/STO heterostructure shows much higher electron mobility (greater than $140\,000\,cm^2\,V^{-1}s^{-1}$) and extremely high carrier densities of more than $10^{15}\,cm^{-2}$.[6] Moreover, micro-patterning of complex oxides with conventional semiconductor techniques is highly needed to meet the promise for post-silicon electronics, i.e., to integrate complex oxide interfaces into integrated chips and spintronics devices. Although nanopatterned interfaces by conducting-atomic force microscopy (c-AFM)[11] have been demonstrated, micro-patterning of complex oxides has been proven to be challenging. This so far has been implemented primarily using amorphous $LaAlO_3$- or AlO_x-hard masks[12–15]or Ar-ion beam irradiation.[16] These processes, generally, require additional care as the deposition of amorphous LAO or AlO_x layers or the Ar-ion irradiation can by itself induce conductivity in STO,[7,17,18] leading to failure of the patterned devices. In contrast to the chemically active hard masks or irradiation, a chemically inert mask of manganites (which shows little redox reaction with STO[16]) has also been applied to pattern oxide interfaces, particularly the 2DEG in a-LAO/STO system formed at room temperature.[19] Whether this technique can also be applicable to pattern the 2DEG grown at high temperatures, where significant oxygen exchange and cation intermixing across the interface could occur, is yet to be investigated.

In this letter, we present the high-temperature patterning of the 2DEG at the GAO/STO interface with $LaMnO_3$ (LMO) as a hard mask. The high-mobility 2DEG is conserved in the patterned structures, but a much suppressed carrier density was obtained, probably due to the presence of the manganite hard mask. Moreover, clear quantum oscillations were observed at these patterned spinel/perovskite interfaces. The balance between the high mobility and low carrier density in patterned GAO/STO interfaces is a step forward to integrate high quality oxide interfaces in future devices.

The Hall bar devices were fabricated by initially depositing an amorphous $LaMnO_3$ (a-LMO) layer (50 nm) (see Fig. 1) on TiO_2-terminated STO (001) substrates[20,21] by pulsed laser deposition (PLD) at room temperature. The a-LMO/STO heterointerface was found to be insulating regardless of the deposition oxygen pressure. Optical lithography was then used to create patterned structures with microscale dimension. Subsequently, the exposed a-LMO was removed by selective wet chemical etching so that the bare STO is patterned in a Hall bar geometry.[22,23] After removing the residual photoresist with a lift-off procedure, the patterned substrate was transferred into the PLD chamber for the

a)Authors to whom correspondence should be addressed: xfwang@nju.edu.cn and yunc@dtu.dk

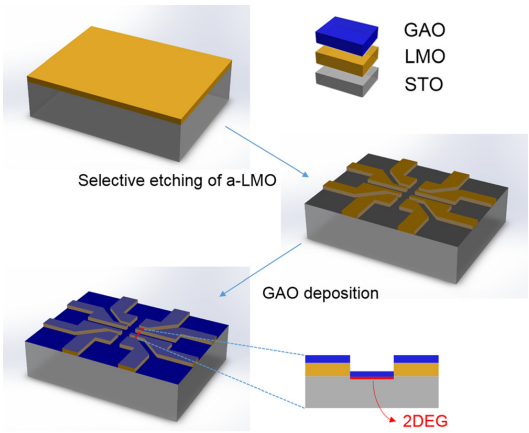

FIG. 1. Schematic illustration of the patterning process for a GAO/STO Hall bar device. The conductive interface of 2DEG is only formed at the interface between GAO and STO, which is illustrated by the red layer in the cross-section.

deposition of GAO. The growth of GAO was performed at 650 °C with an oxygen pressure of 1×10^{-5} mbar, and the samples were cooled down at the growth oxygen pressure at a rate of 15 °C/min to room temperature after deposition. For comparison, unpatterned $5 \times 5\,mm^2$ GAO/STO reference samples were prepared under the same growth conditions and measured in the van der Pauw geometry. For transport measurements in both Hall-bar and van der Pauw geometry, ultrasonically wire-bonded aluminum wires were used as electrodes. For the patterned sample, the film thickness, t, was controlled by the growth rate, which was determined with the unpatterned sample by reflection high-energy electron diffraction (RHEED) oscillations.[6] By carefully optimizing the film growth conditions, t can be controlled down to a quarter of the unit cell (uc), i.e., $a/4 \sim 0.2$ nm.[6,24]

Figure 2(a) shows an optical micrograph of a typical patterned device where the width of the Hall bar is 50 μm and length between two voltage probes is 500 μm. A six-probe configuration of the Hall bar allows for the measurement of both longitudinal and Hall resistances at the same time. Figure 2(b) shows the temperature-dependent sheet resistances of GAO/STO Hall bar devices. The interfacial conduction depends critically on the thickness of the GAO film. When the thickness of GAO is thinner than 1.75 uc, the interface is highly insulating. At $t = 1.75$ uc, the sample becomes metallic but shows carrier freezing out at $T \leq 100$ K. For $t \geq 2$ uc, the interfaces show metallic behaviors over the whole temperature regime down to the base temperature of 2 K. As shown in Figs. 2(c) and 2(d), the corresponding temperature-dependent sheet carrier density, n_s, and mobility, μ, are deduced from the measurements of the linear Hall coefficient R_H, using $n_s = -1/R_H e$. The carrier density seems to be separated into two groups, samples with a similar carrier density in the range of 2–2.5 uc ($7–8 \times 10^{12}\,cm^{-2}$) and samples with the carrier density between 2.5 and 10 uc ($2–3 \times 10^{13}\,cm^{-2}$) (Fig. 2(c)). The highest mobility of $3600\,cm^2\,V^{-1}s^{-1}$ at 2 K was obtained for $t = 2.25$ uc ($n_s \sim 7 \times 10^{12}\,cm^{-2}$). Additionally, the patterned 2DEGs with $\mu > 1000\,cm^2\,V^{-1}s^{-1}$ at 2 K are only detected in the thickness range of 2 uc $\leq t \leq$ 2.5 uc. This thickness range of high-mobility is comparable to the 2 uc $\leq t \leq$ 3 uc range observed for unpatterned samples.[6]

Figures 3(a) and 3(b) summarize the thickness dependent sheet conductance (σ_s) and the carrier density (n_s), respectively, of the patterned samples. When t is increased from 1 uc to 2 uc, the σ_s and n_s values of interfaces jump more than 4 orders, accompanied with the sharp transition from the insulating state to the metallic state. This critical thickness behavior of Hall bar interfaces is in good agreement with the unpatterned GAO/STO interface.[6] However, as illustrated in Fig. 3(b), the n_s of the pattered samples is always in the range of 0.7– $3 \times 10^{13}\,cm^{-2}$, although they were deposited at an oxygen pressure of 10^{-5} mbar. This is dramatically different from the unpatterned sample, where a peak carrier density of up to $1 \times 10^{15}\,cm^{-2}$ is obtained in the range of 2 uc $\leq t \leq$ 3 uc.[6] Notably, the critical thickness dependence of the carrier density for both the patterned and unpatterned samples is highly reproducible. The suppression of carrier density in patterned samples is most likely due to the presence of the manganite mask layer. This is because the GAO/STO heterostructure is one of the typical STO-based heterostructures, where the interface conductivity originates mainly from oxygen vacancies due to interfacial redox reactions.[6,7,9,10] At high deposition temperatures, the oxygen ions in STO can diffuse over many micrometers in minutes.[25] Therefore, a significant transfer of oxygen from STO to GAO is expected. This could

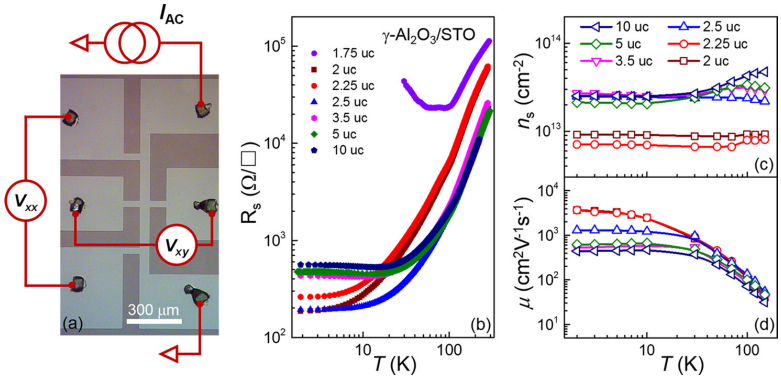

FIG. 2. (a) Optical microscopy image of the Hall bar device with a channel width of 50 μm and a distance between longitudinal voltage probes 500 μm apart. (b) Temperature dependence of the sheet resistance for the interface conduction at different GAO thicknesses. (c) and (d) Temperature dependence of carrier density (n_s) and electron Hall mobility (μ), respectively, for the interface conduction at different GAO thicknesses.

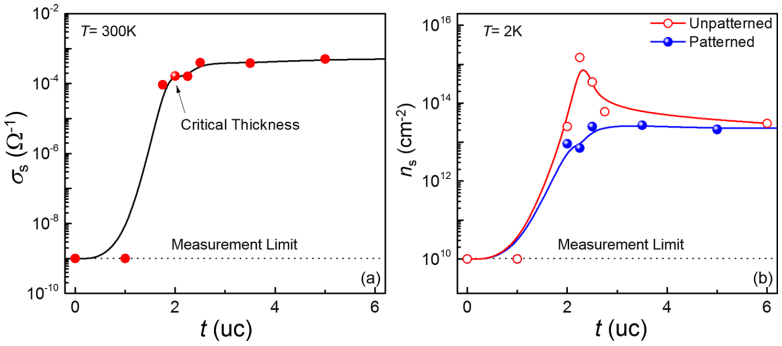

FIG. 3. (a) Thickness-dependent sheet conductance measured at 300 K. (b) Comparison of thickness-dependent carrier density between patterned Hall bar devices and unpatterned van der Pauw devices.

account for the high concentration of oxygen vacancies and high density of charge carriers at the interface of the unpatterned GAO/STO. Different from the GAO film which can promote the formation of oxygen vacancies in STO by chemical redox reactions,[17] the LMO film is one of the most outstanding oxides which show no degradation of the STO. This is due to the fact that the bottom of the LMO conduction band is about 1 eV lower than that of STO, and if any reduction occurs, it would preferably be on the LMO side, i.e., the reconstructed electrons will be first transferred to the Mn sublattice before filling the electronic shell of Ti ions.[4,26] Moreover, LMO could activate the oxygen uptaking in STO due to its catalytic activity for oxygen reduction reaction at high temperatures.[27] In this context, much less oxygen vacancies are expected in the patterned GAO/STO and thus the suppressed carrier density. Additionally, the change in the profile of oxygen vacancies could also account for the difference in mobility between patterned and unpatterned samples.

Finally, the high mobility of our patterned 2DEG together with the low carrier density is further confirmed by experimental observation of Shubnikov-de Haas (SdH) oscillations.[6,28,29] Figure 4(a) shows the longitudinal resistance of the $t = 2.25$ uc sample. The magnetic field (up to 16 T) was applied perpendicular to the interface at $T = 2$ K. The oscillations superimposed on a positive background are visible directly in the raw magnetoresistance data for magnetic fields larger than 6 T. After removing a smooth background, the magnetoresistance exhibits oscillations presented in Fig. 4(b), which are periodic with $1/B$. The inset in Fig. 4(b) shows the position of the oscillation peak in $1/B$ versus the effective Landau level. The fitted line (blue dashed line) indicates the SdH frequency of $F = 71.8$ T. The carrier density can be estimated from SdH oscillation by using following the formula: $n_{2D} = g_V g_S eF/h$, where g_V, g_S, and F are the valley degeneracy, spin degeneracy, and SdH frequency, respectively. By taking a single valley and $g_S = 2$,[6] the carrier density was calculated to be $n_{2D} = 3.47 \times 10^{12}\,\mathrm{cm}^{-2}$. Notably, this carrier density deduced by the SdH oscillation is slightly lower than that obtained from the Hall effect ($7 \times 10^{12}\,\mathrm{cm}^{-2}$), which is common for 2DEG in STO-based heterointerfaces, such as those at the LAO/STO interface[28,29] and in La- or Nb-doped STO heterostructures.[30,31] This discrepancy is either due to the fact that a fraction of carriers measured by the Hall effect do not satisfy the conditions for the SdH oscillation[6,28–30,32] or due to the presence of multiple quantum wells.[29,33]

In conclusion, we have demonstrated the fabrication of patterned 2DEG at GAO/STO interfaces with high mobility using a manganite hard mask. Compared with unpatterned GAO/STO heterostructure analogues, suppressed carrier density is obtained in the patterned interface. The relatively high electron mobility and low carrier density enable the study of quantum oscillations at GAO/STO interfaces. This patterning method provides not only the possibility of making patterned interface devices with high mobility but also a step forward to integrate high quality spinel/perovskite oxide interfaces for device applications.

We thank Jørgen Stubager for the technical assistance. Wei Niu thanks the support by China Scholarship Council. X.F.W. acknowledges the financial support from the National Key Projects for Basic Research of China under Grant No. 2014CB921103 and the Collaborative Innovation Center of Solid-State Lighting and Energy-Saving Electronics.

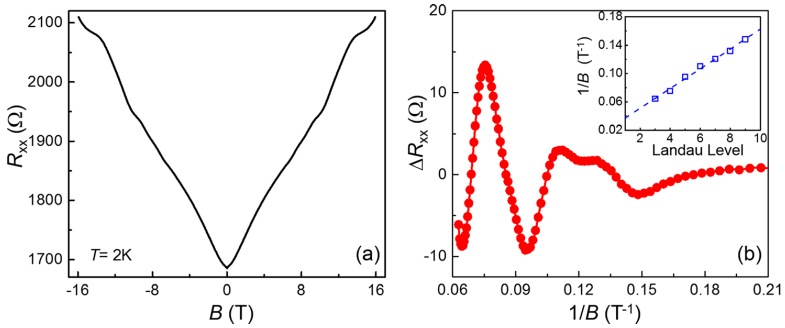

FIG. 4. Shubnikov-de Haas oscillations of the conduction at the GAO/STO interface. (a) Longitudinal resistance, R_{xx}, as a function of the magnetic field with SdH oscillations at 2 K for the 2.25 uc sample. (b) Amplitude of the SdH oscillation versus the reciprocal magnetic field. The inset shows the index plots of $1/B$ versus the effective Landau level.

[1]A. Ohtomo and H. Y. Hwang, Nature **427**, 423 (2004).
[2]N. Reyren, S. Thiel, A. D. Caviglia, L. Fitting Kourkoutis, G. Hammerl, C. Richter, C. W. Schneider, T. Kopp, A.-S. Rüetschi, D. Jaccard, M. Gabay, D. A. Muller, J.-M. Triscone, and J. Mannhart, Science **317**, 1196 (2007).
[3]J. A. Bert, B. Kalisky, C. Bell, M. Kim, Y. Hikita, H. Y. Hwang, and K. A. Moler, Nat. Phys. **7**, 767 (2011).
[4]Y. Z. Chen, F. Trier, T. Wijnands, R. J. Green, N. Gauquelin, R. Egoavil, D. V. Christensen, G. Koster, M. Huijben, N. Bovet, S. Macke, F. He, R. Sutarto, N. H. Andersen, J. A. Sulpizio, M. Honig, G. E. Prawiroatmodjo, T. S. Jespersen, S. Linderoth, S. Ilani, J. Verbeeck, G. Van Tendeloo, G. Rijnders, G. A. Sawatzky, and N. Pryds, Nat. Mater. **14**, 801 (2015).
[5]Y. Lei, Y. Li, Y. Z. Chen, Y. W. Xie, Y. S. Chen, S. H. Wang, J. Wang, B. G. Shen, N. Pryds, H. Y. Hwang, and J. R. Sun, Nat. Commun. **5**, 5554 (2014).
[6]Y. Z. Chen, N. Bovet, F. Trier, D. V. Christensen, F. M. Qu, N. H. Andersen, T. Kasama, W. Zhang, R. Giraud, J. Dufouleur, T. S. Jespersen, J. R. Sun, A. Smith, J. Nygard, L. Lu, B. Buchner, B. G. Shen, S. Linderoth, and N. Pryds, Nat. Commun. **4**, 1371 (2013).
[7]Y. Z. Chen, N. Bovet, T. Kasama, W. W. Gao, S. Yazdi, C. Ma, N. Pryds, and S. Linderoth, Adv. Mater. **26**, 1462 (2014).
[8]Y. Cao, X. Liu, P. Shafer, S. Middey, D. Meyers, M. Kareev, Z. Zhong, J.-W. Kim, P. J. Ryan, E. Arenholz, and J. Chakhalian, npj Quantum Mater. **1**, 16009 (2016).
[9]K. J. Kormondy, A. B. Posadas, T. Q. Ngo, S. Lu, N. Goble, J. Jordan-Sweet, X. P. A. Gao, D. J. Smith, M. R. McCartney, J. G. Ekerdt, and A. A. Demkov, J. Appl. Phys. **117**, 095303 (2015).
[10]D. V. Christensen, F. Trier, M. von Soosten, G. E. D. K. Prawiroatmodjo, T. S. Jespersen, Y. Z. Chen, and N. Pryds, Appl. Phys. Lett. **109**, 021602 (2016).
[11]G. Cheng, M. Tomczyk, A. B. Tacla, H. Lee, S. Lu, J. P. Veazey, M. Huang, P. Irvin, S. Ryu, C.-B. Eom, A. Daley, D. Pekker, and J. Levy, Phys. Rev. X **6**, 041042 (2016).
[12]N. Banerjee, M. Huijben, G. Koster, and G. Rijnders, Appl. Phys. Lett. **100**, 041601 (2012).
[13]D. Stornaiuolo, S. Gariglio, N. J. G. Couto, A. Fête, A. D. Caviglia, G. Seyfarth, D. Jaccard, A. F. Morpurgo, and J. M. Triscone, Appl. Phys. Lett. **101**, 222601 (2012).
[14]C. W. Schneider, S. Thiel, G. Hammerl, C. Richter, and J. Mannhart, Appl. Phys. Lett. **89**, 122101 (2006).
[15]Y. Zhou, P. Wang, Z. Z. Luan, Y. J. Shi, S. W. Jiang, H. F. Ding, and D. Wu, Appl. Phys. Lett. **110**, 141603 (2017).
[16]A. Pier Paolo, K. Alexey, T. Nikolina, O. Eva, C. Tord, and W. Dag, Appl. Phys. Lett. **102**, 201610 (2013).
[17]Y. Chen, N. Pryds, J. E. Kleibeuker, G. Koster, J. Sun, E. Stamate, B. Shen, G. Rijnders, and S. Linderoth, Nano Lett. **11**, 3774 (2011).
[18]D. Kan, T. Terashima, R. Kanda, A. Masuno, K. Tanaka, S. Chu, H. Kan, A. Ishizumi, Y. Kanemitsu, Y. Shimakawa, and M. Takano, Nat. Mater. **4**, 816 (2005).
[19]F. Trier, G. E. D. K. Prawiroatmodjo, M. von Soosten, D. V. Christensen, T. S. Jespersen, Y. Z. Chen, and N. Pryds, Appl. Phys. Lett. **107**, 191604 (2015).
[20]Y. Z. Chen and N. Pryds, Thin Solid Films **519**, 6330 (2011).
[21]W. Niu, M. Gao, X. Wang, F. Song, J. Du, X. Wang, Y. Xu, and R. Zhang, Sci. Rep. **6**, 26081 (2016).
[22]G. Bridoux, J. Barzola-Quiquia, F. Bern, W. Bohlmann, I. Vrejoiu, M. Ziese, and P. Esquinazi, Nanotechnology **23**, 085302 (2012).
[23]K. Zhang, K. Du, H. Liu, X.-G. Zhang, F. Lan, H. Lin, W. Wei, Y. Zhu, Y. Kou, J. Shao, J. Niu, W. Wang, R. Wu, L. Yina, E. W. Plummer, and J. Shen, Proc. Natl. Acad. Sci. U.S.A. **112**, 9558 (2015).
[24]P. Schütz, F. Pfaff, P. Scheiderer, M. Sing, and R. Claessen, Appl. Phys. Lett. **106**(6), 063108 (2015).
[25]J. Mannhart and D. G. Schlom, Nature **430**, 620 (2004).
[26]Y. Z. Chen, Y. L. Gan, D. V. Christensen, Y. Zhang, and N. Pryds, J. Appl. Phys. **121**(9), 095305 (2017).
[27]Y. M. Choi, D. S. Mebane, M. C. Lin, and M. Liu, Chem. Mater. **19**, 1690 (2007).
[28]A. D. Caviglia, S. Gariglio, C. Cancellieri, B. Sacépé, A. Fête, N. Reyren, M. Gabay, A. F. Morpurgo, and J. M. Triscone, Phys. Rev. Lett. **105**, 236802 (2010).
[29]F. Trier, G. E. Prawiroatmodjo, Z. Zhong, D. V. Christensen, M. von Soosten, A. Bhowmik, J. M. Lastra, Y. Chen, T. S. Jespersen, and N. Pryds, Phys. Rev. Lett. **117**, 096804 (2016).
[30]B. Jalan, S. Stemmer, S. Mack, and S. J. Allen, Phys. Rev. B **82**, 081103(R) (2010).
[31]Y. Kozuka, M. Kim, C. Bell, B. G. Kim, Y. Hikita, and H. Y. Hwang, Nature **462**, 487 (2009).
[32]J. Son, P. Moetakef, B. Jalan, O. Bierwagen, N. J. Wright, R. Engel-Herbert, and S. Stemmer, Nat. Mater. **9**, 482 (2010).
[33]Y. Xie, C. Bell, M. Kim, H. Inoue, Y. Hikita, and H. Y. Hwang, Solid State Commun. **197**, 25 (2014).

XX

ARTICLE

P. Schütz, **D. V. Christensen** *et al.*
Microscopic origin of the mobility enhancement at a spinel/perovskite oxide heterointerface revealed by photoemission spectroscopy
Physical Review B 96, 161409 (2017)

Transparent electronics
Photo: Felix Trier

PHYSICAL REVIEW B **96**, 161409(R) (2017)

Microscopic origin of the mobility enhancement at a spinel/perovskite oxide heterointerface revealed by photoemission spectroscopy

P. Schütz,[1] D. V. Christensen,[2] V. Borisov,[3] F. Pfaff,[1] P. Scheiderer,[1] L. Dudy,[1] M. Zapf,[1] J. Gabel,[1] Y. Z. Chen,[2] N. Pryds,[2] V. A. Rogalev,[1,4] V. N. Strocov,[4] C. Schlueter,[5] T.-L. Lee,[5] H. O. Jeschke,[3] R. Valentí,[3] M. Sing,[1] and R. Claessen[1]

[1]*Physikalisches Institut and Röntgen Center for Complex Material Systems (RCCM), Universität Würzburg, Am Hubland, D-97074 Würzburg, Germany*

[2]*Department of Energy Conversion and Storage, Technical University of Denmark, DK-4000 Roskilde, Denmark*

[3]*Institute of Theoretical Physics, Goethe University Frankfurt am Main, D-60438 Frankfurt am Main, Germany*

[4]*Swiss Light Source, Paul Scherrer Institut, CH-5232 Villigen, Switzerland*

[5]*Diamond Light Source, Harwell Sciene and Innovation Campus, Oxfordshire OX11 0DE, United Kingdom*

(Received 5 April 2017; revised manuscript received 11 August 2017; published 27 October 2017)

The spinel/perovskite heterointerface γ-$Al_2O_3/SrTiO_3$ hosts a two-dimensional electron system (2DES) with electron mobilities exceeding those in its all-perovskite counterpart $LaAlO_3/SrTiO_3$ by more than an order of magnitude, despite the abundance of oxygen vacancies which act as electron donors as well as scattering sites. By means of resonant soft x-ray photoemission spectroscopy and *ab initio* calculations, we reveal the presence of a sharply localized type of oxygen vacancies at the very interface due to the local breaking of the perovskite symmetry. We explain the extraordinarily high mobilities by reduced scattering resulting from the preferential formation of interfacial oxygen vacancies and spatial separation of the resulting 2DES in deeper $SrTiO_3$ layers. Our findings comply with transport studies and pave the way towards defect engineering at interfaces of oxides with different crystal structures.

DOI: 10.1103/PhysRevB.96.161409

The search for high-mobility two-dimensional electron systems (2DESs) at atomically engineered transition metal oxide heterointerfaces is an ongoing endeavor, since the strong electronic correlations in partially occupied *d* orbitals promise an even richer physical behavior than found in conventional semiconductor heterostructures [1]. However, the charge carrier mobilities in the most prominent complex oxide 2DES, found at the perovskite-perovskite heterointerface between the band insulators $LaAlO_3$ and $SrTiO_3$, still fall short of those in semiconductors by several orders of magnitude [2]. The hitherto-highest mobility in $SrTiO_3$-based structures (140 000 $cm^2/V\,s$ at 2 K) is found at the spinel/perovskite heterointerface between γ-Al_2O_3 thin films and $SrTiO_3$ [3,4], thus making it a promising candidate for applications in oxide electronics or fundamental studies of quantum transport.

The mechanism of 2DES formation in $SrTiO_3$-based heterostructures has been under debate for many years. The existence of a critical film thickness for metallicity at the epitaxial $LaAlO_3/SrTiO_3$ heterointerface has been associated with the polar discontinuity at the interface and the concomitant buildup of an electrostatic potential gradient as a function of film thickness, which may be countered by a charge redistribution to the interface [3,5–8]. Additionally, substantial oxygen vacancy (V_O) doping within the $SrTiO_3$ substrate may occur, which is the dominant source of charge carriers in 2DESs discovered in $SrTiO_3$ interfaced with amorphous overlayers [9,10] and bare $SrTiO_3$ surfaces irradiated with ultraviolet light [11–13]. In the case of γ-$Al_2O_3/SrTiO_3$, it has been argued that its 2DES originates exclusively from oxygen vacancies in $SrTiO_3$, which are formed due to redox reactions [3]. However, it remains unclear how high mobilities can be achieved, when $SrTiO_3$ hosts both conduction electrons and oxygen vacancies, which act as scattering sites. Here, we reveal the existence of a specific type of oxygen vacancies at the spinel/perovskite γ-$Al_2O_3/SrTiO_3$ interface by means of soft x-ray resonant photoemission spectroscopy (SX-ResPES) and *ab initio* calculations, and propose a spatial separation of the dopants (oxygen vacancies) and the 2DES as the origin for its exceptionally high mobility.

SX-ResPES experiments were performed at the combined soft and hard x-ray beamline I09, Diamond Light Source and at the soft x-ray beamline ADRESS, Swiss Light Source [14,15]. Theoretical calculations were performed based on the density functional theory in the generalized gradient approximation (GGA) [16–24] by explicitly including oxygen vacancies in a γ-$Al_2O_3/SrTiO_3$ superlattice and a $SrTiO_3$ supercell. For theoretical and experimental details including sample fabrication, see the Supplemental Material [25].

While the γ-$Al_2O_3/SrTiO_3$ heterointerface can host a 2DES with extraordinarily high electron mobilities upon careful control of the deposition parameters [3], for a wide range of growth conditions, a lower-mobility 2DES forms [4]. We have found that such lower mobilities can be increased postgrowth by gentle low-temperature annealing or prolonged storage at room temperature, as shown in Fig. 1(a). The electron density of a γ-$Al_2O_3/SrTiO_3$ sample obtained from standard Hall measurements in the van der Pauw geometry [3] remains largely unaffected in this process. In contrast, the mobility at 2 K and the residual resistance ratio $[R_S(300\text{ K})/R_S(2\text{ K})]$ increase by roughly a factor of 4 (12 000–40 000 $cm^2/V\,s$ and 730–3200, respectively).

Since the movement of larger cations is frozen at room temperature [26], cation diffusion can be excluded as the driving mechanism. In contrast, the diffusion of lighter oxygen anions (and hence oxygen vacancies) is feasible and may affect the transport properties at cryogenic temperatures, where electron scattering by ionized donors is the dominant effect [27]. Since the total amount of oxygen vacancies, as reflected in

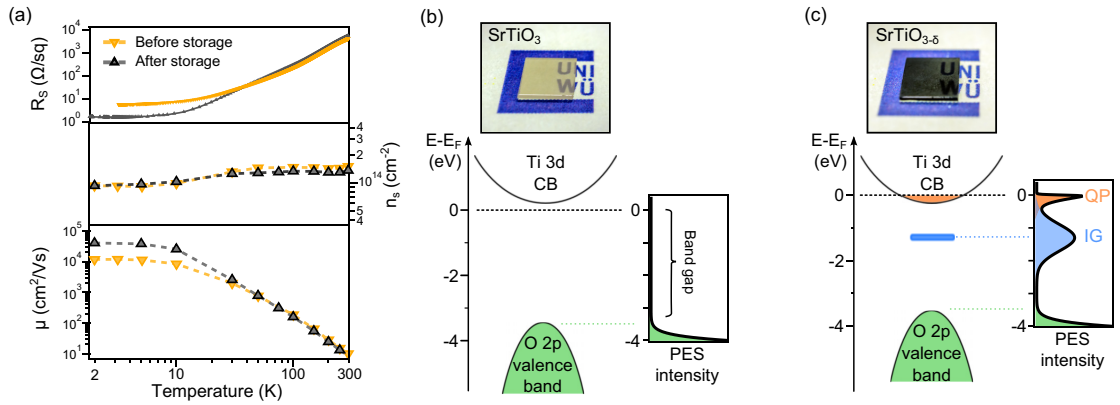

FIG. 1. (a) Sheet resistivity (R_S), carrier density (n_S), and mobility (μ) as a function of temperature T of a γ-$Al_2O_3/SrTiO_3$ heterostructure before and after 6 months of storage at room temperature in a vacuum desiccator. (b) Photograph, electronic structure, and corresponding schematic photoemission spectrum of stoichiometric $SrTiO_3$ and (c) oxygen-deficient $SrTiO_{3-\delta}$.

the charge carrier density, remains constant, one may speculate that a gradual redistribution of oxygen vacancy scattering sites away from the confined 2DES may be the cause for the mobility enhancement.

As shown in Fig. 1(b), nominally stoichiometric $SrTiO_3$ is an intrinsically n-doped wide-gap semiconductor with the Fermi energy pinned close to the conduction band minimum [28]. Upon the introduction of oxygen vacancies, two electrons per vacancy become released and the electronic structure of $SrTiO_3$ changes, as depicted in Fig. 1(c). A fraction of donor electrons becomes trapped in a localized Ti $3d$-derived state next to the vacancy site (blue) and the rest is donated into the Ti $3d$ conduction band (orange) to become itinerant [29,30]. The resulting photoemission spectrum comprises a dispersive feature cut off by the Fermi-Dirac distribution at the chemical potential, the quasiparticle peak (QP), and a broad nondispersive in-gap peak (IG), which can be seen as a hallmark for the presence of oxygen vacancies in $SrTiO_3$ [31–33].

Here, we use synchrotron-based soft x-ray resonant photoemission spectroscopy (SX-ResPES) at the Ti L edge to enhance the spectroscopic contrast for the Ti $3d$-derived states at the buried interface [34,35]. The inset of Fig. 2(a) shows the PES spectra of $LaAlO_3/SrTiO_{3-\delta}$ and γ-$Al_2O_3/SrTiO_{3-\delta}$ at the resonance condition. Despite an overall similarity, i.e., the presence of a QP and an IG peak, the latter is significantly broader and asymmetric for γ-$Al_2O_3/SrTiO_{3-\delta}$, signaling a superposition of (at least) two peaks. Indeed, upon tuning the photon energy across the Ti L absorption edge as shown in Fig. 2(a), two peaks at $E \approx -1.2$ eV (in-gap feature A, IGA) and -2.1 eV (IGB) can be distinguished by their shifted resonances ($h\nu = 458.2$ and 459.1 eV for IGB and IGA, respectively). Note that in these spectra the quasiparticle was suppressed by a specific choice of the measurement geometry [25].

It is well known that the exposure of maximal-valence transition metal oxides such as $SrTiO_3$ to high-intensity synchrotron light causes oxygen vacancy formation [36]. This can be counteracted by simultaneous dosing with molecular oxygen, which dissociates in the high-intensity x-ray beam and diffuses as atomic species into the substrate where it annihilates vacancies [13,37]. As shown in Fig. 2(b), using a metal capillary to direct oxygen onto the sample, IGB can be quenched entirely, whereas IGA is reduced, yet remains finite even for the highest possible oxygen flow. Thus, we conclude that both IG peaks represent oxygen vacancy sites, but apparently of different kinds. The different susceptibility to oxygen dosing indicates a different vertical spatial distribution of the two kinds of vacancies, i.e., the completely quenched IGB has its origin in closer proximity to the interface. Note that the shifted O $2p$ valence band onset is due to variable band bending in $SrTiO_3$ and a concomitant change of the band alignment at the interface.

By acquiring the photoemission signal under various emission angles θ with respect to the surface normal, the effective probing depth can be changed as $\lambda_{\text{eff}} = \lambda \cos\theta$ [38], where λ is the inelastic mean free path. Figure 2(c) shows the resonant Ti $3d$ spectral weight as a function of λ_{eff}, ranging from 1.2 nm (maximum bulk sensitivity, $\theta = 0°$) to 0.8 nm (maximum interface sensitivity, $\theta = 45°$) [39]. Additionally, the Ti $2p$ core level signal excited by the second-order light from the undulator is seen above the chemical potential and serves as a bulk titanium reference signal. The relative spectral weights were extracted from Gaussian fits and are shown in the inset as a function of emission angle. The considerable angle dependence of the IGA-to-IGB-intensity ratio (red) provides evidence for an extraordinarily sharp, vertical separation of the two types of oxygen vacancies, i.e., IGB is situated closer to the interface. Furthermore, IGA scales with the second-order light-induced Ti $2p$ bulk signal (blue), indicating a uniform distribution of IGA states throughout the $SrTiO_3$ substrate (within the information depth of roughly 1.2 nm). We thus readily identify IGA as a signal from bulklike oxygen vacancies situated within the substrate and IGB as a fingerprint of oxygen vacancies at the interface. The existence of *two* distinct types of oxygen vacancies—derived here from PES in a dynamical equilibrium situation inherently different from the near-thermodynamical state probed in transport experiments—

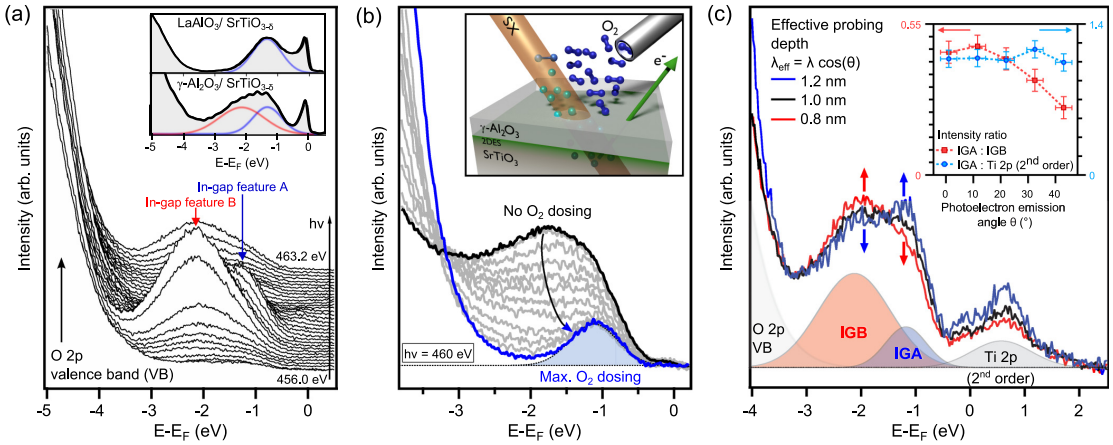

FIG. 2. (a) Photoemission spectra of a γ-$Al_2O_3/SrTiO_3$ heterostructure upon tuning the photon energy across the Ti L absorption edge. Two in-gap features, IGA and IGB, are distinguished by their shifted resonance photon energies. Inset: Comparison between the systems $LaAlO_3/SrTiO_{3-\delta}$ and γ-$Al_2O_3/SrTiO_{3-\delta}$ ($h\nu = 459.4$ eV). (b) Resonant Ti $3d$ spectral weight upon oxygen dosing (schematically depicted in the inset). While IGB becomes quenched entirely, a finite IGA weight remains at maximum dosing. (c) Depth-resolved photoemission spectroscopy of the Ti $3d$ in-gap states and the second-order light-induced Ti $2p$ core level ($h\nu = 459.8$ eV). The spectra are normalized to the spectral weight between $E = -0.5$ and -3.5 eV. Inset: Relative spectral weight as a function of photoemission angle. The strong IGA-to-IGB angle dependence evidences the sharp vertical separation of IGA and IGB.

is nonetheless of high relevance also for the latter situation, as we sketch out in the following.

In a qualitative model, the introduction of a single oxygen vacancy into bulk $SrTiO_3$ results in one itinerant electron in the Ti $3d$ t_{2g} band and one trapped electron in a bonding state derived from adjacent Ti $3d$ $e_g/4p_z$ hybrid states [29,30,40]. Indeed, as shown in Fig. 3(a), the Ti $3d$-projected density of states (PDOS) obtained from GGA+U calculations of a $3 \times 3 \times 3$ $SrTiO_3$ supercell with one oxygen vacancy, using the standard parameters $U = 5$ eV and $J_H = 0.64$ eV, exhibits metallic carriers and an IG state at -1 eV, in good agreement with experiment and the qualitative model. The real-space charge density for a (100) layer cutting through the vacancy and obtained from energy integration of the in-gap state shows a typical Ti $3d$ e_g-based bonding orbital [29], which is strongly localized at the oxygen vacancy and its adjacent Ti atoms.

In $SrTiO_3$-based all-perovskite heterostructures such as $LaAlO_3/SrTiO_3$, all oxygen vacancies in the substrate can be regarded as bulklike to a good approximation. In contrast, the perovskite symmetry is broken at the γ-$Al_2O_3/SrTiO_3$ heterointerface since γ-Al_2O_3 adopts a spinel crystal structure [41–43]. As seen in Fig. 3(b), here, the local ionic coordination of an oxygen vacancy in the uppermost TiO_2 layer (type B) differs significantly from that in deeper, bulklike layers (type A). The peculiar spinel cation sublattice lifts the local C_{4v} symmetry relevant for oxygen vacancies in bulk $SrTiO_3$, likely resulting in states of different orbital compositions [44] and binding energies, as supported by a crystal-field analysis [25].

Figure 3(c) shows GGA+U calculations of a γ-$Al_2O_3/SrTiO_3$ superlattice with one oxygen vacancy in the interfacial TiO_2 layer. The Ti $3d$-projected density of states exhibits two IG peaks (denoted as IGB_1 and IGB_2) at $E \approx -2.3$ and -1.5 eV, that are hosted by the two adjacent inequivalent Ti cations. As expected, the real-space charge density maps corresponding to IGB_1 and IGB_2 show a rather complex d-orbital composition that is, however, reminiscent of e_g-like orbitals. The experimentally observed broad peak at ≈ -2.1 eV (indicated by a guide-to-the-eye curve) results from oxygen vacancy clustering that will occur in any realistic system and leads to a statistical distribution of in-gap states with slightly different binding energies. Note that the formation enthalpy ΔH of single oxygen vacancies located in different $SrTiO_3$ layers exhibits a minimum at the interface [Fig. 3(b)], hence suggesting a favored formation of type B oxygen vacancies and/or diffusion of vacancies from the bulk to the interface. A recent annealing study of γ-$Al_2O_3/SrTiO_3$ indeed identified such diffusion processes, in support of the mechanism proposed here [45].

Figure 4(a) schematically summarizes our experimental and theoretical findings. The peculiar local symmetry breaking at the spinel/perovskite heterointerface γ-$Al_2O_3/SrTiO_3$ results in a unique type of (interfacial) oxygen vacancy neither found in bulk $SrTiO_3$ nor at its perovskite/perovskite counterpart $LaAlO_3/SrTiO_3$. In $SrTiO_3$-based heterostructures oxygen vacancies represent an extrinsic source of electrons [46,47], but also act as strong scatterers for charge carriers when present near the 2DES. As already pointed out by Huijben *et al.*, their deleterious effect on the mobility requires design strategies to remove them from the transport region, e.g., by a postgrowth exposure to an oxygen-rich environment at elevated temperature and possibly an incorporation of a $SrCuO_2$ nanolayer that facilitates oxygen surface exchange ($\mu \approx 50\,000$ cm^2/V s) [48]. However, in contrast to $LaAlO_3/SrTiO_3$, the γ-$Al_2O_3/SrTiO_3$ heterointerface be-

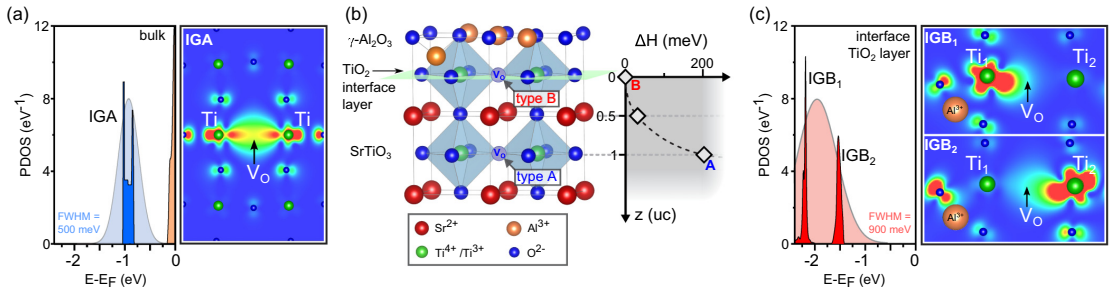

FIG. 3. (a) GGA+U calculated Ti 3d-projected density of states (PDOS) and real-space electron density of bulk $SrTiO_3$ with an isolated oxygen vacancy. The real-space charge map is shown for a (100) layer cutting the oxygen vacancy and obtained through energy integration of the IGA state. The experimentally observed peak is depicted as guide-to-the-eye curve [full width at half maximum (FWHM) = 500 meV]. (b) Local ionic coordination of bulklike (type A) and interfacial (type B) oxygen vacancies in an idealized, unrelaxed spinel/perovskite heterointerface and calculated (relative) formation enthalpy ΔH for oxygen vacancies at and away from the interface. (c) Ti 3d-PDOS and real-space electron density of the γ-$Al_2O_3/SrTiO_3$ interface with one oxygen vacancy in the TiO_2 layer. The real-space charge density is shown for the interfacial TiO_2 layer in direct proximity to the spinel film and obtained through energy integration of the resulting IGB_1 and IGB_2 state, respectively.

comes insulating when exposed to oxygen at high temperatures [3], since its interfacial 2DES essentially stems from oxygen vacancies and lacks an intrinsic component [49] despite a possible polar discontinuity [6,50]. Therefore, a different strategy is needed to achieve high mobilities in γ-$Al_2O_3/SrTiO_3$.

We argue that, as depicted in Fig. 4(a), the oxygen vacancy concentration and distribution in low-mobility γ-$Al_2O_3/SrTiO_3$ heterostructures is similar to that in standard $LaAlO_3/SrTiO_3$ samples with comparable mobilities ($\mu \approx 1000\ cm^2/V\,s$) [3,48]. In contrast, as shown in Fig. 4(b), we propose a different oxygen vacancy distribution in high-mobility γ-$Al_2O_3/SrTiO_3$ heterostructures, where the majority of oxygen vacancies resides at the very interface (type B) and effectively acts as a single layer of electron donors. They provide the itinerant electrons that form the spatially much more extended 2DES. Experimental estimates for its depth from the interface range from 15 [6] to 75 Å [51], where the amount of bulklike (type A) oxygen defects is strongly suppressed. Reminiscent of modulation-doped semiconductor structures, this spatial separation of ionized donor scattering sites and the 2DES results in a significant mobility enhancement and hence reconciles the coexistence of high mobilities with the abundance of oxygen vacancies. Note that an additional contribution to the mobility enhancement may be the increased electronic screening of electron-phonon interactions, that suppresses the formation of polarons with an enhanced effective mass in $SrTiO_3$-based structures [52–54].

Our model also offers a natural explanation for the extremely narrow parameter window for the formation of a high-mobility 2DES [4]. Pulsed laser deposition (PLD) of γ-Al_2O_3 thin films on $SrTiO_3$ results in an oxygen vacancy distribution, which is determined by the intricate interplay between bulk and interface oxygen vacancy formation during the deposition process and by their redistribution during cooldown. Naturally, small deviations from the optimum growth conditions (e.g., oxygen pressure, temperature, and laser fluency) will result in

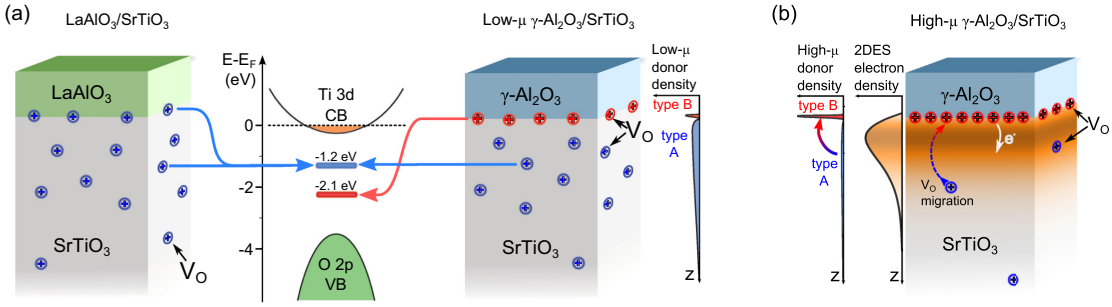

FIG. 4. (a) Schematic comparison of oxygen vacancy distribution and energetics in $LaAlO_3/SrTiO_3$ and low-mobility γ-$Al_2O_3/SrTiO_3$. Possible intrinsic doping mechanisms associated with the polar discontinuity have been omitted here. (b) Proposed mechanism for high-mobility conductivity in γ-$Al_2O_3/SrTiO_3$ heterostructures. The interfacial oxygen vacancies act as the dopant layer, which is spatially separated from the 2DES in the deeper-lying layers of $SrTiO_3$, where ionized donor scattering becomes minimized. Gradual oxygen vacancy diffusion towards the interface during annealing or room-temperature storage changes the oxygen vacancy density from the depicted low-μ into a high-μ density distribution.

oxygen vacancies in the 2DES region, enhanced ionized donor scattering, and a lower mobility. Likewise, the postgrowth mobility enhancement during room-temperature storage can be explained by a gradual oxygen vacancy migration towards the energetically favorable interface, as depicted in Fig. 4(b), resulting in a reduced scattering of the 2DES electrons while conserving the total amount of donors.

Oxygen vacancies at the $LaAlO_3/SrTiO_3$ heterointerface have been associated with ferromagnetism, i.e., ordered local magnetic moments trapped at neighboring Ti sites [55,56]. We speculate that oxygen vacancies at the spinel-perovskite γ-$Al_2O_3/SrTiO_3$ interface may also favor magnetic ordering that could qualitatively differ from their deeper-lying counterparts and $LaAlO_3/SrTiO_3$. A careful experimental investigation of the magnetic properties offers a promising path to a more complete insight into the physics of this intriguing system.

This work was supported by the Deutsche Forschungsgemeinschaft (SFB 1170, SFB/TRR 49, FOR 1162, and FOR 1346) and the German Federal Ministry for Education and Research (05K13WW1). We thank G. Sangiovanni for fruitful discussions and D. McCue for his technical support during the DLS I09 beamtimes.

[1] J. Mannhart and D. G. Schlom, Science **327**, 1607 (2010).
[2] S. Thiel, G. Hammerl, A. Schmehl, C. W. Schneider, and J. Mannhart, Science **313**, 1942 (2006).
[3] Y. Z. Chen, N. Bovet, F. Trier, D. V. Christensen, F. M. Qu, N. H. Andersen, T. Kasama, W. Zhang, R. Giraud, J. Dufouleur, T. S. Jespersen, J. R. Sun, A. Smith, J. Nygård, L. Lu, B. Büchner, B. G. Shen, S. Linderoth, and N. Pryds, Nat. Commun. **4**, 1371 (2013).
[4] Y. Z. Chen, N. Bovet, T. Kasama, W. W. Gao, S. Yazdi, C. Ma, N. Pryds, and S. Linderoth, Adv. Mater. **26**, 1462 (2013).
[5] N. Nakagawa, H. Y. Hwang, and D. A. Muller, Nat. Mater. **5**, 204 (2006).
[6] P. Schütz, F. Pfaff, P. Scheiderer, Y. Z. Chen, N. Pryds, M. Gorgoi, M. Sing, and R. Claessen, Phys. Rev. B **91**, 165118 (2015).
[7] L. Yu and A. Zunger, Nat. Commun. **5**, 5118 (2014) .
[8] P. Scheiderer, F. Pfaff, J. Gabel, M. Kamp, M. Sing, and R. Claessen, Phys. Rev. B **92**, 195422 (2015).
[9] G. Herranz, F. Sánchez, N. Dix, M. Scigaj, and J. Fontcuberta, Sci. Rep. **2**, 758 (2012).
[10] Z. Q. Liu, C. J. Li, W. M. Lü, X. H. Huang, Z. Huang, S. W. Zeng, X. P. Qiu, L. S. Huang, A. Annadi, J. S. Chen, J. M. D. Coey, T. Venkatesan, and Ariando, Phys. Rev. X **3**, 021010 (2013).
[11] A. F. Santander-Syro, O. Copie, T. Kondo, F. Fortuna, S. Pailhès, R. Weht, X. G. Qiu, F. Bertran, A. Nicolaou, A. Taleb-Ibrahimi, P. Le Fèvre, G. Herranz, M. Bibes, N. Reyren, Y. Apertet, P. Lecoeur, A. Barthélémy, and M. J. Rozenberg, Nature (London) **469**, 189 (2011).
[12] W. Meevasana, P. D. C. King, R. H. He, S.-K. Mo, M. Hashimoto, A. Tamai, P. Songsiriritthigul, F. Baumberger, and Z.-X. Shen, Nat. Mater. **10**, 114 (2011).
[13] S. M. Walker, F. Y. Bruno, Z. Wang, A. de la Torre, S. Riccó, A. Tamai, T. K. Kim, M. Hoesch, M. Shi, M. S. Bahramy, P. D. C. King, and F. Baumberger, Adv. Mater. **27**, 3894 (2015).
[14] V. N. Strocov, T. Schmitt, U. Flechsig, T. Schmidt, A. Imhof, Q. Chen, J. Raabe, R. Betemps, D. Zimoch, J. Krempasky, X. Wang, M. Grioni, A. Piazzalunga, and L. Patthey, J. Synchrotron Radiat. **17**, 631 (2010).
[15] V. N. Strocov, X. Wang, M. Shi, M. Kobayashi, J. Krempasky, C. Hess, T. Schmitt, and L. Patthey, J. Synchrotron Radiat. **21**, 32 (2013).
[16] J. P. Perdew, K. Burke, and M. Ernzerhof, Phys. Rev. Lett. **77**, 3865 (1996).
[17] P. E. Blöchl, Phys. Rev. B **50**, 17953 (1994).
[18] G. Kresse and D. Joubert, Phys. Rev. B **59**, 1758 (1999).
[19] G. Kresse and J. Furthmüller, Phys. Rev. B **54**, 11169 (1996).
[20] J. Hafner, J. Comput. Chem. **29**, 2044 (2008).
[21] A. I. Liechtenstein, V. I. Anisimov, and J. Zaanen, Phys. Rev. B **52**, R5467 (1995).
[22] K. Koepernik and H. Eschrig, Phys. Rev. B **59**, 1743 (1999).
[23] S. Okamoto, A. J. Millis, and N. A. Spaldin, Phys. Rev. Lett. **97**, 056802 (2006).
[24] L. Bellaiche and D. Vanderbilt, Phys. Rev. B **61**, 7877 (2000).
[25] See Supplemental Material at http://link.aps.org/supplemental/10.1103/PhysRevB.96.161409 for theoretical and experimental details.
[26] F. Gunkel, S. Wicklein, S. Hoffmann-Eifert, P. Meuffels, P. Brinks, M. Huijben, G. Rijnders, R. Waser, and R. Dittmann, Nanoscale **7**, 1013 (2014).
[27] A. Verma, A. P. Kajdos, T. A. Cain, S. Stemmer, and D. Jena, Phys. Rev. Lett. **112**, 216601 (2014).
[28] E. Ertekin, V. Srinivasan, J. Ravichandran, P. B. Rossen, W. Siemons, A. Majumdar, R. Ramesh, and J. C. Grossman, Phys. Rev. B **85**, 195460 (2012).
[29] C. Lin, C. Mitra, and A. A. Demkov, Phys. Rev. B **86**, 161102 (2012).
[30] C. Lin and A. A. Demkov, Phys. Rev. Lett. **111**, 217601 (2013).
[31] Y. Aiura, I. Hase, H. Bando, T. Yasue, T. Saitoh, and D. S. Dessau, Surf. Sci. **515**, 61 (2002).
[32] S. McKeown Walker, A. de la Torre, F. Y. Bruno, A. Tamai, T. K. Kim, M. Hoesch, M. Shi, M. S. Bahramy, P. D. C. King, and F. Baumberger, Phys. Rev. Lett. **113**, 177601 (2014).
[33] G. Berner, M. Sing, H. Fujiwara, A. Yasui, Y. Saitoh, A. Yamasaki, Y. Nishitani, A. Sekiyama, N. Pavlenko, T. Kopp, C. Richter, J. Mannhart, S. Suga, and R. Claessen, Phys. Rev. Lett. **110**, 247601 (2013).
[34] G. Drera, F. Banfi, F. F. Canova, P. Borghetti, L. Sangaletti, F. Bondino, E. Magnano, J. Huijben, M. Huijben, G. Rijnders, D. H. A. Blank, H. Hilgenkamp, and A. Brinkman, Appl. Phys. Lett. **98**, 052907 (2011).
[35] G. Drera, G. Salvinelli, F. Bondino, E. Magnano, M. Huijben, A. Brinkman, and L. Sangaletti, Phys. Rev. B **90**, 035124 (2014).
[36] M. L. Knotek and P. J. Feibelman, Phys. Rev. Lett. **40**, 964 (1978).

[37] L. Dudy, M. Sing, P. Scheiderer, J. D. Denlinger, P. Schütz, J. Gabel, M. Buchwald, C. Schlueter, T.-L. Lee, and R. Claessen, Adv. Mater. **28**, 7443 (2016) .

[38] M. Sing, G. Berner, K. Goß, A. Müller, A. Ruff, A. Wetscherek, S. Thiel, J. Mannhart, S. A. Pauli, C. W. Schneider, P. R. Willmott, M. Gorgoi, F. Schäfers, and R. Claessen, Phys. Rev. Lett. **102**, 176805 (2009).

[39] S. Tanuma, C. J. Powell, and D. R. Penn, Surf. Interface Anal. **35**, 268 (2003).

[40] H. O. Jeschke, J. Shen, and R. Valentí, New J. Phys. **17**, 023034 (2015).

[41] R. S. Zhou and R. L. Snyder, Acta Crystallogr., Sect. B **47**, 617 (1991).

[42] B. Ealet, M. H. Elyakhloufi, E. Gillet, and M. Ricci, Thin Solid Films **250**, 92 (1994).

[43] S.-D. Mo, Y.-N. Xu, and W.-Y. Ching, J. Am. Ceram. Soc. **80**, 1193 (1997).

[44] Y. Cao, X. Liu, P. Shafer, S. Middey, D. Meyers, M. Kareev, Z. Zhong, J.-W. Kim, P. J. Ryan, E. Arenholz, and J. Chakhalian, npj Quantum Mater. **1**, 16009 (2016).

[45] D. V. Christensen, M. von Soosten, F. Trier, T. S. Jespersen, A. Smith, Y. Chen, and N. Pryds, Adv. Electron. Mater. **3**, 1700026 (2017).

[46] M. Huijben, A. Brinkman, G. Koster, G. Rijnders, H. Hilgenkamp, and D. H. A. Blank, Adv. Mater. **21**, 1665 (2009).

[47] J. Gabel, M. Zapf, P. Scheiderer, P. Schütz, L. Dudy, M. Stübinger, C. Schlueter, T.-L. Lee, M. Sing, and R. Claessen, Phys. Rev. B **95**, 195109 (2017).

[48] M. Huijben, G. Koster, M. K. Kruize, S. Wenderich, J. Verbeeck, S. Bals, E. Slooten, B. Shi, H. J. A. Molegraaf, J. E. Kleibeuker, S. van Aert, J. B. Goedkoop, A. Brinkman, D. H. A. Blank, M. S. Golden, G. van Tendeloo, H. Hilgenkamp, and G. Rijnders, Adv. Funct. Mater. **23**, 5240 (2013).

[49] F. Gunkel, S. Hoffmann-Eifert, R. A. Heinen, D. V. Christensen, Y. Z. Chen, N. Pryds, R. Waser, and R. Dittmann, ACS Appl. Mater. Interfaces **9**, 1086 (2016).

[50] D. V. Christensen and A. Smith, Appl. Surf. Sci. **423**, 887 (2017).

[51] M. Yazdi-Rizi, P. Marsik, B. P. P. Mallett, A. Dubroka, D. V. Christensen, Y. Z. Chen, N. Pryds, and C. Bernhard, Europhys. Lett. **113**, 47005 (2016).

[52] Z. Wang, S. McKeown Walker, A. Tamai, Y. Wang, Z. Ristic, F. Y. Bruno, A. de la Torre, S. Riccò, N. C. Plumb, M. Shi, P. Hlawenka, J. Sánchez-Barriga, A. Varykhalov, T. K. Kim, M. Hoesch, P. D. C. King, W. Meevasana, U. Diebold, J. Mesot, B. Moritz, T. P. Devereaux, M. Radovic, and F. Baumberger, Nat. Mater. **15**, 835 (2016).

[53] Y. J. Chang, A. Bostwick, Y. S. Kim, K. Horn, and E. Rotenberg, Phys. Rev. B **81**, 235109 (2010).

[54] C. Cancellieri, A. S. Mishchenko, U. Aschauer, A. Filippetti, C. Faber, O. S. Barišić, V. A. Rogalev, T. Schmitt, N. Nagaosa, and V. N. Strocov, Nat. Commun. **7**, 10386 (2016).

[55] B. Kalisky, J. A. Bert, B. B. Klopfer, C. Bell, H. K. Sato, M. Hosoda, Y. Hikita, H. Y. Hwang, and K. A. Moler, Nat. Commun. **3**, 922 (2012).

[56] N. Pavlenko, T. Kopp, E. Y. Tsymbal, G. A. Sawatzky, and J. Mannhart, Phys. Rev. B **85**, 020407 (2012).

XXI

ARTICLE

W. Niu, Y. Zhang, Y. Gan, **D. V. Christensen** *et al.*
Giant tunability of the two-dimensional electron gas at the interface of γ-Al_2O_3/$SrTiO_3$
Nano Letters 17, 6878 (2017)

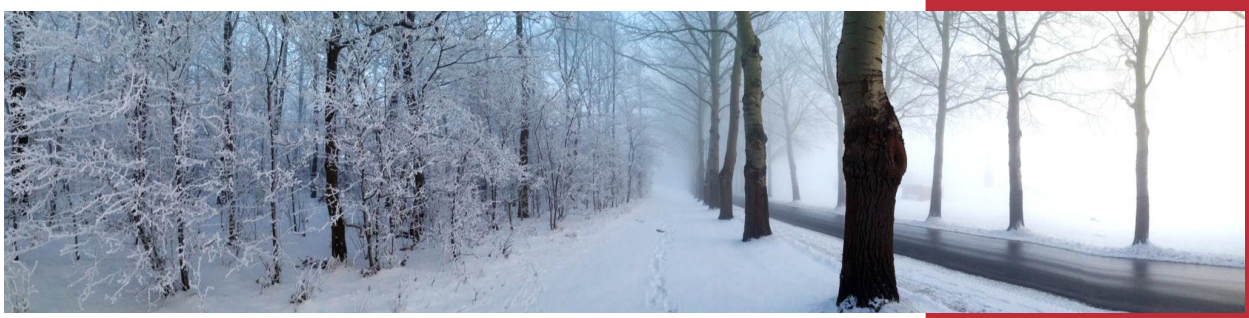

Wintertime at Risø campus
Photo: Dennis Valbjørn Christensen

NANO LETTERS
Cite This: Nano Lett. 2017, 17, 6878-6885
Letter
pubs.acs.org/NanoLett

Giant Tunability of the Two-Dimensional Electron Gas at the Interface of γ-Al_2O_3/$SrTiO_3$

Wei Niu,[†,‡] Yu Zhang,[†] Yulin Gan,[†] Dennis V. Christensen,[†] Merlin V. Soosten,[†] Eduardo J. Garcia-Suarez,[§] Anders Riisager,[§] Xuefeng Wang,*[,‡] Yongbing Xu,[‡] Rong Zhang,[‡] Nini Pryds,[†] and Yunzhong Chen*[,†]

[†]Department of Energy Conversion and Storage, Technical University of Denmark, Risø Campus, 4000 Roskilde, Denmark
[‡]National Laboratory of Solid State Microstructures, School of Electronic Science and Engineering, Nanjing University, 210093 Nanjing, China
[§]Center for Catalysis and Sustainable Chemistry, Department of Chemistry, Technical University of Denmark, 2800 Lyngby, Denmark

Supporting Information

ABSTRACT: Two-dimensional electron gases (2DEGs) formed at the interface between two oxide insulators provide a rich platform for the next generation of electronic devices. However, their high carrier density makes it rather challenging to control the interface properties under a low electric field through a dielectric solid insulator, that is, in the configuration of conventional field-effect transistors. To surpass this long-standing limit, we used ionic liquids as the dielectric layer for electrostatic gating of oxide interfaces in an electric double layer transistor (EDLT) configuration. Herein, we reported giant tunability of the physical properties of 2DEGs at the spinel/perovskite interface of γ-Al_2O_3/$SrTiO_3$ (GAO/STO). By modulating the carrier density thus the band filling with ionic-liquid gating, the system experiences a Lifshitz transition at a critical carrier density of 3.0×10^{13} cm^{-2}, where a remarkably strong enhancement of Rashba spin−orbit interaction and an emergence of Kondo effect at low temperatures are observed. Moreover, as the carrier concentration depletes with decreasing gating voltage, the electron mobility is enhanced by more than 6 times in magnitude, leading to the observation of clear quantum oscillations. The great tunability of GAO/STO interface by EDLT gating not only shows promise for design of oxide devices with on-demand properties but also sheds new light on the electronic structure of 2DEG at the nonisostructural spinel/perovskite interface.

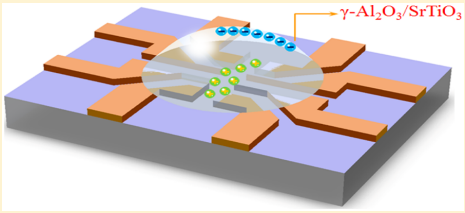

KEYWORDS: *Two-dimensional electron gas, oxide interfaces, ionic liquid, spin−orbital coupling, Lifshitz transition*

The metallic interface between two insulating oxides, a two-dimensional electron gas (2DEG) in nature, provides a rich platform for exploring new fundamental phenomena and device applications.[1−3] In particular, as silicon is the foundation of semiconductor technology, the perovskite oxide insulator $SrTiO_3$ (STO) is the base material for oxide electronics. Different from conventional semiconductor 2DEGs, the STO-based 2DEG originates from Ti 3*d* orbits (d_{xy}, d_{xz}, and d_{yz})[4] and exhibits intriguing properties, such as two-dimensional superconductivity,[5] the signature of magnetism,[6] a high carrier mobility,[7] a nanoscale-controlled insulator−metal transition,[8] 2D quantum oscillations,[9] a large thermopower modulation,[10] and sensitivity to light illumination.[11] These properties depend strongly on the carrier density due to electron−electron correlations. Therefore, extensive efforts have been made to tune the interface properties by electrostatic gating. Generally, the modulation of these novel properties of oxide 2DEGs is performed in conventional field effect configuration where the STO substrate is used as the dielectric insulator. However, this requires high voltages of tens to hundreds of volts to achieve a sizable field effect.[12−14] For example, the Lifshitz transition where the d_{xz} and d_{yz} bands start to become occupied was observed to emerge with the back gate ranging from −50 to 450 V, near a critical carrier density of 1.7×10^{13} cm^{-2} in $LaAlO_3$/$SrTiO_3$ (LAO/STO).[15] Furthermore, applying the back gate between −200 and 200 V, Rashba spin−orbit interaction (SOI) was effectively tuned in the isostructural 2DEG systems, such as LAO/STO[16] and $LaVO_3$/$SrTiO_3$.[17] Different from the studies with conventional electric field effects, the electric double layer transistor (EDLT) with an ionic liquid (IL) as the dielectric layer provides a more powerful means to tune the carrier density as high as $\sim 10^{15}$ cm^{-2} with only a few volts.[18,19] Such ionic gating effect has resulted in the observation of field-induced superconductivity in insulating STO,[20] as well as the Kondo effect in LAO/STO.[21,22]

Received: July 27, 2017
Revised: September 21, 2017
Published: October 2, 2017

DOI: 10.1021/acs.nanolett.7b03209
Nano Lett. 2017, 17, 6878−6885

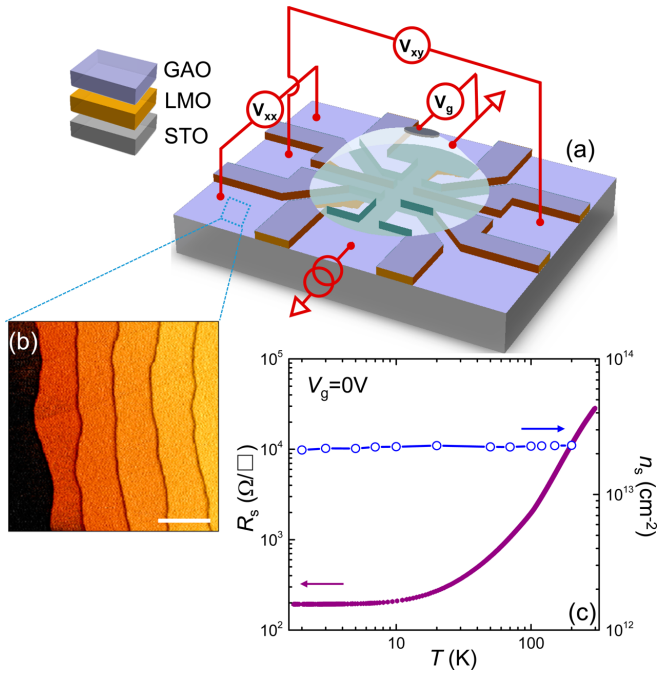

Figure 1. (a) A sketch of the EDLT configuration for the ionic-liquid-gated GAO/STO Hall bar interface; (b) a typical AFM image measured in the region of the Hall bar channel for a 2.5 uc GAO deposited on patterned STO substrate. The scale bar is 500 nm. (c) Transport properties of GAO/STO interface with a GAO thickness of 2.5 uc before dropping the ionic liquid.

Besides the intensively investigated isostructural perovskite/perovskite interfaces, recently, a new 2DEG was discovered at the nonisostructural spinel/perovskite oxide interface of γ-$Al_2O_3/SrTiO_3$ (GAO/STO).[2,14,23−27] Compared to the mostly investigated LAO/STO interface, the GAO/STO system has a better lattice match, much higher electron mobility and does not contain rare earth elements; therefore, it is more attractive for application in high-mobility oxide devices. However, the high-mobility GAO/STO interface is generally accompanied by a high carrier density (on the order of 10^{14} cm^{-2}), which is approximately one order larger than that of LAO/STO (on the order of 10^{13} cm^{-2}).[26] This makes it more challenging to modulate the physical properties of GAO/STO by the conventional configuration.[14] Therefore, it becomes extremely interesting to investigate the GAO/STO electrostatically gated by ionic liquids. Nevertheless, so far the IL-assisted EDLT at oxide interfaces remains at its early stage, which is largely limited to the isostructural LAO/STO heterostructures. Whether the remarkable tunability of interface properties in LAO/STO can be also achieved for the nonisostructural GAO/STO remains open. Moreover, the electronic structure underlying the novel properties of LAO/STO system is well-understood, including the evolution of the Fermi level under electrostatic gating effect. Nevertheless, little is known to the GAO/STO system. Notably, it was recently reported by resonant soft X-ray linear dichroism[23] that GAO/STO could exhibit an unusual orbital symmetry different from that of the LAO/STO. This makes it further interesting to study the gating effect of the spinel-perovskite heterostructure. Herein, for the first time, we applied the EDLT technique to the non-isostructural GAO/STO oxide interface. By continuously tuning the carrier concentration of the interface 2DEG, the system undergoes a series of remarkable transitions from Lifshitz transition, to enhanced SOI, as well as the appearance of Kondo effect. Besides the large tunability of the interface states, our results also shed new light on the electronic structure on the nonisostructural GAO/STO interface.

The GAO/STO EDLT device, as illustrated in Figure 1a, was fabricated on a Hall-bar 2DEG.[28,29] The Hall bar device was fabricated by initially depositing amorphous $LaMnO_3$ (a-LMO) layer (50 nm) as a hard mask layer. Optical lithography and selective wet etching processes were subsequently performed to create patterned STO substrates for the deposition of GAO (see also the Supporting Information, SI). The width of Hall bar is 50 μm, and the length between two voltage probes is 500 μm. A drop of ionic liquid, 1-ethyl-3-methylimidazolium-bis(trifluoromethanesulfonyl) amide (EMI-TFSI) with poly-(styrene-*block*-methylmethacrylate-*block*-styrene) (PS-PMMA-PS) which was made into the form of gel with a freezing point of 230 K, was chosen as the gate dielectric material due to the high capacitance.[30] The gate voltage (V_g) is applied through a Pt electrode to the ionic liquid. Note that, although the Pt contact to LAO/STO results in resistance hysteresis,[31] we did not observed any hysteresis during our gating measurement. In this paper, the data were collected from a typical device with a GAO film thickness, t, of 2.5 unit cells (uc) where the interface is metallic with a relative high electron mobility. Similar measurements were performed on several devices with 2 uc $\leq t \leq$ 2.5 uc. All data show nice consistency and reproducibility, ruling out any possible electrochemical

DOI: 10.1021/acs.nanolett.7b03209
Nano Lett. 2017, 17, 6878−6885

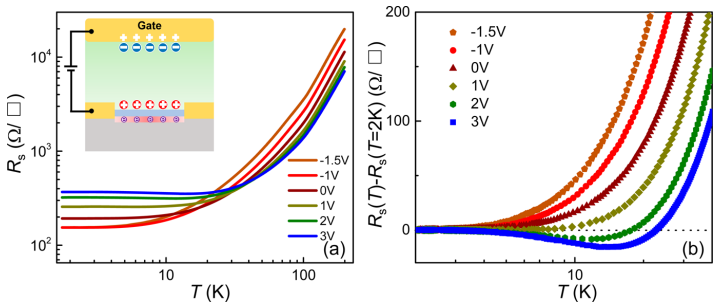

Figure 2. Field effect modulation of transport properties of the GAO/STO interface by EDLT. (a) Temperature-dependent sheet resistance at various gate voltages. The inset shows the basic mechanism of EDLT under applied positive voltages. (b) Normalized sheet resistance $R_s(T) - R_s(2\ K)$ at low temperatures between 2 and 40 K, which shows a strong signature of the Kondo effect.

reaction[32] or aging effect.[33] Notably, the capping layer of GAO film could play a similar role as a boron nitride buffer to prevent the ionic-liquid-induced electrochemical reaction on STO surface.[32] Figure 1b shows an atomic force microscopy (AFM) image of the 2.5 uc GAO film grown on the patterned STO substrate. An atomically smooth surface with clear terraces is observed, indicating the high quality of both the patterned substrate and the grown film.[29] Figure 1c shows the temperature (T)-dependent sheet resistance (R_s) and carrier density (n_s) of this device before dropping the ionic liquid. The patterned GAO/STO is metallic as reported previously.[29] The carrier density, n_s, is approximately 2.2×10^{13} cm^{-2} at room temperature and is nearly independent of temperature in the whole temperature range of 2−300 K. The electron mobility, μ, at 2 K is around 1800 cm^2 V^{-1} s^{-1}. Notably, compared to the n_s = 3.7×10^{14} cm^{-2} of unpatterned GAO/STO system with the same thickness, the carrier density of the patterned 2DEG is suppressed significantly. This is probably due to the presence of $LaMnO_3$ (which is crystallized from the a-LMO hard mask during the high temperature deposition) in the structure which could change significantly the oxygen exchange dynamics across the interface at high temperatures.[26,29]

The work mechanism of our EDLT device is illustrated in the insets of Figure 2a: By applying a positive gate voltage to the Pt electrode, the cations and anions in the ionic liquid move toward the sample and the gate electrode, respectively, forming an electric double layer at the liquid−solid interface (under the negative gate voltage, the cations and anions in the ionic liquid move toward the Pt electrode and the GAO/STO interface, respectively). This electric double layer works as a nanogap supercapacitor tuning the carrier density as well as the Fermi level in the electronic structure. When applying a positive gate voltage, more electrons are accumulated at the interface. However, applying negative voltage to the gate electrode, electrons are depleted. Figure 2a displays the R_s as a function of temperature at various V_g. All of the R_s−T curves show overall metallic behaviors; namely, the sheet resistances decrease upon cooling. In the high temperature regime such as T = 200 K, the sheet resistance decreases monotonously from ∼20 000 Ω/□ to ∼7000 Ω/□ as the V_g increases from −1.5 to 3 V, indicating the accumulation of carriers upon increasing the electrostatic gate potential as expected. However, at low temperature region, a remarkable upturn in the R_s occurs. Particularly, at $V_g \geq 2$ V, R_s reaches first a minimum at a certain temperature and then increases until T decreases to 2 K. Similar electrostatic modulated resistance minimum has also been observed in the LAO/STO system.[21,34] To make the resistance minimum more obvious, in Figure 2b, we show the offset sheet resistance $[R_s(T) - R_s(2\ K)]$ at low temperatures between 2 and 40 K. The abnormal resistance minimum could result from either the weak localization[35,36] or the Kondo effect[37] as reported previously. However, the possible weak localization mechanism can be ruled out here based on our magnetoresistance measurements as discussed in the latter part.[35] We, therefore, account the resistance minimum comes from the Kondo effect, which normally arises from the exchange interaction between itinerant conduction electrons and localized spin centers.[36] The observed resistance minimum can be described well by a simple Kondo model[21]

$$R(T) = R_0 + aT^b + R_{K,0}\left(\frac{1}{1 + (2^{1/s} - 1)(T/T_K)^2}\right)^s \quad (1)$$

where R_0 is the residual resistance and the second power-law term is the contribution from electron−electron and electron−phonon interactions. The last term explains the Kondo effect contribution. T_K is the Kondo temperature that characterizes the strength of the Kondo effect, and the parameter s is fixed at 0.225 for STO-based 2DEG system.[21,22] Good fitting results were obtained (SI, Figure S3) with Kondo temperatures, T_K, of 51.1 and 52.8 K at V_g = 2 and 3 V, respectively. The positive correlation between the resistance upturn and the enhanced carrier density is consistent with the characteristic of the Kondo effect.[21] Localized electrons, particularly with a d_{xy} orbital occupation, could act as magnetic centers for STO-based heterostructures,[4,22] including GAO/STO.[38] But the emergence of the Kondo effect at V_g = 2 V, that is, at a high carrier density of $n_s \sim 3 \times 10^{13}$ cm^{-2}, is unconventional since the magnetic scattering due to the presence of the magnetic impurities is expected to be stronger at a lower carrier density. The observed appearance of the Kondo effect in our interface as a function of an applied electric field is quite similar to the case of the ionic gated STO surface[22] and points to the emergence of magnetic interactions between electrons in STO due to electron−electron correlations rather than the presence of dopants. However, the precise threshold density for the emergence of the Kondo effect of these two system is different; that is, the threshold density of the ionic gated bare STO is 9.2×10^{13} cm^{-2}, much higher than that of GAO/STO interface (3.0×10^{13} cm^{-2}).

DOI: 10.1021/acs.nanolett.7b03209
Nano Lett. 2017, 17, 6878−6885

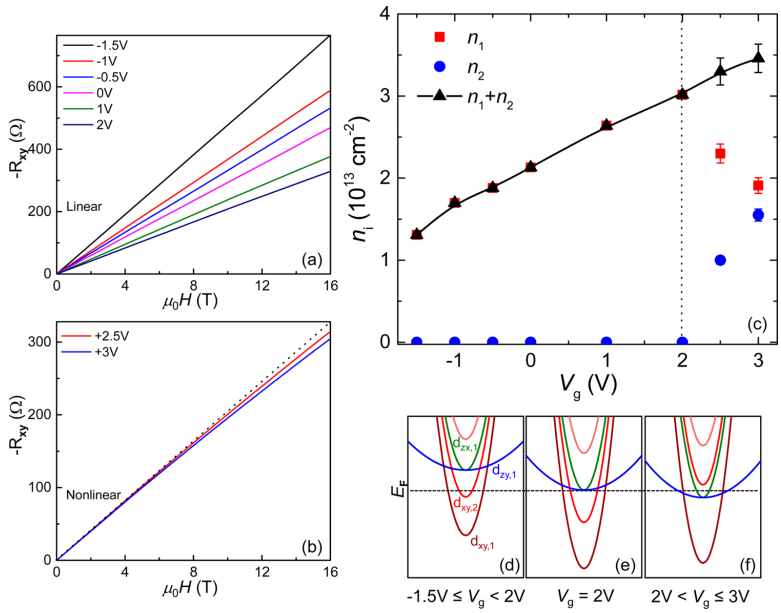

Figure 3. Observation of the Lifshitz transition in transport at GAO/STO interface and its energy bands origin. (a) Measured Hall resistance versus magnetic field for −1.5 V ≤ V_g ≤ 2 V, at T = 2 K. (b) Magnetic field dependence of Hall resistance for 2 V < V_g ≤ 3 V, at T = 2 K. The black dashed line is linear which is a guide to the eye. A transition is observed between two different types of magnetic field dependencies at V_g = 2 V, from linear to nonlinear behavior, which is the characteristic feature of Lifshitz transition. (c) Carrier density versus gate voltage measured at 2 K. The dashed line indicates the Lifshitz carrier density, $n_L = 3 \times 10^{13}$ cm^{-2}. (d–f) Schematic band structures of GAO/STO interface under −1.5 V ≤ V_g < 2 V, V_g = 2 and 2 V < V_g ≤ 2 V, respectively.

Figure 3a and b show the Hall resistance, R_{xy}, as a function of magnetic field (up to 16 T) for −1.5 V ≤ V_g ≤ 2 and 2 V < V_g ≤ 3 V, respectively. Starting from the lowest gate voltage V_g = −1.5 V and up to a transition value of V_g = 2 V, R_{xy} is linear, and the Hall coefficient, R_H, decreases with increasing V_g, as shown in Figure 3a, which indicates a single band conductivity. The carrier density can be deduced using $n_s = -1/R_H e$, which gives $n_s = 1.3 \times 10^{13}$ cm^{-2} at V_g = −1.5 V and $n_s = 3.0 \times 10^{13}$ cm^{-2} at V_g = 2 V. However, as V_g > 2 V (Figure 3b), the nonlinear Hall effect appears, which is likely due to the presence of the multiband transport carriers as observed in perovskite/perovskite 2DEG systems.[39] We, therefore, use the two-band model to fit the results (details in SI, Figure S4), where n_1 and n_2 represent the electron densities for the two different bands. Figure 3c summarizes the extracted carrier density as a function of gate voltage. As we can see, n_1 contributes exclusively to the conduction at V_g< 2 V, and it increases linearly with increasing V_g. This is consistent with the single-band-type carrier conduction model. At V_g > 2 V, n_2 emerges and increases with the increase of the V_g. However, n_1 begins to decrease unexpected. On the other hand, the total carrier densities, $n_{total}=n_1 + n_2$, increases (from 1.3 to 3.5 × 10^{13} cm^{-2}) within gate voltage range from −1.5 to 3 V.

For the STO-based 2DEGs, it is established that the thin sheet conducting electrons are confined strongly within a few-nanometers at the interface on the STO side.[40] The interfacial electrons originate from the electronic shell of the Ti 3d orbits (d_{xy}, d_{xz}, and d_{yz}).[4] Subsequently, the spin and momentum of electrons in 2DEGs are entangled, and complicated sub-bands are formed due to the strongly anisotropic nature of d orbits and the quantum confinement.[41] Generally, the band bending at the interface lifts the degeneracy of Ti t_{2g} levels and produces an energy splitting between the different levels: d_{xy} electrons occupy the lowest energy states of the 2DEG; they account for most of the charge in the system. By contrast, d_{xz}/d_{yz} electrons amount to only a small fraction of the population but occupy further higher energy states. With this universal electronic structure in mind,[4,42] we therefore propose that, at V_g< 2 V, electrons (n_1) locate at the lowest d_{xy} levels (as depicted in Figure 3d). Upon the population of electron as increasing V_g, the Fermi level is lifted across the bottom of d_{xz}/d_{yz} bands, the system undergoes a remarkable Lifshitz transition at a critical carrier density,[15,39] $n_L \sim 3.0 \times 10^{13}$ cm^{-2} (Figure 3e), above which the d_{xz}/d_{yz} bands start to populate (corresponding to the appearance of experimental n_2) (Figure 3f).

Notably, the critical carrier density, $n_L \sim 3.0 \times 10^{13}$ cm^{-2}, for the Lifshitz transition of GAO/STO is higher than most of the reports for LAO/STO where the transition is achieved with a back gate. However, it is remarkably close to the n_L reported previously for top-gated LAO/STO systems.[39] Nontrivially, the unexpected decrease in n_1 upon increasing V_g, that is, the depletion in the occupation of d_{xy} states at 2 V < V_g ≤ 3 V, was also observed in the top-gated LAO/STO systems.[39] Such a decrease of d_{xy} electrons is inconsistent with a model requiring a fixed electronic band structure, as raising the Fermi energy should always increase the number of available conduction states.[39] Therefore, our data also indicate that the underlying band structure of GAO/STO is not fixed under ionic gating. Instead, carriers in d_{xy} and d_{xz}/d_{yz} bands will redistribute, and the band structure evolves with the electrostatic gating effect.

DOI: 10.1021/acs.nanolett.7b03209
Nano Lett. 2017, 17, 6878−6885

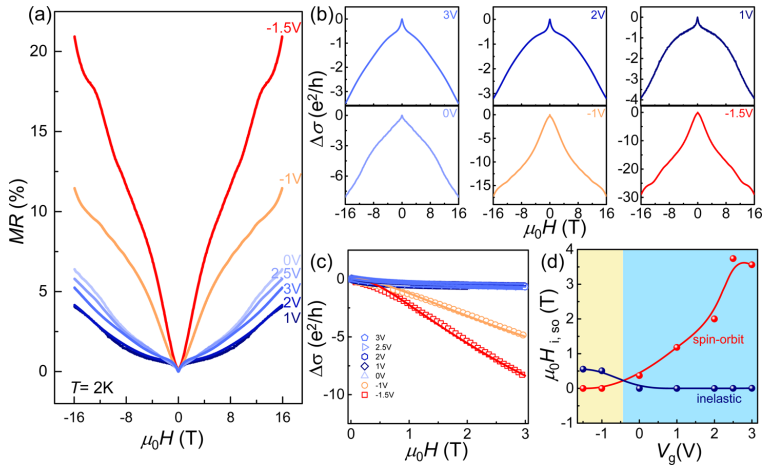

Figure 4. Tunable Rashba spin−orbit interaction at GAO/STO interface modulated by ionic liquid assisted gate voltages. (a) Magnetoresistance MR = $[R(\mu_0H) - R(0)]/R(0) \times 100\%$ at various gate voltages. (b) Normalized conductivity $\Delta\sigma = \sigma(\mu_0H) - \sigma(0)$ in units of quantum conductance (e^2/h, e is the unit charge, and h is the Planck constant) as a function of magnetic fields at different V_g. The cusps near zero magnetic field are the typical evidence of WAL. (c) Fitting the WAL effect according to the Maekawa−Fukuyama theory. The solid lines are the fitting results. (d) Gate voltage dependence of the contribution of spin−orbit interaction and inelastic scattering.

On the basis of Schrödinger−Poisson calculations proposed in ref 39, the d_{xz}/d_{yz} energy increases faster than the energy of the d_{xy} states and the potential well at the Lifshitz point is narrow with the top-gate configuration. In addition, a positive top-gate voltage enhances the confining potential gradient, resulting in a larger splitting of the bands as depicted in Figure 3f. Therefore, once the d_{xz}/d_{yz} electrons are populated, band occupations are influenced, and d_{xy} electrons are suppressed, strongly highlighting the electron−electron interactions at complex oxide interfaces as reported recently.[39] This is consistent with the conclusion proposed by Maniv et al. that electronic interactions cause a competition between the occupancies of different bands.[43] Notably, the Kondo effect emerges as d_{xy} electrons decreases upon increasing V_g, although it appears unusually as the total carrier density increases. Shortly, the IL gating effectively accumulate/dissipate carriers at the interface by modifying deeply the band structure of the 2DEG as well as electron−electron interactions.

Besides carrier densities, Rashba spin−orbit interaction (SOI) arising from the interfacial breaking of inversion symmetry can also be modulated by the external electric field, particularly at the crossing point of d_{xy} and d_{xz}/d_{yz} orbitals. This could be useful to control the spin precession in spintronics devices.[16] The significant tuning of Ti 3d bands as revealed in Figure 3 may lead to unique spin−orbit textures, particular at V_g = 2 V, that is, in proximity to the Lifshitz transition. This inspires us to further study the gate-dependent SOI at the GAO/STO interface. Figure 4a shows the magnetoresistance (MR) as a function of magnetic field measured at 2 K with various applied V_g. Notably, no negative magnetoresistance or weak localization effect was observed in our measurements. This rules out the possibility of a weak localization effect that leads to the resistance minimum discussed in Figure 2b. Positive MR curves were observed in the whole field region of $-1.5\ \text{V} \leq V_g \leq 3\ \text{V}$. Remarkably, the MR exhibits sharp cusps at low magnetic fields for $V_g \geq 0$ V, which is the characteristic feature of the weak antilocalization (WAL) effect originating from the interference of the quantum coherent electronic waves in the presence of SOI.[44−46] In Figure 4b, we plot the $\Delta\sigma = \sigma(\mu_0H) - \sigma(0)$ at different V_g, where the WAL effect at low magnetic fields becomes more visible as $V_g \geq 0$ V.

To understand the SOI tuned by the IL-assisted gating, we analyzed the observed WAL effect using the Maekawa−Fukuyama (MF) localization theory:[16,47]

$$\Delta\sigma(H) = \frac{e^2}{\pi h}\left[\Psi\left(\frac{H}{H_i + H_{so}}\right) + \frac{1}{2\sqrt{1-\gamma^2}}\Psi\left(\frac{H}{H_i + H_{so}(1+\sqrt{1-\gamma^2})}\right) - \frac{1}{2\sqrt{1-\gamma^2}}\Psi\left(\frac{H}{H_i + H_{so}(1-\sqrt{1-\gamma^2})}\right)\right] \quad (2)$$

Here, the function Ψ is defined as $\Psi(x) = \ln(x) + \psi(1/2 + 1/x)$, where $\psi(x)$ is the digamma function. H_i, H_{so}, and γ are parameters indicate the characteristic inelastic scattering field, spin−orbit interaction field, and Zeeman correction term, respectively. The magnitude of the characteristic spin−orbit interaction field (μ_0H_{so}) reflects the SOI strength. Figure 4c displays the fitting results of the experimental data according to eq 2. The parameters μ_0H_i and μ_0H_{so} extracted from fitting are shown in Figure 4d, which shed light on the modulation of SOI by the electric field. The values of μ_0H_{so} are in the same range as the ones reported previously for other STO-based 2DEGs.[16,48,49] For negative gate voltages, the inelastic scattering field is larger than the spin−orbit interaction field, indicating that the orbit effect of magnetic field dominates compared with the effect of spin−orbit interaction. While at $V_g \geq 0$ V, the spin−orbit interaction field is larger than the inelastic scattering field and increases significantly at $V_g > 2$

DOI: 10.1021/acs.nanolett.7b03209
Nano Lett. 2017, 17, 6878−6885

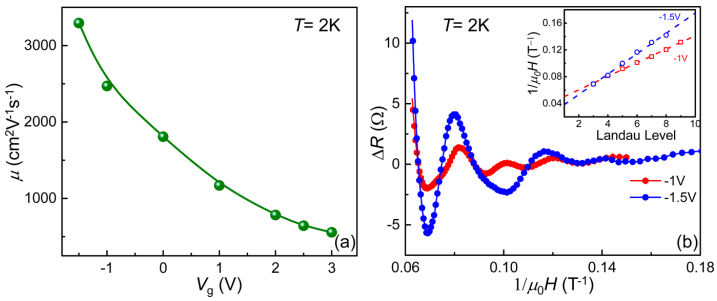

Figure 5. Enhanced mobility and quantum oscillations modulated by ionic liquid gating at the GAO/STO interface. (a) Mobility as a function of the applied V_g, measured at 2 K. (b) Amplitude of the SdH oscillation versus the reciprocal magnetic field. The inset shows the position of the oscillation peak in $1/\mu_0 H$ versus the effective Landau level.

V.This further confirms the scenario of band structure discussed above in Figure 3d–f, since significant SOI enhancement has been theoretically predicted and experimental proved to occur at the crossing region from d_{xy} to d_{xz})/d_{yz}due to the orbital hybridization.[17,42,50,51] At negative V_g regions of single-band at lower density, electrons only occupy the d_{xy} sub-bands without the crossing between d_{xy} and d_{xz}/d_{yz}, the SOI does not dominate. However, at V_g > 2 V, that is, after the Lifshitz transition, the d_{xy} and d_{xz}/d_{yz} sub-bands begin to cross at Fermi level and subsequently have the biggest crossing area around Fermi level (V_g = 2.5 V). The demonstration of the field control of Rashba SOI in GAO/STO EDLTs presents not only a step toward realizing spintronics devices based on IL gating, but also shed some light on the underlying mechanism of the Rashba SOI and 3*d* band filling of GAO/STO interface modulated by IL gating.

Finally, as shown in Figure 4a, we found clear Shubnikov-de Hass (SdH) oscillations in the MR curves for V_g=-1 V and −1.5 V, which is a characteristic behavior for high-mobility high quality materials.[9,26] To further demonstrate the modulation of mobility by IL-assisted electrostatic effect, Figure 5a shows the mobility as a function of V_g. The mobility is enhanced by depleting the carriers with decreasing the gate voltages.[34] Notably, at V_g< 0 V, the electron mobility is increased larger than 2000 $cm^2 V^{-1} s^{-1}$ at 2 K. Figure 5b shows SdH oscillations recorded at 2 K as a function of the inverse magnetic field $1/\mu_0 H$ after removing a smooth background. The inset of Figure 5b shows the position of oscillation peaks in $1/\mu_0 H$ versus the effective Landau level, of which the fitted lines indicate the frequency of SdH oscillations. The oscillation frequency decreases as carrier density decreases, which is consistent with a previous result for doped STO.[52] The carrier density determined from Hall measurements ($n_{Hall\_-1.5V}$ = 1.3 × 10^{13} cm^{-2}, and n_{Hall_-1V} = 1.7 × 10^{13} cm^{-2} for V_g = −1.5 V and −1 V, respectively) and SdH oscillations ($n_{SdH\_-1.5V}$ = 3.2 × 10^{12} cm^{-2}, n_{SdH_-1V} = 4.8 × 10^{12} cm^{-2}) differ by a factor of 3–4 in the present experiments. Similar behaviors have been observed in previous reports for unpatterned samples.[26,29,43,53] This discrepancy is either due to the fact that a fraction of carriers do not satisfy conditions for the SdH oscillation but nevertheless contribute to the Hall signal or due to the presence of multiple conduction channels with the same carrier mobility. Since our SdH oscillations are observed in the single band conduction region (V_g = −1.5 V and −1 V) with only d_{xy} electrons populated to the conduction, we assume that the GAO/STO interface consists of a single quantum well with approximately 4–fold degeneracy, such as two d_{xy} conduction channels with spin splitting.[53,54] Overall, by an IL-assisted field effect, the mobility can be highly enhanced leading to quantum oscillations.

In summary, we have demonstrated the tuning of the 2DEG at the GAO/STO interface by electric-double-layer gating. A dramatic tuning of the electronic structure of GAO/STO is realized in which the electron gas undergoes a number of remarkable transitions from the Lifshitz transition to the occurrence of Kondo effect, as well as a large enhancement in the Rashba SOI. Furthermore, EDLT at the GAO/STO interface also shows an important avenue to construct high-mobility oxide interface where nontrivial quantum phenomena could be explored. The present findings suggest the IL-assisted field effect of nonisostructural oxide interface of GAO/STO is promising for novel all-oxide devices.

■ ASSOCIATED CONTENT

Supporting Information

The Supporting Information is available free of charge on the ACS Publications website at DOI: 10.1021/acs.nanolett.7b03209.

Sample growth, device and ionic liquid gel fabrication, figures of the EDLT device, leak current, Kondo effect, and two-band model (PDF)

■ AUTHOR INFORMATION

Corresponding Authors

*E-mail: (Y. C.) yunc@dtu.dk.

*E-mail: (X. W.) xfwang@nju.edu.cn.

ORCID

Anders Riisager: 0000-0002-7086-1143

Yunzhong Chen: 0000-0001-8368-5823

Notes

The authors declare no competing financial interest.

■ ACKNOWLEDGMENTS

We are thankful for the technical help from Jørgen Geyti and the scientific discussion with Søren Linderoth. W.N. thanks the China Scholarship Council for support. X.F.W. acknowledges the financial support from the National Key Projects for Basic Research of China under grant no. 2014CB921103, the National Natural Science Foundation of China under grant no. U1732159, U1732273 and the Collaborative Innovation

Center of Solid-State Lighting and Energy-Saving Electronics. Y.B.X. acknowledges the financial support from the Natural Science Foundation of Jiangsu Province of China under Grant No. BK20140054.

REFERENCES

(1) Ohtomo, A.; Hwang, H. Y. *Nature* **2004**, *427*, 423.
(2) Chen, Y. Z.; Bovet, N.; Kasama, T.; Gao, W. W.; Yazdi, S.; Ma, C.; Pryds, N.; Linderoth, S. *Adv. Mater.* **2014**, *26*, 1462−1467.
(3) Cantoni, C.; Gazquez, J.; Miletto Granozio, F.; Oxley, M. P.; Varela, M.; Lupini, A. R.; Pennycook, S. J.; Aruta, C.; di Uccio, U. S.; Perna, P.; Maccariello, D. *Adv. Mater.* **2012**, *24*, 3952−7.
(4) Gabay, M.; Triscone, J.-M. *Nat. Phys.* **2013**, *9*, 610−611.
(5) Reyren, N.; Thiel, S.; Caviglia, A. D.; Kourkoutis, L. F.; Hammerl, G.; Richter, C.; Schneider, C. W.; Kopp, T.; Rüetschi, A.-S.; Jaccard, D.; Gabay, M.; Muller, D. A.; Triscone, J.-M.; Mannhart, J. *Science* **2007**, *317*, 1196.
(6) Bert, J. A.; Kalisky, B.; Bell, C.; Kim, M.; Hikita, Y.; Hwang, H. Y.; Moler, K. A. *Nat. Phys.* **2011**, *7*, 767−771.
(7) Chen, Y. Z.; Trier, F.; Wijnands, T.; Green, R. J.; Gauquelin, N.; Egoavil, R.; Christensen, D. V.; Koster, G.; Huijben, M.; Bovet, N.; Macke, S.; He, F.; Sutarto, R.; Andersen, N. H.; Sulpizio, J. A.; Honig, M.; Prawiroatmodjo, G. E.; Jespersen, T. S.; Linderoth, S.; Ilani, S.; Verbeeck, J.; Van Tendeloo, G.; Rijnders, G.; Sawatzky, G. A.; Pryds, N. *Nat. Mater.* **2015**, *14*, 801−6.
(8) Cheng, G.; Siles, P. F.; Bi, F.; Cen, C.; Bogorin, D. F.; Bark, C. W.; Folkman, C. M.; Park, J. W.; Eom, C. B.; Medeiros-Ribeiro, G.; Levy, J. *Nat. Nanotechnol.* **2011**, *6*, 343−7.
(9) Caviglia, A. D.; Gariglio, S.; Cancellieri, C.; Sacépé, B.; Fête, A.; Reyren, N.; Gabay, M.; Morpurgo, A. F.; Triscone, J. M. *Phys. Rev. Lett.* **2010**, *105*, 236802.
(10) Ohta, H.; Mizuno, T.; Zheng, S.; Kato, T.; Ikuhara, Y.; Abe, K.; Kumomi, H.; Nomura, K.; Hosono, H. *Adv. Mater.* **2012**, *24*, 740−4.
(11) Lei, Y.; Li, Y.; Chen, Y. Z.; Xie, Y. W.; Chen, Y. S.; Wang, S. H.; Wang, J.; Shen, B. G.; Pryds, N.; Hwang, H. Y.; Sun, J. R. *Nat. Commun.* **2014**, *5*, 5554.
(12) Caviglia, A. D.; Gariglio, S.; Reyren, N.; Jaccard, D.; Schneider, T.; Gabay, M.; Thiel, S.; Hammerl, G.; Mannhart, J.; Triscone, J. M. *Nature* **2008**, *456*, 624−7.
(13) Thiel, S.; Hammerl, G.; Schmehl, A.; Schneider, C. W.; Mannhart, J. *Science* **2006**, *313*, 1942.
(14) Christensen, D. V.; Trier, F.; von Soosten, M.; Prawiroatmodjo, G. E. D. K.; Jespersen, T. S.; Chen, Y. Z.; Pryds, N. *Appl. Phys. Lett.* **2016**, *109*, 021602.
(15) Joshua, A.; Pecker, S.; Ruhman, J.; Altman, E.; Ilani, S. *Nat. Commun.* **2012**, *3*, 1129.
(16) Caviglia, A. D.; Gabay, M.; Gariglio, S.; Reyren, N.; Cancellieri, C.; Triscone, J. M. *Phys. Rev. Lett.* **2010**, *104*, 126803.
(17) Liang, H.; Cheng, L.; Wei, L.; Luo, Z.; Yu, G.; Zeng, C.; Zhang, Z. *Phys. Rev. B: Condens. Matter Mater. Phys.* **2015**, *92*, 075309.
(18) Lu, N.; Zhang, P.; Zhang, Q.; Qiao, R.; He, Q.; Li, H. B.; Wang, Y.; Guo, J.; Zhang, D.; Duan, Z.; Li, Z.; Wang, M.; Yang, S.; Yan, M.; Arenholz, E.; Zhou, S.; Yang, W.; Gu, L.; Nan, C. W.; Wu, J.; Tokura, Y.; Yu, P. *Nature* **2017**, *546*, 124−128.
(19) Bisri, S. Z.; Shimizu, S.; Nakano, M.; Iwasa, Y. *Adv. Mater.* **2017**, *29*, 1607054.
(20) Ueno, K.; Nakamura, S.; Shimotani, H.; Ohtomo, A.; Kimura, N.; Nojima, T.; Aoki, H.; Iwasa, Y.; Kawasaki, M. *Nat. Mater.* **2008**, *7*, 855−8.
(21) Lin, W.-N.; Ding, J.-F.; Wu, S.-X.; Li, Y.-F.; Lourembam, J.; Shannigrahi, S.; Wang, S.-J.; Wu, T. *Adv. Mater. Interfaces* **2014**, *1*, 1300001.
(22) Lee, M.; Williams, J. R.; Zhang, S.; Frisbie, C. D.; Goldhaber-Gordon, D. *Phys. Rev. Lett.* **2011**, *107*, 256601.
(23) Cao, Y.; Liu, X.; Shafer, P.; Middey, S.; Meyers, D.; Kareev, M.; Zhong, Z.; Kim, J.-W.; Ryan, P. J.; Arenholz, E.; Chakhalian, J. *NPJ. Quan. Mater.* **2016**, *1*, 16009.
(24) Schütz, P.; Pfaff, F.; Scheiderer, P.; Sing, M.; Claessen, R. *Appl. Phys. Lett.* **2015**, *106*, 063108.
(25) Kormondy, K. J.; Posadas, A. B.; Ngo, T. Q.; Lu, S.; Goble, N.; Jordan-Sweet, J.; Gao, X. P. A.; Smith, D. J.; McCartney, M. R.; Ekerdt, J. G.; Demkov, A. A. *J. Appl. Phys.* **2015**, *117*, 095303.
(26) Chen, Y. Z.; Bovet, N.; Trier, F.; Christensen, D. V.; Qu, F. M.; Andersen, N. H.; Kasama, T.; Zhang, W.; Giraud, R.; Dufouleur, J.; Jespersen, T. S.; Sun, J. R.; Smith, A.; Nygard, J.; Lu, L.; Buchner, B.; Shen, B. G.; Linderoth, S.; Pryds, N. *Nat. Commun.* **2013**, *4*, 1371.
(27) Lee, S. W.; Liu, Y.; Heo, J.; Gordon, R. G. *Nano Lett.* **2012**, *12*, 4775−83.
(28) Trier, F.; Prawiroatmodjo, G. E. D. K.; von Soosten, M.; Christensen, D. V.; Jespersen, T. S.; Chen, Y. Z.; Pryds, N. *Appl. Phys. Lett.* **2015**, *107*, 191604.
(29) Niu, W.; Gan, Y.; Zhang, Y.; Christensen, D. V.; von Soosten, M.; Wang, X.; Xu, Y.; Zhang, R.; Pryds, N.; Chen, Y. *Appl. Phys. Lett.* **2017**, *111*, 021602.
(30) Lee, K. H.; Kang, M. S.; Zhang, S.; Gu, Y.; Lodge, T. P.; Frisbie, C. D. *Adv. Mater.* **2012**, *24*, 4457−62.
(31) Wu, S.; Luo, X.; Turner, S.; Peng, H.; Lin, W.; Ding, J.; David, A.; Wang, B.; Van Tendeloo, G.; Wang, J.; Wu, T. *Phys. Rev. X* **2013**, *3*, 041027.
(32) Gallagher, P.; Lee, M.; Petach, T. A.; Stanwyck, S. W.; Williams, J. R.; Watanabe, K.; Taniguchi, T.; Goldhaber-Gordon, D. *Nat. Commun.* **2015**, *6*, 6437.
(33) Park, J.; Soh, Y.-A.; Aeppli, G.; David, A.; Lin, W.; Wu, T. *Appl. Phys. Lett.* **2014**, *104*, 081604.
(34) Zeng, S.; Lu, W.; Huang, Z.; Liu, Z.; Han, K.; Gopinadhan, K.; Li, C.; Guo, R.; Zhou, W.; Ma, H. H.; Jian, L.; Venkatesan, T.; Ariando. *ACS Nano* **2016**, *10*, 4532−7.
(35) Niu, W.; Gao, M.; Wang, X.; Song, F.; Du, J.; Wang, X.; Xu, Y.; Zhang, R. *Sci. Rep.* **2016**, *6*, 26081.
(36) Kondo, J. *Prog. Theor. Phys.* **1964**, *32*, 37−49.
(37) Brinkman, A.; Huijben, M.; van Zalk, M.; Huijben, J.; Zeitler, U.; Maan, J. C.; van der Wiel, W. G.; Rijnders, G.; Blank, D. H.; Hilgenkamp, H. *Nat. Mater.* **2007**, *6*, 493−6.
(38) Christensen, D. V.; Frenkel, Y.; Smith, A.; Chen, Y. Z.; Klein, L.; Pryds, N.; Kalisky, B. *Strain tunable magnetism in* γ-$Al_2O_3/SrTiO_3$ (unpublished).
(39) Smink, A. E.; de Boer, J. C.; Stehno, M. P.; Brinkman, A.; van der Wiel, W. G.; Hilgenkamp, H. *Phys. Rev. Lett.* **2017**, *118*, 106401.
(40) Chen, Y.; Pryds, N.; Kleibeuker, J. E.; Koster, G.; Sun, J.; Stamate, E.; Shen, B.; Rijnders, G.; Linderoth, S. *Nano Lett.* **2011**, *11*, 3774−8.
(41) Santander-Syro, A. F.; Copie, O.; Kondo, T.; Fortuna, F.; Pailhes, S.; Weht, R.; Qiu, X. G.; Bertran, F.; Nicolaou, A.; Taleb-Ibrahimi, A.; Le Fevre, P.; Herranz, G.; Bibes, M.; Reyren, N.; Apertet, Y.; Lecoeur, P.; Barthelemy, A.; Rozenberg, M. J. *Nature* **2011**, *469*, 189−93.
(42) Khalsa, G.; Lee, B.; MacDonald, A. H. *Phys. Rev. B: Condens. Matter Mater. Phys.* **2013**, *88*, 041302.
(43) Maniv, E.; Shalom, M. B.; Ron, A.; Mograbi, M.; Palevski, A.; Goldstein, M.; Dagan, Y. *Nat. Commun.* **2015**, *6*, 8239.
(44) Bergmann, G. *Phys. Rep.* **1984**, *107*, 1.
(45) Hikami, S.; Larkin, A. I.; Nagaoka, Y. *Prog. Theor. Phys.* **1980**, *63*, 707−710.
(46) Niu, W.; Du, K.; Wang, S.; Zhang, M.; Gao, M.; Chen, Y.; Liu, H.; Zhou, W.; Song, F.; Wang, P.; Xu, Y.; Wang, X.; Shen, J.; Zhang, R. *Nanoscale* **2017**, *9*, 12372−12378.
(47) Maekawa, S.; Fukuyama, H. *J. Phys. Soc. Jpn.* **1981**, *50*, 2516.
(48) Herranz, G.; Singh, G.; Bergeal, N.; Jouan, A.; Lesueur, J.; Gazquez, J.; Varela, M.; Scigaj, M.; Dix, N.; Sanchez, F.; Fontcuberta, J. *Nat. Commun.* **2015**, *6*, 6028.
(49) Das, S.; Hossain, Z.; Budhani, R. C. *Phys. Rev. B: Condens. Matter Mater. Phys.* **2016**, *94*, 115165.
(50) King, P. D.; McKeown Walker, S.; Tamai, A.; de la Torre, A.; Eknapakul, T.; Buaphet, P.; Mo, S. K.; Meevasana, W.; Bahramy, M. S.; Baumberger, F. *Nat. Commun.* **2014**, *5*, 3414.

DOI: 10.1021/acs.nanolett.7b03209
Nano Lett. 2017, 17, 6878−6885

(51) Zhong, Z.; Tóth, A.; Held, K. *Phys. Rev. B: Condens. Matter Mater. Phys.* **2013**, *87*, 161102.
(52) Son, J.; Moetakef, P.; Jalan, B.; Bierwagen, O.; Wright, N. J.; Engel-Herbert, R.; Stemmer, S. *Nat. Mater.* **2010**, *9*, 482−4.
(53) Trier, F.; Prawiroatmodjo, G. E.; Zhong, Z.; Christensen, D. V.; von Soosten, M.; Bhowmik, A.; Lastra, J. M.; Chen, Y.; Jespersen, T. S.; Pryds, N. *Phys. Rev. Lett.* **2016**, *117*, 096804.
(54) Xie, Y.; Bell, C.; Kim, M.; Inoue, H.; Hikita, Y.; Hwang, H. Y. *Solid State Commun.* **2014**, *197*, 25−29.

DOI: 10.1021/acs.nanolett.7b03209
Nano Lett. 2017, 17, 6878−6885

XXIII

ARTICLE

D. V. Christensen *et al.*
Electron mobility in γ-Al_2O_3/$SrTiO_3$
Physical Review Applied 9, 054004 (2018)

Summertime sunset at Risø campus
Photo: DTU

PHYSICAL REVIEW APPLIED **9,** 054004 (2018)

Electron Mobility in γ-Al_2O_3/$SrTiO_3$

D. V. Christensen,[1,*] Y. Frenkel,[2] P. Schütz,[3] F. Trier,[1,4] S. Wissberg,[2] R. Claessen,[3] B. Kalisky,[2] A. Smith,[1] Y. Z. Chen,[1] and N. Pryds[1]

[1]*Department of Energy Conversion and Storage, Technical University of Denmark, Risø Campus, DK-4000 Roskilde, Denmark*

[2]*Department of Physics and Institute of Nanotechnology and Advanced Materials, Bar-Ilan University, 5290002 Ramat-Gan, Israel*

[3]*Physikalisches Institut and Röntgen Center for Complex Material Systems (RCCM), Universität Würzburg, Am Hubland, 97074 Würzburg, Germany*

[4]*Unité Mixte de Physique CNRS, Thales, Université Paris-Sud, Université Paris-Saclay, 91767 Palaiseau, France*

(Received 8 August 2017; revised manuscript received 14 February 2018; published 3 May 2018)

One of the key issues in engineering oxide interfaces for electronic devices is achieving high electron mobility. $SrTiO_3$-based interfaces with high electron mobility have gained a lot of interest due to the possibility of combining quantum phenomena with the many functionalities exhibited by $SrTiO_3$. To date, the highest electron mobility (140 000 $cm^2/V\,s$ at 2 K) is obtained by interfacing perovskite $SrTiO_3$ with spinel γ-Al_2O_3. The origin of the high mobility, however, remains poorly understood. Here, we investigate the scattering mechanisms limiting the mobility in γ-Al_2O_3/$SrTiO_3$ at temperatures between 2 and 300 K and over a wide range of sheet carrier densities. For $T > 150$ K, we find that the mobility is limited by longitudinal optical phonon scattering. For large sheet carrier densities ($>8 \times 10^{13}$ cm^{-2}), the screened electron-phonon coupling leads to room-temperature mobilities up to $\mu \sim 12$ $cm^2/V\,s$. For 5 K $< T <$ 150 K, the mobility scales as approximately T^{-2}, consistent with electron-electron scattering limiting the electron mobility. For $T < 5$ K and at an optimal sheet carrier density of approximately 4×10^{14} cm^{-2}, the electron mobility is found to exceed 100 000 $cm^2/V\,s$. At sheet carrier densities less than the optimum, the electron mobility decreases rapidly, and the current flow becomes highly influenced by domain walls and defects in the near-interface region of $SrTiO_3$. At carrier densities higher than the optimum, the $SrTiO_3$ heterostructure gradually becomes bulk conducting, and the electron mobility decreases to approximately 20 000 $cm^2/V\,s$. We argue that the high electron mobility observed arises from a spatial separation of donors and electrons with oxygen-vacancy donors preferentially forming at the interface, whereas the itinerant electrons extend deeper into $SrTiO_3$. Understanding the scattering mechanism in γ-Al_2O_3/$SrTiO_3$ paves the way for creation of high-mobility nanoscale electronic devices.

DOI: 10.1103/PhysRevApplied.9.054004

I. INTRODUCTION

Achieving high electron mobility is pivotal for material research. In particular, it is paramount for application in efficient electronic components and studying quantum phenomena. A large Hall mobility $\mu = e\tau/m^*$ is realized by either a low effective mass (m^*) or a long momentum relaxation time (τ). For instance, the pioneering work on $Al_xGa_{1-x}As$/GaAs heterostructures led to a record-high electron mobility of $\mu \sim 3.6 \times 10^7$ $cm^2/V\,s$ at 0.36 K through the combination of a low effective mass of $m^*_{GaAs} \sim 0.06m_e$ and improvements in τ [1]. In contrast, $Mg_xZn_{1-x}O$/ZnO with $\mu \sim 1.3 \times 10^6$ $cm^2/V\,s$ at 0.1 K [2] and $SrTiO_3$ (STO) based heterostructures with $\mu \sim 1.4 \times 10^5$ $cm^2/V\,s$ at 2 K [3] both exhibit high mobilities at low temperatures despite being characterized by large effective masses of $m^*_{ZnO} \sim 0.3m_e$ and $m^*_{STO} \sim 1m_e$. The high electron mobility in $Mg_xZn_{1-x}O$/ZnO is achieved by reducing the defect scattering. This is accomplished using molecular beam epitaxy (MBE) leading to a crystal quality close to that of traditional semiconductors. STO, however, typically contains a large amount of impurities [4], but the large dielectric constant at low temperatures [5,6] counteracts the interaction between electrons and ionized scattering sites. The forgiving nature of the STO crystal together with the manifold of physical phenomena

*Corresponding author.
dechr@dtu.dk

observed in STO and STO-based heterostructures have fueled the recent interest in achieving high mobility.

At room temperature, the electron mobility in doped STO is typically 1–12 $cm^2/V\,s$ and generally believed to be limited by electron-electron interactions or longitudinal optical phonon scattering [7–9]. At temperatures below 5 K, the mobility in bulk, doped STO substrates reaches a value of approximately 22 000 $cm^2/V\,s$ with static, ionized scattering sites being the limiting factor [9]. Various strategies have been utilized in the search for high mobility in STO and STO-based heterostructures, including MBE thin-film growth [10], strain [11], δ doping [12,13], modulation doping [14], surface passivation [15], and defect engineering [14,16]. To date, the largest mobility of 140 000 $cm^2/V\,s$ has been observed when STO is interfaced with γ-Al_2O_3 (GAO) [3], where oxygen vacancies account for the formation of the interface conductivity [3,17,18]. Contrary to the majority of other STO-based heterostructures [19,20], the highest mobilities in GAO/STO surprisingly occur at a high sheet carrier density exceeding 10^{14} cm^{-2}, despite the abundance of oxygen-vacancy donors in STO, which act as scattering sites [3,18,21]. A spatial separation of the electrons and donors within STO was recently proposed to be the origin of the high mobility in GAO/STO at low temperatures [21], but it remains to be settled unambiguously. In addition, the dominant scattering mechanisms in GAO/STO at intermediate and high temperatures have yet to be identified.

Here, we investigate the electron mobilities of GAO/STO heterostructures over a wide range of carrier densities, which are obtained by controlling the density of oxygen vacancies via a variation of growth parameters or postgrowth annealing in oxygen at elevated temperatures (approximately 200 °C). We show that the carrier density can be used as a handle to tune the mobility, electron-phonon coupling, and effective mass at room temperature. In addition, we use transport and scanning superconducting quantum-interference device (SQUID) measurements to probe the relationship between the mobility, carrier density, current flow, and scattering at low temperature. The study opens a path toward designing all-oxide quantum devices and extraordinary magnetoresistive devices.

II. METHODS

The transport data of the GAO/STO samples presented here are a compilation of three sets of measurements: The transport data from the first set is taken from Ref. [3], where the GAO/STO samples are produced using pulsed laser deposition (PLD) at a temperature of 600 °C, a laser fluence of 1.5 J/cm^2, and an oxygen partial pressure of 10^{-4} mbar. The changes in the carrier densities and mobilities occur due to a variation of the GAO film thickness between 2 and 4 unit cells, with the largest mobility occurring at 2.5 unit cells. In the second set of samples, we grow more than 40 GAO/STO heterostructures using PLD but in another growth chamber. Here, high mobility is obtained by growing approximately 3.5 unit cells of GAO at 650 °C with a fluence of 3.8 J/cm^2 in a growth pressure of 10^{-5} mbar. Changes in the carrier density and mobility are primarily obtained by varying the growth pressure from 10^{-4} to 10^{-6} mbar with a lowering of the pressures causing a higher carrier density. In the third set of measurements, a GAO/STO sample is produced with the same deposition conditions as the second set with a pressure of 2×10^{-5} mbar. Several sequential postdeposition annealing steps are then used to change the carrier density and mobility by annihilation of the oxygen-vacancy donors. Here, the transport properties are measured after annealing the sample in approximately 200 °C in 1-bar oxygen for 2–8 h at each step. The sheet resistance is measured during the annealing process, as this allows us to estimate the change in the carrier density. The duration of the annealing is between 2 and 8 h (typically 6 h) depending on when a desired change in the carrier density occurs. More details of changing the carrier density systematically using postdeposition annealing of GAO/STO with *in situ* transport measurements can be found in Ref. [18]. In all cases, GAO is deposited on STO with a TiO_2-termination using the same protocol described elsewhere [22]. The carrier density and mobility are determined from the slope of the Hall coefficients at low magnetic fields in the van der Pauw geometry. We note that for the high carrier density samples, the Hall coefficient is nonlinear as a function of the magnetic field for $T < 40$ K with the steepest slope occurring at high magnetic fields. This behavior is in contrast to $LaAlO_3$ (LAO)/STO at carrier densities above the Lifshitz carrier density ($n_s \sim 1.7\times10^{13}$ cm^{-2}), where the Hall coefficient has the steepest slope at low fields due to transport occurring in two n-type bands [23]. As we discuss elsewhere, we attribute the nonlinear Hall coefficient observed for GAO/STO at high carrier densities to a nonsaturating anomalous Hall coefficient, which scales linearly with the magnetoresistance. In this case, the carrier density is most accurately determined from the Hall coefficient at low magnetic fields where the magnetoresistance varies slowly as B^2. The use of the low-field Hall coefficient to extract the carrier density is consistent with previous reports on GAO/STO [3]. As shown in Figs. 1 and 2, this analysis leads to (i) a temperature-independent carrier density and (ii) $\mu \propto T^{-2}$ for $5\text{ K} < T < 150$ K, which is consistent with that observed in other bulk STO and STO-based heterostructures. Note that if one uses the high-field Hall coefficient to extract the carrier density (as appropriate if the anomalous Hall coefficient is saturating or within the two-band model to deduce the total carrier density), it will lead to (i) a decrease of the total itinerant carrier density below 40 K, (ii) an effective mobility exceeding 300 000 $cm^2/V\,s$, and (iii) large deviations of the T^{-2} behavior.

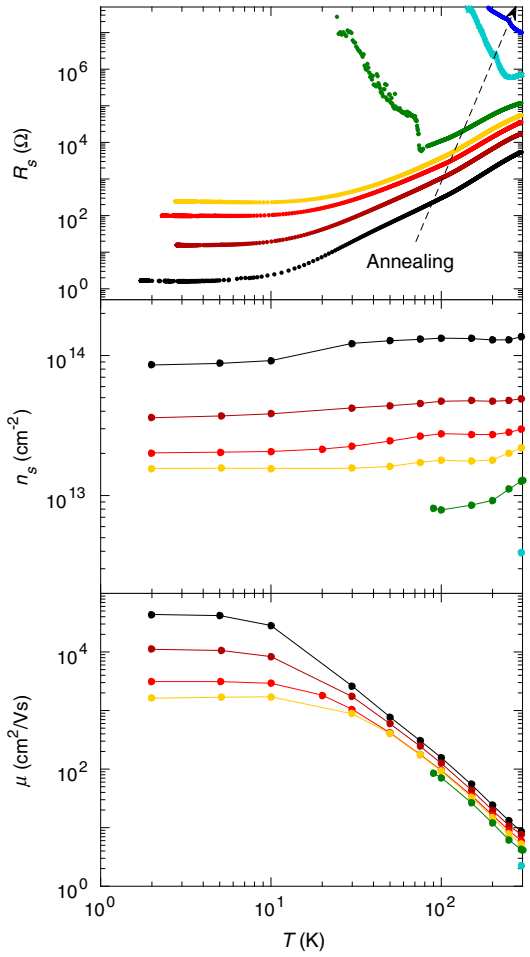

FIG. 1. Sheet resistance (R_s), Hall sheet carrier density (n_s), and Hall electron mobility (μ) as a function of the temperature for a single γ-Al_2O_3/$SrTiO_3$ heterostructure at various annealing steps. The heterostructure is annealed in 1-bar pure oxygen at approximately 200 °C for 2–8 h between each Hall measurement, which causes a monotonic decrease in the carrier density from 1×10^{14} cm^{-2} (black) to 3×10^{12} cm^{-2} (cyan). All lines are guides to the eye.

The current density is imaged using a scanning SQUID. An alternating current is driven through the sample, which produces a magnetic flux picked up by a pickup loop of diameter 1.8 μm. The pickup loop is connected to a SQUID, which measures the magnetic flux with lock-in detection. By scanning the pickup loop along the sample surface, a two-dimensional map of the magnetic flux can be measured. The measured flux is given by $\phi_s = \int g(x,y)\vec{B} \cdot d\vec{a}$, where the integral is taken over the plane of the pickup loop, $g(x,y)$ is the point-spread function of the pickup loop, $\vec{B}$ is the magnetic field produced by the current in the sample, and $d\vec{a}$ is the infinitesimal area vector element pointing normal to the plane of the pickup loop (i.e., along z). Each flux image is a convolution of the z component of the magnetic field and the SQUID point-spread function. A current-carrying wire produces circulating magnetic field around it; therefore, it appears in our images as a black stripe next to a white stripe.

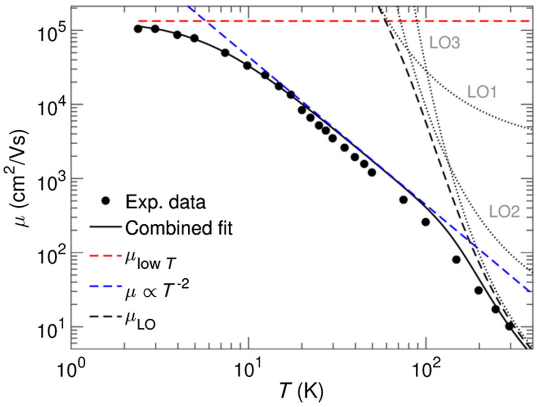

FIG. 2. Electron mobility as a function of the temperature where two fitting parameters are used to describe the three contributions to the mobility according to Eq. (3). LO1–3 describe the three longitudinal optical phonon modes. Note that the data originate from a sample that is not postdeposition annealed.

III. TEMPERATURE DEPENDENCE OF THE MOBILITY

Figure 1 shows the sheet resistance, carrier density, and mobility in a GAO/STO heterostructure after six annealing steps, each comprising storage in 1-bar oxygen at approximately 200 °C for 2–8 h. Changes in the transport properties are probed *in situ* by measuring the sheet resistance during the annealing process (see Sec. II and Ref. [18] for more details). The annealing lowers the carrier density monotonically and drives the sample from a metallic to an insulating state. The mobility decreases systematically over the whole temperature range from 2 to 300 K with the most prominent change below 30 K and less pronounced changes near room temperature. In the following, we first identify the contributions to the mobility in order to fit its temperature dependence, and then we discuss the corresponding scattering mechanisms at the various temperatures in detail.

The temperature dependence of the mobility (μ) in STO and STO-based heterostructures is assumed to be described by the Matthiessen rule [24],

$$\mu^{-1} = \sum_i \mu_i^{-1}, \tag{1}$$

where each scattering mechanism has an associated temperature-dependent mobility contribution $\mu_i(T)$.

In the low-temperature regime ($T < 5$ K), the dominant scattering of electrons in STO and STO-based heterostructures is attributed to ionized impurities in STO [9], ionized donors [25], or surface roughness scattering [26]. The mobility contribution in this temperature regime $\mu_{\mathrm{low}\,T}$ is often taken to be temperature independent [7,25], and for simplicity, we do the same here, $\mu_{\mathrm{low}\,T} = \mu_{T\to 0\ \mathrm{K}}$, and discuss the scattering mechanism later.

For 5 K $< T <$ 150 K, the dominant scattering mechanism remains unsettled even for bulk STO despite intensive research. The change in mobility is explained by the low-temperature scattering mechanism with a temperature-dependent dielectric constant [26], acoustic phonon scattering [25], transverse optical phonon scattering [25], longitudinal optical (LO) phonon scattering [26], temperature-dependent polaron properties [27], or electron-electron scattering [7]. Consistent with previous studies of STO and other STO-based heterostructures, we achieve a good agreement if we describe the mobility contribution with AT^m in the intermediate temperature regime with A being a temperature-independent coefficient and m being approximately equal to -2. As we discuss later, this is suggestive of electron-electron scattering being dominant in this temperature interval.

For 150 K $< T <$ 300 K, the limiting factor for the mobility has been attributed to electron-electron interactions [7], temperature-dependent transmission coefficients in Landauer channels connecting dopants [28], or LO phonon scattering [7–9]. The temperature dependence of the electron-electron contribution follows approximately T^{-2} behavior [7], whereas the scattering from a LO phonon with frequency ω_{LO} is $\mu_{\mathrm{LO}} \propto \exp(\hbar\omega_{\mathrm{LO}}/k_B T)$. Hence, a hallmark to discriminate between the two contributions is the presence of a nonlinearity when $\log(\mu)$ is plotted as a function of $\log(T)$. Such a nonlinearity can be seen for $T > 150$ K as a deviation from the approximately T^2 behavior of the sheet resistance (Fig. 1) and the approximately T^{-2} behavior of the mobility (Figs. 1 and 2), respectively. We, therefore, use an expression for the longitudinal optical phonon scattering in the weak or intermediate coupling regime where the electron-phonon coupling constant α is less than 6 [29]:

$$\mu_{\mathrm{LO}} = \frac{\hbar}{2\alpha\hbar\omega_{\mathrm{LO}}}\frac{e}{m_p}\left(\frac{m_p}{m_b}\right)^3 f(\alpha)\exp\left(\frac{\hbar\omega_{\mathrm{LO}}}{k_B T}\right). \tag{2}$$

Here, $f(\alpha)$ is a monotonic function of α that varies slowly from 1 to 1.35 as α increases from 0 to 6 [29]. The bare effective mass is taken to be $m_b \sim 0.6 m_e$ with m_e being the free-electron mass [30]. As the electron moves through the lattice, it attracts positive ions leading to an enhanced effective mass described by the polaron effective mass m_p. For a three-dimensional Fröhlich polaron [29], $m_p = m_b(1 + \alpha/6)$, whereas a two-dimensional electron gas with Fröhlich interactions to a three-dimensional lattice [31] leads to $m_p = m_b[1 + (\pi/8)\alpha + 0.1272\alpha^2]$. The dimensionality of the electron gas in STO-based heterostructures is dependent on the carrier density and growth conditions [32], but here we assume two-dimensional polarons consistent with a mobility study of LAO/STO [26]. We note that in 1953, Low and Pines published a similar expression [33] with $\mu_{\mathrm{LO}} \propto (m_p/m_b)^2$, which is often used to describe the mobility in STO, but in 1955, the same authors published the above expression with $\mu_{\mathrm{LO}} \propto (m_p/m_b)^3$ along with a short discussion on the discrepancy (see footnote 8 in Ref. [29]).

Cubic STO contains three LO phonon modes with energies $\hbar\omega_{\mathrm{LO1}} = 21.4$ meV, $\hbar\omega_{\mathrm{LO2}} = 58.6$ meV, and $\hbar\omega_{\mathrm{LO3}} = 100.1$ meV and corresponding coupling constants $\alpha_{\mathrm{LO1}} = 0.009$, $\alpha_{\mathrm{LO2}} = 0.47$, and $\alpha_{\mathrm{LO3}} = 1.83$ reported by Barker [34]. We add the contribution from the three phonon modes according to Matthiessen rule to obtain the total contribution of the longitudinal optical phonons, $\mu_{\mathrm{LO\ total}}$.

To conclude, we can express the total (inverse) electron mobility as

$$\frac{1}{\mu(T)} = \frac{1}{\mu_{T\to 0}} + \frac{1}{AT^{-2}} + \frac{1}{\mu_{\mathrm{LO\,total}}(T)}. \tag{3}$$

Using the two free parameters $\mu_{T\to 0\ \mathrm{K}}$ and A, we find a good agreement with the experimental mobility in GAO/STO as observed in Fig. 2. With a slight adjustment of α_{LO3} as we describe below, a similar agreement is found for all tested GAO/STO mobilities, including those in Fig. 1, with low-temperature mobilities ranging from 1000 to 100 000 $\mathrm{cm^2/V\,s}$ and Hall sheet carrier densities between 10^{13} and 10^{15} $\mathrm{cm^{-2}}$. In the following, we discuss the individual temperature regimes in detail.

IV. MOBILITY AT ROOM TEMPERATURE

The electron mobility at room temperature is important for device application. From Fig. 2, we deduce that the room-temperature electron mobility is primarily limited by scattering from LO3 phonons. This is in contrast to Ref. [7], where electron-electron scattering is found to be dominating in $GdTiO_3$/STO heterostructures and heavily doped STO, but it is consistent with a number of other studies on bulk STO and STO-based heterostructures [7–9]. We obtain the room-temperature mobility for a number of samples with varying carrier density achieved through either annealing or a variation of the deposition parameters (see Fig. 3). The latter parameter variation encompasses samples from this study as well as from a previous study

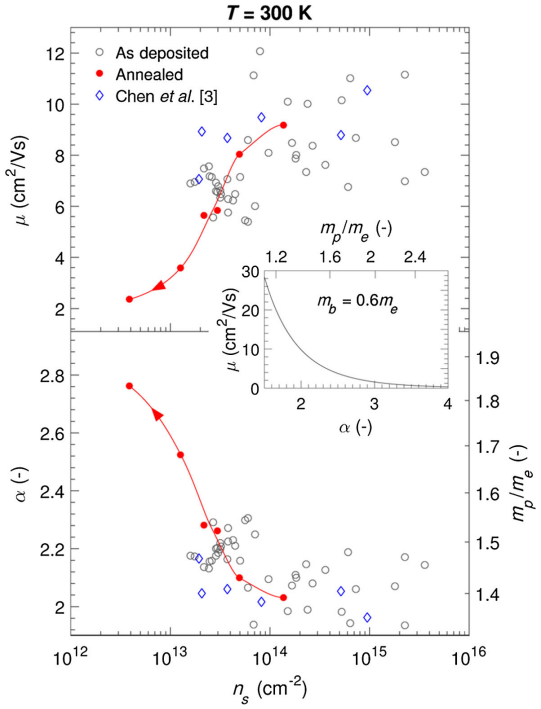

FIG. 3. Top: Room-temperature electron mobility (μ) as a function of carrier density (n_s) for as-deposited and postannealed GAO/STO. Note that the data for as-deposited GAO/STO by Chen *et al.* [3] are also included. Bottom: Electron-phonon coupling (α) and polaron effective mass (m_p) as a function of the carrier density. Inset: The mobility as a function of the electron-phonon coupling as calculated from Eq. (4) assuming a band effective mass of $m_b = 0.6m_e$ and two-dimensional polarons. The red lines are guides to the eye.

done by Chen *et al.* [3]. All three sample series give consistent results. The lowest measured electron mobility (approximately 2 $cm^2/V\,s$) occurs at low carrier densities ($n_s \sim 4 \times 10^{12}$ cm^{-2}) after annealing and is consistent with the low electron mobilities of slightly reduced bulk STO [35,36]. The highest electron mobilities (approximately 12 $cm^2/V\,s$) are obtained for high sheet carrier densities ($n_s > 8 \times 10^{13}$ cm^{-2}). The positive correlation between the room-temperature mobility and the carrier density may be understood by investigating the carrier density dependence of Eq. (2). From angle-resolved photoemission spectroscopy (ARPES) studies [27,30] of the polaronic satellite feature, ω_{LO3} is found to be negligibly dependent on the carrier density. As the bare-band effective mass is not expected to vary significantly with the carrier density, the only strong carrier density dependence, therefore, enters the expression for μ_{LO} [Eq. (2)] through the electron-phonon coupling constant $\alpha(n_s)$. Note that $m_p[\alpha(n_s)]$ and $f[\alpha(n_s)]$ inherit this density dependence. We can write out the dependence on α in Eq. (2) explicitly,

$$\mu_{LO}(\alpha) = \frac{\hbar}{2\alpha\hbar\omega_{LO}}\frac{e}{m_b}\left[1 + \left(\frac{\pi}{8}\right)\alpha + 0.1272\alpha^2\right]^2 \times f(\alpha)\exp\left(\frac{\hbar\omega_{LO}}{k_B T}\right), \quad (4)$$

where $\mu_{LO}(\alpha)$ is plotted in the inset of Fig. 3 using $m_b = 0.6m_e$. Inverting this function numerically to obtain $\alpha(\mu_{LO})$ allows one to deduce the electron-phonon coupling constant and corresponding polaron effective mass from the measured mobility as presented in the bottom panel of Fig. 3. The electron-phonon coupling ranges from 2.8 at low carrier densities to 2 at high carrier densities and is similar to the literature values of 2.6 [8] and 1.83 [34] and ARPES results [30] at 20 K where the coupling ranges from 2.8 to 1.3 upon increasing the carrier density from 4×10^{13} to 9×10^{13} cm^{-2}. Our deduced effective polaron mass changes from $1.8m_e = 3m_b$ to $1.4m_e = 2.3m_b$ upon increasing the carrier density, in good agreement with Nb-doped STO having an effective mass of approximately $3m_b$ for 0.1% Nb doping and a saturation at approximately $2m_b$ above 1% Nb doping [37].

Based on this analysis, we conclude that the high mobility at room temperature occurs at high carrier densities where the electron-phonon coupling is weak due to screening from electrons [30]. The reduced coupling results in less scattering and a lower effective mass.

V. MOBILITY AT INTERMEDIATE TEMPERATURES

At intermediate temperatures, $T_{low} < T < 150$ K, the mobility varies as approximately T^{-2} independent of the carrier density with $T_{low} \sim 5$ K for high-mobility samples and $T_{low} \sim 30$ K for low-mobility samples. The mobility in this temperature range cannot be explained satisfactorily by scattering from a single branch of acoustic phonons $\mu \sim T^{-1}$ or nonpolar optical phonons with frequency ω_{TO}, $\mu \sim e^{\hbar\omega_{TO}/k_B T}$ using the expressions from Ref. [24]. The scattering can, in principle, be caused by a combination of several different scattering mechanisms, but this seems unlikely since the mobility scales with the carrier density in the same way ($\mu \propto n_s^{0.28\pm0.04}$) in the entire temperature interval 30 K $< T <$ 150 K. As the scaling is significantly different from that at low temperatures (see the following section), the changes in the mobility at intermediate temperatures appear not to be governed by the temperature-dependent dielectric constant either. In contrast, the T^{-2} dependence in STO-based systems has been explained by electron-electron scattering [7,37–39]. In the classical picture, the Hall electron mobility is unaffected by collisions between two electrons if the velocity (and, hence, the total

charge current) is preserved. Momentum can, however, be transferred to the lattice during an electron-electron scattering event, for instance, if the scattering process involves phonons. The microscopic mechanism and characteristics of the electron-electron scattering process has been a subject of several studies [37–41], but a unifying picture remains elusive for STO. In particular, deviations from Fermi-liquid behavior have been shown to occur [38], and another study advises against readily using the $\mu \propto T^{-2}$ scaling as evidence for electron-electron scattering [41].

VI. MOBILITY AT LOW TEMPERATURES

At low temperatures, a high mobility of up to 22 000 $cm^2/V\,s$ can be obtained in bulk conducting STO owing to the large dielectric constant [9]. Given optimized growth parameters (which may differ from one chamber to another), the electron mobility at the GAO/STO heterointerface may significantly exceed this value. In our previous results, Chen *et al.* reported the highest electron mobility when 2.5-unit cells (u.c.) of GAO was deposited at 600 °C using pulsed laser deposition with a high laser fluence of 1.5 J/cm^2 in an oxygen pressure of 10^{-4} mbar [3]. In this study, high electron mobility is instead found when depositing approximately 3.5 unit cells of GAO at 650 °C with a fluence of 3.8 J/cm^2 and a pressure of 10^{-5} mbar. The α-Al_2O_3 single-crystal target, substrate supplier, and TiO_2-termination process are identical to that used by Chen *et al.* [3]. Using a fixed GAO thickness (2.5 or 3.5 u.c.) and a high laser fluence, the high carrier density and mobility are primarily obtained by optimizing the oxygen partial pressure. At low carrier densities (approximately 10^{13} cm^{-2}), the mobility at 2 K is of the order of 1000 $cm^2/V\,s$ (see Fig. 4) and similar to typical mobilities in LAO/STO [20]. At even lower carrier densities, the interface undergoes a metal-to-insulator transition, which impedes the reliable determination of the low-temperature electron mobility. Increasing the carrier density results in a pronounced increase in the mobility roughly described by $\mu \sim n_s^{1.5}$ until the mobility peaks at more than 100 000 $cm^2/V\,s$ when the carrier density reaches $n_s(\mu_{max}) \sim 4 \times 10^{14}$ cm^{-2}. The positive correlation between the mobility and carrier density in GAO/STO is radically different from LAO/STO where the exponent is negative [19,20]. Interestingly, a positive exponent of approximately 1.5 is also observed in modulation-doped electronic systems where the donors and electrons are spatially separated [42,43]. Heterostructures fabricated close to this mobility peak typically have a room-temperature sheet resistance of approximately 1 kΩ and a large residual resistance ratio of $R_s(300\ K)/R_s(2\ K) \sim 10\,000$, consistent with the 4 orders of magnitude mobility enhancement upon cooling from $T = 300$ to 2 K. The room-temperature sheet resistance or the residual resistance ratio can often be used as a tool for fast screening of high-mobility samples during growth optimization.

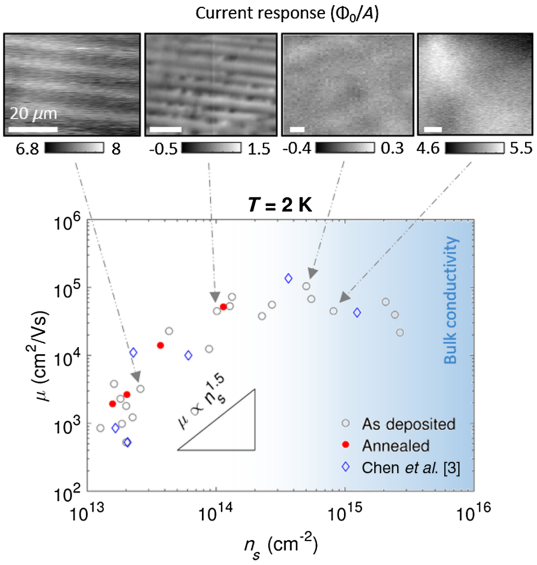

FIG. 4. Electron mobility (μ) as a function of the sheet carrier density (n_s) at 2 K for as-deposited GAO/STO, postdeposition annealed GAO/STO, and as-deposited GAO/STO from Chen *et al.* [3]. For four samples with varying carrier density, the scanning SQUID images show the magnetic flux created by the current flow in the samples. Occasionally, the current flow in low-density GAO/STO samples shows areas with scattered points of local (resolution-limited) reduction in the current density, probably related to point defects or defect clusters. Such an area is presented in the second scanning SQUID image, but similar areas are found in the sample with the low carrier density. Note that the absolute value of the magnetic flux measured on different samples cannot be directly compared, as it depends on the position on the sample. The scale bars are 20 μm in all images.

Increasing the carrier density beyond approximately 4×10^{14} cm^{-2} results in a gradual conversion into bulk three-dimensional conductivity of the STO substrate. Here, samples with $n_s > 3 \times 10^{15}$ cm^{-2} represent the extreme case where the conductivity measured on the backside of the STO substrate with a thickness of 0.5 mm does not differ from that measured at the interface. In this case, the samples can be viewed as a homogeneously conducting 0.5-mm-thick sheet with a 3D carrier density of $n_s/0.05\ cm = 6 \times 10^{16}$ cm^{-3}. The mobility decreases to approximately 20 000 $cm^2/V\,s$, which is consistent with bulk conducting STO with a similar three-dimensional carrier density formed by introducing donors throughout STO [32].

To investigate whether low and high mobility in GAO/STO heterostructures have distinct signatures in

the spatial distribution of the current flow on the microscale, we investigate GAO/STO with varying carrier densities and mobilities using a scanning SQUID. Here, an alternating current in the sample creates a magnetic field, which is detected by the SQUID through a pickup loop with a diameter of 1.8 μm. Our SQUID images (see Fig. 4) show a qualitative difference in the spatial distribution of current flow between the samples with low and high carrier density with a threshold of approximately 3×10^{14} cm^{-2}. At low electron densities ($\lesssim 1 \times 10^{14}$ cm^{-2}), we see striped modulations of the current flow, similar to previous reports on LAO/STO [44,45]. The orientations of the stripes match the orientations of the ferroelastic domain walls formed when STO undergoes a cubic to tetragonal phase transition below 105 K [45]. At high densities ($\gtrsim 5 \times 10^{14}$cm^{-2}), the striped modulations are no longer observed. Interestingly, the threshold carrier density for the disappearance of the stripes coincides with the carrier density resulting in the highest observed mobility. We suggest two possible explanations for the different observations made here with the scanning SQUID:

(i) Higher carrier densities should screen potential steps between different structural domains, resulting in small carrier density modulations compared to the total density [44].

(ii) As the carrier density rises, the degree of bulk conductivity also increases. When the thickness of the conductive layer exceeds the typical thickness of the domains or point defects, additional pathways are formed so the current can bypass the ferroelastic domain walls, and, thus, no modulations in the current densities are observed along the walls.

Overall, the SQUID and transport measurements suggest an increase of the mobility at high carrier density correlated with screening of scattering sites up to a point where the bulk conductivity in STO dominates the overall transport.

In the following, we summarize the experimental findings related to the high mobility from this and other studies and use this as a foundation for the subsequent discussion of the origin. Using pulsed laser deposition, GAO/STO heterostructures with high electron mobility at low temperatures are achieved in a narrow growth window under conditions where both oxygen vacancies and itinerant electrons are located in STO. The Hall mobility is found to be a factor 6 larger than the quantum mobility derived from Shubnikov–de Haas oscillations [3]. Spectroscopic measurements and density functional theory calculations reveal that the breaking of the symmetry at the spinel-perovskite interface creates interface oxygen vacancies with a deeper in-gap state and a lower formation energy compared to oxygen vacancies located deeper in STO [21]. We recently showed that low-temperature annealing (typically $<100\,^{\circ}$C) can enhance the mobility without altering the carrier density [21]. This, combined with annealing studies of oxygen vacancies in GAO/STO [18], suggests that oxygen vacancies reorder such that the overall scattering decreases. Changing the oxygen-vacancy concentration through growth results in a peak mobility exceeding 100 000 cm^2/V s at a sheet carrier density of $n_s(\mu_{\max}) \sim 4 \times 10^{14}$ cm^{-2}. Above $n_s(\mu_{\max})$, the current flows almost homogeneously in the system, and the conductivity gradually increases its three-dimensional character with a concomitant mobility decrease. Below $n_s(\mu_{\max})$, the mobility decreases as $\mu \sim n_s^{1.5}$, and the current flow becomes more inhomogeneous with stripe and pointlike modulations, indicative of less electronic screening in the (quasi-) two-dimensionally confined system. GAO also has a smaller lattice mismatch (approximately 1%) with STO than, e.g., LAO (approximately 3%), and we note that other high-mobility STO-based heterostructures are also composed of at least one material with a low nominal lattice match, i.e., $La_{7/8}Sr_{1/8}MnO_3$, STO, or $SrCuO_3$ in a-LAO/$La_{7/8}Sr_{1/8}MnO_3$/STO [14] with a mobility of 70 000 cm^2/V s, STO/$SrCuO_2$/LAO/STO [16] with 50 000 cm^2/V s, and LAO/STO/STO [15] with 118 000 cm^2/V s. At last, one report shows that bands with d_{xz} and d_{yz} symmetry are lower in energy than d_{xy} bands, which is opposite to what is observed for LAO/STO [46]. However, it remains undemonstrated whether this is the case for high-mobility GAO/STO samples as well.

Whereas a good lattice match with STO might be a prerequisite for obtaining high-mobility STO-based interfaces, we note that obtaining a mobility exceeding that observed in bulk suggests a spatial separation between donors and electrons. Following the spectroscopic and density functional theory findings in Ref. [21], it seems plausible that oxygen vacancies preferentially accumulate at the spinel-perovskite GAO/STO interface due to the broken symmetry. The electrons distribute deeper into STO owing to the high dielectric constant of STO and the slowly decaying electron distribution in STO [26,47–49]. If the donor-electron separation is sufficient, the electrons at low concentrations will predominantly be scattered off the unintentional ionized impurities and residual oxygen-vacancy donors in STO. In line with the $\mu \sim n_s^{1.5}$ predicted for modulation doping [42,43], the high electron concentration particularly obtained in GAO/STO could result in a higher mobility by (i) an increase of the Fermi surface with a concomitant small-angle scattering [42] and (ii) a screening of ionized scattering sites and potential variations across domain walls [24]. The momentum relaxation measured via the Hall effect is mostly sensitive to large-angle scattering events, whereas the quantum mobility is sensitive to any scattering event causing phase decoherence. The considerable difference between the Hall and quantum mobility observed at high-mobility GAO/STO is, therefore, supportive of the preferential small-angle scattering.

At low-oxygen-growth pressures resulting in $n_s \gg n_s(\mu_{\max})$, oxygen vacancies are present in concentrations exceeding one vacancy per STO surface unit cell. At such conditions, the vacancies distribute deep into STO, and the mobility decreases to that observed in bulk conducting STO. The delicate balance between interface and bulk oxygen vacancies naturally leads to a narrow growth window for obtaining high-mobility GAO/STO along with the possibility to alter the mobility by oxygen-vacancy redistribution. The maximum mobility obtained when growing half-integer thicknesses of GAO (2.5 unit cells in Ref. [3] and 3.5 unit cells here) appears to originate from the enhanced carrier density at these thicknesses, which, however, remains unaccounted for. Further investigations are also needed to characterize the donor-electron separation suggested by the experimental results here and in Ref. [21]. At present, the oxygen-vacancy profile has not yet been investigated directly, whereas studies of the extent of the electron gas suggest that the majority of the electrons are confined within 1.5–7.5 nm from the interface at 10 K [50,51]. A possible way to investigate the donor-electron separation is to image the depth profile of oxygen vacancies and itinerant electrons using transmission electron microscopy on carefully prepared GAO/STO cross sections. Density functional theory calculations can also be used to probe whether the TiO_2 layer right at the GAO/STO interface is conducting, despite significant distortion from the perovskite-spinel symmetry breaking, large amounts of oxygen vacancies, and significant interdiffusion of Al into the first 1–2 unit cells of STO [3]. Lastly, a systematic study of how the ratio between quantum and Hall mobility depends on the carrier density would be interesting to check the hypothesis on decreasing the scattering angle when the carrier density increases. Such a study may, however, be challenging as the Shubnikov–de Haas oscillations reside on a large magnetoresistive background [3].

VII. CONCLUSION

In conclusion, we investigate the mobility in GAO/STO by varying the carrier density via control of the growth parameters and postdeposition annealing. We find that for all investigated carrier densities, the mobility at $T > 150$ K is dominated by optical phonon scattering. High mobility (approximately 12 $cm^2/V\,s$ at room temperature) is found for high carrier densities where the electron-phonon coupling is weak and the effective polaron mass is small. At intermediate temperatures, the experimental findings are consistent with electron-electron scattering. At low temperatures, the mobility exceeds 100 000 $cm^2/V\,s$ at a sheet carrier density of around 4×10^{14} cm^{-2}. The optimum appears to be a delicate balance between, on one hand, the enhanced screening and small-angle scattering occurring at high carrier densities and, on the other hand, the bulk conductivity arising when oxygen vacancies are formed deep into STO. Indeed, we find that $\mu \sim n_s^{1.5}$ at lower carrier densities, whereas at high densities, the mobility is reduced to that of bulk conducting STO. This study paves the way for designing and reproducing all-oxide material platforms with high electron mobility. There are several interesting perspectives of the present study on achieving high mobility in GAO/STO:

(i) One of the aspects of STO-based heterostructures that has attracted much attention is that the carrier density is several orders of magnitude higher than for typical high-mobility two-dimensional electron gases in conventional semiconductors. In the case of GAO/STO, we observe high mobility at carrier densities 1 order of magnitude higher than typical LAO/STO heterostructures, which leads to sheet resistances less than 0.1 Ω at 2 K and very low Joule losses.

(ii) A high quantum mobility opens up the possibility to study quantum coherence in nanoscale devices such as the Aharonov-Bohm interferometer.

(ii) The electronic properties are found to be highly influenced by the domain walls of ferroelastic STO, which can be controlled using electric fields and strain [44,45]. The domain walls may, therefore, be used to design nanoelectronics with writable, erasable, and movable properties.

(iv) The high mobility in GAO/STO offers the possibility of realizing so-called extraordinary magnetoresistance in oxide-metal hybrid devices [52]. In the absence of a magnetic field, the current in such extraordinary magnetoresistive devices primarily flows in the metallic regions, which leads to a low resistance. However, when a magnetic field is applied to a device with high carrier mobility, the Lorentz force deflects the current away from the metallic regions, resulting in a large positive magnetoresistance. GAO/STO may be particularly promising for designing such extraordinary magnetoresistive devices at low temperatures as it combines two important properties: First, GAO/STO has a high mobility, giving a low resistance in the absence of a magnetic field and an efficient Lorentz deflection in the presence of a magnetic field [53,54]. Second, even in the absence of metal inclusions, the GAO/STO heterostructure already shows a very high positive magnetoresistance. Adding geometrically optimized metal inclusions to GAO/STO may lead to an exceptionally high magnetoresistance by combining the intrinsic high magnetoresistance of GAO/STO with the extraordinary magnetoresistance stemming from the geometrical enhancement.

ACKNOWLEDGMENTS

P. S. and R. C. gratefully acknowledge support by the Deutsche Forschungsgemeinschaft through SFB 1170

ToCoTronics. Y. F., S. W., and B. K. were supported by the European Research Council Grant No. ERC-2014-STG-639792 and the Israel Science Foundation Grant No. ISF-1281/17. F. T. acknowledges support by research Grant No. VKR023371 (SPINOX) from VILLUM FONDEN.

[1] V. Umansky, M. Heiblum, Y. Levinson, J. Smet, J. Nübler, and M. Dolev, MBE growth of ultra-low disorder 2DEG with mobility exceeding 35×10^6 $cm^2/V\,s$, J. Cryst. Growth **311**, 1658 (2009).

[2] J. Falson, Y. Kozuka, M. Uchida, J. H. Smet, T. Arima, A. Tsukazaki, and M. Kawasaki, MgZnO/ZnO heterostructures with electron mobility exceeding 1×10^6 $cm^2/V\,s$, Sci. Rep. **6**, 26598 (2016).

[3] Y. Z. Chen, N. Bovet, F. Trier, D. V. Christensen, F. M. Qu, N. H. Andersen, T. Kasama, W. Zhang, R. Giraud, J. Dufouleur, T. S. Jespersen, J. R. Sun, A. Smith, J. Nygård, L. Lu, B. Büchner, B. G. Shen, S. Linderoth, and N. Pryds, A high-mobility two-dimensional electron gas at the spinel/perovskite interface of γ-$Al_2O_3/SrTiO_3$, Nat. Commun. **4**, 1371 (2013).

[4] W. D. Rice, P. Ambwani, M. Bombeck, J. D. Thompson, G. Haugstad, C. Leighton, and S. A. Crooker, Persistent optically induced magnetism in oxygen-deficient strontium titanate, Nat. Mater. **13**, 481 (2014).

[5] H.-M. Christen, J. Mannhart, E. J. Williams, and C. Gerber, Dielectric properties of sputtered $SrTiO_3$ films, Phys. Rev. B **49**, 12095 (1994).

[6] E. Sawaguchi, A. Kikuchi, and Y. Kodera, Dielectric constant of strontium titanate at low temperatures, J. Phys. Soc. Jpn. **17**, 1666 (1962).

[7] E. Mikheev, B. Himmetoglu, A. P. Kajdos, P. Moetakef, T. A. Cain, C. G. Van de Walle, and S. Stemmer, Limitations to the room temperature mobility of two- and three-dimensional electron liquids in $SrTiO_3$, Appl. Phys. Lett. **106**, 062102 (2015).

[8] H. P. R. Frederikse and W. R. Hosler, Hall mobility in $SrTiO_3$, Phys. Rev. **161**, 822 (1967).

[9] O. N. Tufte and P. W. Chapman, Electron mobility in semiconducting strontium titanate, Phys. Rev. **155**, 796 (1967).

[10] J. Son, P. Moetakef, B. Jalan, O. Bierwagen, N. J. Wright, R. Engel-Herbert, and S. Stemmer, Epitaxial $SrTiO_3$ films with electron mobilities exceeding $30,000$ $cm^2\,V^{-1}\,s^{-1}$, Nat. Mater. **9**, 482 (2010).

[11] B. Jalan, S. J. Allen, G. E. Beltz, P. Moetakef, and S. Stemmer, Enhancing the electron mobility of $SrTiO_3$ with strain, Appl. Phys. Lett. **98**, 132102 (2011).

[12] Y. Matsubara, K. S. Takahashi, M. S. Bahramy, Y. Kozuka, D. Maryenko, J. Falson, A. Tsukazaki, Y. Tokura, and M. Kawasaki, Observation of the quantum Hall effect in δ-doped $SrTiO_3$, Nat. Commun. **7**, 11631 (2016).

[13] B. Jalan, S. Stemmer, S. Mack, and S. J. Allen, Two-dimensional electron gas in δ-doped $SrTiO_3$, Phys. Rev. B **82**, 081103 (2010).

[14] Y. Z. Chen *et al.*, Extreme mobility enhancement of two-dimensional electron gases at oxide interfaces by charge-transfer-induced modulation doping, Nat. Mater. **14**, 801 (2015).

[15] A. David, Y. Tian, P. Yang, X. Gao, W. Lin, A. B. Shah, J.-M. Zuo, W. Prellier, and T. Wu, Colossal positive magnetoresistance in surface-passivated oxygen-deficient strontium titanite, Sci. Rep. **5**, 10255 (2015).

[16] M. Huijben, G. Koster, M. K. Kruize, S. Wenderich, J. Verbeeck, S. Bals, E. Slooten, B. Shi, H. J. A. Molegraaf, J. E. Kleibeuker, S. van Aert, J. B. Goedkoop, A. Brinkman, D. H. A. Blank, M. S. Golden, G. van Tendeloo, H. Hilgenkamp, and G. Rijnders, Defect engineering in oxide heterostructures by enhanced oxygen surface exchange, Adv. Funct. Mater. **23**, 5240 (2013).

[17] F. Gunkel, S. Hoffmann-Eifert, R. Dittmann, S. B. Mi, C. L. Jia, P. Meuffels, and R. Waser, High temperature conductance characteristics of $LaAlO_3/SrTiO_3$-heterostructures under equilibrium oxygen atmospheres, Appl. Phys. Lett. **97**, 012103 (2010).

[18] D. V. Christensen, M. von Soosten, F. Trier, T. S. Jespersen, A. Smith, Y. Chen, and N. Pryds, Controlling the carrier density of $SrTiO_3$-based heterostructures with annealing, Adv. Electron. Mater. 1700026 (2017).

[19] F. Trier, K. V. Reich, D. V. Christensen, Y. Zhang, H. L. Tuller, Y. Chen, B. I. Shklovskii, and N. Pryds, Universality of electron mobility in $LaAlO_3/SrTiO_3$ and bulk $SrTiO_3$, Appl. Phys. Lett. **111**, 092106 (2017).

[20] T. D. Sanders, M. T. Gray, F. J. Wong, and Y. Suzuki, $LaAlO_3/SrTiO_3$ interfaces doped with rare-earth ions, Phys. Rev. B **91**, 205112 (2015).

[21] P. Schütz, D. V. Christensen, V. Borisov, F. Pfaff, P. Scheiderer, L. Dudy, M. Zapf, J. Gabel, Y. Z. Chen, N. Pryds, V. A. Rogalev, V. N. Strocov, T.-L. Lee, H. O. Jeschke, R. Valentí, M. Sing, and R. Claessen, Microscopic origin of the mobility enhancement at a spinel/perovskite oxide heterointerface revealed by photoemission spectroscopy, Phys. Rev. B **96**, 161409 (2017).

[22] D. V. Christensen, F. Trier, M. von Soosten, G. E. D. K. Prawiroatmodjo, T. S. Jespersen, Y. Z. Chen, and N. Pryds, Electric field control of the γ-$Al_2O_3/SrTiO_3$ interface conductivity at room temperature, Appl. Phys. Lett. **109**, 021602 (2016).

[23] A. Joshua, S. Pecker, J. Ruhman, E. Altman, and S. Ilani, A universal critical density underlying the physics of electrons at the $LaAlO_3/SrTiO_3$ interface, Nat. Commun. **3**, 1129 (2012).

[24] C. Hamaguchi, *Basic Semiconductor Physics* (Springer, Berlin, 2010).

[25] A. Verma, A. P. Kajdos, T. A. Cain, S. Stemmer, and D. Jena, Intrinsic Mobility Limiting Mechanisms in Lanthanum-Doped Strontium Titanate, Phys. Rev. Lett. **112**, 216601 (2014).

[26] S. Su, J. Ho You, and C. Lee, Electron transport at interface of $LaAlO_3$ and $SrTiO_3$ band insulators, J. Appl. Phys. **113**, 093709 (2013).

[27] C. Cancellieri, A. S. Mishchenko, U. Aschauer, A. Filippetti, C. Faber, O. S. Barišić, V. A. Rogalev, T. Schmitt, N. Nagaosa, and V. N. Strocov, Polaronic metal state at the $LaAlO_3/SrTiO_3$ interface, Nat. Commun. **7**, 10386 (2016).

[28] X. Lin, C. W. Rischau, L. Buchauer, A. Jaoui, B. Fauque, and K. Behnia, Metallicity without quasi-particles in

room-temperature strontium titanate, npj Quantum Mater. **2**, 41 (2017).

[29] F. E. Low and D. Pines, Mobility of slow electrons in polar crystals, Phys. Rev. **98**, 414 (1955).

[30] Z. Wang *et al.*, Tailoring the nature and strength of electron-phonon interactions in the $SrTiO_3(001)$ 2D electron liquid, Nat. Mater. **15**, 835 (2016).

[31] F. M. Peeters, X. Wu, and J. T. Devreese, Exact and approximate results for the mass of a two-dimensional polaron, Phys. Rev. B **37**, 933 (1988).

[32] G. Herranz, M. Basletić, M. Bibes, C. Carrétéro, E. Tafra, E. Jacquet, K. Bouzehouane, C. Deranlot, A. Hamzić, J.-M. Broto, A. Barthélémy, and A. Fert, High Mobility in $LaAlO_3/SrTiO_3$ Heterostructures: Origin, Dimensionality, and Perspectives, Phys. Rev. Lett. **98**, 216803 (2007).

[33] F. E. Low and D. Pines, The mobility of slow electrons in polar crystals, Phys. Rev. **91**, 193 (1953).

[34] A. S. Barker, Jr., Temperature dependence of the transverse and longitudinal optic mode frequencies and charges in $SrTiO_3$ and $BaTiO_3$, Phys. Rev. **145**, 391 (1966).

[35] C. Lee, J. Yahia, and J. L. Brebner, Electronic conduction in slightly reduced strontium titanate at low temperatures, Phys. Rev. B **3**, 2525 (1971).

[36] T. Okuda, K. Nakanishi, S. Miyasaka, and Y. Tokura, Large thermoelectric response of metallic perovskites: $Sr_{1-x}La_xTiO_3$ $(0 \leq x \leq 0.1)$, Phys. Rev. B **63**, 113104 (2001).

[37] D. van der Marel, J. L. M. van Mechelen, and I. I. Mazin, Common Fermi-liquid origin of T^2 resistivity and superconductivity in n-type $SrTiO_3$, Phys. Rev. B **84**, 205111 (2011).

[38] E. Mikheev, S. Raghavan, J. Y. Zhang, P. B. Marshall, A. P. Kajdos, L. Balents, and S. Stemmer, Carrier density independent scattering rate in $SrTiO_3$-based electron liquids, Sci. Rep. **6**, 20865 (2016).

[39] S. N. Klimin, J. Tempere, D. van der Marel, and J. T. Devreese, Microscopic mechanisms for the Fermi-liquid behavior of Nb-doped strontium titanate, Phys. Rev. B **86**, 045113 (2012).

[40] X. Lin, B. Fauqué, and K. Behnia, Scalable T^2 resistivity in a small single-component Fermi surface, Science **349**, 945 (2015).

[41] M. Swift and C. G. Van de Walle, Conditions for T^2 resistivity from electron-electron scattering, Eur. Phys. J. B **90**, 151 (2017).

[42] D. Monroe, Comparison of mobility-limiting mechanisms in high-mobility $Si_{1-x}Ge_x$ heterostructures, J. Vac. Sci. Technol. B **11**, 1731 (1993).

[43] X. Mi, T. M. Hazard, C. Payette, K. Wang, D. M. Zajac, J. V. Cady, and J. R. Petta, Magnetotransport studies of mobility limiting mechanisms in undoped Si/SiGe heterostructures, Phys. Rev. B **92**, 035304 (2015).

[44] M. Honig, J. A. Sulpizio, J. Drori, A. Joshua, E. Zeldov, and S. Ilani, Local electrostatic imaging of striped domain order in $LaAlO_3/SrTiO_3$, Nat. Mater. **12**, 1112 (2013).

[45] B. Kalisky, E. M. Spanton, H. Noad, J. R. Kirtley, K. C. Nowack, C. Bell, H. K. Sato, M. Hosoda, Y. Xie, Y. Hikita, C. Woltmann, G. Pfanzelt, R. Jany, C. Richter, H. Y. Hwang, J. Mannhart, and K. A. Moler, Locally enhanced conductivity due to the tetragonal domain structure in $LaAlO_3/SrTiO_3$ heterointerfaces, Nat. Mater. **12**, 1091 (2013).

[46] Y. Cao, X. Liu, P. Shafer, S. Middey, D. Meyers, M. Kareev, Z. Zhong, J.-W. Kim, P. J. Ryan, E. Arenholz *et al.*, Anomalous orbital structure in a spinel-perovskite interface, npj Quantum Mater. **1**, 16009 (2016).

[47] W. Son, E. Cho, B. Lee, J. Lee, and S. Han, Density and spatial distribution of charge carriers in the intrinsic n-type $LaAlO_3$-$SrTiO_3$ interface, Phys. Rev. B **79**, 245411 (2009).

[48] Y. Yamada, H. K. Sato, Y. Hikita, H. Y. Hwang, and Y. Kanemitsu, Spatial density profile of electrons near the $LaAlO_3/SrTiO_3$ heterointerface revealed by time-resolved photoluminescence spectroscopy, Appl. Phys. Lett. **104**, 151907 (2014).

[49] K. V. Reich, M. Schecter, and B. I. Shklovskii, Accumulation, inversion, and depletion layers in $SrTiO_3$, Phys. Rev. B **91**, 115303 (2015).

[50] P. Schütz, F. Pfaff, P. Scheiderer, Y. Z. Chen, N. Pryds, M. Gorgoi, M. Sing, and R. Claessen, Band bending and alignment at the spinel/perovskite γ-$Al_2O_3/SrTiO_3$ heterointerface, Phys. Rev. B **91**, 165118 (2015).

[51] M. Yazdi-Rizi, P. Marsik, B. P. P. Mallett, A. Dubroka, D. V. Christensen, Y. Z. Chen, N. Pryds, and C. Bernhard, Infrared ellipsometry study of the confined electrons in a high-mobility γ-$Al_2O_3/SrTiO_3$ heterostructure, Europhys. Lett. **113**, 47005 (2016).

[52] S. A. Solin, T. Thio, D. R. Hines, and J. J. Heremans, Enhanced room-temperature geometric magnetoresistance in inhomogeneous narrow-gap semiconductors, Science **289**, 1530 (2000).

[53] M. Holz, O. Kronenwerth, and D. Grundler, Magnetoresistance of semiconductor-metal hybrid structures: The effects of material parameters and contact resistance, Phys. Rev. B **67**, 195312 (2003).

[54] J. Sun and J. Kosel, Extraordinary magnetoresistance in semiconductor/metal hybrids: A review, Materials **6**, 500 (2013).

D. V. Christensen *et al.*
Strain tunable magnetism at ferroelastic domain walls
Accepted by *Nature Physics* (2018)

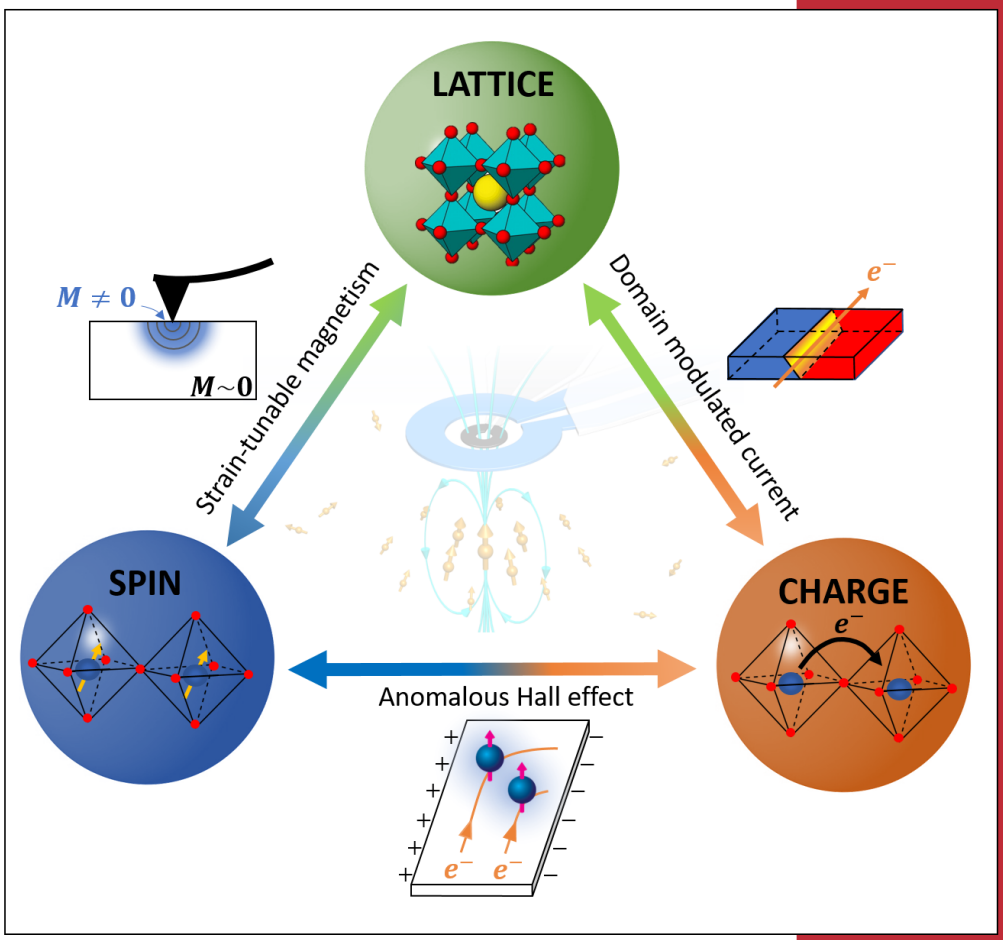

Coupling lattice, spin and charge
Figure: Nini Pryds and Dennis Valbjørn Christensen

Strain tunable magnetism at ferroelastic domain walls

D. V. Christensen[1†], Y. Frenkel[2†], Y. Xie[3,4,5], Z. Chen[4], Y. Hikita[3], A. Smith[1], Y. Z. Chen[1], L. Klein[6], H. Y. Hwang[3], N. Pryds[1], and B. Kalisky[2*]*

[1] *Department of Energy Conversion and Storage, Technical University of Denmark, Risø Campus, DK-4000 Roskilde, Denmark.*

[2] *Department of Physics and Institute of Nanotechnology and Advanced Materials, Bar-Ilan University, Ramat-Gan 5290002, Israel.*

[3] *Stanford Institute for Materials and Energy Sciences, SLAC National Accelerator Laboratory, Menlo Park, California 94025, USA*

[4] *Department of Applied Physics, Geballe Laboratory for Advanced Materials, Stanford University*

[5] *Department of Physics, Zhejiang University, Hangzhou, 310027, China*

[6] *Department of Physics, Nano-magnetism Research Center, Institute of Nanotechnology and Advanced Materials, Bar-Ilan University, Ramat-Gan, 5290002 Israel.*

[†] These authors contributed equally to this work

* Email: nipr@dtu.dk and beena@biu.ac.il.

Abstract:

The ability to write, erase and move domain walls between ferroelastic domains paves the way for making nanoelectronics where the domain wall is the device. Little is, however, known about the magnetic properties of the ferroelastic domain walls. A fascinating model system is $SrTiO_3$ where the ferroelastic domain walls display strain tunable polarity and enhanced conductivity besides being likely to host paired electrons existing both in the superconducting and non-superconducting state. Here, we reveal a long-range ferromagnetic order with stripy modulations along the ferroelastic domain walls in $SrTiO_3$ and $SrTiO_3$-based heterointerfaces using a scanning superconducting quantum interference device. The magnetism is coupled to high-mobility itinerant electrons with clear signatures in magnetotransport measurements. Strikingly, the magnetic state is also coupled dynamically to the lattice and can be reversibly tuned by applying local external forces. The study opens up for designing nanoscale devices based on domain walls where strain-tunable ferroelectric, ferroelastic and ferromagnetic orders may coexist.

of this material would require a thorough knowledge of all of solid state physics". This statement by M. L. Cohen[1] succinctly draws attention to the challenges of understanding the physical properties of $SrTiO_3$ (STO). Among its many features are a high electron mobility[2] and a low carrier density superconducting ground state[3,4]. In the search for properties beyond those found in pristine or doped STO, the coupling between the lattice and electronic degrees of freedom has been utilized successfully: Straining STO has led to a transition into ferroelectricity[5] and a 300% increase of the electron mobility[6]. Where the lattice symmetry of the bulk STO crystal is broken, e.g. at the interface between $LaAlO_3$ (LAO) and STO, electrons can be confined to the interface, leading to gate-tunability of a wide range of properties[7]. An additional intrinsic lattice symmetry breaking occurs below ~105 K when the cubic unit cell of STO becomes tetragonal with the long axis along either the [001], [010] or [100] direction[8–11]. In bulk STO, orienting the long axis in each of the three crystallographic directions results in equally stable tetragonal domains, which are separated by domain walls with well-defined orientations and modified electronic properties[12,13]. Thermal cycles of STO above 105K have been observed to result in new configurations of tetragonal domains[12,14,15]. Applied mechanical stresses moves the domain walls by enlarging favorable domains resulting in a hysteretic stress/strain response characteristic for ferroelastic materials. The position of such ferroelastic domain walls can also be conveniently controlled by electric fields, which allows for regulating the electronic properties of LAO/STO at the nanoscale[12,13].

Surprisingly, magnetic islands were imaged in the LAO/STO heterostructure with LAO thicknesses of at least 3 unit cells[16]. Later, it was shown that the magnitude and orientation of the magnetization on the islands can change in response to local stress[17]. A new dimension was hereby added to the functionalities of STO as spin and its coupling to charge and lattice can be utilized. However, the spin state of the confined electron gas turned out to display some intriguing scientific puzzles that continue to challenge our current understanding of physics on a fundamental level: First, the ferromagnetic order coexists with superconducting order despite ferromagnetism occurring by alignment of spins whereas electrons pair in a singlet state to form the conventional superconducting state[18,19]. Second, the superconductivity can be broken by application of a magnetic field, but the pairing of the electrons can survive in a non-superconducting state[20]. A recent experiment suggests that the electron pairing occurs at the ferroelastic domain walls[21] where they form a non-superconducting singlet state[20] or possibly even a spin-polarized state with more than two paired electrons. The magnetic state and the electron pairing are therefore intimately linked[22]. Despite years of intensive research the magnetic state remains one of the properties of the heterointerface which is poorest understood, hardest to reproduce and most challenging to control.

Several theoretical models have been proposed, including spiral magnetism in a charge-ordered state[23] and oxygen vacancy induced magnetism[24]. Experimentally, spatially resolved magnetometry measurements have played a key role. A scanning superconducting quantum interference device (SQUID) operating at low temperatures revealed disperse ferromagnetic patches smaller than the 3 µm resolution limit[16,18]. Room temperature magnetic force microscopy was also used to probe the magnetic landscape emerging as the electrons at the LAO/STO interface was depleted using a top gate[25]. Additional experimental signatures of magnetism stem from (i) magnetometry measurements without spatial resolution, such as SQUID[26] & torque magnetometry[19], (ii) transport measurements reporting Kondo-like resistance minima[27,28], anomalous Hall effect[29–31] & negative or anisotropic magnetoresistance[26,28–30,32,33] and (iii) irradiation-based techniques such as β-decay from nuclear magnetic resonance[34] & X-ray magnetic circular dichroism[35]. On the other hand, a magnetic state was not detected in several studies using, e.g., scanning SQUID[36] and neutron reflectometry[37], and not only the nature of the magnetic state in these systems is an open question but even its mere existence.

Here, we probe the magnetic state of LAO/STO, γ-Al_2O_3 (GAO)/STO and bare STO surfaces using scanning SQUID magnetometry. In all cases, we observe a long-range magnetic order with striped modulations oriented parallel to the ferroelastic domain walls of STO. The magnetic state is coupled to the lattice and can be reversibly tuned by applying local external forces. In addition, clear magnetic signatures in the magnetotransport measurements show that the magnetic order is coupled to the itinerant charges. This striking observation opens up for realizing multifunctional nanoelectronics at domain walls with strain-tunable ferromagnetic, ferroelastic and ferroelectric properties.

Imaging striped magnetic order along ferroelastic domain walls:

We map the microscopic landscape of the magnetic state in the STO-based systems using scanning SQUID microscopy (see Suppl. Section 1 for materials and methods). The scanning SQUID measures the magnetic flux entering a 1.8 µm wide pick-up loop, and produces a two-dimensional map of the flux when the pick-up loop scans across the sample surface. The measurements are performed in the absence of an externally applied magnetic field (background field < 0.1 µT) and therefore probe the magnetic field originating from a spontaneous magnetic order in the sample. In the case of LAO/STO, such measurements originally showed the presence of ferromagnetic patches[16] and their coexistence with superconductivity[18]. Looking into regions without ferromagnetic patches and enhancing the

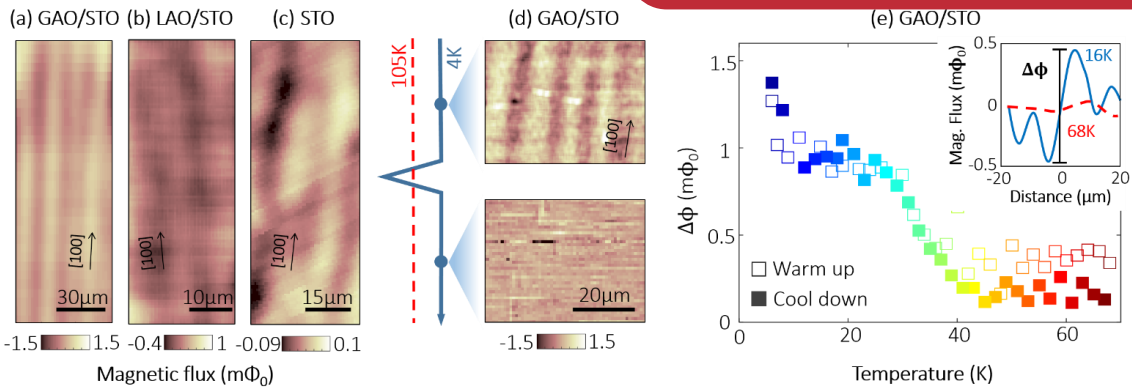

Fig. 1: Scanning SQUID maps of striped magnetic order. (a-c) Large area scans showing magnetic stripes along the [100] crystallographic direction in γ-Al_2O_3 (GAO)/$SrTiO_3$ (STO), $LaAlO_3$ (LAO)/$SrTiO_3$ (STO) and vacuum-annealed $SrTiO_3$. (d) The same location on GAO/STO imaged in two subsequent scans before and after thermal cycling the sample above 105 K (the structural transition temperature of STO). (e) Temperature dependence of the peak-to-peak modulation amplitude (Δφ) defined using line scans as shown in the inset. The modulations disappear as the temperature exceeds 40 K, and reappear without noticeable hysteresis during the subsequent cool down below 40 K. The magnetic flux is offset by the average value of the scan for all figures.

signal-to-noise ratio, our magnetic flux maps reveal wide, striped modulations in both LAO/STO, GAO/STO and vacuum-annealed STO (see Figure 1a-c). The striped modulations extend over hundred micrometers showing a long-range magnetic order. The striped modulations in the magnetic flux have been observed in five GAO/STO heterostructures with a typical magnitude on the order of 1 $m\phi_0$ at 5 K. The modulations are generally stronger in GAO/STO compared to LAO/STO and STO.

As the magnetic flux escaping a homogeneously magnetized sample will show a homogeneous flux map in regions far from the sample edges, the flux modulations we observe point to a magnetization with spatial inhomogeneities. We estimate that the typical modulation magnitude of ~1 $m\phi_0$ corresponds to changes in the magnetization on the order of 0.05 μ_B pr. surface unit cell (see Suppl. Section 2). The inhomogeneities are observed along the $[100]$, $[010]$, $[110]$ and $[1\bar{1}0]$ crystallographic directions of STO in all three material systems. Remarkably, these orientations coincide with the orientation of ferroelastic domain walls on the (001) surface of STO[9,13]. When we cycle the temperature above 105 K in the case of GAO/STO we observe that a set of [100]-oriented striped magnetic modulations with an amplitude of 0.5 $m\phi_0$ changes to barely detectable [110]-oriented modulations with an amplitude of less than 0.05 $m\phi_0$ (see Figure 1d). Changes in the striped magnetic landscape after thermal cycling also occur for bare STO without the GAO layer (see Suppl. Section 3). The results of the thermal cycling exclude the possibility that the magnetic stripes are caused by a trivial magnetic contamination.

Scanning SQUID has also been used to map the spatial distribution of current flow in LAO/STO[12] and GAO/STO[38], which revealed striped current modulations with the same crystallographic orientations as the magnetic stripes. Comparing the current flow with optical imaging of the domain structure furthermore showed that their orientations coincide[14]. Here, we perform magnetometry and current mapping on the same area, and observe a clear relation between the magnetic and current modulations (see Suppl. Section 4), implying that both the magnetic and current modulations are related to the domain structure.

When the temperature is raised gradually from 5 K to 70 K, the magnetic modulations monotonically decrease in size until their disappearance at around 40 K (see Figure 1e). This characteristic temperature also roughly marks another anomaly of the STO substrate where its quantum paraelectric transition causes the dielectric constant to diverge[39,40]. Other interesting observations below this temperature are polarity at the STO domain walls[41,42] and striped modulations in the current flow. Cooling the GAO/STO heterostructure to 5 K again reintroduces the magnetic modulations without noticeable changes in size or location as long as the 105 K transition temperature is not crossed.

Coupling between the magnetic state and current flow:

The disappearance of the magnetic modulations above 40 K is reflected in the Hall and magnetoresistance measurements as observed particularly clearly in the case of GAO/STO. A Hall effect which is linear as a function of the magnetic field serves as a valuable tool for extracting the carrier density in a single-band conductor, while deviations from linearity can be used to deduce the band structure or magnetism. In the case of LAO/STO[43], the Hall resistance is S-shaped at low temperatures for carrier densities exceeding ~$1.7 \cdot 10^{13}$ cm^{-2}. The S-shape originates from transport occurring in two n-type bands with d_{xy} and d_{xz}/d_{yz} character[43]. The presence of magnetism can lead to the anomalous Hall effect, which has been observed as small perturbations to the S-shape[29–31]. In the case of GAO/STO, the Hall resistance (R_{xy}) is linear for $T > 40$ K revealing, for

sity of $n_s \sim 6 \cdot 10^{14}$ cm^{-2}. For $T < 40$ K, pronounced non-linearities arise without hysteresis. At these low temperatures, $|dR_{xy}/dB|$ increases at high magnetic fields, opposite to the S-shaped non-linearities observed in LAO/STO. If the

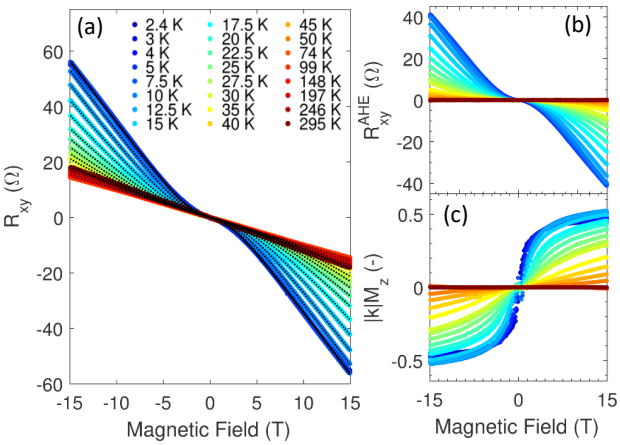

Fig. 2: Anomalous Hall effect. (a) Hall resistance (R_{xy}) as a function of the magnetic field applied perpendicular to the interface of GAO/STO. Non-linearities are observed below 40 K. (b) Anomalous Hall resistance (R_{xy}^{AHE}) obtained from R_{xy} by subtracting the ordinary Hall effect determined from the low-field slope of R_{xy}. (c) The component of the magnetization perpendicular to the interface (M_z) multiplied by a proportionality constant k as described in the main text.

nonlinearity of the Hall resistance in GAO/STO were due to two-band conductivity, it would entail a coexistence of a large number of electrons and holes, which we reject as detailed in Suppl. Section 5. Instead, we attribute the non-linearity to the anomalous Hall effect resistance (R_{xy}^{AHE}) arising from the interaction between the itinerant electrons and the component of the magnetization normal to the interface[44], $R_{xy}^{AHE} = R_s^{AHE} M_z$. We find that the anomalous Hall prefactor (R_s^{AHE}) scales linearly with the sheet resistance (R_s) as expected when skew scattering mechanism dominates[44] (see Suppl. Section 6). This leads to the following expression

$$R_{xy} = R_{xy}^{OHE} + R_{xy}^{AHE} = -\frac{1}{en_s}B + kR_s(B,T)M_z(B,T)$$

where R_s^{OHE} is the ordinary Hall effect and k is a field and temperature independent constant. For GAO/STO the d_{xz}/d_{yz} bands have been reported[45] to be comparable or even lower in energy than d_{xy}. This, together with the high density of states of the d_{xz}/d_{yz} bands, means that the majority of the electrons are expected to populate the d_{xz}/d_{yz} bands. For simplicity we describe the ordinary Hall effect through the sheet carrier density (n_s) with a one band model. Our data cannot exclude the presence of a second *n*-type band, but as outlined in Suppl. Section 6 this will not change the conclusions drawn here. At high magnetic fields, the sheet resistance increases linearly with the magnetic field, which, remarkably, results in a non-saturating anomalous Hall effect up to at least 15 T (see Figure 2b). The usual extraction of the carrier density from the slope of the Hall resistance at high magnetic fields is therefore invalid as this region includes contributions from both the ordinary and anomalous Hall effect. The carrier densities can be most accurately determined at low magnetic fields where the contribution from the anomalous Hall effect is small (see Suppl. Section 6). The low-field slope of the Hall resistance is constant at all temperatures (see Figure 2a) and we can therefore extract a temperature-independent carrier density of $\sim 6 \cdot 10^{14}$ cm^{-2}. This is consistent with the temperature independent carrier density deduced optically from the infrared Berreman mode similar to Ref. 46.

By extracting $kM_z(B,T) = (R_{xy} - R_{xy}^{OHE})/R_s$ we infer that the component of the magnetization parallel to the perpendicular magnetic field starts to saturate at $\sim$2 T for temperatures below $\sim$8 K (see Figure 2c). Increasing the temperature opposes the alignment of magnetic moments up to $T \sim 40$ K where the magnetization is no longer detectable. This agrees well with the disappearance of the magnetic modulations observed with scanning SQUID. Together with the appearance of magnetic modulations and non-linear Hall resistances for $T < 40$ K, we also observe that the magnetoresistance deviates from Kohler's rule[47] at these temperatures. This is consistent with the fact that Kohler's rule does not consider the reduction of charge carrier scattering due to field-induced suppression of spin fluctuations (see Suppl. Section 6). A similar behavior of the Hall resistance and magnetoresistance is observed in four samples (see Suppl. Section 6-7).

Mechanical tuning of the magnetic state:
A particularly intriguing feature of the magnetic stripes observed is their tunability under small stresses. When applying a constant force to GAO/STO using the scanning SQUID probe, the temperature dependence of the magnetic modulations is markedly different (see Figure 3a). Instead of the gradual decrease of the modulation strength observed up to 40 K, sharp, stripy features emerge when a force of 56 nN is applied. This applied force corresponds to a pressure on the order of 10^7 Pa (see Methods). The features start to emerge around 10 K and the flux modulations are increased by a factor of four when reaching 16 K. The sharp features are only obtained after applying a local force to the sample surface with the probe, and the features become monotonically stronger when increasing the applied force (see Figure 3b). Interestingly, in all cases, the original magnetic landscape without the sharp magnetic modulations can be restored without noticeable hysteresis by lowering the temperature or removing the force. A similar behavior is also observed in LAO/STO (see Suppl. Section 8). We emphasize that this observation is different from the

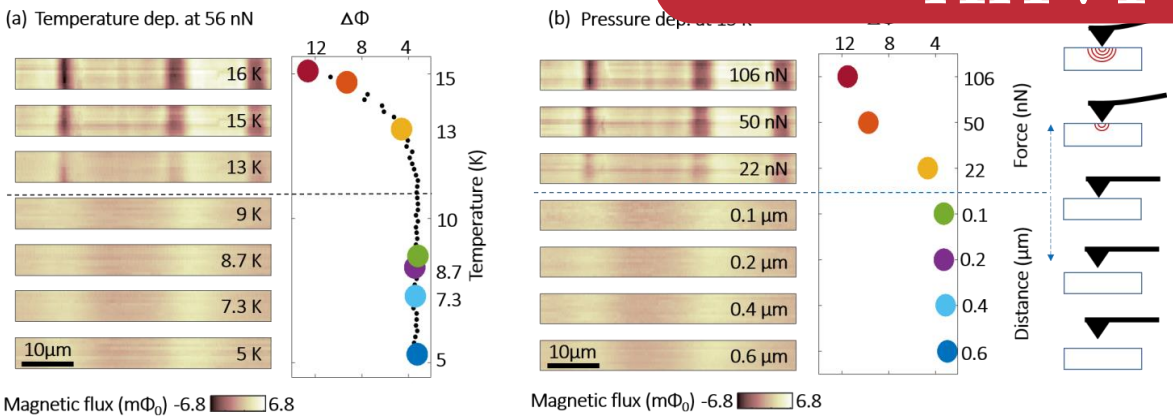

Fig. 3: Pressure dependent magnetic signal. (a) Spatial modulation in the magnetic flux as a function of temperature while pushing the tip of the SQUID into the GAO/STO sample with a force of 56 nN. Above ~10 K the magnetic modulations become very sharp and the peak-to-peak modulation amplitude (Δϕ) increases monotonically with temperature. (b) Magnetic modulations at a fixed temperature of 15 K as the SQUID tip approaches the GAO/STO sample. When the SQUID reaches the sample, sharp magnetic modulations emerge. Further lowering the SQUID results in applying a stronger external force to the sample, which causes an increase in the peak-to-peak modulation amplitude. The force is measured capacitatively via the deflection of the SQUID cantilever. In all cases, the magnetic flux is offset by the average value of the scan.

report of Kalisky *et al.*[17], where they imaged and reoriented the magnetization of magnetic islands in LAO/STO by applying local stress with a scanning probe. The signal of the magnetic islands was almost two orders of magnitude stronger, they appeared in isolated and dispersed locations, and did not change with temperature[16]. The magnetic stripes we observe here are weaker, long range in nature, become stronger with temperature under the application of stress, and appear at different locations after temperature cycles. The relation between stress and magnetism can also be examined by investigating the naturally occurring stresses in the samples by mapping large areas. We find that areas with complex domain structures, formed to relieve local stress in the sample, are more likely to exhibit magnetic stripes (such as Figure 1a-c). In the samples measured in this study, there were large areas with an extent of hundreds of microns, where no magnetic stripes were observed within our detection limit of 0.05 $m\phi_0$ (d.c.). After temperature cycles above 105 K, magnetic stripes can be found within these areas as in Figure 2b. Modulations are observed more strongly in the vicinity of areas expected to exhibit stress such as close to sample borders or around a scratch introduced intentionally on the surface of one sample. Concurrent with higher stresses, these areas may also attact the largest amount of defects such as oxygen vacancies.

We further measure the magnetic response (susceptibility) by applying a small oscillating magnetic field of ± 0.3 mT locally to the GAO/STO heterostructure while simultaneously applying a local force of 56 nN with the scanning probe. We find that the weak magnetic susceptibility observed below 5 K increases markedly above ~8 K (see Figure 4a) and reaches a strong paramagnetic response up to 8 Φ_0/A at 16 K. The spatially resolved susceptibility data (Suppl. Section 9) reveal that the areas in Figure 3 with strong magnetic signals also show a slower increase in the paramagnetic susceptibility above ~8 K. Interestingly, this characteristic temperature also appears in the anomalous Hall effect analysis. The characteristic magnetic field (B_c) for the emergence of the anomalous Hall resistance can be described by the half width at half maximum of the bell-shaped $\mathrm{d}R_{xy}/\mathrm{d}B$. Below ~8 K, the characteristic field is temperature independent, consistent with reports on NGO/STO[31], as expected if an exchange coupling in a magnetically ordered state prevents the magnetization to be induced or aligned along the field (see Figure 4a). At higher temperatures, B_c is linearly increasing with temperature pointing towards a behavior similar to paramagnetism where the alignment of magnetic moments is countered by thermal fluctuations.

Discussion:

Evidence of ferromagnetism in STO-based heterostructures has been reported by several independent experimental techniques[22]. Despite theoretical and experimental efforts, the origin of the unexpected ferromagnetism in these heterostructures is still not clear. Here, we observe a long-range magnetic state that is modulated by the crystallographic domains in STO and is highly tunable by local application of external forces. The striped magnetic modulations originate from the tetragonal domain structure of STO and are thus displayed in both STO and the STO-based heterostructures. The undoped STO studied here is, however, electrically insulating, which hinders spintronic applications and investigation of the magnetic state through the anomalous Hall effect and magnetoresistance. Interfacing STO with GAO or LAO on the other hand provides itinerant carriers to the surface of STO, which couple closely to the

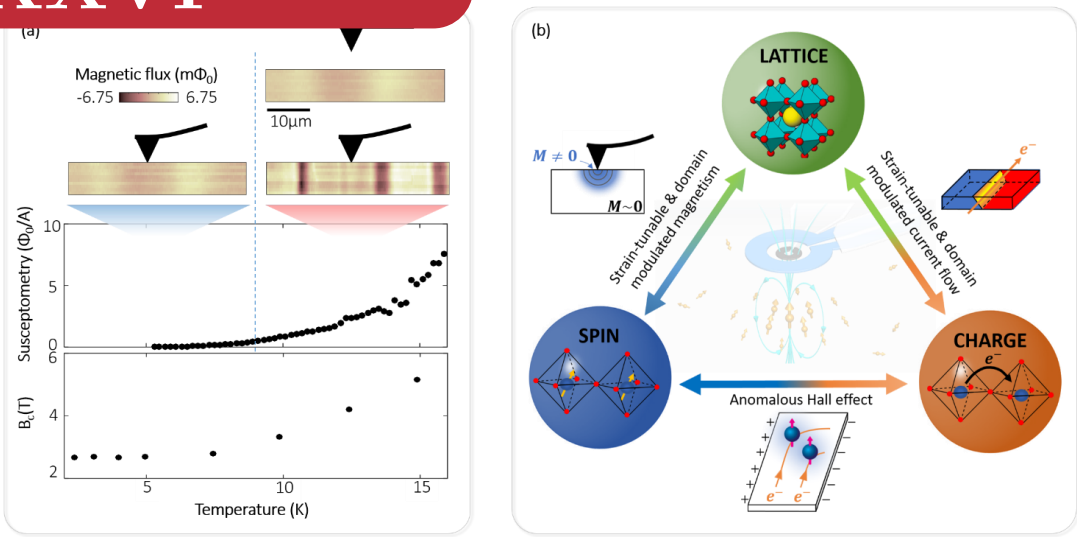

Fig. 4: Coupling between lattice, spin and charge. (a) Temperature dependence of the magnetic properties in GAO/STO showing (i) emergence of sharp magnetic features above ~10 K upon application of an external force, (ii) an increase in the magnetic susceptibility with an onset of ~8 K and (iii) the characteristic field B_c, defined as the half width at half maximum of dR_{xy}/dB from Figure 2a, undergoing a change from temperature-independent to linearly increasing with temperature at ~8 K. (b) A close coupling between the lattice, spin and charge degrees of freedom. The magnetic state is closely coupled to the lattice as revealed by applying external force locally to the sample with the scanning probe. The tetragonal domain formation also causes local lattice distortions, which both favors ferromagnetic order and modulates the charge current. The charge current is, in turn, scattered asymmetrically by the magnetic moments, giving rise to the anomalous Hall resistance.

magnetic moments. Our observations uncover characteristic temperatures of ~8 K and ~40 K occurring in both transport and SQUID measurements. We propose that these characteristic temperature regimes originate from the following reasons:

(1) Below 8 K, the STO-based heterostructures are in a magnetically ordered state, which manifests itself in small or no modulations in magnetization in the scanning SQUID maps (Figure 3a-b). This state is characterized by a very weak (almost zero) susceptibility in response to small magnetic fields of ±0.3 mT. Applying a temperature-independent magnetic field of B_c ~ 2 T aligns the magnetic moments perpendicular to the interface, which causes the anomalous Hall effect (Figure 1a and 4a). At these temperatures, a local application of an external force of up to 106 nN has no observable effect on the ordered state.

(2) Above ~ 8 K, the magnetic order is less robust. This is supported by the increase in the paramagnetic susceptibility under a small applied force of 56 nN (Figure 4a) suggesting a gradual change where ordered magnetic moments convert into paramagnetic moments. The conversion is slower at the domain walls where the magnetic moments appear to be ordered more strongly, leading to areas with a slower growth in the magnetic susceptibility and large modulations of the magnetic signal (Suppl. Section 9). The alignment of the paramagnetic moments with the magnetic field is countered by thermal fluctuations resulting in a linear increase of B_c with temperature (see Figure 4a). The fragile magnetic order above 8 K is highly sensitive to externally applied forces, and stronger magnetic modulations can be induced here (Figure 4a). This points towards a delicate balance between the unperturbed magnetic order existing in the absence of stress and a ferromagnetic order induced by the stress. Applying force causes a shift towards the ferromagnetic order in this temperature range. One of the possible mechanisms for the appearance of ferromagnetism is that the magnetic moments are produced by oxygen vacancies[24,48]. This is supported by the vast number of oxygen vacancies present particularly in GAO/STO[49,50] as well as the localized in-gap states formed by the oxygen vacancies[51].

The unperturbed magnetic order may be due to e.g. spiral magnetic ordering[23] or electron pairing[20,22] where it is expected that the state is non-hysteretic and results in a small magnetic susceptibility when applying small magnetic fields. Strikingly, it has been predicted that a pressure-sensitive transition from a spiral order to a ferromagnetic order occurs due to a polar distortion in STO where titanium ions are displaced relative to the oxygen ions[23]. This agrees well with recent experiments in LAO/STO showing that applying a local external force changes the polar state at the ferroelastic domain walls of STO[42]. Such a polarity-induced ferromagnetic order may also explain why the magnetic stripes (even in absence of an external force) are parallel to the domain walls in STO, as the domain walls have been observed to be polar[41,42].

(3) Above 40 K, all signatures of magnetism from anomalous Hall effect, magnetoresistance and scanning SQUID vanish. This characteristic temperature also marks the disappearance of the striped current modulations in LAO/STO[12] as well as the disappearance of magnetism in LAO/STO according to some studies[32,33]. It also agrees reasonably well with the emergence of polar domain walls[41,42] only below approximately 50 K, again hinting towards the influence of STO polarity.

The advances made here demonstrate that the STO-based material systems show an intriguing link between the charge, spin and lattice degrees of freedom in STO-based heterostructures as illustrated in Figure 4b. The magnetic state couples to the current flow causing an asymmetric scattering of the charge carriers (Figure 2). The lattice and its domains also highly influence both the magnetic state (Figure 1) and current flow[12,38,42]. In particular, applying an external pressure in vicinity of the ferroelastic domain walls dramatically alters the magnetic state (Figure 3 and Suppl. Section 9), the current flow[42] and the polarity of the ferroelastic domain walls[42]. We therefore propose that an exciting multiferroic state awaits to be discovered where a strain-tunable ferroelectric, ferroelastic and ferromagnetic order coexists. The key role played by the ferroelastic domain walls of STO further demonstrates the prospects of using domain walls for functional nanoelectronics with tunable magnetic properties. STO proves, once again, to be an exciting multifunctional material that truly requires 'a thorough knowledge of all of solid state physics'.

Methods:

See Suppl. Section 1.

Data availability:

The data that support the plots within this paper and other findings of this study are available from the corresponding authors upon reasonable request.

References:

1. Cohen, M. L. Superconductivity in Low-Carrier-Density Systems: Degenerate Semiconductors. *Supercond. Part I* 615 (1969).
2. Frederikse, H. P. R. & Hosler, W. R. Hall Mobility in $SrTiO_3$. *Phys. Rev.* **161,** 822 (1967).
3. Schooley, J. F., Hosler, W. R. & Cohen, M. L. Superconductivity in Semiconducting $SrTiO_3$. *Phys Rev Lett* **12,** 474–475 (1964).
4. Schooley, J. F. *et al.* Dependence of the Superconducting Transition Temperature on Carrier Concentration in Semiconducting $SrTiO_3$. *Phys Rev Lett* **14,** 305–307 (1965).
5. Haeni, J. H. *et al.* Room-temperature ferroelectricity in strained $SrTiO_3$. *Nature* **430,** 758 (2004).
6. Jalan, B., Allen, S. J., Beltz, G. E., Moetakef, P. & Stemmer, S. Enhancing the electron mobility of $SrTiO_3$ with strain. *Appl. Phys. Lett.* **98,** 132102 (2011).
7. Pai, Y.-Y., Tylan-Tyler, A., Irvin, P. & Levy, J. Physics of $SrTiO_3$-based heterostructures and nanostructures: a review. *Rep. Prog. Phys.* **81,** 036503 (2018).
8. Rimai, L. Electron paramagnetic resonance of trivalent gadolinium ions in strontium and barium titanates. *Phys. Rev.* **127,** 702 (1962).
9. C[illegible] Titanate. *Phys. Rev.* **134,** A981–A997 (1964).
10. Heidemann, A. & Wettengel, H. Die Messung der Gitterparameteränderung von $SrTiO_3$. *Z. Für Phys. Hadrons Nucl.* **258,** 429–438 (1973).
11. Lytle, F. W. X-Ray Diffractometry of Low-Temperature Phase Transformations in Strontium Titanate. *J. Appl. Phys.* **35,** 2212 (1964).
12. Kalisky, B. *et al.* Locally enhanced conductivity due to the tetragonal domain structure in $LaAlO_3/SrTiO_3$ heterointerfaces. *Nat. Mater.* 1–5 (2013). doi:10.1038/nmat3753
13. Honig, M. *et al.* Local electrostatic imaging of striped domain order in $LaAlO_3/SrTiO_3$. *Nat. Mater.* **12,** 1112–1118 (2013).
14. Erlich, Z. *et al.* Optical Study of Tetragonal Domains in $LaAlO_3/SrTiO_3$. *J. Supercond. Nov. Magn.* **28,** 1017–1020 (2015).
15. Frenkel, Y. *et al.* Anisotropic Transport at the $LaAlO_3/SrTiO_3$ Interface Explained by Microscopic Imaging of Channel-Flow over $SrTiO_3$ Domains. *ACS Appl. Mater. Interfaces* **8,** 12514–12519 (2016).
16. Kalisky, B. *et al.* Critical thickness for ferromagnetism in $LaAlO_3/SrTiO_3$ heterostructures. *Nat. Commun.* **3,** 922 (2012).
17. Kalisky, B. *et al.* Scanning Probe Manipulation of Magnetism at the $LaAlO_3/SrTiO_3$ Heterointerface. *Nano Lett.* **12,** 4055–4059 (2012).
18. Bert, J. A. *et al.* Direct imaging of the coexistence of ferromagnetism and superconductivity at the $LaAlO_3/SrTiO_3$ interface. *Nat. Phys.* **7,** 767–771 (2011).
19. Li, L., Richter, C., Mannhart, J. & Ashoori, R. C. Coexistence of magnetic order and two-dimensional superconductivity at $LaAlO_3/SrTiO_3$ interfaces. *Nat. Phys.* **7,** 762–766 (2011).
20. Cheng, G. *et al.* Electron pairing without superconductivity. *Nature* **521,** 196–199 (2015).
21. Pai, Y.-Y. *et al.* One-Dimensional Nature of Pairing and Superconductivity at the $SrTiO_3$/LaAlO<sub>3 Interface. *Phys. Rev. Lett.* **120,** 147001 (2018).
22. Pai, Y.-Y., Tylan-Tyler, A., Irvin, P. & Levy, J. $LaAlO_3/SrTiO_3$: a tale of two magnetisms. *ArXiv Prepr. ArXiv161000789* (2016).
23. Banerjee, S., Erten, O. & Randeria, M. Ferromagnetic exchange, spin-orbit coupling and spiral magnetism at the $LaAlO_3/SrTiO_3$ interface. *Nat. Phys.* **9,** 626–630 (2013).
24. Pavlenko, N., Kopp, T., Tsymbal, E. Y., Sawatzky, G. A. & Mannhart, J. Magnetic and superconducting phases at the $LaAlO_3/SrTiO_3$ interface: The role of interfacial Ti 3d electrons. *Phys. Rev. B* **85,** 020407 (2012).
25. Bi, F. *et al.* Room-temperature electronically-controlled ferromagnetism at the $LaAlO_3/SrTiO_3$ interface. *Nat. Commun.* **5,** 5019 (2014).
26. Ariando *et al.* Electronic phase separation at the $LaAlO_3/SrTiO_3$ interface. *Nat. Commun.* **2,** 188 (2011).
27. Brinkman, A. *et al.* Magnetic effects at the interface between non-magnetic oxides. *Nat. Mater.* **6,** 493–496 (2007).
28. Hu, H.-L. *et al.* Subtle Interplay between Localized Magnetic Moments and Itinerant Electrons in $LaAlO_3/SrTiO_3$ Heterostructures. *ACS Appl. Mater. Interfaces* **8,** 13630–13636 (2016).
29. Joshua, A., Ruhman, J., Pecker, S., Altman, E. & Ilani, S. Gate-tunable polarized phase of two-dimensional electrons at the $LaAlO_3/SrTiO_3$ interface. *Proc. Natl. Acad. Sci.* **110,** 9633–9638 (2013).
30. Seri, S., Schultz, M. & Klein, L. Interplay between sheet resistance increase and magnetotransport properties in $LaAlO_3/SrTiO_3$. *Phys. Rev. B* **86,** 085118 (2012).
31. Gunkel, F. *et al.* Defect Control of Conventional and Anomalous Electron Transport at Complex Oxide Interfaces. *Phys. Rev. X* **6,** 031035 (2016).
32. Ben Shalom, M. *et al.* Anisotropic magnetotransport at the $SrTiO_3/LaAlO_3$ interface. *Phys. Rev. B* **80,** 140403 (2009).

three-dimensional electron gas in $LaAlO_3/SrTiO_3$ heterostructures: Influence of magnetic ordering, interface scattering, and dimensionality. *Phys. Rev. B* **84,** 075312 (2011).
34. Salman, Z. *et al.* Nature of Weak Magnetism in $SrTiO_3/LaAlO_3$ Multilayers. *Phys. Rev. Lett.* **109,** 257207 (2012).
35. Lee, J.-S. *et al.* Titanium d_{xy} ferromagnetism at the $LaAlO_3/SrTiO_3$ interface. *Nat. Mater.* 1–4 (2013). doi:10.1038/nmat3674
36. Wijnands, T. Scanning superconducting quantum interference device microscopy: sensitive mapping of magnetic flux on thin films. (Scanning superconducting quantum interference device microscopy, University of Twente, 2013).
37. Fitzsimmons, M. R. *et al.* Upper Limit to Magnetism in $LaAlO_3/SrTiO_3$ Heterostructures. *Phys. Rev. Lett.* **107,** 217201 (2011).
38. Christensen, D. V. *et al.* Electron Mobility in γ-$Al_2O_3/SrTiO_3$. *Phys. Rev. Appl.* **9,** (2018).
39. Neville, R. C., Hoeneisen, B. & Mead, C. A. Permittivity of Strontium Titanate. *J. Appl. Phys.* **43,** 2124–2131 (1972).
40. Rowley, S. E. *et al.* Ferroelectric quantum criticality. *Nat. Phys.* **10,** 367–372 (2014).
41. Scott, J. F., Salje, E. K. H. & Carpenter, M. A. Domain Wall Damping and Elastic Softening in $SrTiO_3$: Evidence for Polar Twin Walls. *Phys. Rev. Lett.* **109,** (2012).
42. Frenkel, Y. *et al.* Imaging and tuning polarity at $SrTiO_3$ domain walls. *Nat. Mater.* (2017). doi:doi:10.1038/nmat4966
43. Joshua, A., Pecker, S., Ruhman, J., Altman, E. & Ilani, S. A universal critical density underlying the physics of electrons at the $LaAlO_3/SrTiO_3$ interface. *Nat. Commun.* **3,** 1129 (2012).
44. Nagaosa, N., Sinova, J., Onoda, S., MacDonald, A. H. & Ong, N. P. Anomalous Hall effect. *Rev. Mod. Phys.* **82,** 1539–1592 (2010).
45. Cao, Y. *et al.* Anomalous orbital structure in a spinel–perovskite interface. *Npj Quantum Mater.* **1,** 16009 (2016).
46. Yazdi-Rizi, M. *et al.* Infrared ellipsometry study of the confined electrons in a high-mobility γ-$Al_2O_3/SrTiO_3$ heterostructure. *EPL Europhys. Lett.* **113,** 47005 (2016).
47. Pippard, A. B. *Magnetoresistance in metals*. (Cambridge University Press, 1989).
48. Coey, J. M. D., Venkatesan, M. & Stamenov, P. Surface magnetism of strontium titanate. *J. Phys. Condens. Matter* **28,** 485001 (2016).
49. Chen, Y. Z. *et al.* A high-mobility two-dimensional electron gas at the spinel/perovskite interface of γ-$Al_2O_3/SrTiO_3$. *Nat. Commun.* **4,** 1371 (2013).
50. Christensen, D. V. *et al.* Controlling the carrier density of $SrTiO_3$-based heterostructures with annealing. *Adv. Electron. Mater.* 1700026 (2017).
51. Schütz, P. *et al.* Microscopic origin of the mobility enhancement at a spinel/perovskite oxide heterointerface revealed by photoemission spectroscopy. *Phys. Rev. B* **96,** 161409 (2017).

Acknowledgements:
We acknowledge the useful discussions with Raelph Claessen and Philipp Schütz from the University of Würzburg, Jeremy Levy from Pittsburgh University and Yu Zhang and Yulin Gan from the Technical University of Denmark. In addition, we thank Christian Bernhard and Meghdad Yazdi for insight in the temperature dependence of the carrier density extracted by infrared ellipsometry.

Author Contributions:
D.V.C., Y.F., N.P. and B.K. initiated this work. D.V.C. performed the transport measurements and prepared the GAO/STO samples. Y.X., Z.C., Y.H. and H.Y.H. prepared the LAO/STO samples. D.V.C., Y.F. and B.K. performed the scanning SQUID measurements. D.V.C., and Y.F. performed data analysis. D.V.C., Y.F., A.S., Y.Z.C., L.K., N.P. and B.K. interpreted the data. D.V.C. wrote the manuscript with Y.F. and input from all authors.

Additional information:
Supplementary information is available in the online version of the paper. Reprints and permissions information is available online at www.nature.com/reprints. Correspondence and requests for materials should be addressed to B. Kalisky (beena@biu.ac.il) and N. Pryds (nipr@dtu.dk), respectively.

Competing Financial Interests:
The authors declare no competing financial interests.

Supplementary material for

Strain tunable magnetism at ferroelastic domain walls

D. V. Christensen[1†], Y. Frenkel[2†], Y. Xie[3,4,5], Z. Chen[4], Y. Hikita[3], A. Smith[1], Y. Z. Chen[1], L. Klein[6], H. Y. Hwang[3], N. Pryds[1], and B. Kalisky[2*]*

[1] *Department of Energy Conversion and Storage, Technical University of Denmark, Risø Campus, DK-4000 Roskilde, Denmark.*

[2] *Department of Physics and Institute of Nanotechnology and Advanced Materials, Bar-Ilan University, Ramat-Gan 5290002, Israel.*

[3] *Stanford Institute for Materials and Energy Sciences, SLAC National Accelerator Laboratory, Menlo Park, California 94025, USA*

[4] *Department of Applied Physics, Geballe Laboratory for Advanced Materials, Stanford University*

[5] *Department of Physics, Zhejiang University, Hangzhou, 310027, China*

[6] *Department of Physics, Nano-magnetism Research Center, Institute of Nanotechnology and Advanced Materials, Bar-Ilan University, Ramat-Gan, 5290002 Israel.*

† These authors contributed equally to this work

* Email: nipr@dtu.dk and beena@biu.ac.il.

Table of contents

The PDF file contains:

Section 1:
Materials, methods and magnetic impurities

Sample preparation:
The LAO/STO and GAO/STO heterostructures were prepared from TiO_2-terminated STO using standard protocols for the two heterostructures with details found in Ref. (*1*) and (*2*). Importantly, 5 unit cells of LAO was deposited on STO at 800 °C in an oxygen pressure of 10^{-5} mbar and cooled down to 600 °C, where it was annealed in an atmosphere of 0.4 bar oxygen for one hour. The GAO film was deposited on STO at 650 °C in an oxygen pressure of 10^{-5} mbar and cooled down to room temperature in the deposition pressure in absence of an annealing step. The STO substrates were exposed to the same conditions as the GAO/STO heterostructure, except for the deposition.

Transport measurements:
The buried interfaces were contacted by wedge-bonding with aluminum wires in the van der Pauw geometry to avoid influence of patterning the interface into Hall-bars. The magnetoresistance and Hall resistance were symmetrized and antisymmetrized, respectively, prior to the analysis to minimize spurious intermixing. The main features remained unchanged by symmetrization. The transport measurements were conducted from room temperature to 2 K in magnetic fields up to 15 T with standard DC measurements with a typical probing current of 10 μA. No hysteresis was detected in the magnetoresistance or the Hall resistance.

Scanning-SQUID measurements:
The scanning SQUID system is a custom-built piezoelectric-based scanning SQUID microscope with a 1.8 μm diameter pick-up loop (*3*, *4*). We used the scanning SQUID to image magnetic flux from the sample as a function of position. The measured magnetic flux is given by $\phi_s = \int g(x,y)\vec{B} \cdot d\vec{a}$ where the integral is taken over the plane of the SQUID, $g(x,y)$ is the point spread function of the pickup loop, $\vec{B}$ is the background-corrected magnetic field produced by the sample and $d\vec{a}$ is the infinitesimal area vector element pointing normal to the plane of the SQUID. The SQUID was used in three modes: Magnetometry, susceptometry and current detection mode (see Figure S1).
The magnetometry measurements are simply the z component of the magnetic flux, picked up by the SQUID's pick up loop in absence of an applied magnetic field. For the susceptometry measurements we applied a local magnetic field of up to 0.3 mT to the sample using a field coil with a diameter of 8 μm that surrounds the pick loop of the SQUID. If the sample magnetization changes upon applying the local magnetic field, the sample itself produces a magnetic field in the pick-up loop that was measured by a standard lock-in technique. An identical field coil surrounds a second pick-up loop used to correct for background magnetic fields in the magnetometry mode (gradiometric design). In current detection mode, an alternating current is applied to the sample and the pickup loop is used to detect the magnetic flux generated by these currents using a lock-in technique. A single current-carrying wire will appear in our images as a stripe with a negative magnetic signal next to a stripe of a positive signal.

In all measuring modes, the magnetic landscape was imaged by the SQUID loop rastering parallel to the surface at a height down to a micrometer. The contact with the surface was probed capacitively using a cantilever and a fixed electrode. Using the tip of the SQUID probe, we applied forces up to $F = 106$ μN, which corresponds to a pressure of the order of 10^7 Pa, taking into account the estimated contact radius. Following Ref. (*5*), the contact radius (a) was estimated using the Hertzian contact formula:

$$a^3 = \frac{3F}{8}\frac{\frac{(1-\nu_1)}{E_1} + \frac{(1-\nu_2)}{E_2}}{1/d_1}$$

where ν, E, and d are the Poisson ratio, Young's modulus and radius of curvature, respectively. Subscript 1 refers to the silicon tip and subscript 2 is used for the STO substrate.
The imaging is not affected by thin layers of non-conducting materials located between the SQUID and the source of the magnetic field, and the scanning SQUID is therefore an ideal, non-invasive tool to probe magnetism and current paths in buried interfaces.

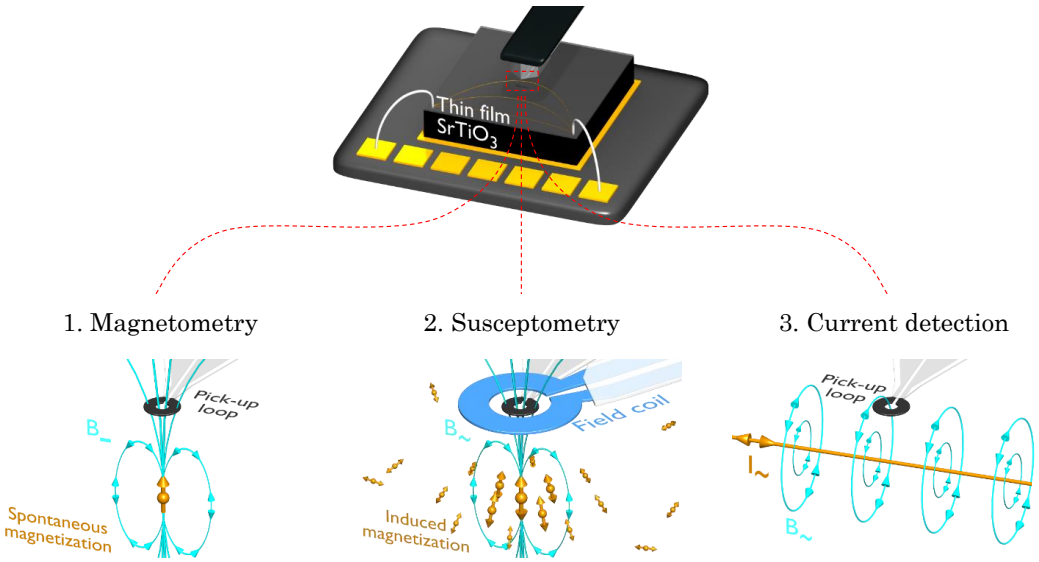

Figure S1: Top: Schematics of the SQUID scanning on the surface of a STO-based material platform. The measurements with the scanning SQUID were performed in three different modes: 1: Magnetometry mode, 2: susceptometry mode and 3: current detection mode.

Magnetic contamination:
Special care was taken to avoid introducing magnetic impurities to the samples throughout the sample preparation, handling and measurements. The samples were handled with non-magnetic plastic tweezers, and the STO was TiO_2-terminated using a tube furnace, glassware and chemicals dedicated to STO treatment. The GAO deposition was done in a pulsed laser deposition chamber dedicated to growing STO-based heterostructures with non-magnetic top layers. The transport and scanning SQUID measurements were conducted using new, thoroughly cleaned chip carriers.

Occasionally, we observe magnetic signals with a similar shape as the resolution limited dipoles observed by Bert et al. (1), but with the ability to be moved on the sample surface using the scanning probe. We attribute these signals to magnetic surface contaminants. In addition, we also sporadically observe signals with the shape of a magnetic dipole buried deep below the sample surface, which we interpret as magnetic impurities or a defect cluster in STO. Lastly, it is well-established that magnetic elements such as Fe, Co and Ni exist in STO (6). We note that special care should be taken to discriminate whether magnetic dipole signals are intrinsic to the sample or stem from magnetic impurities. This is in sharp contrast to the present study where we report 100 μm long magnetic stripes, which are sensitive to applied pressure and change orientation and magnitude upon thermal cycling.

Section 2:
Estimating the magnitude of the magnetization

The magnetization ($\vec{M} = M_x\hat{x} + M_y\hat{y} + M_z\hat{z}$) cannot be calculated uniquely from the measured magnetic flux. The number of Bohr magneton pr. surface unit cell (μ_B/a^2) that create the field can, however, be estimated by assuming that the magnetization is oriented in-plane or out-of-plane. Our estimation uses a simple model where the magnetization is uniform in a sheet with width 2 µm, and zero otherwise. We calculate the field (B_z) at a height of $z = 1$ µm above the sample surface (see Figure S2) using the equation:

$$\vec{B}(\vec{r}) = \frac{\mu_0}{4\pi}\int d\vec{r}'\left(\frac{3\vec{r}(\vec{M}(\vec{r}')\cdot\vec{r})}{|\vec{r}-\vec{r}'|^5} - \frac{\vec{M}(\vec{r}')}{|\vec{r}-\vec{r}'|^3}\right)$$

With this model, we estimate that for the strongest signal we measure (15 mΦ_0 ~ 12µT for GAO/STO as presented in Figure 3 in the main text), a change on the order of 0.7 μ_B/a^2 is needed to create such a field if the magnetization is out-of-plane (see Figure S2c). A similar value is obtained if the magnetization is in-plane (Figure S2b & d). The typical modulation amplitude for GAO/STO (1 mΦ_0, Figure 1 in the main text) corresponds to roughly 0.05 μ_B/a^2.

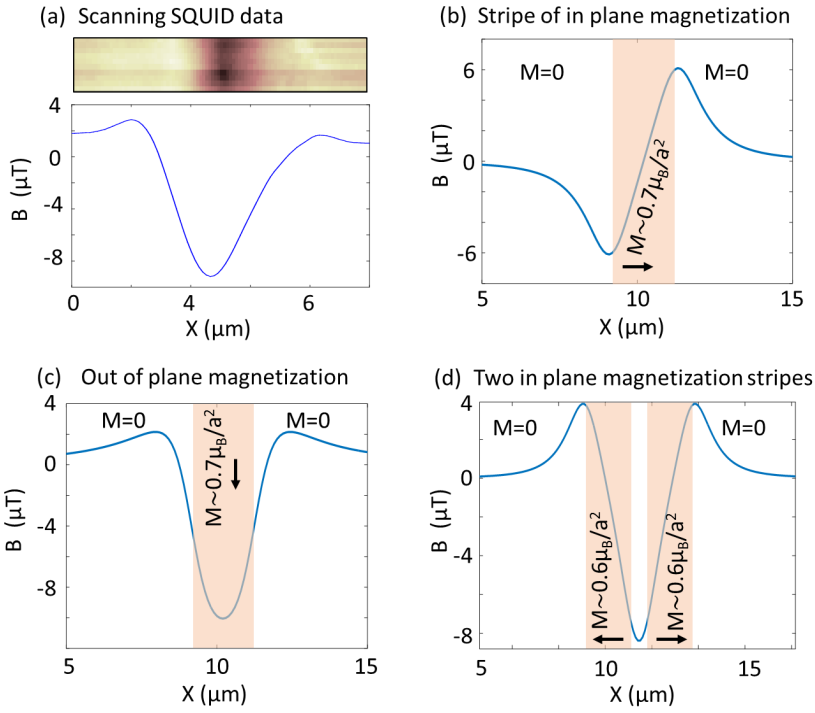

Figure S2: (a) top: SQUID image of the z-component of the magnetic field (B_z) above a magnetic stripe on GAO/STO. Bottom: a line cut along the data. (b), (c) and (d): calculated magnetic field (B_z) over a stripe of in plane (b) and out of plane (c) magnetization. (d): Two in plane magnetic stripes pointing in opposite direction giving rise to a similar B_z. Shaded area in (b), (c) and (d) indicate the location of the $|\vec{M}| \neq 0$ stripes. The magnitude of M in (d) is ~0.6µB/a² for each stripe.

Section 3:
Magnetic landscape of STO before and after thermal cycling

STO undergoes a structural phase transition at 105K. As the material is cooled through the transition the room temperature cubic unit cell becomes tetragonal. Each unit cell is elongated along one of the crystallographic directions [001] (*x*), [010] (y) and [100] (*z*), which creates structural domains in STO. At the (001) surface of STO, the domain walls form straight lines along the [100], [010], [110] and [1$\bar{1}$0] directions. The striped magnetic modulations observed in vacuum annealed STO (see Methods) are parallel to these directions (see Figure S3). Heating the material to room temperature and cooling back down to 2 K creates a different magnetic landscape as a different domain structure is formed. Note that the change in the magnetic landscape when performing a temperature cycle helps in ruling out the possibility of the magnetism stemming from contamination.

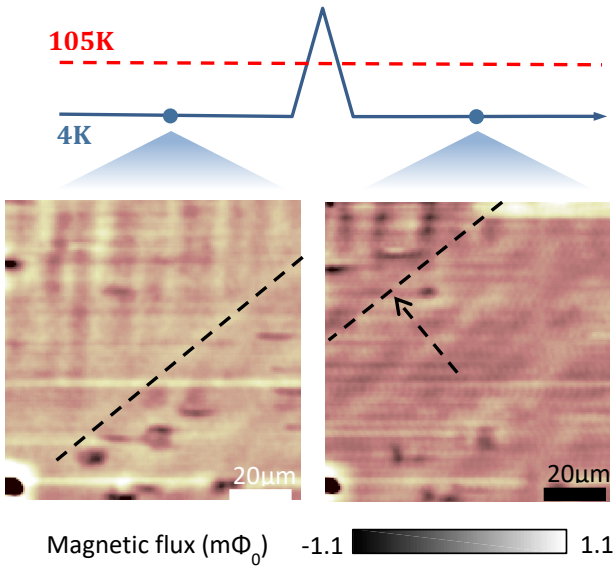

Figure S3: SQUID images of magnetic flux from vacuum-annealed STO before (left) and after (right) a thermal cycling where the sample is warmed up to room temperature. It is notable that the stripy features have changed after the thermal cycle, as indicated by the arrow.

Section 4:
Correlation between stripes in magnetism and current

The structural domain boundaries have been shown to result in a strongly modified current flow in LAO/STO (*6*) and GAO/STO (*7*). Using the current flow and magnetometry modes of the scanning SQUID (see Methods) on the same area of a GAO/STO sample, we observe a clear correlation between the striped current modulations and the magnetic stripes (see Figure S4).

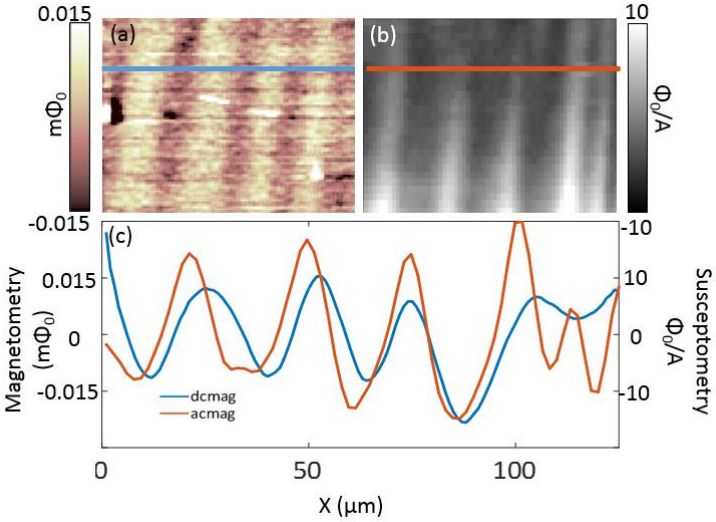

Figure S4: Two consecutive scans of magnetometry (a) and current flow (b) at the same area of GAO/STO showing a similar pattern of stripes. The magnetometry is probed in dc mode with the SQUID by detecting the magnetic field escaping the sample. The current flow is detected in ac mode by applying an alternating current to the GAO/STO sample and measuring the alternating magnetic field produced by the current. (c) Line cuts showing the correlation between the magnetic and current modulations.

Section 5:
Non-linear Hall coefficient & 2-band conductivity

If the non-linear Hall coefficient (ρ_{xy}) is attributed to conduction through two bands, it can be fitted with the following model (*8*):

$$\rho_{xy} = \frac{\sigma_1^2 R_1 + \sigma_2^2 R_2 + \sigma_1^2 \sigma_2^2 R_1 R_2 (R_1 + R_2) B^2}{(\sigma_1 + \sigma_2)^2 + \sigma_1^2 \sigma_2^2 (R_1 + R_2) B^2} B$$

with the constraint

$$\rho_{xx}(0T) = \frac{1}{\sigma_1 + \sigma_2}$$

and the carrier density ($n_{1,2}$) and carrier mobility ($\mu_{1,2}$) of the two bands defined through

$$\sigma_{1,2} = |n_{1,2} e \mu_{1,2}| \quad \text{and} \quad R_{1,2} = \left(n_{1,2} e\right)^{-1}$$

The applicability of a 2-band model to describe the non-linear Hall curves in LAO/STO is discussed extensively in the literature (*9*, *10*). For LAO/STO, the Hall coefficient is generally S-shaped, i.e. the Hall coefficient curves towards $R_{xy} = 0$, and several reports (*9*, *10*) find that the overall shape of the non-linear Hall coefficient is governed by the existence of 2 *n*-type bands (d_{xy} and d_{xz}/d_{yz}) with different electronic properties. A small non-linear component attributed to the anomalous Hall coefficient is, however, present as observed e.g. from the first derivative ($\mathrm{d}R_{xy}/\mathrm{d}B$ plotted as a function of B) (*10*) or when the external magnetic field is oriented such that only a small field component is normal to the interface (*11*). In the case of GAO/STO, the Hall plots are non-linear away from $R_{xy} = 0$ (see Figure S5a). Analysis with a 2-band model therefore entails the coexistence of a large density of holes and electrons, as it is also evident from the fitting parameters (see Figure S5b). Such coexistence without a fast recombination is possible if the two types of carriers are separated in real or reciprocal space. However, we reject this scenario on four grounds:

- The GAO/STO has been studied by x-ray absorption spectroscopy (XAS), resonance photoemission spectroscopy (ResPES) and hard x-ray photoemission spectroscopy (HAXPES) without any signature of a band structure that could accommodate holes.
- Large concentrations of co-existing holes and electrons will require a band structure where the Fermi level crosses both an *n*-type (conduction) and *p*-type (valence) band, which is challenging to obtain in $SrTiO_3$ owing to its large band gap of approximately 3.2 eV.
- As shown elsewhere (*12*), annealing decreases the Fermi level as a result of lowering the amount of oxygen vacancy donors. An increasing density of holes and decreasing density of electrons are therefore expected from a simple band picture. Experimentally, however, a decrease in both carrier populations is inferred from the 2-band fit as shown in Figure S6.
- Attributing the non-linear Hall effect to the anomalous Hall effect is consistent with scanning SQUID measurements and magnetoresistance measurements as explain in Suppl. Sections 6 and 7.

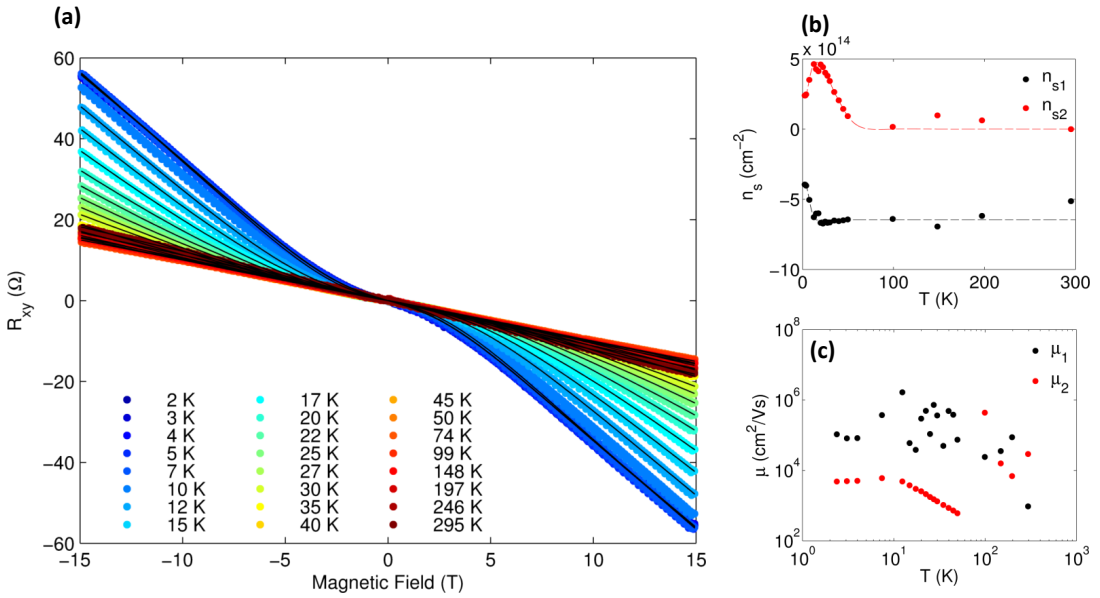

Figure S5: (a) Reasonable fits (black lines) can be obtained by fitting the non-linear Hall coefficient R_{xy} of GAO/STO with a 2-band model using (b) the carrier density ($n_{s1,2}$) and (c) mobility ($\mu_{1,2}$) of the two bands as fitting parameters. This require a large number of coexisting electrons ($n_{s1} < 0$) and holes ($n_{s2} > 0$).

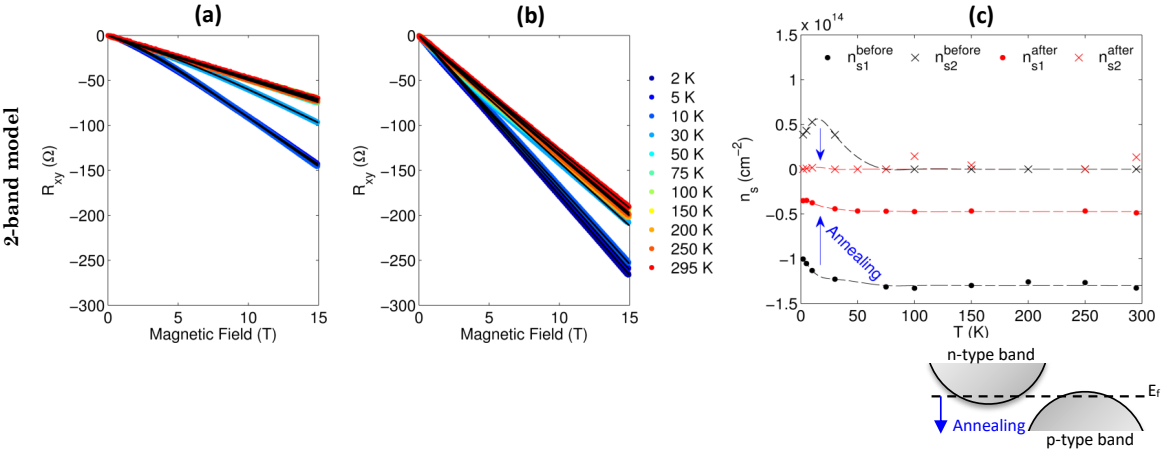

Figure S6: The Hall coefficient measured as a function of the external magnetic field (a) before and (b) after annealing GAO/STO in 1 bar oxygen. The Hall coefficients are fitted with a 2-band model. (c) The two carrier densities n_{s1} and n_{s2} obtained by the fits are shown as a function of temperature (right pane). The schematic drawing shows the effect of downshifting the Fermi energy level (E_f) by annealing in a bandstructure that can accommodate holes and electrons simulaneously.

Section 6:
Anomalous Hall Effect

As described in the main text, the non-linear Hall coefficient of GAO/STO is taken to be a sum of an ordinary Hall effect from a one-band model and the anomalous Hall effect:

$$R_{xy} = R_{xy}^{OHE} + R_{xy}^{AHE} = -\frac{1}{en_s}B + R_s^{AHE}M_z(B,T) \qquad (1)$$

We can now distinguish between two cases according to whether R_s^{AHE} saturates at high magnetic fields or not. For most materials, the anomalous Hall effect saturates at high magnetic fields (*13*). We first argue that whereas this assumption gives reasonable fits, it leads to predictions for the mobility and carrier density that are unlikely. Second, we show that R_s^{AHE} scales with the magnetoresistance, which for GAO/STO does not saturate at high magnetic fields and hence leads to a non-saturating Hall effect.

1: Saturating R_s^{AHE}:

If both R_s^{AHE} and M_z saturate at high magnetic fields of the order of 15 T, the anomalous Hall effect also saturates. In this case, the ordinary Hall contribution and hence the carrier density can be determined from the high-field slope of R_{xy}. Following the treatment by Gunkel et al (*10*), we can describe the magnetization in Eq. (1) with a Langevin-type expression,

$$M_z(B,T) = M_s \tanh(B/B_c')$$

using the saturation magnetization, M_s, and the characteristic magnetic field needed for alignment of magnetic moments, B_c'. Similar fits are obtained if the qualitatively similar Brillouin function is used as appropriate for describing paramagnets with a total angular moment, J, larger than ½:

$$M_z(B,T) = M_s \mathfrak{B}_J(B,T)$$

$$\mathfrak{B}_J(B,T) = \frac{2J+1}{2J}\coth\left(\frac{2J+1}{2J}\frac{g\mu_B JB}{k_B T}\right) - \frac{1}{2J}\coth\left(\frac{1}{2J}\frac{g\mu_B JB}{k_B T}\right)$$

For paramagnets the characteristic magnetic field for aligning the magnetic moments is expected to scale linearly with the temperature. Gunkel et al (*10*), however, found a temperature independent B_c' as expected from an ordered state. As the magnetization curves resembles those derived from the Stoner-Wohlfahrt model, it may be argued that the magnetic equation of states can be used phenomenologically to describe a ferromagnetic state where in-plane magnetic moments are being aligned out-of-plane by the transverse magnetic field *(10)*. In the case of GAO/STO, both magnetic equation of states provide good fit. In Figure S7a we present the fits by dotted lines using the Brillouin function ($J > ½$) and a field-independent R_s^{AHE}.

The outcome of describing R_s^{AHE} as field-independent is shown in Figure S7b and c. Note that only J is dependent on the magnetic equation chosen for the fit. B_c is defined as the half maximum at half width (HMHW) of dR_{xy}/dB as in the main text, which gives similar values

as the fitting parameter B_c' from the Langevin-type expression. The remaining parameters can be derived from the high-field region where $M_z = M_s$. The temperature dependences of primarily three parameters caution the use of a field-independent R_s^{AHE}:

1. The anomalous Hall saturation ($R_s^{AHE}M_s$) peaks at around 20 K, where for $T < 20$ K a linear correlation with the sheet resistance is observed. This suggests that the skew-scattering underlies anomalous Hall effect (*13*), but in this case R_s^{AHE} is expected to be field-dependent.
2. Extracting the ordinary Hall effect at high magnetic fields implies that the carrier density decreases with a factor of 3-4 when cooling the GAO/STO sample from 100 to 10 K. This is inconsistent with infrared measurements where a temperature-independent carrier density is extracted from the Berreman mode similar to Ref. (*14*).
3. The proposed decrease in the carrier density induces a corresponding increase in the electron mobility, $\mu = 1/eR_s|n_s|$. This would cause the mobility to reach an unprecedented value of ~350,000 cm²/Vs at 2 K. In addition, upon cooling the mobility increases much faster than the $\mu \sim T^{-2}$-behavior typically observed in STO and STO-based structures (*10*, *15–17*).

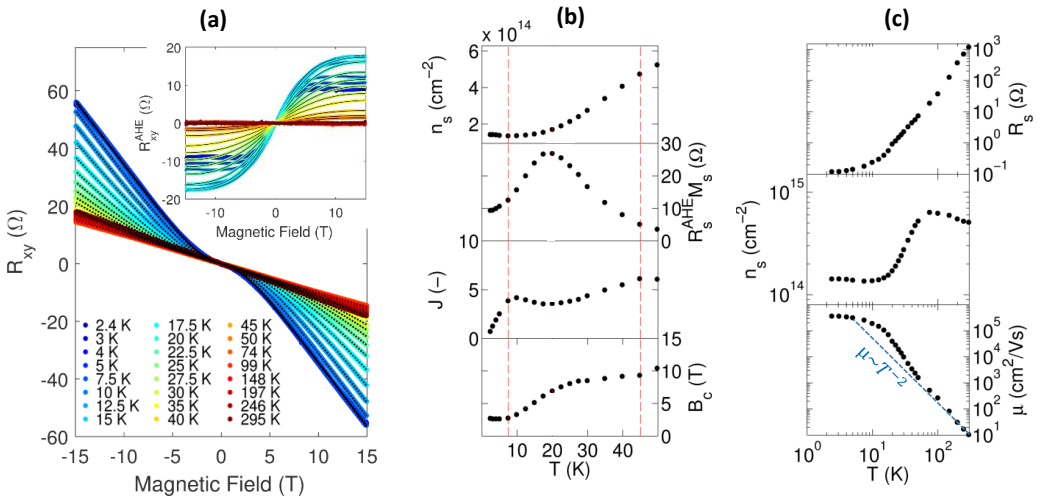

Figure S7: (a) Hall effect ($\boldsymbol{R_{xy}}$) as a function of the magnetic field including fits (black dots) to Eq. (1) using the Brillouin function and a field-independent $\boldsymbol{R_s^{AHE}}$. (b+c) Carrier density ($\boldsymbol{n_s}$), mobility (μ), sheet resistance ($\boldsymbol{R_s}$), anomalous Hall saturation ($\boldsymbol{R_s^{AHE}M_s}$), total angular momentum ($\boldsymbol{J}$) and characteristic magnetic field ($\boldsymbol{B_c}$) as a function of temperature as derived from the description with a field independent $\boldsymbol{R_s^{AHE}}$.

2: Non-saturating $\boldsymbol{R_s^{AHE}}$:

We now relax the assumption of a field-independent or saturating R_s^{AHE}. Investigating the case of sample 10a-GAO/STO, we find that the shape of both the Hall coefficient and the sheet resistance are very similar with the curvature changing sign at the same magnetic fields (see

Figure S8b). This is suggestive of a scenario in which the non-linear Hall coefficient arises from the anomalous Hall effect caused by skew scattering where $R_s^{AHE} \propto R_s$, see Ref. (*13*). Here, an asymmetric scattering of electrons occurs in the presence of spin-orbit coupling. According to this hypothesis, we can write:

$$R_{xy} = R_{xy}^{OHE} + R_{xy}^{AHE} = -\frac{1}{en_s}B + kR_s(B,T)M_z(B,T)$$

where k is a field and temperature independent constant and the ordinary Hall effect is described using a one-band model as explained in the main text. At B~0 T the sheet resistance is small and scales as B^2, and as a result the anomalous Hall effect becomes small. R_{xy} is therefore dominated by the ordinary Hall effect at low magnetic fields, which offers a natural explanation for the temperature independent Hall slope at low fields, $\left|dR_{xy}/dB\right|_{B\sim 0\mathrm{T}}$, as this originates from a temperature independent carrier density.

Armed with the ordinary Hall effect we can readily extract the anomalous Hall effect as well as the magnetization (apart from the constant factor k):

$$R_{xy}^{AHE} = R_{xy} - R_{xy}^{OHE} \qquad \& \qquad kM_z = \frac{R_{xy} - R_{xy}^{OHE}}{R_s}$$

We plot both properties for four different samples in Figure S8. Most noticeable is that by combining the $R_{xy}(B)$ and $R_s(B)$ we obtain a plausible shape of the magnetization for all samples. This would by no means be obvious without applying the anomalous Hall effect theory, and it is, together with the correlation to the scanning SQUID images, a strong evidence that the anomalous Hall effect is the origin of the non-linear Hall effect. Further support is found when considering T = 2 K and B > 7 T where the magnetization is expected to be saturated. In this case, the anomalous Hall effect ($R_{xy}^{AHE} = R_s^{AHE}M_z$) scales linearly with the sheet resistance (R_s) as shown in Figure S9.

We note that the analysis render the low-field part of the magnetization particular prone to noise, and care should be taken when extracting information from this region.

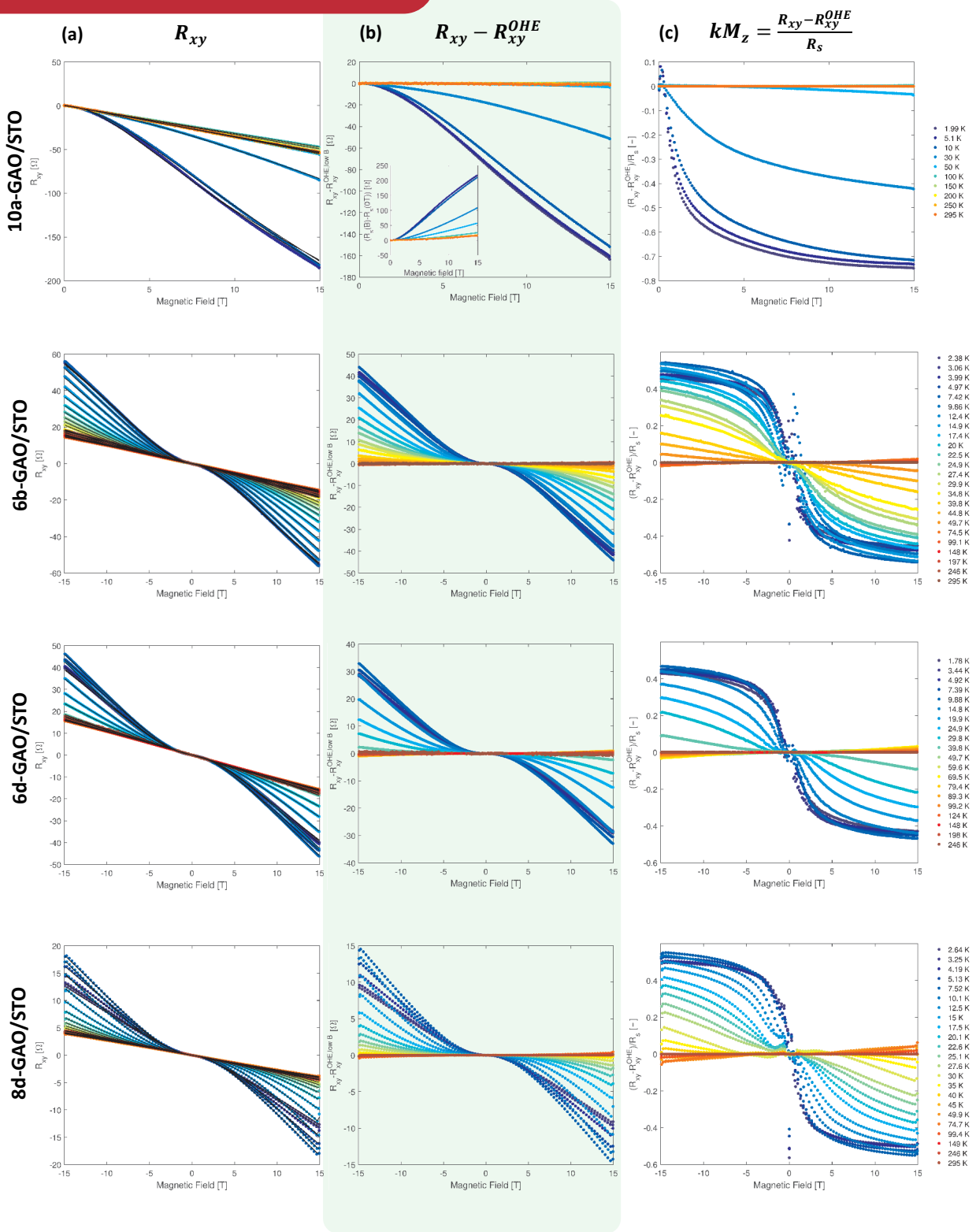

Figure S8: (a) Hall coefficient ($\boldsymbol{R_{xy}}$) as a function of magnetic field for four GAO/STO samples. (b) $\boldsymbol{R_{xy}^{AHE}} = \boldsymbol{R_{xy}} - \boldsymbol{R_{xy}^{OHE}}$ where the ordinary Hall effect $\boldsymbol{R_{xy}^{OHE}}$ is defined as the low field slope of $\boldsymbol{R_{xy}}$. For sample 10a, the sheet resistance ($\boldsymbol{R_s}$) is shown for comparison. (c) By calculating $(\boldsymbol{R_{xy}} - \boldsymbol{R_{xy}^{OHE}})/\boldsymbol{R_s}$ we obtain the component of the magnetization parallel to the magnetic field ($\boldsymbol{M_z}$) multiplied by a constant factor k.

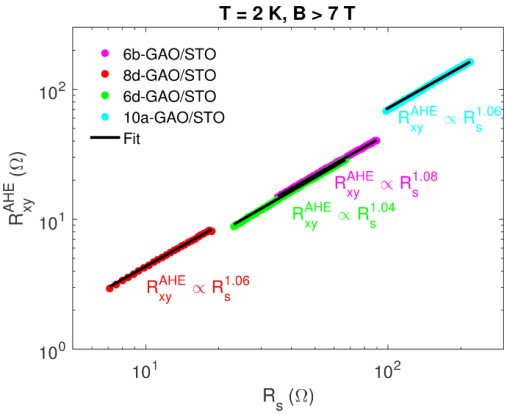

Figure S9: Anomalous Hall effect ($\boldsymbol{R_{xy}^{AHE}}$) as a function of the sheet resistance (R_s) for four GAO/STO samples measured at low temperature and high magnetic field where the magnetization is expected to be saturated. Here, increasing the magnetic field results in a linear increase in both the magnetoresistance and the anomalous Hall effect.

Anomalous Hall effect with carrier transport in two n-type bands:

As outlined in Suppl. Section 5, we reject that the non-linear Hall effect results from simultaneous carrier transport in both an *n*-type and *p*-type band. In this section, we have instead concluded that the overall non-linearity in the Hall effect stems from the anomalous Hall effect. For simplicity, we described the ordinary Hall effect using a one band model. We here show that the conclusion remains unchanged if we consider carrier transport in two or more *n*-type bands. For the $SrTiO_3$-based heterostructures the two bands correspond to d_{xy} and d_{xz}/d_{yz} (9, 18).

1. Saturating R_s^{AHE}:

A two band conduction will contribute with an S-shaped Hall curve characterized by $\left|\lim_{B\to 0}\left(\frac{dR_{xy}}{dB}\right)\right| \geq \left|\lim_{B\to \infty}\left(\frac{dR_{xy}}{dB}\right)\right|$. The limit of $B \to \infty$ can be used to extract the total carrier density of the two bands using $\lim_{B\to \infty}\left(\frac{dR_{xy}}{dB}\right) = -\frac{1}{en_{s,\mathrm{total}}}$. When discussing parameters derived from the high-field region, n_s can simply be replaced with $n_{s,\mathrm{total}}$. Assuming a saturating R_s^{AHE} as above therefore implies the same predictions, namely a freeze-out in the total carrier density, a mobility increase as well as the same shape of $R_s^{AHE}M_s$.

2. Non-saturating R_s^{AHE}:

The anomalous Hall effect curve we derive is, to some extent, sensitive to whether we describe the ordinary Hall effect as an S-shaped curve (two band conduction) or a linear curve (single band conduction). However, since the S-shape has the opposite curvature with respect to the measured Hall data, the overall shape of the anomalous Hall curve will remain unchanged. Importantly, the conclusion that the overall non-linearity stems from the anomalous Hall effect with an onset temperature of 40 K remains also invariant to whether the ordinary Hall effect is described by transport in one or multiple *n*-type bands.

Section 7:
Kohler Plots

Signatures of magnetic ordering may be observed in the magnetoresistance. Many materials obey Kohler's rule (20), which predicts that the resistance ratio $R_s(B,T)/R_s(0,T)$ is some function f of $B/R_s(0,T)$.

$$\frac{R_s(B,T)}{R_s(B=0,T)} = F(\omega_c\tau) = f\left(\frac{B}{R_s\ (B=0,T)}\right)$$

Kohler's rule originates from the magnetic field entering the semi-classical Boltzmann equation as the product of the cyclotron frequency and scattering life time, $\omega_c\tau = eB\tau/m^*$ with m^* being the effective mass and τ generally being inversely proportional to R_s. As presented in Figure S10, Kohler's rule is obeyed in GAO/STO for $T > 40$ K, however, clear deviations are observed for $T < 40$ K, which coincides with the emergence of the non-linear Hall coefficients. No hysteresis was detected in the magnetoresistance at any temperature. Deviations from Kohler's rule can have various origins (*19*). In the presence of magnetism, the electrons are scattered by spatially fluctuating magnetic moments leading to a negative magnetoresistance as increasing the magnetic field leads to alignment of the spins and lower degree of scattering. This scattering leads to a deviation of Kohler's rule as τ becomes dependent on B. In particular, we expect a lowering of the magnetoresistance at temperatures where spin scattering occurs compared to temperatures where the Kohler scaling is obeyed in the absence of high temperatures. This is also observed in Figure S10. Note that $\left(\frac{R_S(B)}{R_S(B=0)}\right)^{-1}$ is shown for convenience to put emphasis on the low-field part.

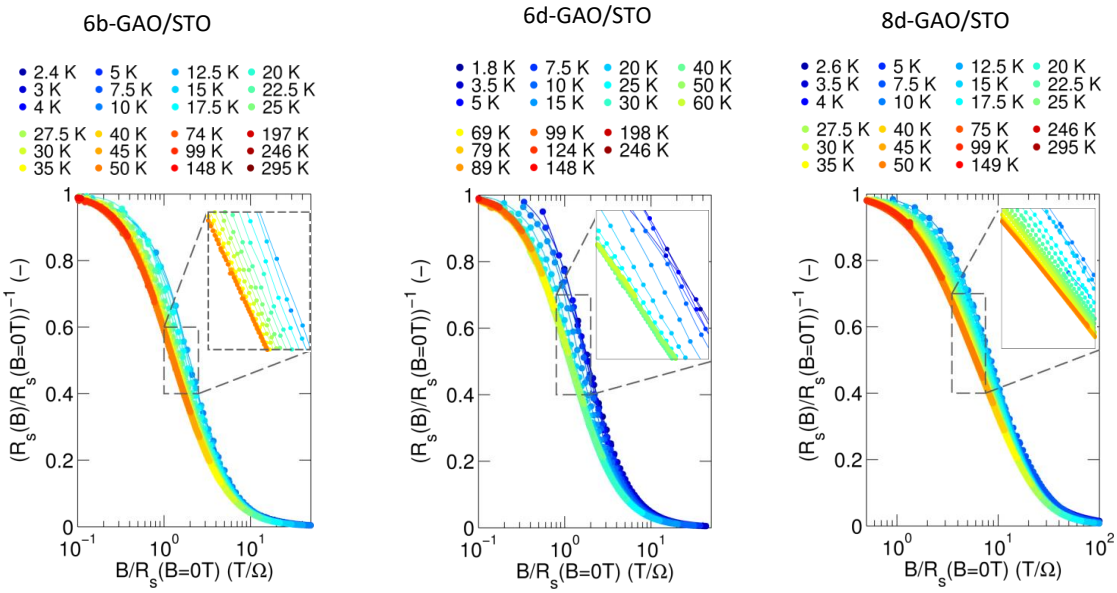

Figure S10: Kohler plots of three different samples showing deviations from the Kohler scaling below $T < 40$ K.

Section 8:
Mechanical tunability of the magnetic landscape of LAO/STO

Similar to the data presented in figure 3 in the main text, the magnetic stripes we observed in LAO/STO are also highly stress dependent (see Figure S11). At $T = 15$ K we observe no or weak modulations when we raster scan the SQUID across the sample in non-contact mode. After contacting the sample with the tip of the scanning probe, we observe stronger stripy modulations of the magnetic signal. These modulations grow stronger as we increase the applied force.

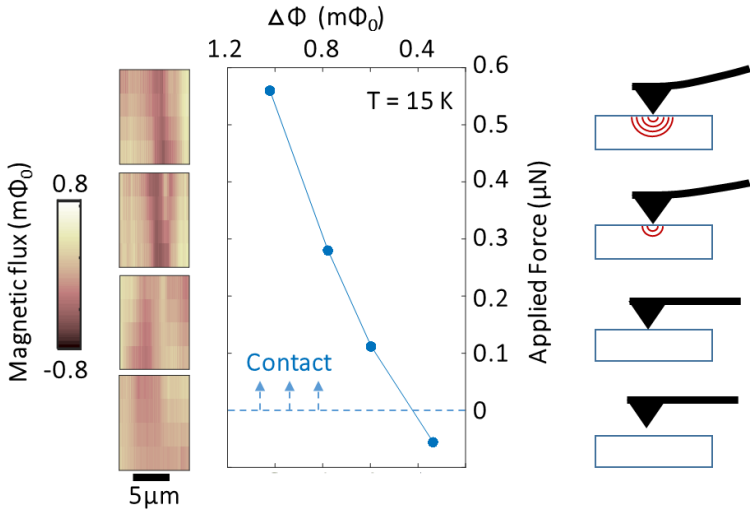

Figure S11: Magnetic modulation vs. force applied with the scanning SQUID tip at $T = 15$ K. No or weak modulations are observed before contacting the sample. As we increase the force applied to the sample by the tip, the magnetic modulations become stronger. The left column shows 2D maps of the measured magnetic flux where the probe applies different forces to the sample surface. For convenience, the peak-to-peak modulation amplitude (ΔΦ) is also shown in the middle panel. The magnetic flux is offset by the average value of the scan for all figures.

Section 9:
Local susceptibility measurements vs. temperature and pressure

We apply magnetic fields locally using the scanning SQUID field coil and measure how it modulates the magnetic signal from the sample, as in Figure 3 of the main text. The magnetic susceptibility shows similar behavior with stress and temperature as the magnetometry data. Below ~8 K only minor modulations are observed, whereas above 8 K the susceptibility signal increases rapidly. We observe that there are small areas where the susceptibility signal grows slower as the temperature and stress are increased. We suggest that the magnetic moments in most areas gradually convert into paramagnetic moment and therefore show an increase in the susceptibility. At the domain walls (the small areas), the magnetic moments remain largely ordered and therefore show a reduced growth in the magnetic susceptibility as well as a large D.C. magnetic signal in absence of an external magnetic field.

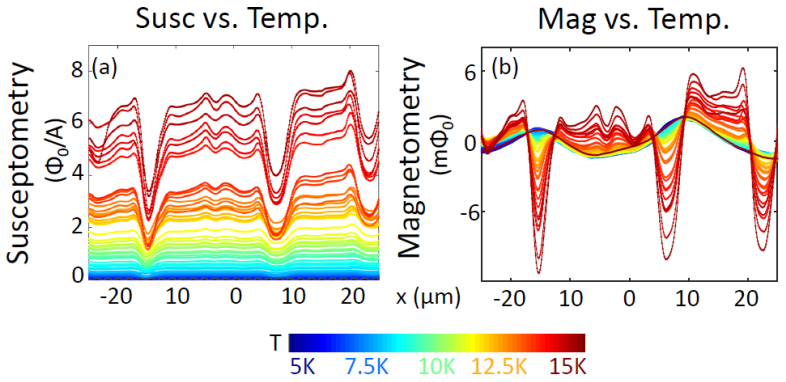

Figure S12: Magnetic and susceptibility measurements as a function of temperature. The measurements were performed on GAO/STO with an applied force of 56nN in the same locations as in Figure 3 in the main text. (a) Susceptibility measurements primarily showing an increasing paramagnetic signal as the temperature is increased. Smaller segments that we attribute to the domain walls show a slower increase of the paramagnetic signal with temperature. (b) Magnetometry measurements showing an increase in the modulation magnitude with temperature in absence of an applied magnetic field. We detect stronger magnetic signal on the small segments attributed to domain walls. (a) and (b) were measured simultaneously.

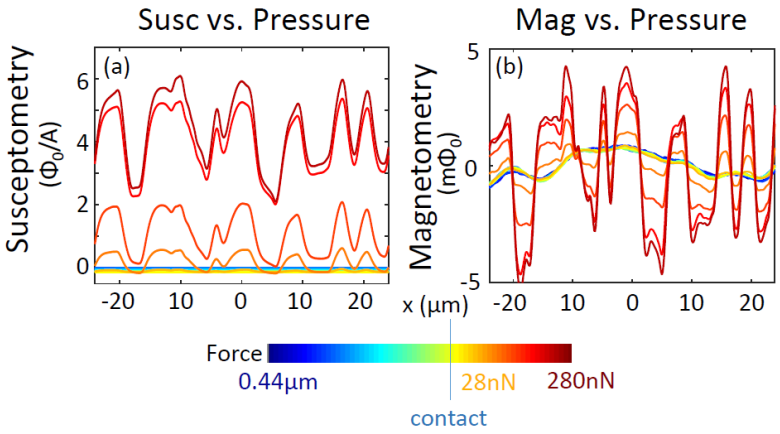

Figure S13: Magnetic and susceptibility measurements as a function of applied pressure. The measurements were performed at 17 K on GAO/STO at a different location compared to Figure S12. (a) Susceptibility measurements showing small segments attributed to the domain walls showing a slower increase of the paramagnetic signal as the applied pressure is increased. (b) Magnetometry measurements showing that the magnetic modulations become stronger as the pressure is increased. We detect stronger magnetic signal on the small segments attributed to domain walls. (a) and (b) were measured simultaneously.

Section 10:
References

1. J. A. Bert *et al.*, Direct imaging of the coexistence of ferromagnetism and superconductivity at the $LaAlO_3/SrTiO_3$ interface. *Nat. Phys.* **7**, 767–771 (2011).
2. D. V. Christensen *et al.*, Electric field control of the γ-$Al_2O_3/SrTiO_3$ interface conductivity at room temperature. *Appl. Phys. Lett.* **109**, 021602 (2016).
3. M. E. Huber *et al.*, Gradiometric micro-SQUID susceptometer for scanning measurements of mesoscopic samples. *Rev. Sci. Instrum.* **79**, 053704 (2008).
4. J. R. Kirtley *et al.*, Scanning SQUID susceptometry of a paramagnetic superconductor. *Phys. Rev. B.* **85**, 224518 (2012).
5. Y. Frenkel *et al.*, Imaging and tuning polarity at $SrTiO_3$ domain walls. *Nat. Mater.* (2017), doi:doi:10.1038/nmat4966.
6. B. Kalisky *et al.*, Locally enhanced conductivity due to the tetragonal domain structure in $LaAlO_3/SrTiO_3$ heterointerfaces. *Nat. Mater.*, 1–5 (2013).
7. D. V. Christensen *et al.*, Electron mobility in γ-$Al_2O_3/SrTiO_3$. *Submitt. Phys Rev Appl* (2017).
8. Y. Z. Chen *et al.*, A high-mobility two-dimensional electron gas at the spinel/perovskite interface of γ-$Al_2O_3/SrTiO_3$. *Nat. Commun.* **4**, 1371 (2013).
9. A. Joshua, S. Pecker, J. Ruhman, E. Altman, S. Ilani, A universal critical density underlying the physics of electrons at the $LaAlO_3/SrTiO_3$ interface. *Nat. Commun.* **3**, 1129 (2012).
10. F. Gunkel *et al.*, Defect Control of Conventional and Anomalous Electron Transport at Complex Oxide Interfaces. *Phys. Rev. X.* **6**, 031035 (2016).
11. A. Joshua, J. Ruhman, S. Pecker, E. Altman, S. Ilani, Gate-tunable polarized phase of two-dimensional electrons at the $LaAlO_3/SrTiO_3$ interface. *Proc. Natl. Acad. Sci.* **110**, 9633–9638 (2013).
12. D. V. Christensen *et al.*, Controlling the carrier density of $SrTiO_3$-based heterostructures with annealing. *Adv. Electron. Mater.*, 1700026 (2017).
13. N. Nagaosa, J. Sinova, S. Onoda, A. H. MacDonald, N. P. Ong, Anomalous Hall effect. *Rev. Mod. Phys.* **82**, 1539–1592 (2010).
14. M. Yazdi-Rizi *et al.*, Infrared ellipsometry study of the confined electrons in a high-mobility γ-$Al_2O_3/SrTiO_3$ heterostructure. *EPL Europhys. Lett.* **113**, 47005 (2016).
15. E. Mikheev *et al.*, Limitations to the room temperature mobility of two- and three-dimensional electron liquids in $SrTiO_3$. *Appl. Phys. Lett.* **106**, 062102 (2015).
16. P. Irvin *et al.*, Anomalous High Mobility in $LaAlO_3/SrTiO_3$ Nanowires. *Nano Lett.* **13**, 364–368 (2013).
17. A. Ohtomo, H. Y. Hwang, A high-mobility electron gas at the $LaAlO_3/SrTiO_3$ heterointerface. *Nature.* **427**, 423–426 (2004).
18. R. H. McKenzie, J. S. Qualls, S. Y. Han, J. S. Brooks, Violation of Kohler's rule by the magnetoresistance of a quasi-two-dimensional organic metal. *Phys. Rev. B.* **57**, 11854 (1998).

Bibliography

[1] Mistry, K. 10 nm technology leadership. accessed 15/7-2017: https://newsroom.intel.com/newsroom/wp-content/uploads/sites/11/2017/03/Kaizad-Mistry-2017-Manufacturing.pdf (2017).

[2] Intel and Micron unveiled 3D Xpoint Technology, a Faster Non-volatile Memory. Accessed 15/7-2017: https://www.youtube.com/watch?v=xlPANUeHo1i (2015).

[3] Intel and Micron Produce Breakthrough Memory Technology | Intel Newsroom. Accessed 15/7-2017: https://newsroom.intel.com/news-releases/intel-and-micron-produce-breakthrough-memory-technology/ (2015).

[4] Shanefield, D. J. Operating circuit for phase change memory devices. Patent number 3,448,302. (1969).

[5] DiStefano, T. H. & Eastman, D. E. The band edge of amorphous SiO_2 by photoinjection and photoconductivity measurements. *Solid State Communications* **9**, 2259–2261 (1971).

[6] Weaver, H. E. Dielectric Properties of Single Crystals of $SrTiO_3$ at Low Temperatures. *Journal of Physics and Chemistry of Solids* **11**, 274–277 (1959).

[7] Falson, J. *et al.* MgZnO/ZnO heterostructures with electron mobility exceeding 1×10^6 cm^2/Vs. *Scientific Reports* **6**, 26598 (2016).

[8] Schilling, A., Cantoni, M., Guo, J. D. & Ott, H. R. Superconductivity above 130 K in the Hg-Ba-Ca-Cu-O system. *Nature* **363**, 56–58 (1993).

[9] Park, S.-E. & Shrout, T. R. Ultrahigh strain and piezoelectric behavior in relaxor based ferroelectric single crystals. *Journal of Applied Physics* **82**, 1804 (1997).

[10] Wang, Z. *et al.* Tailoring the nature and strength of electron–phonon interactions in the $SrTiO_3$(001) 2D electron liquid. *Nature Materials* **15**, 835–839 (2016).

[11] Petrich, G., Von Molnár, S. & Penney, T. Exchange-induced autoionization in Eu-rich EuO. *Physical Review Letters* **26**, 885–888 (1971).

[12] Soulen Jr, R. J. *et al.* Measuring the spin polarization of a metal with a superconducting point contact. *Science* **282**, 85–88 (1998).

[13] Maignan, A., Simon, C., Caignaert, V. & Raveau, B. Giant magnetoresistance ratios superior to 10^{11} in manganese perovskites. *Solid state communications* **96**, 623–625 (1995).

[14] Spaldin, N. A., Cheong, S.-W. & Ramesh, R. Multiferroics: Past, present, and future. *Physics Today* **63**, 38–43 (2010).

[15] Lorenz, M. *et al.* The 2016 oxide electronic materials and oxide interfaces roadmap. *Journal of Physics D: Applied Physics* **49**, 433001 (2016).

[16] Cohen, M. L. Superconductivity in Low-Carrier-Density Systems: Degenerate Semiconductors. *Superconductivity: Part I* 615 (1969).

[17] Coey, J. M. D., Venkatesan, M. & Stamenov, P. Surface magnetism of strontium titanate. *Journal of Physics: Condensed Matter* **28**, 485001 (2016).

[18] Ariando *et al.* Electronic phase separation at the $LaAlO_3/SrTiO_3$ interface. *Nature Communications* **2**, 188 (2011).

[19] Yamanaka, T., Hirai, N. & Komatsu, Y. Structure change of $Ca_{1-x}Sr_xTiO_3$ perovskite with composition and pressure. *American Mineralogist* **87**, 1183–1189 (2002).

[20] Neville, R. C., Hoeneisen, B. & Mead, C. A. Permittivity of Strontium Titanate. *Journal of Applied Physics* **43**, 2124–2131 (1972).

[21] Müller, K. A. & Burkard, H. $SrTiO_3$: An intrinsic quantum paraelectric below 4 K. *Physical Review B* **19**, 3593 (1979).

[22] Haeni, J. H. *et al.* Room-temperature ferroelectricity in strained $SrTiO_3$. *Nature* **430**, 758 (2004).

[23] Scott, J. F., Salje, E. K. H. & Carpenter, M. A. Domain Wall Damping and Elastic Softening in $SrTiO_3$: Evidence for Polar Twin Walls. *Physical Review Letters* **109** (2012).

[24] Frederikse, H. P. R. & Hosler, W. R. Hall Mobility in $SrTiO_3$. *Physical Review* **161**, 822 (1967).

[25] Jalan, B., Allen, S. J., Beltz, G. E., Moetakef, P. & Stemmer, S. Enhancing the electron mobility of $SrTiO_3$ with strain. *Applied Physics Letters* **98**, 132102 (2011).

[26] Schooley, J. F., Hosler, W. R. & Cohen, M. L. Superconductivity in Semiconducting $SrTiO_3$. *Phys. Rev. Lett.* **12**, 474–475 (1964).

[27] Schooley, J. F. *et al.* Dependence of the Superconducting Transition Temperature on Carrier Concentration in Semiconducting $SrTiO_3$. *Phys. Rev. Lett.* **14**, 305–307 (1965).

[28] Koster, G., Kropman, B. L., Rijnders, G. J., Blank, D. H. & Rogalla, H. Quasi-ideal strontium titanate crystal surfaces through formation of strontium hydroxide. *Applied Physics Letters* **73**, 2920–2922 (1998).

[29] Komiyama, M. & Gu, M. Atomic force microscopy images of MgO (100) and TiO_2 (110) under water and aqueous aromatic molecule solutions. *Applied surface science* **120**, 125–128 (1997).

[30] Connell, J. G., Isaac, B. J., Ekanayake, G. B., Strachan, D. R. & Seo, S. S. A. Preparation of atomically flat $SrTiO_3$ surfaces using a deionized-water leaching and thermal annealing procedure. *Applied Physics Letters* **101**, 251607–251607 (2012).

[31] Segal, Y., Ngai, J. H., Reiner, J. W., Walker, F. J. & Ahn, C. H. X-ray photoemission studies of the metal-insulator transition in $LaAlO_3/SrTiO_3$ structures grown by molecular beam epitaxy. *Physical Review B* **80**, 241107 (2009).

[32] Lee, S. W., Liu, Y., Heo, J. & Gordon, R. G. Creation and Control of Two-Dimensional Electron Gas Using Al-Based Amorphous Oxides/$SrTiO_3$ Heterostructures Grown by Atomic Layer Deposition. *Nano Letters* **12**, 4775–4783 (2012).

[33] Sbrockey, N. M. *et al.* $LaAlO_3/SrTiO_3$ Epitaxial Heterostructures by Atomic Layer Deposition. *Journal of Electronic Materials* **41**, 819–823 (2012).

[34] Delahaye, J. & Grenet, T. Metallicity of the $SrTiO_3$ surface induced by room temperature evaporation of alumina. *Journal of Physics D: Applied Physics* **45**, 315301 (2012).

[35] Ohtomo, A. & Hwang, H. Y. A high-mobility electron gas at the $LaAlO_3/SrTiO_3$ heterointerface. *Nature* **427**, 423–426 (2004).

[36] Brinkman, A. *et al.* Magnetic effects at the interface between non-magnetic oxides. *Nature Materials* **6**, 493–496 (2007).

[37] Chen, Y. *et al.* Metallic and Insulating Interfaces of Amorphous $SrTiO_3$-Based Oxide Heterostructures. *Nano Letters* **11**, 3774–3778 (2011).

[38] Zhao, J., Ross, N. L. & Angel, R. J. Polyhedral control of the rhombohedral to cubic phase transition in $LaAlO_3$ perovskite. *Journal of Physics: Condensed Matter* **16**, 8763–8773 (2004).

[39] Reyren, N. *et al.* Superconducting Interfaces Between Insulating Oxides. *Science* **317**, 1196–1199 (2007).

[40] Sulpizio, J. A., Ilani, S., Irvin, P. & Levy, J. Nanoscale Phenomena in Oxide Heterostructures. *Annual Review of Materials Research* **44**, 117–149 (2014).

[41] Stemmer, S. & James Allen, S. Two-Dimensional Electron Gases at Complex Oxide Interfaces. *Annual Review of Materials Research* **44**, 151–171 (2014).

[42] Thiel, S., Hammerl, G., Schmehl, A., Schneider, C. W. & Mannhart, J. Tunable quasi-two-dimensional electron gases in oxide heterostructures. *Science* **313**, 1942–1945 (2006).

[43] Cen, C. *et al.* Nanoscale control of an interfacial metal–insulator transition at room temperature. *Nature Materials* **7**, 298–302 (2008).

[44] Caviglia, A. D. *et al.* Two-Dimensional Quantum Oscillations of the Conductance at $LaAlO_3/SrTiO_3$ Interfaces. *Physical Review Letters* **105**, 236802 (2010).

[45] Herranz, G. *et al.* High Mobility in $LaAlO_3/SrTiO_3$ Heterostructures: Origin, Dimensionality, and Perspectives. *Physical Review Letters* **98**, 216803 (2007).

[46] Irvin, P. *et al.* Anomalous High Mobility in $LaAlO_3/SrTiO_3$ Nanowires. *Nano Letters* **13**, 364–368 (2013).

[47] Cen, C., Thiel, S., Mannhart, J. & Levy, J. Oxide Nanoelectronics on Demand. *Science* **323**, 1026–1030 (2009).

[48] Bert, J. A. *et al.* Direct imaging of the coexistence of ferromagnetism and superconductivity at the $LaAlO_3/SrTiO_3$ interface. *Nature Physics* **7**, 767–771 (2011).

[49] Bi, F. *et al.* Room-temperature electronically-controlled ferromagnetism at the $LaAlO_3/SrTiO_3$ interface. *Nature Communications* **5**, 5019 (2014).

[50] Caviglia, A. D. *et al.* Electric field control of the $LaAlO_3/SrTiO_3$ interface ground state. *Nature* **456**, 624–627 (2008).

[51] Cheng, G. *et al.* Electron pairing without superconductivity. *Nature* **521**, 196–199 (2015).

[52] Cancellieri, C. *et al.* Polaronic metal state at the $LaAlO_3/SrTiO_3$ interface. *Nature Communications* **7**, 10386 (2016).

[53] Caviglia, A. D. *et al.* Tunable Rashba Spin-Orbit Interaction at Oxide Interfaces. *Physical Review Letters* **104**, 126803 (2010).

[54] Ben Shalom, M., Sachs, M., Rakhmilevitch, D., Palevski, A. & Dagan, Y. Tuning Spin-Orbit Coupling and Superconductivity at the $SrTiO_3/LaAlO_3$ Interface: A Magnetotransport Study. *Physical Review Letters* **104**, 126802 (2010).

[55] Tebano, A., Fabbri, E., Pergolesi, D., Balestrino, G. & Traversa, E. Room-Temperature Giant Persistent Photoconductivity in $SrTiO_3/LaAlO_3$ Heterostructures. *ACS Nano* **6**, 1278–1283 (2012).

[56] Ma, Y. *et al.* Broadband Terahertz Generation and Detection at 10 nm Scale. *Nano Letters* **13**, 2884–2888 (2013).

[57] Honig, M. *et al.* Local electrostatic imaging of striped domain order in $LaAlO_3/SrTiO_3$. *Nature Materials* **12**, 1112–1118 (2013).

[58] Pallecchi, I. *et al.* Giant oscillating thermopower at oxide interfaces. *Nature Communications* **6**, 6678 (2015).

[59] Kalabukhov, A. *et al.* Effect of oxygen vacancies in the $SrTiO_3$ substrate on the electrical properties of the $LaAlO_3/SrTiO_3$ interface. *Physical Review B* **75**, 121404 (2007).

[60] Nakagawa, N., Hwang, H. Y. & Muller, D. A. Why some interfaces cannot be sharp. *Nature Materials* **5**, 204–209 (2006).

[61] Yu, L. & Zunger, A. A polarity-induced defect mechanism for conductivity and magnetism at polar–nonpolar oxide interfaces. *Nature Communications* **5**, 5118 (2014).

[62] Santander-Syro, A. F. *et al.* Two-dimensional electron gas with universal subbands at the surface of $SrTiO_3$. *Nature* **469**, 189–193 (2011).

[63] Chae, S., Choi, W., Yoo, H. & Kang, B. Metal-Insulator-like transition in the $LaAlO_3/BaTiO_3$ interface. *Current Applied Physics* **11**, 521–524 (2011).

[64] Minohara, M. *et al.* Atomically Engineered Metal–Insulator Transition at the $TiO_2/LaAlO_3$ Heterointerface. *Nano Letters* **14**, 6743–6746 (2014).

[65] Chen, Y. Z. *et al.* A high-mobility two-dimensional electron gas at the spinel/perovskite interface of γ-$Al_2O_3/SrTiO_3$. *Nature Communications* **4**, 1371 (2013).

[66] Shibuya, K., Ohnishi, T., Lippmaa, M. & Oshima, M. Metallic conductivity at the $CaHfO_3/SrTiO_3$ interface. *Applied Physics Letters* **91**, 232106 (2007).

[67] Zhou, R.-S. & Snyder, R. L. Structures and transformation mechanisms of the η, γ and θ transition aluminas. *Acta Crystallographica Section B: Structural Science* **47**, 617–630 (1991).

[68] Chen, Y. Z. *et al.* Room Temperature Formation of High-Mobility Two-Dimensional Electron Gases at Crystalline Complex Oxide Interfaces. *Advanced Materials* **26**, 1 (2013).

[69] Schütz, P., Pfaff, F., Scheiderer, P., Sing, M. & Claessen, R. Monitoring non-pseudomorphic epitaxial growth of spinel/perovskite oxide heterostructures by reflection high-energy electron diffraction. *Applied Physics Letters* **106**, 063108 (2015).

[70] Kormondy, K. J. *et al.* Quasi-two-dimensional electron gas at the epitaxial alumina/$SrTiO_3$ interface: Control of oxygen vacancies. *Journal of Applied Physics* **117**, 095303 (2015).

[71] Ngo, T. Q. *et al.* Quasi-two-dimensional electron gas at the interface of γ-Al_2O_3/$SrTiO_3$ heterostructures grown by atomic layer deposition. *Journal of Applied Physics* **118**, 115303 (2015).

[72] Lee, S. W. Two-Dimensional Electron Gas at $SrTiO_3$ -Based Oxide Heterostructures via Atomic Layer Deposition. *Journal of Nanomaterials* **2016**, 1–9 (2016).

[73] Chen, Y. *et al.* On the origin of metallic conductivity at the interface of $LaAlO_3$/$SrTiO_3$. *Applied Surface Science* **258**, 9242–9245 (2012).

[74] Fuchs, D. *et al.* Two-dimensional superconductivity between $SrTiO_3$ and amorphous Al_2O_3. *Applied Physics Letters* **105**, 092602 (2014).

[75] Sambri, A. *et al.* Plasma plume effects on the conductivity of amorphous-$LaAlO_3$/$SrTiO_3$ interfaces grown by pulsed laser deposition in O_2 and Ar. *Applied Physics Letters* **100**, 231605 (2012).

[76] Lu, S. *et al.* Spectrum and phase mapping across the epitaxial γ-Al_2O_3/$SrTiO_3$ interface. *Applied Physics Letters* **108**, 051606 (2016).

[77] Sing, M. *et al.* Profiling the Interface Electron Gas of $LaAlO_3$/$SrTiO_3$ Heterostructures with Hard X-Ray Photoelectron Spectroscopy. *Physical Review Letters* **102**, 176805 (2009).

[78] Basletic, M. *et al.* Mapping the spatial distribution of charge carriers in $LaAlO_3$/$SrTiO_3$ heterostructures. *Nature Materials* **7**, 621–625 (2008).

[79] Salluzzo, M. *et al.* Orbital Reconstruction and the Two-Dimensional Electron Gas at the $LaAlO_3$/$SrTiO_3$ Interface. *Physical Review Letters* **102**, 166804 (2009).

[80] Schütz, P. *et al.* Band bending and alignment at the spinel/perovskite γ−Al_2O_3/$SrTiO_3$ heterointerface. *Physical Review B* **91**, 165118 (2015).

[81] Fu, Q. & Wagner, T. Metal/Oxide Interfacial Reactions: Oxidation of Metals on $SrTiO_3$ (100) and TiO_2 (110). *The Journal of Physical Chemistry B* **109**, 11697–11705 (2005).

[82] Fu, Q. & Wagner, T. Interaction of nanostructured metal overlayers with oxide surfaces. *Surface Science Reports* **62**, 431–498 (2007).

[83] Chambers, S. A. *et al.* Band Alignment, Built-In Potential, and the Absence of Conductivity at the $LaCrO_3/SrTiO_3$ (001) Heterojunction. *Physical Review Letters* **107**, 206802 (2011).

[84] Hu, C. *et al.* Voltage-controlled ferromagnetism and magnetoresistance in $LaCoO_3/SrTiO_3$ heterostructures. *Journal of Applied Physics* **114**, 183909 (2013).

[85] Comes, R. & Chambers, S. Interface Structure, Band Alignment, and Built-In Potentials at $LaFeO_3$/n−$SrTiO_3$ Heterojunctions. *Physical Review Letters* **117**, 226802 (2016).

[86] Xu, P. *et al.* Reversible Formation of 2D Electron Gas at the $LaFeO_3/SrTiO_3$ Interface via Control of Oxygen Vacancies. *Advanced Materials* **29**, 1604447 (2017).

[87] Haynes, W. M. *CRC handbook of chemistry and physics* (CRC Press, 2011), 92nd edn.

[88] Cabrera, N. & Mott, N. F. Theory of the oxidation of metals. *Reports on Progress in Physics* **12**, 163 (1949).

[89] Tasker, P. W. The Stability of Ionic Crystal Surfaces. *Journal of Physics C: Solid State Physics* **12**, 4977–4984 (1979).

[90] Joshua, A., Pecker, S., Ruhman, J., Altman, E. & Ilani, S. A universal critical density underlying the physics of electrons at the $LaAlO_3/SrTiO_3$ interface. *Nature Communications* **3**, 1129 (2012).

[91] Smink, A. E. M. *et al.* Gate-Tunable Band Structure of the $LaAlO_3$-$SrTiO_3$ Interface. *Physical Review Letters* **118**, 106401 (2017).

[92] Cao, Y. *et al.* Anomalous orbital structure in a spinel–perovskite interface. *Npj Quantum Materials* **1**, 16009 (2016).

[93] Bert, J. A. *et al.* Gate-tuned superfluid density at the superconducting $LaAlO_3/SrTiO_3$ interface. *Physical Review B* **86**, 060503 (2012).

[94] Joshua, A., Ruhman, J., Pecker, S., Altman, E. & Ilani, S. Gate-tunable polarized phase of two-dimensional electrons at the $LaAlO_3/SrTiO_3$ interface. *Proceedings of the National Academy of Sciences* **110**, 9633–9638 (2013).

[95] Tufte, O. N. & Chapman, P. W. Electron mobility in semiconducting strontium titanate. *Physical Review* **155**, 796 (1967).

[96] Pavlenko, N., Kopp, T., Tsymbal, E. Y., Sawatzky, G. A. & Mannhart, J. Magnetic and superconducting phases at the $LaAlO_3/SrTiO_3$ interface: The role of interfacial Ti 3d electrons. *Physical Review B* **85**, 020407 (2012).

[97] Lontsi-Fomena, M., Villesuzanne, A., Doumerc, J.-P., Frayret, C. & Pouchard, M. A density functional theory study of oxygen diffusion in $LaAlO_3$ and $SrTiO_3$. *Computational Materials Science* **44**, 53–60 (2008).

[98] Cordero, F. Hopping and clustering of oxygen vacancies in $SrTiO_3$ by anelastic relaxation. *Physical Review B* **76**, 172106 (2007).

[99] Delahaye, J. & Grenet, T. Gate voltage control of the $AlO_x/SrTiO_3$ interface electrical properties. *Journal of Physics D: Applied Physics* **49**, 395303 (2016).

[100] Christensen, D. V. *et al.* Controlling interfacial states in amorphous/crystalline $LaAlO_3/SrTiO_3$ heterostructures by electric fields. *Applied Physics Letters* **102**, 021602 (2013).

[101] Leisegang, T. *et al.* Switching Ti Valence in $SrTiO_3$ by a dc Electric Field. *Physical Review Letters* **102**, 087601 (2009).

[102] Waser, R. & Aono, M. Nanoionics-based resistive switching memories. *Nature materials* **6**, 833–840 (2007).

[103] Szot, K., Speier, W., Bihlmayer, G. & Waser, R. Switching the electrical resistance of individual dislocations in single-crystalline $SrTiO_3$. *Nature Materials* **5**, 312–320 (2006).

[104] Ueno, K. *et al.* Electric-field-induced superconductivity in an insulator. *Nature Materials* **7**, 855–858 (2008).

[105] Lee, Y. *et al.* Phase Diagram of Electrostatically Doped $SrTiO_3$. *Physical Review Letters* **106**, 136809 (2011).

[106] Li, M., Graf, T., Schladt, T. D., Jiang, X. & Parkin, S. S. P. Role of Percolation in the Conductance of Electrolyte-Gated $SrTiO_3$. *Physical Review Letters* **109**, 196803 (2012).

[107] Sato, Y., Doi, K., Katayama, Y. & Ueno, K. Electrolyte dependence of transport properties of $SrTiO_3$ electric double layer transistors. *Japanese Journal of Applied Physics* **56**, 051101 (2017).

[108] Ueno, K. *et al.* Effective thickness of two-dimensional superconductivity in a tunable triangular quantum well of $SrTiO_3$. *Physical Review B* **89**, 020508 (2014).

[109] Bi, F. *et al.* "Water-cycle" mechanism for writing and erasing nanostructures at the $LaAlO_3/SrTiO_3$ interface. *Applied Physics Letters* **97**, 173110 (2010).

[110] Huijben, M. *et al.* Electronically coupled complementary interfaces between perovskite band insulators. *Nature Materials* **5**, 556–560 (2006).

[111] Di Gennaro, E. *et al.* Persistent Photoconductivity in 2D Electron Gases at Different Oxide Interfaces. *Advanced Optical Materials* **1**, 834–843 (2013).

[112] Laguta, V. V. *et al.* The photoinduced Ti^{3+} centre in $SrTiO_3$. *Journal of Physics: Condensed Matter* **14**, 13813 (2002).

[113] Lei, Y. *et al.* Visible-light-enhanced gating effect at the $LaAlO_3/SrTiO_3$ interface. *Nature Communications* **5**, 5554 (2014).

[114] Bell, C. *et al.* Dominant Mobility Modulation by the Electric Field Effect at the $LaAlO_3/SrTiO_3$ Interface. *Physical Review Letters* **103**, 226802 (2009).

[115] Hamaguchi, C. *Basic semiconductor physics* (Springer Berlin Heidelberg, Berlin, Heidelberg, 2010).

[116] Huijben, M. *et al.* Defect Engineering in Oxide Heterostructures by Enhanced Oxygen Surface Exchange. *Advanced Functional Materials* **23**, 5240–5248 (2013).

[117] Umansky, V. *et al.* MBE growth of ultra-low disorder 2DEG with mobility exceeding 35×10^6 cm^2/Vs. *Journal of Crystal Growth* **311**, 1658–1661 (2009).

[118] Mikheev, E. *et al.* Limitations to the room temperature mobility of two- and three-dimensional electron liquids in $SrTiO_3$. *Applied Physics Letters* **106**, 062102 (2015).

[119] van der Marel, D., van Mechelen, J. L. M. & Mazin, I. I. Common Fermi-liquid origin of T^2 resistivity and superconductivity in n-type $SrTiO_3$. *Physical Review B* **84**, 205111 (2011).

[120] Mikheev, E. *et al.* Carrier density independent scattering rate in $SrTiO_3$-based electron liquids. *Scientific Reports* **6**, 20865 (2016).

[121] Klimin, S. N., Tempere, J., van der Marel, D. & Devreese, J. T. Microscopic mechanisms for the Fermi-liquid behavior of Nb-doped strontium titanate. *Physical Review B* **86**, 045113 (2012).

[122] Low, F. E. & Pines, D. Mobility of slow electrons in polar crystals. *Physical Review* **98**, 414 (1955).

[123] Peeters, F. M., Wu, X. & Devreese, J. T. Exact and approximate results for the mass of a two-dimensional polaron. *Physical Review B* **37**, 933 (1988).

[124] Lee, C., Yahia, J. & Brebner, J. L. Electronic conduction in slightly reduced strontium titanate at low temperatures. *Physical Review B* **3**, 2525 (1971).

[125] Okuda, T., Nakanishi, K., Miyasaka, S. & Tokura, Y. Large thermoelectric response of metallic perovskites: $Sr_{1-x}La_xTiO_3$ ($0\leq x\leq 0.1$). *Physical Review B* **63**, 113104 (2001).

[126] Sanders, T. D., Gray, M. T., Wong, F. J. & Suzuki, Y. $LaAlO_3/SrTiO_3$ interfaces doped with rare-earth ions. *Physical Review B* **91**, 205112 (2015).

[127] Gardner, B. W. *et al.* Scanning superconducting quantum interference device susceptometry. *Review of Scientific Instruments* **72**, 2361–2364 (2001).

[128] Huber, M. E. *et al.* Gradiometric micro-SQUID susceptometer for scanning measurements of mesoscopic samples. *Review of Scientific Instruments* **79**, 053704 (2008).

[129] Kalisky, B. *et al.* Locally enhanced conductivity due to the tetragonal domain structure in $LaAlO_3/SrTiO_3$ heterointerfaces. *Nature Materials* 1–5 (2013).

[130] Monroe, D. Comparison of mobility-limiting mechanisms in high-mobility $Si_{1-x}Ge_x$ heterostructures. *Journal of Vacuum Science & Technology B: Microelectronics and Nanometer Structures* **11**, 1731 (1993).

[131] Posadas, A. B., Lin, C., Demkov, A. A. & Zollner, S. Bandgap engineering in perovskite oxides: Al-doped $SrTiO_3$. *Applied Physics Letters* **103**, 142906 (2013).

[132] Sun, J. & Kosel, J. Extraordinary Magnetoresistance in Semiconductor/Metal Hybrids: A Review. *Materials* **6**, 500–516 (2013).

[133] Lenz, J. & Edelstein, S. Magnetic sensors and their applications. *IEEE Sensors Journal* **6**, 631–649 (2006).

[134] Jin, S., McCormack, M., Tiefel, T. H. & Ramesh, R. Colossal magnetoresistance in La-Ca-Mn-O ferromagnetic thin films (invited). *Journal of Applied Physics* **76**, 6929–6933 (1994).

[135] Los, V. F. & Pogorily, A. N. Magnetoresistance of metallic magnetic multilayers in the ballistic regime for a spacer. *Journal of Physics D: Applied Physics* **33**, 1267 (2000).

[136] David, A. *et al.* Colossal positive magnetoresistance in surface-passivated oxygen-deficient strontium titanite. *Scientific Reports* **5**, 10255 (2015).

[137] Solin, S. A., Thio, T., Hines, D. R. & Heremans, J. J. Enhanced room-temperature geometric magnetoresistance in inhomogeneous narrow-gap semiconductors. *Science* **289**, 1530–1532 (2000).

[138] Hewett, T. H. & Kusmartsev, F. V. Geometrically enhanced extraordinary magnetoresistance in semiconductor-metal hybrids. *Physical Review B* **82** (2010).

[139] Xu, R. *et al.* Large magnetoresistiance in non-magnetic silver chalcogenides. *Nature* **390**, 57–60 (1997).

[140] Hu, J. & Rosenbaum, T. F. Classical and quantum routes to linear magnetoresistance. *Nature Materials* **7**, 697–700 (2008).

[141] Porter, N. A. & Marrows, C. H. Linear magnetoresistance in n-type silicon due to doping density fluctuations. *Scientific Reports* **2**, 565 (2012).

[142] Parish, M. M. & Littlewood, P. B. Classical magnetotransport of inhomogeneous conductors. *Physical Review B* **72**, 094417 (2005).

[143] Kozlova, N. *et al.* Linear magnetoresistance due to multiple-electron scattering by low-mobility islands in an inhomogeneous conductor. *Nature Communications* **3**, 1097 (2012).

[144] Li, L., Richter, C., Mannhart, J. & Ashoori, R. C. Coexistence of magnetic order and two-dimensional superconductivity at $LaAlO_3/SrTiO_3$ interfaces. *Nature Physics* **7**, 762–766 (2011).

[145] Stornaiuolo, D. *et al.* Tunable spin polarization and superconductivity in engineered oxide interfaces. *Nature Materials* **15**, 278–283 (2015).

[146] Tomarken, S. L., Young, A. F., Lee, S. W., Gordon, R. G. & Ashoori, R. C. Torque magnetometry of an amorphous-alumina/strontium-titanate interface. *Physical Review B* **90**, 201113 (2014).

[147] Nagaosa, N., Sinova, J., Onoda, S., MacDonald, A. H. & Ong, N. P. Anomalous Hall effect. *Reviews of Modern Physics* **82**, 1539–1592 (2010).

[148] Pippard, A. B. *Magnetoresistance in metals* (Cambridge University Press, 1989), 1st edn.

[149] McKenzie, R. H., Qualls, J. S., Han, S. Y. & Brooks, J. S. Violation of Kohler's rule by the magnetoresistance of a quasi-two-dimensional organic metal. *Physical Review B* **57**, 11854 (1998).

[150] Kalisky, B. *et al.* Critical thickness for ferromagnetism in $LaAlO_3/SrTiO_3$ heterostructures. *Nature Communications* **3**, 922 (2012).

[151] Wang, X. *et al.* Magnetoresistance of two-dimensional and three-dimensional electron gas in $LaAlO_3/SrTiO_3$ heterostructures: Influence of magnetic ordering, interface scattering, and dimensionality. *Physical Review B* **84**, 075312 (2011).

[152] Ben Shalom, M. *et al.* Anisotropic magnetotransport at the $SrTiO_3/LaAlO_3$ interface. *Physical Review B* **80**, 140403 (2009).

[153] Gunkel, F. *et al.* Defect Control of Conventional and Anomalous Electron Transport at Complex Oxide Interfaces. *Physical Review X* **6**, 031035 (2016).

[154] Banerjee, S., Erten, O. & Randeria, M. Ferromagnetic exchange, spin-orbit coupling and spiral magnetism at the $LaAlO_3/SrTiO_3$ interface. *Nature Physics* **9**, 626–630 (2013).

{2.7182818284}